NNT/NL : 2021AIXM0356/039ED352

THÈSE DE DOCTORAT

Soutenue à Aix-Marseille Université
le 22 Septembre 2021 par

Junais

Star formation and its history in low surface brightness galaxies

Discipline
Sciences de l'Univers

Spécialité
Astrophysique et Cosmologie

École doctorale
Ecole Doctorale Physique et Sciences de la Matière ED352

Laboratoire/Partenaires de recherche
Laboratoire d'Astrophysique de Marseille (LAM)

Composition du jury

Françoise COMBES Observatoire de Paris, LERMA	Rapporteur
Gaspar GALAZ Pontificia Universidad Católica de Chile	Rapporteur
Pierre-Alain DUC Observatoire astronomique de Strasbourg	Examinateur
Ignacio Trujillo Instituto de Astrofísica de Canarias	Examinateur
Véronique BUAT LAM	Présidente du jury
Samuel BOISSIER LAM	Directeur de thèse

I, Junais, hereby declare that the work presented in this manuscript is my own work, carried out under the scientific direction of Samuel Boissier, in accordance with the principles of honesty, integrity and responsibility inherent to the research mission. The research work and the writing of this manuscript have been carried out in compliance with both the french national charter for Research Integrity and the Aix-Marseille University charter on the fight against plagiarism.

This work has not been submitted previously either in this country or in another country in the same or in a similar version to any other examination body.

Marseille, 12 July 2021

JUNAIS

Résumé

Les galaxies sont l'une des principales sources de matière baryonique brillante dans l'univers, ce qui en fait un outil important dans l'étude de la formation et de l'évolution de notre univers. En astronomie, nous dépendons principalement de la "lumière" (rayonnement électromagnétique) d'une galaxie lointaine pour étudier ses propriétés. Aussi utile soit-elle, cette lumière représente également un sérieux défi dans notre capacité à observer toutes les galaxies qui existent. De nombreuses galaxies sont perdues dans le bruit de la lumière diffusée dans le fond du ciel. Cela pourrait donner lieu à un biais considérable dans la sélection des galaxies dans nos catalogues (nous ne verrions que les galaxies relativement plus lumineuses). Si les galaxies doivent être utilisées comme des sondes cosmologiques efficaces pour l'étude de l'univers, alors nos catalogues doivent être complets et homogènes (Impey & Bothun 1997). Il est probable qu'il y ait un grand nombre de galaxies faibles manquantes dans nos observations.

Les galaxies peu lumineuses et diffuses qui émettent beaucoup moins de lumière par unité de surface que les galaxies normales sont connues sous le nom de LSB (*Low Surface Brightness*, en anglais). Bien qu'il n'existe pas de convention absolue pour caractériser les LSB, elles sont généralement définies comme des galaxies dont la luminosité de surface centrale du disque (μ_0) est beaucoup plus faible que la valeur de Freeman (1970) typique des galaxies à disque ($\mu_{0,B} = 21,65 \pm 0,30$ mag arcsec^{-2}). Cependant, il existe aussi plusieurs autres définitions dans la littérature pour les classer.

Les LSBs représentent probablement une fraction significative (50% ou plus) de toutes les galaxies de l'univers (O'Neil & Bothun 2000; Martin et al. 2019). Cette grande population de LSB sera cruciale pour nos modèles cosmologiques actuels car elle affecte la forme de la fonction de luminosité des galaxies (Blanton et al. 2005); et aussi pour comprendre la nature de la matière noire (DM) puisque les LSB sont généralement considérées comme dominées par la DM (Pickering et al. 1997). Les LSBs permettent également d'étudier la formation d'étoiles dans le régime de faible densité (Boissier et al. 2008; Wyder et al. 2009; Bigiel et al. 2010), pour laquelle de nombreuses questions sont encore débattues (par exemple, la moindre efficacité, l'existence d'un seuil pour la formation d'étoiles, les variations de la fonction de masse initiale). Résoudre ces questions cruciales dans les LSBs pourrait changer entièrement notre compréhension actuelle des scénarios de formation et d'évolution des galaxies.

L'origine des LSBs est encore mal comprise en raison de leur extrême faiblesse qui empêche des observations approfondies. Ces dernières années, grâce à de puissants instruments (par exemple le télescope Dragonfly, la camera MEGACAM du Télescope

Canada France Hawaï, la caméra Hyper Suprime-Cam de Subaru), nous avons ouvert une nouvelle fenêtre pour étudier les LSBs en détail.

Les LSBs couvrent une large gamme de tailles, de masses et de morphologies, depuis les plus grandes galaxies existantes jusqu'aux naines les plus communes. Les galaxies géantes à faible brillance de surface (GLSBs, pour *Giant Low Surace Brightness galaxies* en anglais) et les galaxies ultra-diffuses (UDGs, pour *Ultra Diffuse Galaxies*, en anglais) sont deux sous-populations importantes de LSBs. Les GLSBs ont généralement un disque LSB extrêmement étendu avec des longueurs d'échelle allant de ~10 kpc à ~50 kpc (Bothun et al. 1987). Elles sont également riches en gaz ($M_{HI} \sim 10^{10} M_{\odot}$; Matthews et al. 2001). Malgré leur faible brillance de surface centrale, elles sont parfois aussi massives que de nombreuses galaxies "régulières" (Sprayberry et al. 1995). D'autre part, les UDGs sont des galaxies étendues peu lumineuses, aussi grandes que la Voie lactée (rayon effectif de l'ordre de $1-5$ kpc et $\mu_{0,g} > 24$ mag arcsec^{-2} ; van Dokkum et al. 2015), mais avec des masses stellaires similaires à celles des galaxies naines ($\sim 10^7 - 10^8\ M_{\odot}$). Le but de ma thèse est d'étudier les propriétés des LSBs en général, avec une attention particulière sur la population des GLSBs et UDGs.

Cette thèse est divisée en trois parties. La partie I qui comprend les chapitres 1 et 2 donne une introduction de base sur le contexte des galaxies et l'étude des LSBs. Le chapitre 1 décrit l'importance des galaxies en tant qu'élément constitutif de l'univers et leurs différentes classifications. Plusieurs outils tels que la photométrie et la spectroscopie, qui sont généralement utilisés pour l'étude des galaxies et ceux spécifiquement utilisés dans mon travail sont discutés. De plus, dans ce chapitre, j'aborde également les différents facteurs environnementaux (par exemple, le stripping de la pression de bélier, les interactions de marée) qui façonnent l'évolution des galaxies, dont certains seront étudiés en détail plus tard dans ce travail.

Avec le chapitre 2, j'entre dans le monde des galaxies à faible brillance de surface. Je décris brièvement le contexte des galaxies LSB et leur signification. Les différentes définitions existantes dans la littérature pour les LSB sont également discutées. A la fin du chapitre, j'explique au lecteur l'importance de l'étude de la grande population des LSBs et l'intérêt récent des chercheurs dans ce domaine (dont certains ont été abordés ci-dessus). De nombreuses recherches sur la formation et l'évolution des galaxies LSB sont actuellement en cours, auxquelles je participerai désormais avec ce travail de thèse.

J'ai dédié la partie II avec les chapitres 3 et 4 à la classe des galaxies géantes à faible brillance de surface. Parmi les GLSBs, la galaxie Malin 1 est la plus connue. C'est aussi un cas extrême avec une extension radiale de ~120 kpc (Moore & Parker 2006), $\mu_{0,V} \sim 25.5$ mag arcsec^{-2} (Impey & Bothun 1997) et $M_{HI} \sim 5 \times 10^{10} M_{\odot}$ (Pickering et al. 1997; Matthews et al. 2001). C'est l'une des plus grandes galaxies LSB connues et un archétype de la classe des GLSBs (voir Fig. 0.1). Cependant, la structure et l'origine de cette bête géante ne sont toujours pas claires, notamment en raison du manque de données cinématiques et spectroscopiques à haute résolution. Par conséquent, dans le chapitre 3 Je réalise une nouvelle étude spectroscopique sur Malin 1 afin d'apporter de nouvelles contraintes sur la nature de cette galaxie. J'ai utilisé les

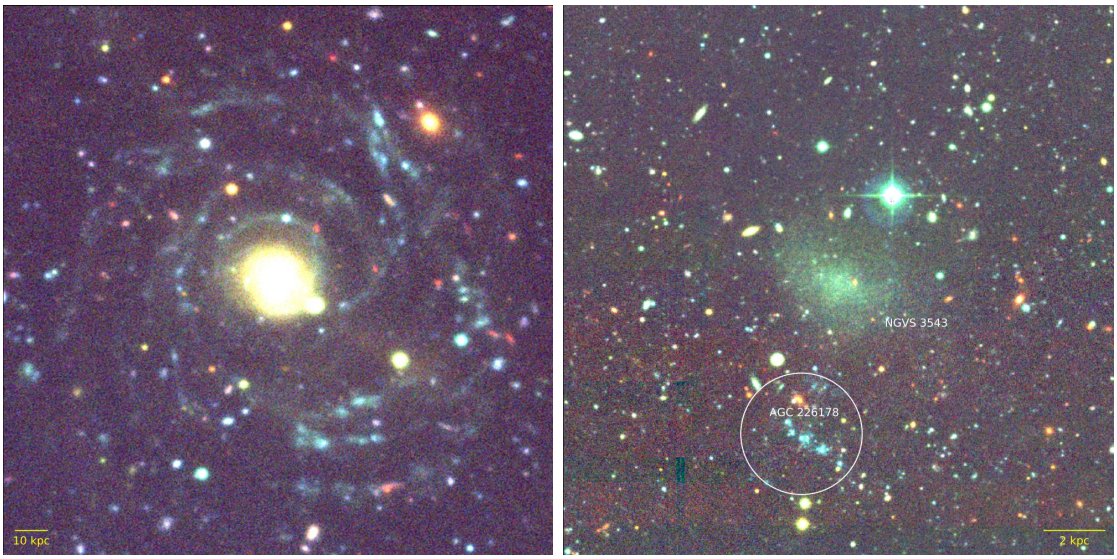

Figure 0.1.: Images couleur du projet NGVS (Ferrarese et al. 2012) dans les bandes *u*, *g* et *i* de la galaxie GLSB Malin 1 (à gauche) et de la galaxie ultra-diffuse NGVS 3543 (à droite). La galaxie candidate presque sombre AGC 226178 avec la position de son nuage de gaz H I est représentée par le cercle blanc. Voir les chapitres 3 et 7 pour plus de détails sur ces sources.

données spectroscopiques à longue fente de Malin 1 obtenues par le spectrographe IMACS-Magellan (Observatoire de Las Campanas, Chili). Après avoir effectué un processus rigoureux de réduction des données, j'ai extrait un total de 16 spectres de différentes régions de Malin 1, y compris une région allant jusqu'à ~26 kpc dans son disque étendu. En utilisant les raies d'émission Hα et [O II] dans ces spectres, j'ai obtenu une nouvelle courbe de rotation pour Malin 1. Les raies d'émission Hα ont également été utilisées pour faire une estimation de la densité de surface du taux de formation d'étoiles dans quelques régions. Pour la première fois, nous observons une montée très raide dans la courbe de rotation interne de Malin 1 jusqu'à ~400 km s^{-1}, suivie d'une région de plateau cohérente avec les observations H I de Lelli et al. (2010). Une modélisation de la masse basée sur ces données indique que la dynamique de la région interne de Malin 1 peut être dominée par les étoiles mais qu'à de grands rayons, un halo de matière noire massif est nécessaire. Les taux de formation d'étoiles (SFR, pour *Star Formation Rate*, en anglais) dérivés du flux Hα sont également cohérents avec un disque de type précoce pour la région interne. Cependant, le niveau de SFR dans le disque étendu de Malin 1 est proche du niveau trouvé dans les galaxies UV étendues (XUVs ; Thilker et al. 2007; Bigiel et al. 2010), indiquant une similarité entre les XUVs et les GLSBs. Pour comprendre la nature de Malin 1 plus en détail, nous aurons besoin à l'avenir de données de meilleure qualité comme les observations IFU (par exemple MUSE). Le travail sur Malin 1, présenté dans ce chapitre est publié dans Junais et al. (2020).

Dans le chapitre 4 Je discute de toute la famille des GLSBs, y compris Malin 1. Un

bref historique de l'étude des GLSBs dans la littérature y est abordé, ainsi que les différents scénarios de formation proposés pour ces sources. Les GLSB sont aujourd'hui considérées comme rares (nous n'en avons découvert que quelques-unes) et existent sous forme de galaxies isolées. Par conséquent, dans ce chapitre, je présente un échantillon de 21 galaxies GLSB sélectionnées par leur masse importante de gaz H I (et pour lesquelles nous avons des données UV traçant la formation stellaire) qui nous sont actuellement connues. Cet échantillon servira de référence pour lancer une nouvelle étude sur la population des GLSBs dans mes travaux futurs. J'ai initié ce processus en proposant plusieurs observations de suivi sur cet échantillon à différentes longueurs d'onde (par exemple, photométrie UV avec UVIT, spectroscopie optique avec IMACS-Magellan, observation IFU MUSE de Malin 1). Quelques observations parmi celles-ci sont déjà terminées. Cependant, pour une étude détaillée de la population des GLSBs, nous devons obtenir de nouvelles données d'observation pour l'ensemble de l'échantillon. À la fin du chapitre 4, je discute de quelques perspectives sur ce qui sera réalisé dans notre compréhension des GLSBs dans les travaux futurs, une fois que nous commencerons à obtenir plus de données sur ces galaxies.

La partie III, qui comprend les chapitres 5, 6, 7, est consacrée à mes travaux sur les UDGs et autres LSBs dans l'amas de la Vierge. Les UDGs se trouvent généralement en grand nombre dans les amas de galaxies (Koda et al. 2015; van Dokkum et al. 2015; van der Burg et al. 2016). Par conséquent, l'amas de la Vierge, qui est l'amas de galaxies le plus proche de nous et le plus riche, est un endroit idéal pour l'étude des UDGs. Cela permettra également de sonder le rôle de l'environnement dans le façonnement de la formation des UDG.

Il existe plusieurs ensembles de données multi-longueurs d'onde provenant d'une poignée de relevés effectués sur l'amas de la Vierge au cours des dernières années. En utilisant le potentiel de données de haute qualité provenant d'études comme NGVS (optique ; Ferrarese et al. 2012), VESTIGE (Hα bande étroite ; Boselli et al. 2018a) et GUViCS (UV ; Boselli et al. 2011), j'ai réalisé une étude complète d'un échantillon de 135 galaxies LSB/UDG dans l'amas de la Vierge. La sélection de l'échantillon a été effectuée en combinant les différentes définitions de galaxies LSB existant dans la littérature (Sprayberry et al. 1995; van Dokkum et al. 2015; Lim et al. 2020). Le chapitre 5 traite d'abord de la collecte des données et de la préparation des images et des masques de contaminants avant d'effectuer les mesures photométriques sur l'échantillon. Ensuite, j'explique la mesure des profils radiaux de luminosité de surface et d'autres quantités photométriques (par exemple, magnitudes, couleurs, rayons effectifs) pour l'ensemble de l'échantillon. Ensuite, une analyse de ces propriétés est effectuée. Par exemple la distribution des couleurs $g-i$ de l'échantillon culmine à $g-i \sim 0.7$ mag, indiquant que les UDGs de mon échantillon sont cohérentes avec la population d'UDGs rouges généralement trouvés dans les amas. Cependant, la présence de quelques UDGs bleus ($g-i < 0.6$ mag) peut également être identifiée dans l'échantillon, similaire aux UDGs bleus trouvés dans les environnements de champs (Prole et al. 2019). Pour approfondir cette différence de couleurs, j'ai analysé la distribution des couleurs de l'échantillon par rapport à la distance du centre de l'amas.

Cette analyse indique l'existence d'un gradient couleur-distance, où les sources les plus éloignées du centre de l'amas ont les couleurs les plus bleues. De plus, un grand nombre de ces sources plus bleues ont des contreparties H I associées lorsqu'elles sont croisées avec le catalogue H I du relevé ALFALFA (Haynes et al. 2018). Cette variation des propriétés observées par rapport à la distance de l'amas indique une dépendance environnementale dans la formation de ces sources. J'étudierai cette question plus en détail dans le chapitre 6.

Le chapitre 6 traite de la comparaison des données observées présentées au chapitre 5 avec un ensemble de modèles d'évolution chimique et spectrophotométrique des galaxies, initialement développés par Boissier & Prantzos (1999, 2000). Cet ensemble simple de modèles numériques, qui a été étendu par Boselli et al. (2006), reproduit l'évolution d'une galaxie à disque dans un environnement d'amas lorsqu'elle est soumise à des effets environnementaux tels que le dépouillement par pression dynamique (RPS, pour *Ram Pressure Stripping*, en anglais). Une comparaison de la prédiction de ces modèles avec les mesures photomériques dans mon échantillon indique que presque toutes les sources de l'échantillon sont des galaxies étendues de faible masse (ce qui est typique des UDGs) qui ont subi de forts événements RPS au cours de leur vie. De plus, d'après les modèles, ces galaxies avant de subir des effets RPS (ou en d'autres termes, avant d'entrer dans l'amas) étaient des galaxies riches en gaz. Ceci est similaire à la population d'UDG riche en gaz H I trouvées dans les environnements de champs (Leisman et al. 2017; Janowiecki et al. 2019). Cependant, les effet de RPS les ont radicalement transformées en sources rouges pauvres en gaz que nous observons maintenant. De plus, tout comme le gradient de couleur observé dans l'échantillon, il y a également une indication d'un gradient de l'époque de l'épisode RPS avec la distance. Les galaxies vers le bord de l'amas ont des événements RPS en cours ou récents (dans les 200 derniers million d'années) que celles près du centre de l'amas avec des événements RPS qui se sont produits dans un passé lointain (typiquement il y a environ 1,5 Gyr). Les résultats de l'observation et de la modélisation suggèrent que le *stripping* par pression dynamique joue un rôle important dans l'évolution des UDG dans les amas. Les résultats du chapitre 5 et du chapitre 6 seront prochainement publiés dans un prochain article (Junais et al. en préparation).

Une autre confirmation des résultats des chapitres 5 et 6 a été obtenue par une analyse détaillée de l'une des UDGs de mon échantillon. Ceci est discuté dans le chapitre 7. Au cours de l'analyse du grand échantillon de LSBs/UDGs dans l'amas de la Vierge, j'ai identifié une queue de régions de formation d'étoiles récente avec des émissions optiques, Hα et UV, proches d'une UDG (NGVS 3543; voir Fig. 0.1). Ces émissions coïncident également avec un nuage de gaz H I précédemment identifié comme une "galaxie presque sombre" AGC 226178 (Cannon et al. 2015). Les galaxies sombres (galaxies avec du gaz mais sans étoiles) étaient généralement considérées comme une solution possible au grand nombre de petites galaxies prédites par la cosmologie ΛCDM (Verde et al. 2002). Cependant, des étoiles ont finalement été découvertes dans la plupart des galaxies sombres candidates, et le nouvel intérêt s'est

porté sur les objets "presque sombres" ou "quasi sombres" qui sont des objets riches en gaz sans beaucoup de lumière stellaire (Cannon et al. 2015; Janowiecki et al. 2015). La formation de ce type d'objets fait encore l'objet de débats.

J'ai donc cherché des réponses sur la connexion possible entre AGC 226178 et NGVS 3543 en analysant le système en détail. Les résultats de la modélisation de l'UDG indiquent que NGVS 3543 subit un événement RPS en cours qui a débuté il y a près de 200 millions d'années et qui a entraîné la disparition de la quasi-totalité de son gaz (M_{gas} de $\sim 10^8$ à 10^5 $M_\odot$) pour former une UDG rouge pauvre en gaz. Après cet événement, une partie du gaz dénudé s'est refroidie pour former les régions de formation d'étoiles et le nuage de gaz H I associé de AGC 226178. ($M_{HI} = 4 \times 10^7$ $M_\odot$). De même, une analyse des propriétés photométriques des régions associées à AGC 226178 indique qu'elles sont jeunes avec des âges de quelques dizaines de millions d'années seulement, ce qui est cohérent avec l'échelle de temps de l'événement RPS qui a commencé il y a près de 200 millions d'années. Ceci nous indique que AGC 226178, habituellement considérée comme une galaxie presque obscure, pourrait en fait être formée à la suite du dépouillement par pression dynamique du gaz de son compagnon proche UDG. Un tel scénario nous fournit un indice important sur la prédominance des UDGs rouges dans les amas proches et la formation des galaxies presque sombres discutée dans la littérature. Ces résultats du chapitre 7 sont publiés dans Junais et al. (2021).

Ce travail de thèse explore la puissance des données d'observation combinées à des modèles numériques simples pour comprendre la nature des LSB. Je pense que mon travail contribuera de manière significative à répondre à de nombreuses questions concernant la formation et l'évolution de ces sources, qui sont toujours débattues au sein de la communauté astronomique. De plus, les résultats que j'ai obtenus dans ce travail peuvent être facilement testés (et devraient être testés) en utilisant des observations de suivi. Nous sommes maintenant à un moment où les études sur les LSB prennent un rythme rapide. Nous avons une occasion parfaite de découvrir le monde des galaxies LSB avec les futurs relevés profonds couvrant une très grande partie du ciel (par exemple LSST, Euclid, SKA), dans lesquels des LSB devraient être trouvées en très grand nombre, ou bien avec des spectrographes à champ intégral (IFU pour *Integral Field Unit* en anglais), comme MUSE (actuellement sur le VLT) ou Blue MUSE (en projet), qui permettront en outre de les étudier en détail. Soyons prêts et excités pour ces jours glorieux à venir.

Abstract

Low surface brightness galaxies (LSBs) may represent a significant fraction (50% or more) of all the galaxies in the universe. However, their origin is still poorly understood due to their extreme faintness hindering in-depth observations. In recent years with powerful instruments, we opened a new window towards studying LSBs in great detail.

Giant low surface brightness galaxies (GLSBs) and Ultra-Diffuse Galaxies (UDGs) are two prominent sub-population of LSBs. GLSBs are generally found to have extremely extended and massive gas-rich LSB discs, whereas UDGs are faint extended galaxies with stellar masses similar to dwarf galaxies, but with scale-lengths as large as the Milky Way.

In this thesis, I use long-slit spectroscopic data of Malin 1, the archetype of GLSB galaxies, to bring new constraints on the nature of this galaxy. Using the Hα and [O II] emission lines, I extracted a new rotation curve and estimated the star formation rate surface density within a few regions of Malin 1. For the first time, we observe a very steep rise in the inner rotation curve of Malin 1 up to ~400 km s^{-1}, followed by a plateau consistent with HI observations. A mass modelling based on this indicates that the dynamics of the inner region of Malin 1 may be dominated by the stars but at large radii a massive dark matter halo is necessary. The derived star formation rates (SFR) are also consistent with an early-type disc for the inner region, but the extended disc with an SFR level much less than normal spirals. To understand the nature of Malin 1 and other GLSBs in more detail, in future we need better quality data like IFU observations.

In a second approach, I made a comprehensive study on a sample of 135 LSB/UDG galaxies in the Virgo cluster using a multiwavelength set of photometric data obtained from the NGVS (optical), VESTIGE (Hα narrow-band) and GUViCS (UV) surveys. The photometric properties of this sample indicate that they are consistent with the population of red UDGs generally found in clusters. There is also an indication of a colour-distance gradient, where sources farther from the cluster centre have bluer colours. A comparison of the sample with models of galaxy evolution including environmental effects like ram-pressure stripping (RPS), also points to a similar direction. Almost all of the sources in the sample have undergone strong RPS events in their lifetime, turning otherwise gas-rich galaxies into these red galaxies we observe now. The onset of the RPS event also shows a similar distance gradient, where the galaxies towards the edge of the cluster have ongoing or recent RPS events than those near the cluster centre with RPS events occurred in the distant past.

I performed a detailed analysis of one of these UDGs that showed signs of a stripped tail of star forming regions in its vicinity, coinciding with an HI cloud previously

identified as an “almost dark galaxy” AGC 226178. My results indicate that AGC 226178 may have formed from an ongoing RPS event that started nearly 200 Myr ago, transforming it into a red UDG. This provides us with an important clue on the predominance of red UDGs in nearby clusters and the formation of almost dark galaxies discussed in the literature.

This work will also be crucial in the identification of LSB galaxies and the study of their properties for future deep surveys (e.g. LSST, Euclid, SKA) that will observe LSBs in very large numbers.

Acknowledgements

To thank someone is not always to say "Thank you". Sometimes there are instances where words could just poorly express what one feels like communicating. A thank you note may not able to carry that feeling.

Doing a Ph.D and writing a thesis by the end of it was not just a process of doing research for me. It had a life on its own. There was a birth, when I first stepped into the world of research. Then a growth phase. Slowly, I took some baby steps, learned new things. Sometimes there were pitfalls and I had to rise up again. The cycle continued. Along the way, there were new faces and connections. Some stayed and some faded away. All of them had a role in making it a cocktail of emotions, achievements and memories.

Now, to write the same in a more conventional way, I thank everyone for being a part of my journey through this PhD work. Especially my supervisor Samuel Boissier for all his support and nice interactions that helped in shaping this thesis. It was great working with you, and I hope I will be able to continue that later in my career too. I would also like to express my gratitude to my family (Mom, Thatha, Semi, Kakku, Rasna, Anees, Asna and the kids), friends (Ajmal, Basith, Bidhun, Gayathri, Jana, Jibin, Manu, Mathew, Midhun, Roshin, Sarra, Shibili, Shreya, Siddarth) and all those were always there for my support. It is hard to name all of the people who I would like to thank, but I hope everyone who knows me will understand that I will always have that gratitude for them.

I dedicate this to ALL OF YOU!

Sincerely,
Junais

Contents

Résumé 8

Abstract 10

Acknowledgements 11

Contents 12

List of Figures 15

List of Tables 26

I Introduction 28

1 What are galaxies and why do we study them ? 29
- 1.1 Galaxies as a building block of the universe . . . 29
- 1.2 Galaxy classifications . . . 30
- 1.3 Observable tools for galaxy properties . . . 31
  - 1.3.1 Photometric colours . . . 31
  - 1.3.2 Spectroscopy . . . 32
- 1.4 Role of environment in shaping galaxy evolution . . . 35
- 1.5 What is still missing from our picture? . . . 36

2 The Realm of Low Surface Brightness Galaxies 37
- 2.1 What are Low Surface Brightness Galaxies? . . . 37
- 2.2 Significance of LSBs . . . 38
- 2.3 LSB definitions and sub-populations . . . 40
- 2.4 A new interest in the recent years . . . 43

II Giant Low Surface Brightness Galaxies 44

3 The Mysterious case of Malin 1 45
- 3.1 A peek into the past . . . 45
- 3.2 A new spectroscopic study . . . 47
  - 3.2.1 Source of Data . . . 48
  - 3.2.2 Data reduction . . . 48

3.2.3 Measurements . . . 55
3.2.4 Results . . . 58
3.2.5 A new mass model for Malin 1 . . . 65
3.2.6 Conclusions . . . 69

4 The family of giant LSBs **70**
4.1 A history of what we know about GLSB galaxies . . . 70
4.2 A sample of GLSBs . . . 71
4.2.1 Followup spectroscopy and photometry . . . 73
4.3 Perspectives . . . 78

III Ultra Diffuse Galaxies **80**

5 A new sample of LSBs in the Virgo cluster **81**
5.1 Context . . . 81
5.2 Data . . . 83
5.2.1 NGVS . . . 83
5.2.2 GUViCS . . . 84
5.2.3 VESTIGE . . . 84
5.3 Sample selection . . . 84
5.4 Measurements . . . 94
5.4.1 Creation of stamps . . . 94
5.4.2 Preparation of masks and further processing of the stamps . . . 95
5.4.3 Background sky measurements . . . 96
5.4.4 Extraction of surface brightness profiles . . . 96
5.4.5 Surface brightness profile decomposition . . . 98
5.4.6 New determination of effective radii . . . 102
5.4.7 Integrated magnitudes . . . 102
5.5 Preliminary analysis . . . 111
5.5.1 Colour distribution . . . 111
5.5.2 Gradient in colour . . . 111
5.5.3 Colour-Magnitude Diagram . . . 111
5.6 A sub-sample: cross-correlation with H I from ALFALFA . . . 115
5.7 Conclusions . . . 115

6 Galaxy evolution modelling **119**
6.1 The framework of the models . . . 119
6.1.1 Main ingredients of the Milky Way model . . . 119
6.1.2 Extension to other disk galaxies . . . 120
6.1.3 Modelling the effect of ram-pressure stripping . . . 121
6.2 Grid of parameters . . . 122
6.3 Fitting of models . . . 123
6.4 Results . . . 124

6.4.1 Distribution of V_C, λ and t_{rps} . . . 124
6.4.2 Colour and t_{rps} gradient . . . 127
6.4.3 Evolution of gas mass, stellar mass and star formation rate . . . 127
6.5 Conclusions . . . 129

7 A Detailed case: Transition of a gas-rich UDG into a gas-poor UDG 135
7.1 Introduction . . . 135
7.2 Data . . . 137
7.3 Galaxy evolution models with ram-pressure stripping applied to NGVS 3543 . . . 137
7.4 Identification and selection of young regions around the UDG . . . 141
7.4.1 u-band selection of regions . . . 142
7.4.2 NUV selection of regions . . . 142
7.5 Photometry of the selected regions . . . 145
7.6 Age and stellar mass estimation . . . 145
7.6.1 Fitting Starburst99 models with the photometry . . . 145
7.6.2 Confirmation with CIGALE . . . 150
7.6.3 Gradients among the regions . . . 152
7.7 A global scenario for the blue to red transition of a UDG . . . 152

Conclusion and perspectives 159

Bibliography 160

ANNEXES 169
A Published papers . . . 169
A.1 First spectroscopic study of ionised gas emission lines in the extreme low surface brightness galaxy Malin 1 . . . 169
A.2 A Virgo Environmental Survey Tracing Ionised Gas Emission (VESTIGE) — X. Formation of a red ultra-diffuse galaxy and an almost dark galaxy during a ram-pressure stripping event . . . 187

List of Figures

0.1 Images couleur du projet NGVS (Ferrarese et al. 2012) dans les bandes *u*, *g* et *i* de la galaxie GLSB Malin 1 (à gauche) et de la galaxie ultra-diffuse NGVS 3543 (à droite). La galaxie candidate presque sombre AGC 226178 avec la position de son nuage de gaz H I est représentée par le cercle blanc. Voir les chapitres 3 et 7 pour plus de détails sur ces sources. . . . 5

1.1 The Hubble tuning fork diagram. Image credit: Prole (2019) and CANDELS survey. . . . 30
1.2 Multi-wavelength images of the nearby spiral galaxy M81 from X-ray to Radio (Ferreras 2019). . . . 32
1.3 Timescales for the star formation history as a function of the wavelength in different photometric filters (black squares from left to right - UV: GALEX FUV, NUV, and FOCA; optical/blue: Sloan *u* and Jonhson U; optical/red/near-infrared: *g*, *r*, *i*, *z*, B, V, R, Rc, I, Ic, J, H, K). The green solid line shows the time taken for a stellar population to reach 90% of its 1 Gyr luminosity evolution having a constant SFR of 1 $M_{\odot}$ yr^{-1}. The shaded area shows the same evolution from 85% to 95%. Image credit: Boissier (2013a). . . . 33
1.4 Comparison of a lenticular (left) and spiral galaxy (right) spectrum from SDSS[1]. Several important absorption and emission lines are marked with red and blue lines, respectively. The difference in the characteristic shape of both the spectra are evident where the lenticular galaxy is more prominent in the red wavelength range, whereas the spiral galaxy is more bluish with strong emission lines. . . . 34

2.1 Comparison of a high and low surface brightness galaxy NGC 7757 (left) and UGC 1230 (right), respectively. These galaxies are about the same distance and span roughly the same physical diameter with a network of spiral structures, but differ mostly in their surface brightness (McGaugh 2021). . . . 38

2.2 *Top*: The observed number density of galaxies as a function of their central surface brightness (O'Neil & Bothun 2000). The Gaussian-like distribution in black solid line shows the expected behaviour from Freeman (1970), which neglects surface-brightness selection effects. The horizontal solid black line below the Freeman (1970) peak value shows the observed distribution after applying volumetric corrections and selection effects (McGaugh 1996). The blue and red shaded regions shows separation of LSBs and HSBs, respectively, based on the Freeman (1970) value. *Bottom*: Simulation results from Martin et al. (2019) depicting a similar plot with the number density of galaxies (separated as UDGs, classical LSBs and HSBs) as a function of their average surface brightness within the effective radii. The solid lines show the variation among different environments, and the dashed line is the trend when the resolution of the simulations are extrapolated from 10^8 $M_\odot$ to 10^7 $M_\odot$. 39

2.3 Selection criteria of LSB galaxies with central disk surface brightness as a function of disk scale length (Hagen et al. 2016). The horizontal brown dashed marks the Freeman (1970) surface brightness value. The blue solid line is the division between normal and giant LSB galaxies from Sprayberry et al. (1995). The red dot-dashed box marks the selection of ultra-diffuse galaxies from van Dokkum et al. (2015), corresponding to an effective radius $R_e > 1.5$ kpc and $\mu_0 > 24$ mag arcsec^{-2}. The dashed black line represents a constant disk luminosity of $M_B = -19.7$ (corresponding to an $L_\star$ disk). This plot is based on Hagen et al. (2016). 41

2.4 Scaling relationships (in the g-band) between luminosity, effective radius and surface brightness, and mean effective surface brightness for galaxies in the Virgo cluster denoted as small black points (Lim et al. 2020). The dotted and dashed curves show the mean scaling relations and their 2.5σ confidence limits, respectively. The blue and red circles show the 2.5σ outliers in one or more scaling relationships. The gray solid curve in each panel shows the UDG definitions adopted by van Dokkum et al. (2015). 42

3.1 *Left*: V-band greyscale image of Malin 1 from Bothun et al. (1987) discovery paper. *Right*: u, g and i-band colour image of Malin 1 from Boissier et al. (2016), using the Next Generation Virgo Cluster Survey (NGVS; Ferrarese et al. 2012). The sides of both the above images extend up to ~150 kpc. 46

3.2 Slit positions of our observations (shown as blue rectangles) superposed over the NGVS image of Malin 1. The tilted slits and the vertical slit are from the 2016 and 2019 observations, respectively. 49

3.3 Malin 1 2D spectra of the CCD chip 1 (6600 - 7380 Å) obtained in the 2016 observations. The raw image, master bias image, master flat field image and the final reduced image (including cosmic ray correction) are shown in the images from top to bottom, respectively. The vertical and horizontal axes are respectively the spatial and spectral directions. In the bottom reduced image, the bright horizontal line passing through $y \approx 500$ pixel is the central part of Malin 1. The bright vertical lines are skylines. A relatively bright blob at $(x, y) \approx (750, 500)$ is the position of the Hα line in Malin 1. 52
3.4 Positions of the 16 apertures in which we could extract a spectrum. The 2016 and 2019 observations are denoted as red and black regions, respectively, along with their designated region names. The regions are named in the order in which I extracted the spectrum beginning from the center of each slit and then moving outwards in both directions. There is a small overlap of $0.1''$ in slits one and two caused due to the shifting of the slits during the 2016 observation. This overlap, however, is negligible compared to the size of apertures studied in this work. The green circular region indicated in the centre is the location of an SDSS spectrum of Malin 1 with an aperture of $3''$ diameter. 53
3.5 Central region spectra of Malin 1. The blue curve is the spectrum I extracted in the central $1'' \times 2.5''$ aperture (region *a* in Fig. 3.4). The red curve is the SDSS spectrum of Malin 1, extracted within a circular optical fibre of diameter $3''$ (shown as a green circle in Fig. 3.4). The green open circles and black open squares indicate the photometric flux levels obtained within the SDSS and my aperture, respectively, using the NGVS *g* and *i* band photometric images of Malin 1. The grey shaded area represents the region outside the wavelength coverage of observations used in this work. The blue and red vertical shaded regions indicate the main identified emission and absorption lines. 54
3.6 Hα and [O II] spectra extracted from 16 different regions of Malin 1 (12 Hα spectra in the top three rows and 4 [O II] spectra in the fourth row). The solid red curve is the best fit along with its decomposition in a single Gaussian shown as thin red dotted lines. The grey dashed line and shaded region indicate the continuum level obtained from the fitting with the 1σ noise level. The black dashed, dotted, and dot-dashed vertical lines indicate the positions of the $[\mathrm{N\,II}]_{6548}$, Hα and $[\mathrm{N\,II}]_{6583}$ emission lines, respectively, for the three top rows. The dashed and dotted lines in the bottom row show the position of the two components of the [O II] doublet. The region name and the reduced χ^2 are indicated on top of each panel. 56

3.7 Rotation curve of Malin 1, projected on the plane of the galaxy. The red and black points indicate the Hα and [O II] data, respectively. The green open circle shows Lelli et al. (2010) H I data points in the same radial range. The region name of each point is indicated with blue letters. . . 59
3.8 Radial profiles (in units of effective radius) of the star formation rate surface density of Malin 1 in comparison with different morphology of spiral galaxies from González Delgado et al. (2016) (shown as solid curves). The red open circles show the estimated Σ_{SFR} for Malin 1 using Hα data. The blue dashed line indicates the mean level of Σ_{SFR} in the extended disc of spiral galaxies from Bigiel et al. (2010) with a 1σ level of dispersion (blue shaded region). The error bar in black indicates the typical dispersion among galaxies provided by González Delgado et al. (2016) around each solid curve. 60
3.9 The Balmer ratio for the eight different regions in Malin 1. The red and blue open circles show the observed and equivalent width corrected values, respectively. The green dashed line marks the theoretical value of 2.86 in the absence of dust. 61
3.10 Oxygen abundance measured for different regions of Malin 1. The red and blue open circles are the calibrations using Pettini & Pagel (2004) and Marino et al. (2013), respectively. The blue dashed line is the solar oxygen abundance value. 63
3.11 Line diagnostic BPT diagram with $\log([\mathrm{N\,II}]_{6583}/\mathrm{H}\alpha)$ vs. $\log([\mathrm{O\,III}]_{5007}/\mathrm{H}\beta)$. The red circle and the green triangles respectively indicate the data points of Malin 1 for the nucleus and other detected regions in this work. The red plus and black crosses are the LSB sample from Subramanian et al. (2016), including Malin 1. The blue solid and dashed lines are defined by Kewley et al. (2001) and Schawinski et al. (2007), respectively, for the separation of AGN from star-forming regions. The grey contours show the distribution of a random sample of nuclear spectra of SDSS galaxies in the redshift range 0.01–1 and stellar mass 10^9-10^{11} (Boselli et al. 2018c). The black solid thick lines show the expected behaviour of star-forming regions as derived from the photo-ionisation models of Kewley et al. (2001) for three different metallicities (0.2, 0.4, 1 $Z_\odot$). . . . 64
3.12 Distribution of galaxies along the cosmic web. The black circle in the center of the plot shows the location of Malin 1. The horizontal and vertical axes correspond to the projection of the redshift ($0.02 \leq z \leq 0.15$) and right ascension ($150^\circ \leq \alpha(J2000) \leq 230^\circ$) in Cartesian coordinates. The declination range of $12^\circ < \delta(J2000) < 16^\circ$ is projected onto the plane. The black solid lines are the filaments identified using the DISPERSE code (Sousbie 2011). The galaxies are colour-coded as a function of the 3D density within a 5 Mpc radius of each galaxy (density is shown in the colour bar with an arbitrary unit). 66

3.13 Malin 1 I-band surface brightness profile decomposition. The bottom panel of the plot represents the difference between the observed surface brightness distribution and the model fit shown in the top panel. . . . 67
3.14 Rotation curve of Malin 1 with the results from the mass modelling. The red solid line is the quadratic sum of the gas, disc, bulge, and DM halo components obtained as the best fit model. The shaded area around the model components are the confidence leveld from best fit χ^2 value ($\chi^2_{min} \approx 13$). The orange crosses represent the difference between the observed rotation velocities and the model for each point of the RC. . 68

4.1 GLSB galaxy PGC 135754 in optical and UV. Left panel is the SDSS *u*, *g* and *i*-band colour composite image. The right panel is the GALEX NUV and FUV colour image. The green boxes show the three observed IMACS Magellan long slit positions for this source, with a slit width of 2.5″. . . 73
4.2 An example of the performance of UVIT compared to GALEX for Malin 1 (UVIT archival FUV image in the left and GALEX FUV image in the right). The green circle indicates the compact region in the extended disk of Malin 1 (~26 kpc away from the galaxy center) with Hα detection in the spectroscopic data discussed in Chapter 3. 74
4.3 GLSB galaxy UGC 6614 (top panel) and XUV galaxy NGC 1042 (bottom panel) in optical and UV. Left panels show the SDSS *u*, *g* and *i* band colour image and the right panel with the GALEX FUV and NUV colour image. 75
4.4 Preliminary UVIT FUV images obtained for UGC 6614 and NGC 1042. . 76
4.5 Proposed MUSE fields for Malin 1 observation, overlaid on the NGVS image. The four yellow square boxes are the MUSE fields each with a $1' \times 1'$ coverage. The white contours are GALEX UV data from Boissier et al. (2016). 77
4.6 Position of the narrow-band Hα filter for Malin 1 (in grey shaded area). The top and bottom panels show the sky background observed with MUSE. Note that very few skylines are found in the range 7090-7127 Å. 78

5.1 Multi-wavelength surveys of the Virgo cluster. The different surveys are indicated in the legend at the top of the figure. This work utilises the data from the NGVS, VESTIGE (same coverage area as NGVS) and GUViCS surveys, discussed in detail in the Sect. 5.2. The image is centered around the brightest cluster elliptical galaxy M87 ($\alpha, \delta\,[J2000] = 187.706°, +12.391°$). Image credits: Ferrarese et al. (2012). 82

5.2 Selected sample of 150 LSBs from the NGVS catalogue. The black dots are all the galaxies in the NGVS catalogue. The blue circles, red crosses and green squares are the UDGs, diffuse galaxies and the outliers, respectively based on various selection criteria (discussed in Sect. 2.3 and Fig. 2.3). The brown horizontal dashed line is the classical Freeman (1970) value. The green dashed line shows the Sprayberry et al. (1995) diffuseness selection. The red dotted box is the UDG selection criteria from van Dokkum et al. (2015). The disc scale length values are obtained by converting the R_e values given in Table 5.2, where $r_s = R_e/1.678$ assuming an exponential disc (Peng et al. 2002). 86
5.3 On sky distribution of the selected sample of LSBs. The symbols are same Fig. 5.2. The black star symbol in the centre marks the position of M87. 87
5.4 An example of the stamps created for the source ID 2143 (see Table. 5.2). The name of the bands is given in yellow below each panel. The green ellipse shows the effective radius and position angle of the galaxy from the NGVS catalogue. 94
5.5 An illustration of the cleaning of the stamps using the optical and UV masks for the source 2143. From left to right in the top panels are the g-band stamp, optical mask, cleaned g-band stamp after applying the mask and the g-band cleaned image smoothed at the resolution of GALEX, respectively. Similarly, the bottom panels are the FUV stamp, UV mask and the cleaned FUV mask after applying the UV mask. 95
5.6 The sky measurement boxes (green squares) and ellipses (in blue) used for the surface brightness profile measurements of the source 2143. The image is g-band smoothed image same as shown in Fig. 5.5, with different contrast. 97
5.7 Radial surface brightness profiles of galaxy 2143 measured in eight bands, shown as blue filled dots. The surface brightness units are in mag arcsec^{-2} for all the bands except for Hα which is in erg s^{-1} cm^{-2} arcsec^{-2}. The blue shaded area marks the 1σ error (for data points) and upper limits (3σ). The vertical red dotted line gives g-band effective radius of the galaxy from Table. 5.2. The grey line, blue dashed line and yellow dashed line are the best fit, disk component and the central component, respectively, obtained from the surface brightness decomposition procedure discussed in Sect. 5.4.5. The profiles shown here are not corrected for the galaxy inclination and Milky Way foreground galactic extinction. 99

5.8 *Left:* Distribution of the g-band central surface brightness from the decomposition results. The solid blue line and the black dashed lines are the $\mu_{0,g}$ distribution corresponding to the exponential disk and Sérsic central component, respectively. The green dotted distribution is the $\mu_{0,g}$ from the NGVS catalogue (as given in Table 5.2). *Right:* The corresponding distribution of the disk scale lengths obtained from the surface brightness decomposition. 100
5.9 The g-band mask applied and smoothed images of the 15 sources that were removed from the sample after manual inspection of their surface brightness profiles. The green ellipse shows the effective radius and position angle of the sources identified in the NGVS catalogue. These sources have either only upper limits or suspicious detections close to the sky level in their g-band surface brightness profile. 101
5.10 Comparison of the newly determined g-band effective radii (top panel) and magnitudes (bottom panel) of the sample with the initial values from the NGVS catalogue. Different sub-samples (UDGs, Diffuse and Outliers) are marked with circles, squares and crosses, respectively (similar to Fig. 5.2). The grey shaded area in the top panel marks the region below the UDG selection limit of $R_{e,g} = 1.5$ kpc (van Dokkum et al. 2015). The blacked dotted lines give a one-to-one relation. 103
5.11 $g-i$ colour distribution of the sample. The blue, green and red solid lines show the UDGs, Diffuse and Outlier sub-samples. Sources with only upper-limits on the colour are removed from this distribution. The black dashed line marks the separation of red and blue LSBs from the Dark Energy Survey (DES; Tanoglidis et al. 2021). 112
5.12 $g-i$ (top panel) and $u-r$ (bottom panel) colour distribution of the sample as a function of their distance from the Virgo cluster centre (distance from M87). The UDGs, Diffuse and Outlier sub-sumples are marked with the open blue circles, green squares and red crosses, respectively. The upper-limits in color are shown as open triangles. The black dashed lines are the error-weighted best-fit line obtained for each distribution. The blue shaded region in the top panel marks the region of blue LSBs with $g-i < 0.6$ mag (Greco et al. 2018; Tanoglidis et al. 2021). The black star symbols are the sources with H I detection in ALFALFA survey (see Sect. 5.6). 113
5.13 $NUV-r$ versus r-band absolute magnitude colour-magnitude-diagram. The symbols for the sample are the same as Fig. 5.12. The black diamond symbols and tiny dots are the detected Coma cluster UDGs and upper limits, respectively from Singh et al. (2019), along with a separation of red and blue sequence galaxies from their sample (shown as red and blue dashed lines). The grey iso-density contours represent the volume density of local galaxies from Wyder et al. (2007). 114

5.14 Sub-sample of LSBs with ALFALFA H I detection is given in Table 5.4. The greyscale images are the NGVS g-band mask applied images. The green ellipse shows the effective radius and position angle of the galaxy from the NGVS catalogue. The blue dashed circles marks the position of the ALFALFA H I centroid. For illustrative purpose, here, the ALFALFA centroid is depicted with a size of 1′ (diameter of the blue dashed circles), unlike the original ALFALFA beam of ∼3.5′ which covers a larger extend. 116

6.1 *Top*: An example of χ^2 distribution for the determination of the best model parameters (V_C, λ, t_{rps}) for the source ID 2143. The best-fit parameters are given in the upper part of each panel. The given confidence limits (3σ) in each parameter are obtained following Avni (1976). The green horizontal dashed line in the right panel marks the χ^2 value corresponding to a model without RPS, keeping the same values of V_C and λ as in the best-fit model. *Bottom*: The χ^2 values of the full sample as a function of the total number of data used in the χ^2 computation. The colour bar shows the goodness of the fit indicated by the reduced χ^2 value for each source. 125

6.2 Radial surface-brightness profiles of source ID 2143 with best fit models. The surface brightness units are in mag arcsec^{-2} for all the bands except for Hα which is in erg s^{-1} cm^{-2} arcsec^{-2}. The blue shaded area marks the 1σ error (for data points) and upper limits (3σ). The black dotted line indicates the best-fit model described in Sect. 6.3 for a ram-pressure stripped galaxy ($V_C = 58 \pm 2$ km s^{-1}, $\lambda = 0.09 \pm 0.01$ and $t_{rps} = 11.80 \pm 0.10$ Gyr), with the red shaded area as the 3σ confidence level of the best fit model. The green dot-dashed line shows the same model for an unperturbed system (without RPS). The vertical red dotted line gives the g-band effective radius I measured for the galaxy. 126

6.3 The distribution of the V_C, λ and t_{rps} parameters from the best fit models, done after redistributing them within their uncertainties (see Sect. 6.4.1). The blue, green and red lines correspond to the UDG, Diffuse and Outlier sub-populations, respectively. The vertical black dashed lines show the median values corresponding to each parameter in the entire sample. 127

6.4 *Top*: Observed $g - i$ colour as a function of the t_{rps} value from the models. *Bottom*: The t_{rps} values with respect to the distance from the cluster centre. Sources with only upper limits in $g - i$ and those with t_{rps} uncertainty > 0.3 Gyr are eliminated from these plots. The black dashed lines marks the region of ongoing RPS ($t_{rps} > 13.3$ Gyr) beyond a distance of 0.75 Mpc from the cluster centre. 128

6.5 Distribution of the gas mass, stellar mass and SFR of the sample obtained from the models, after redistributing them within their uncertainties as discussed in Sect. 6.4.1. The dashed lines and solid lines show the values before and after the RPS event, respectively. 129

7.1 NGVS *u, g, i*-colour composite image of the UDG galaxy NGVS 3543. The yellow arrows indicate the direction towards the Virgo cluster elliptical galaxies M87 and M60 at a distance of 1.26 Mpc and 0.39 Mpc, respectively. Blue dashed contours indicate the GALEX NUV detection at a surface brightness level of 27 mag arcsec^{-2} and red contours indicate the Hα detection in VESTIGE at the level of 1.6×10^{-17} erg s^{-1} cm^{-2} arcsec^{-2} (3σ). The white circle marks the position of the VLA HI detection of the source AGC 226178 from Cannon et al. (2015) with a beam size of $49''$. 136

7.2 Radial surface-brightness profiles of NGVS 3543 measured in eight bands, shown as blue filled dots (similar to the profiles from Fig. 5.7). The surface brightness units are in mag arcsec^{-2} for all the bands except for Hα which is in erg s^{-1} cm^{-2} arcsec^{-2}. The blue shaded area marks the 1σ error (for data points) and upper limits (3σ). The orange dashed line indicates the best-fit model described in Sect. 7.3 for a ram-pressure stripped galaxy (V_C = 42 km s^{-1}, λ = 0.15 and t_{rps} = 13.53 Gyr). The green dot-dashed line shows the same model for an unperturbed system (without RPS). The vertical red dotted line gives the *g*-band effective radius I measured for the galaxy. 138

7.3 χ^2 distribution for the determination of the best model parameters (V_C, λ, t_{rps}) for NGVS 3543, as discussed in Sect. 6.3. The best-fit parameters are given in the upper part of each panel. The given confidence limits (3σ) in each parameter are obtained following Avni (1976). The green horizontal dashed line in the right panel marks the χ^2 value corresponding to a model without RPS, keeping the same values of V_C and λ as in the best-fit model. 139

7.4 Evolution of the surface densities of SFR and gas for the disk of NGVS 3543 obtained from the models. The dotted and solid lines show the best model with RPS and without RPS, respectively. The blue and red curves show the evolution at 0.9 kpc and 4.3 kpc from the galaxy centre. 140

7.5 $u-g$ color evolution of a single-burst population derived using `Starburst99` models for different metallicities. The black dashed line marks the $u-g$ colour limit (corresponding to an approximate age of less than 100 Myr) I adopted for the selection of young regions discussed in Sect. 7.4.1. . . 143

7.6 Number density of the u-selected blue ($u-g<0.4$ mag) regions around the galaxy NGVS 3543 (marked as the green ellipse). The white circle marks the position of the VLA HI detection of AGC 226178 from Cannon et al. (2015), with a beam size of 49″. The white dashed box indicates the region above 3σ level of the mean background number density. The red dashed box (190″ × 120″) shows the area where the properties of the blue regions are analysed in this work. 144
7.7 *Top:* u-band grayscale image along the area selected for my analysis. *Bottom:* VESTIGE continuum-subtracted Hα image smoothed at the resolution of GALEX. The yellow circles and the green boxes, marked with their names, are respectively the u-band-selected and UV-selected regions, discussed in Sect. 7.4. The region names are attributed based on increasing declination. The blue dashed lines are the same NUV contours from GALEX as shown in Fig. 7.1. 146
7.8 Evolution of the `Starburst99` models for a single-burst population of stellar-mass 1 $M_{\odot}$, for all the photometric bands, studied in this work. The magnitudes are absolute magnitudes in AB units (except for the Hα flux in erg s^{-1} cm^{-2}). The different coloured lines indicate the models in four different metallicities. 148
7.9 Example of the χ^2 distribution for determination of the stellar mass, age and metallicity of region 25 (shown in Table 7.2). The vertical shaded bands are the 3σ confidence limits around the best-fit ages. Note that all the models with an age of less than 6 Myr for this region are rejected due to upper limit violations, resulting in the unusual single-sided χ^2 distribution above. 149
7.10 Age and stellar mass determined for all the selected regions. The blue circles and green squares represent u-band- and UV-selected regions, respectively. The grey shaded area is the u-band detection limit (lower mass or older clusters in this area would not be detected based on the luminosity predicted by the `Starburst99` models). The red crosses identify the Hα detected regions. 150
7.11 Age and stellar mass determined for all the regions using CIGALE. This figure can be directly compared to the Fig. 7.10 obtained with `Starburst99` models. 151
7.12 $u-g$ color and age of the young regions as a function of their distance from the center of NGVS 3543. Black triangles represent the knots and filaments from Fumagalli et al. (2011). The black dotted and dashed lines indicate the age gradients we measured for a 9.4 kpc stream following Eqn. 2 of Kenney et al. (2014), for two different ICM densities with $\rho_{\rm ICM}=10^{-4}$ and 10^{-3} cm^{-3}, respectively, as discussed in Sect. 7.6.3. The blue open circles and green open squares mark our u-band and UV-selected regions, respectively. The red crosses identify the Hα detected regions. 153

7.13 Stellar mass vs. H I mass of the H I-selected sample of spirals, UDGs and "dark" galaxies. The blue circle and the red star respectively mark the position of NGVS 3543 before and after the RPS event, as given in Table 7.1. The total gas masses from the models were converted into H I by multiplying by a factor of 0.74 to take into account Helium and metals. Part of the stripped gas from the UDG can form AGC 226178, shown as the green square. The small black squares show the dark galaxies from Janowiecki et al. (2015), the black open circles and triangle are those from Cannon et al. (2015). The black points and the black dashed line are the H I-selected spirals and their median HI mass, respectively, from Parkash et al. (2018). The small yellow circles and error bars are the H I bearing UDGs and the mean dispersion from Leisman et al. (2017), respectively. The black dot-dashed line marks the H I mass detection limit of the ALFALFA survey (Martin et al. 2010). 155
7.14 The overlapping coverage of various current and future surveys (DES, CFIS-UNIONS, Euclid, LSST). The blue dot-dashed lines show the coverage of several existing UDG and XUV samples (Thilker et al. 2007; Koda et al. 2015; Leisman et al. 2017; Prole et al. 2019; Junais et al. in preparation; Bouquin et al. in preparation). The black crosses mark a sample of H I and UV selected GLSBs from Chapter 4. 159

List of Tables

3.1 Properties of Malin 1 48
3.2 IMACS Magellan instrument specifications and observation log. 50
3.3 Measured data for Malin 1 from the 2016 and 2019 observations. (1) Name of the spectral extraction region. The * symbol indicates spectra that I re-binned for the analysis. (2) Radius in the galaxy plane. (3) Hα or [O II]$_{3727}$ observed wavelength. (4) Rotational velocity in the plane of the galaxy. (5-8) Observed flux of Hα , [N II]$_{6583}$, H$_{\beta}$, and [O III]$_{5007}$ emission lines, respectively, within the $1'' \times 2.5''$ regions. The flux units are in 10^{-17} erg s^{-1} cm^{-2}. 57

4.1 Sample of H I and UV selected GLSB galaxies from the literature. References: (1) Boissier et al. (2008), (2) Matthews et al. (2001), (3) Hagen et al. (2016), (4) Mishra et al. (2017), (5) Sprayberry et al. (1995), (6) Noordermeer et al. (2005), (7) van Moorsel (1982) 72

5.1 Filters and resolution of the data from NGVS (Ferrarese et al. 2012), GUViCS (Boselli et al. 2011) and VESTIGE (Boselli et al. 2018a) used in this work. 83
5.2 Properties of the selected sample from the NGVS catalogue. (1) Source ID based on the position in the NGVS catalogue. (2) Name of the source in NGVS. (3-4) Coordinates of the source in J2000. (5) *g*-band magnitude (6) Effective radius of the source. (7) Axis ratio. (8) Position angle. (9) *g*-band central surface brightness. (10) Foreground galactic extinction from Schlegel et al. (1998). (11) Selection flag based on the LSB definition where the flags 1,2, and 3 corresponds to UDG, Diffuse and Outlier sources, respectively. All the parameters given in this table are taken from the NGVS catalogue, except for the 9 sources where I performed Galfit myself. 88
5.3 Photometric measurements of the sample. Column details: (1) ID of the source. (2-6) *u*, *g*, *r*, *i* and *z*-band magnitudes. (7) VESTIGE Hα flux. (8-9) GALEX *NUV* and *FUV* magnitudes. The upper limits (3σ) in the broad-band magnitudes and in the Hα fluxes are denoted with > and < symbols, respectively. The sources with no coverage in the VESTIGE Hα or *r*-band are marked with the "−" symbol. All the magnitudes and flux values were measured within an aperture of the last *g*-band observed radius and corrected for Galactic extinction. 105

5.4 Sub-sample of LSBs at the distance of Virgo cluster with H I detection in the ALFALFA survey (Haynes et al. 2018). Column details: (1) Name of the source from my LSB sample (spiral galaxies are marked with ⋆ symbol); (2) Arecibo General Catalogue (AGC) ID; (3) Distance of the source based on ALFALFA H I measurements; (4) H I mass; (5) Offset of the ALFALFA beam centroid with respect to the NGVS coordinate of the source. This offset is normalised with the effective radius of the galaxy given in Table 5.2 (an offset > 1 indicates that the H I centroid is outside the effective radius of the galaxy). 117

6.1 Grids of V_C, λ and t_{rps} values used for the modelling in this work. For the three different types of grids, the range and corresponding spacing of each parameter are provided as separate columns. Apart from the models with RPS, all the grids also include models without RPS. 123

6.2 Properties of the best RPS models, and the model with the same spin and velocity but without RPS. Column details: (1) Name of the source; (2-4) Best fit model t_{rps}, λ and V_C values; (5-8) Stellar-mass, gas mass, SFR and gas-phase metallicity from the best fit model; (9-12) Same quantities in the absence of RPS. The uncertainties given in the RPS models are from the confidence limits in t_{rps}, λ and V_C parameters. For the non-RPS models, the uncertainties are from the error in λ and V_C alone. The ⋆ symbol indicates a best-fit model without RPS. 131

7.1 Properties of the best RPS models, and the model with the same spin and velocity but without the RPS. The uncertainties given in the RPS models are from the confidence limits in t_{rps}, λ and V_C parameters. For the non-RPS models, the uncertainties are from the error in λ and V_C alone. 141

7.2 Photometry for the u-band selected (top panel) and UV selected regions (bottom panel). Column details: (1) Name of the region. (2) Projected distance of the region from the centre of NGVS 3543. (3-7) u, g, r, i and z-band magnitudes. (8) VESTIGE Hα flux. (9-10) GALEX *NUV* and *FUV* magnitudes. The upper limits (3σ) in the broad-band magnitudes and in the Hα fluxes are denoted with > and < symbols, respectively. 147

Part I.

Introduction

1. What are galaxies and why do we study them ?

Summary

1.1 Galaxies as a building block of the universe 29
1.2 Galaxy classifications 30
1.3 Observable tools for galaxy properties 31
1.3.1 Photometric colours 31
1.3.2 Spectroscopy 32
1.4 Role of environment in shaping galaxy evolution 35
1.5 What is still missing from our picture? 36

1.1. Galaxies as a building block of the universe

Our eyes are sometimes deceiving. We see things, process them and reach conclusions, which in many cases will be far from the full picture. This is what happens when we look at the night sky with our naked eyes. We mostly see a collection of bright nearby stars part of our galaxy, the Milky Way. If we start thinking this is all that is out there, we are wrong. What we see with our naked eyes is only a small portion of even the Milky Way, let alone for what is beyond that. For a large part of human history, our perception of the cosmos was confined to the idea that the Milky Way comprises all of the universe. Then in the seventeenth century, Galileo started to observe the sky with a telescope. This transformed our previous perceptions and enabled us to see beyond our natural limitations of the eye. Later, advances in the telescope enabled eighteenth-century astronomer William Herschel to estimate the shape of our galaxy by counting stars and measuring their distance. However, there were certain faint patches of light, called *nebulae*, that Herschel could not explain using the instruments at the time. The renowned philosopher Immanuel Kant, based on little observational evidence, called these fuzzy nebulae "island universes" as large as the Milky Way. However, it was only until the early twentieth century that Edwin Hubble, with the largest telescope at the time (2.5 meter Hooker Telescope) precisely measured the size and distance of the Andromeda nebula. Hubble confirmed Kant's hypothesis that Andromeda is in fact very distant and enormous, and it lies outside the Milky Way. This discovery changed our perception of the universe beyond our home galaxy. The field of extra-galactic astronomy was born here.

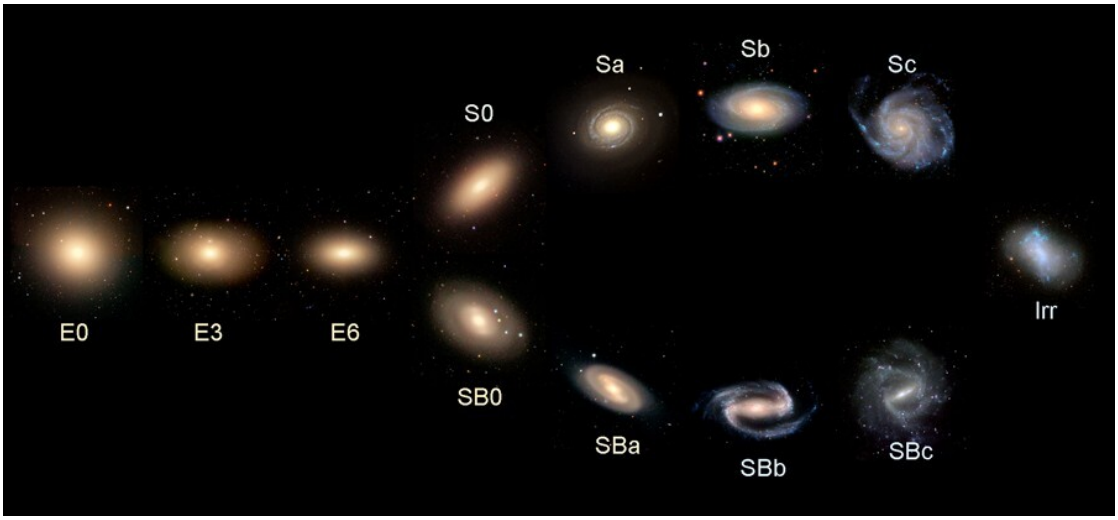

Figure 1.1.: The Hubble tuning fork diagram. Image credit: Prole (2019) and CANDELS survey.

Now we know that there are billions of galaxies in the universe. In fact, they are the very building blocks of the universe and are therefore vital in observational cosmology to study the properties of the universe as a whole. However, galaxies are complex systems. Typically, they consist of billions of stars surrounded by an interstellar medium (ISM) of an enormous amount of gas and dust. This interstellar gas then becomes the cradle for the formation of new stars, which in turn evolve to expel out more dust and metals back to the ISM in the form of supernovae and stellar winds. This cycle continues and becomes a major part of the secular evolution of a galaxy until there is no more gas left to form new stars. Apart from this, galaxies also experience environmental interactions, for instance with other galaxies or with the intergalactic medium, which influences their evolution. To complicate things further, a large portion of the matter budget in galaxies is composed of dark matter, something which we still don't know very well. Therefore, however complicated they are, it is always exciting to study the wonderful structures that are galaxies.

1.2. Galaxy classifications

Classification is the first step in studying any class of objects. In Biology, we classified organisms into different species centuries ago, which later led to the current Darwinian theory of evolution we know. Similarly, one can classify the large complex population of galaxies too into smaller groups using a set of commonly shared characteristics.

The basis for modern galaxy classifications is Hubble's "tuning" fork of galaxy morphologies (shown in Fig. 1.1).

Hubble classified galaxies into three broad categories; Ellipticals (E), Spirals (S) and Barred Spirals (SB). There is also the irregular types (Irr) that are not easily classified in

the tuning fork. This system of classification was based on the idea of galaxy evolution at the time of Hubble, where elliptical galaxies (also called "early-type" galaxies) evolve to form spiral (barred or non-barred) galaxies (also called "late-type" galaxies). However, now we know that this not entirely the picture. The galaxy evolution process is influenced by a lot of factors (e.g. environment, mass), which probably results in the diversity of the morphology. Still, the morphology tells us something about a galaxy: spirals are rotating disks, while ellipticals are dominated by dispersion. In the years following the Hubble classification, several revised and new systems of classifications were also proposed (e.g. de Vaucouleur and Sandage classifications). However, the terminology of the Hubble system, due to its simplicity, still remains popularly used in astronomy.

1.3. Observable tools for galaxy properties

Galaxy studies are commonly performed using several key observables to infer their properties. Few such important tools that I used in my work are discussed here.

1.3.1. Photometric colours

Similar to the observation of the night sky I discussed before, what we see of a galaxy at once is not actually the complete picture. A galaxy shows different structures and properties when observed at different wavelengths. So galaxy studies inevitably require multi-wavelength observations to understand all the physical processes going on with them. Here comes the importance of the colour of a galaxy, which is a very common tool used in astronomy.

The colour of a galaxy is commonly defined as the ratio between the flux measured in two different wavelength filters. The interpretation of each colour depends on the filters used. For instance, a colour based on the UV, relative to optical or Infrared (IR) gives a proxy of the star formation history of a galaxy. UV radiation is emitted by younger massive stars (O and B type) with an average timescale of 100 Myr, whereas optical emission has a timescale of at least ~500 Myr (see Fig. 1.3). Therefore a UV-optical colour with excess in UV emission implies a population that was more recently star-forming (or in other terms a blue population) and vice versa for a relatively older/red population. This variation in colour is also visible from Fig. 1.1 where moving from Spiral to Elliptical, galaxies transform from blue to red. However, a red colour not always implies an older stellar population. This also depends on the amount of dust in galaxies, which is traced by the far infra-red (FIR) wavelengths. The UV radiation emitted by recently star-forming regions can be absorbed and re-emitted in FIR by the presence of dust. Therefore, having access to the IR wavelengths help us to disentangle the contribution of dust.

Figure 1.2 shows the images of a nearby spiral galaxy M81 covering a large part of the electromagnetic spectrum. The X-ray image gives clue on the presence of a central

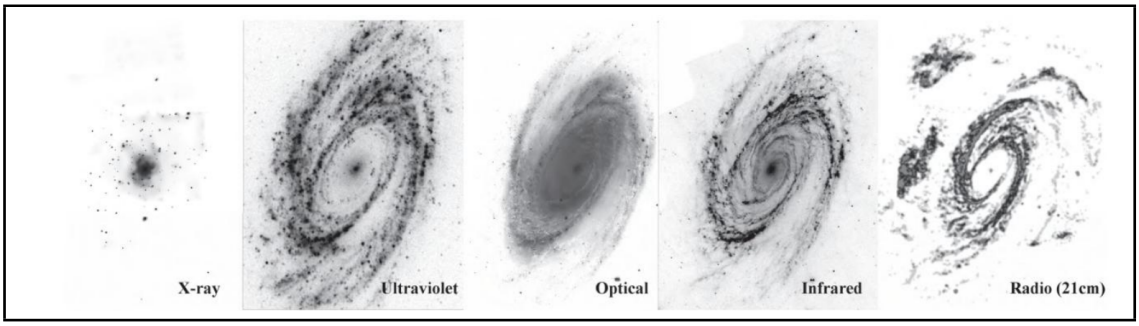

Figure 1.2.: Multi-wavelength images of the nearby spiral galaxy M81 from X-ray to Radio (Ferreras 2019).

bright source like a supermassive black hole and the hot diffuse gas surrounding it. The UV to infrared emission, as mentioned above traces the recent star formation, older stellar population and dust content. Going to further longer wavelengths, in the radio, the 21 cm emission traces the presence of neutral Hydrogen gas (H I), which is a dominant constituent in many galaxies and a fuel for the cycle of star formation.

In this way, comparing and analysing multi-wavelength data of a galaxy is a powerful tool to study their otherwise hidden secrets.

1.3.2. Spectroscopy

Spectroscopy is another important tool for the study of galaxies. A spectrum of a galaxy is the flux density observed as a function of the wavelength. A spectrum usually consists of several characteristic spectral lines (both in emission and absorption) along with the continuum level, encompassing valuable information on the overall composition of the stellar as well as gas components of a galaxy (see Fig. 1.4). The observed wavelength position of the spectral lines in galaxies, in comparison with their theoretical values, give precise estimates on their redshift, which is related to the distance. A spectral line observed from different regions of a galaxy can also be used to obtain the stellar and gas kinematics, where a Doppler shift imprints a signature on a spectral line from regions with different velocities. The obtained kinematics can then be used to estimate the overall mass budget of the galaxy, including the dark matter content.

The absorption and emission-line fluxes are other great tools. The absorption lines are caused by the stellar atmospheres, making them a proxy for the properties of the stellar population. Several key absorption lines in the optical include the Balmer lines (Hβ, Hγ, Hδ), Magnesium (Mg_{5176}), Sodium (Na_{5895}) or the Calcium (Ca II$_{8500}$, Ca II$_{8544}$, Ca II$_{8664}$) lines. In emission, the spectral lines are formed due to the ionised gas regions, which therefore traces the properties of the gas content in galaxies. Key

[1]The spiral and lenticular galaxy spectra were obtained from the Galaxy Zoo project: https://www.zooniverse.org/projects/zookeeper/galaxy-zoo/talk/1269/582784?comment=967382&page=1

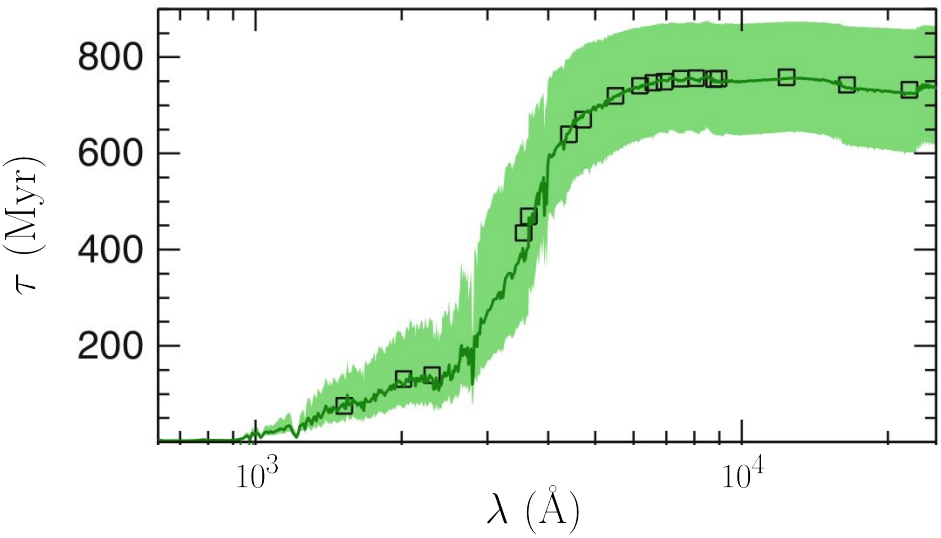

Figure 1.3.: Timescales for the star formation history as a function of the wavelength in different photometric filters (black squares from left to right - UV: GALEX FUV, NUV, and FOCA; optical/blue: Sloan *u* and Jonhson U; optical/red/near-infrared: *g*, *r*, *i*, *z*, B, V, R, Rc, I, Ic, J, H, K). The green solid line shows the time taken for a stellar population to reach 90% of its 1 Gyr luminosity evolution having a constant SFR of 1 $M_\odot$ yr^{-1}. The shaded area shows the same evolution from 85% to 95%. Image credit: Boissier (2013a).

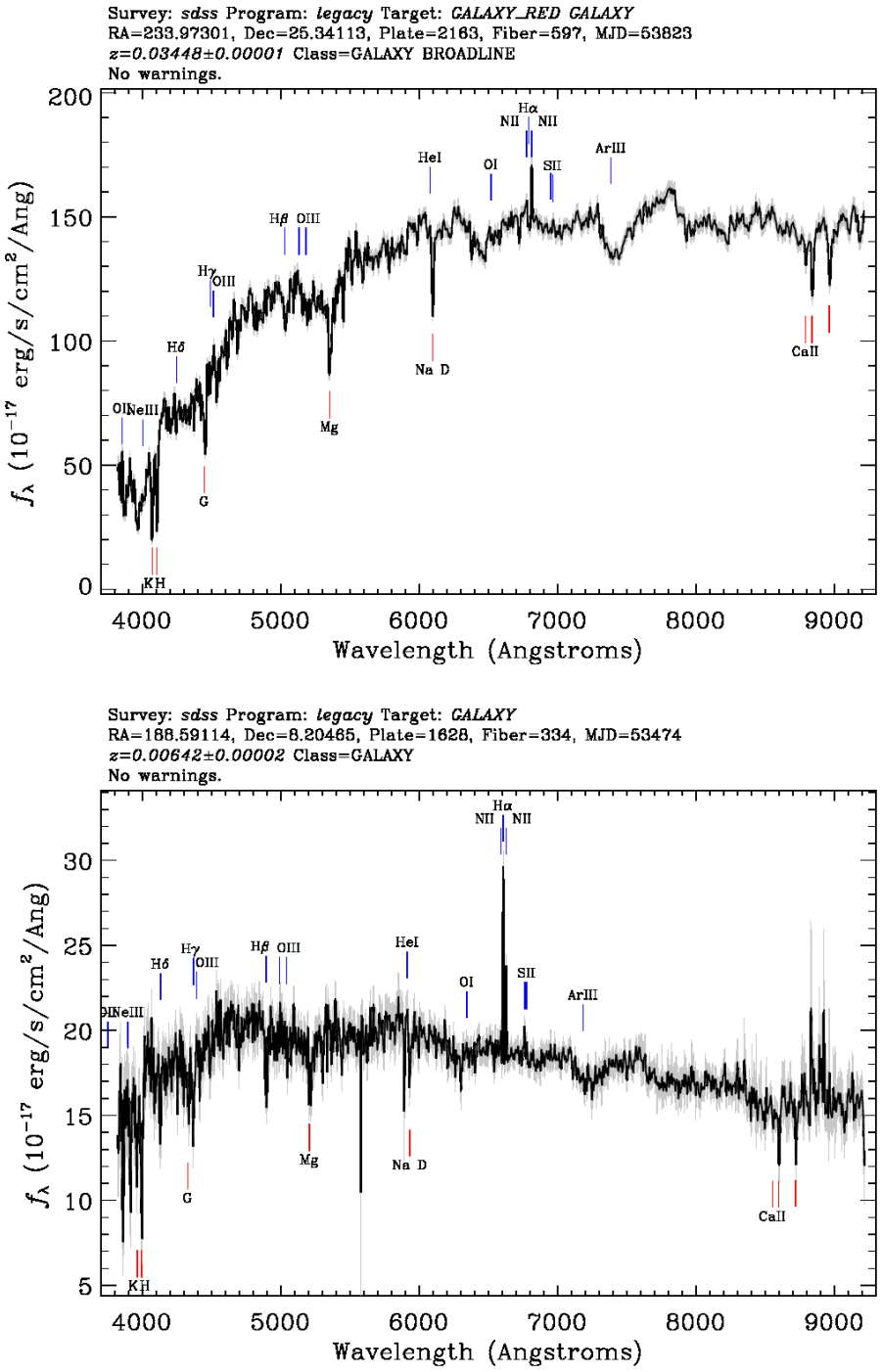

Figure 1.4.: Comparison of a lenticular (left) and spiral galaxy (right) spectrum from SDSS[1]. Several important absorption and emission lines are marked with red and blue lines, respectively. The difference in the characteristic shape of both the spectra are evident where the lenticular galaxy is more prominent in the red wavelength range, whereas the spiral galaxy is more bluish with strong emission lines.

emission lines include Hα, Hβ, Oxygen (O II$_{3727}$, O II$_{5007}$), Nitrogen (N II$_{6549}$, N II$_{6585}$) and Silicon (S II$_{6718}$, S II$_{6732}$) lines. Similar to the UV radiation discussed above, the Hα emission line is an excellent tracer of recent star formation within a timescale of 10 Myr. This is due to the fact that the radiation from very young and massive stars ionises the Hydrogen gas surrounding them, which then recombines to emit Hα radiation. Other than the stellar and gas properties, several spectral lines can also be used to probe the dust properties in galaxies. For instance, the Balmer ratio (Hα/Hβ) ratio traces the dust attenuation (Hβ being on the lower wavelength end of the spectrum is absorbed more by the dust than Hα, resulting in a deviation from the standard Balmer ratio), that can be used to estimate the dust content in galaxies.

The combination of photometric and spectroscopic observations is usually necessary to perform our studies of galaxies, as it is the case in this thesis.

1.4. Role of environment in shaping galaxy evolution

Apart from the internal mechanisms influencing the evolution of a galaxy (e.g. AGN outflows, supernovae feedback, stellar winds), the environment in which a galaxy resides also play a major role in its evolution. Looking at the large-scale structure of the universe, one can roughly classify four different kinds of environments: voids, fields, groups and clusters. Voids are the extremely under-dense regions in the large-scale structure, where galaxies are basically absent. Fields generally contain isolated galaxies without experiencing many environmental interactions. Groups and clusters are the most common regions (around 50-70% of all galaxies reside in groups; Vollmer 2013). A typical group consists of few tens of galaxies whereas a cluster contains thousands of galaxies gravitationally bound to each other. Our Milky Way galaxy resides in a group called the Local Group and the nearest cluster to us is the Virgo Cluster at a distance of ~16.5 Mpc (Mei et al. 2007).

It is in groups and clusters that galaxies are subjected to a lot of environmental interactions. The intergalactic medium in these regions mainly consists of hot gas, otherwise known as intra-cluster medium (ICM). Galaxies moving through this medium experience a drag force proportional to the ICM density and their relative velocity. This is known as ram-pressure. If this pressure is large enough to overcome the gravitational potential of the galaxy, "*ram-pressure stripping*" occurs resulting in the removal of the gas content within the galaxy. The lack of gas seriously affects the star formation activity of the galaxy, which leads to its eventual quenching. Similar kinds of effects can also occur when galaxies actively forming stars are cut off from their external source of gas infall from their extended halo, resulting in the effect of *starvation* or *strangulation*. Galaxies entering groups or clusters commonly experience such effects. However, the above interactions are hydro-dynamical in nature, which only instantly affects the gas content of galaxies.

There are also other kinds of interaction that are gravitational in nature, among clusters or group galaxies. The high-velocity dispersion and number density of galaxies

found in this environment lead to galaxy-galaxy interactions or mergers. The continuous effect of such fast encounters is usually known as galaxy *harassment*. This dramatically changes both the physical and chemical composition of a galaxy. Other than galaxy-galaxy interactions, the cluster gravitational potential itself can apply tidal forces on galaxies resulting in losing their gas or creating extended diffuse tidal streams. Moreover, the gas lost in such interactions can also in some cases result in the formation of tidal dwarf galaxies or sometimes "dark galaxies" (large H I gas clouds without any evident optical counterparts; Cannon et al. 2015).

Therefore, it is evident that galaxies have a very complex relationship with their environment, where many of the effects discussed above can act simultaneously, which eventually determines their fate.

1.5. What is still missing from our picture?

We have now entered the era of large multi-wavelength sky surveys (e.g. SDSS, DES, ALFALFA). We revolutionised the understanding of galaxies and the universe as a whole since Hubble's groundbreaking discovery opened the window of extra-galactic astronomy. However, despite our catalogues consisting of millions of galaxies, we still have a long way to go. Our current knowledge of galaxy formation and evolution could be heavily biased due to the limitations of our surveys in detecting only a population of relatively brighter galaxies. This leads to an incomplete picture of the "true" galaxy population out there. However, day by day we are progressing in moving past these limitations and a whole new population of previously hidden, faint galaxies started marking their position in our catalogues. These are the "low surface brightness galaxies", which I discuss more in Chapter 2.

Note: The above general introduction part on galaxies and their importance is inspired by the two excellent books Oswalt & Keel (2013) and Ferreras (2019). I encourage the reader to refer them for a more detailed view on the topic, since I only presented here a brief part of the vast field of extra-galactic astronomy.

2. The Realm of Low Surface Brightness Galaxies

Summary

2.1 What are Low Surface Brightness Galaxies? 37
2.2 Significance of LSBs 38
2.3 LSB definitions and sub-populations 40
2.4 A new interest in the recent years 43

2.1. What are Low Surface Brightness Galaxies?

In order to understand about Low Surface Brightness Galaxies (LSBs), first, we need to start from the very term "surface brightness". In astronomy, surface brightness (μ) is defined as the brightness or flux projected within a unit area on the sky. It is usually expressed in units of mag arcsec^{-2}. By definition, the surface brightness of an extended source is independent of its distance since the flux from a source falls as the inverse square of its distance ($1/d^2$), but the area within a 1 arcsec^2 region increases as d^2.[1]

In general, galaxies that emit much less light per unit area than "normal" galaxies are called low surface brightness galaxies (see Fig. 2.1 for a comparison of an LSB galaxy with a normal high surface brightness galaxy). Although there is no clear-cut definition for LSBs existing in the literature, they are historically defined as galaxies with a B-band disk central surface brightness ($\mu_{0,B}$) much fainter than 21.65 ± 0.30 mag arcsec^{-2} (Freeman 1970). The Freeman (1970) value was based on a study of all the disk galaxies with surface photometry available at the time (only 36 galaxies), leading to the observation that these galaxies have disk central surface brightness peaking at 21.65 mag arcsec^{-2} with a dispersion of 0.3 mag arcsec^{-2} (see Fig. 2.2). This was known as the Freeman's Law. If true for all disk galaxies, it would have great implications for their formation. However, Disney (1976) later presented the first evidence showing that surface brightness selection effects could explain the peaked distribution of Freeman (1970). The limit of 21.65 mag arcsec^{-2} arises from the fact that the sky surface brightness in the photographic plates used by Freeman (1970) is just about that value. The sky surface brightness cannot be subtracted from these photographic plates, as we do now for CCD observations. Therefore, Freeman's Law is a clear result of selection bias where galaxies only above the night sky surface brightness level were observed at the time. LSBs are fainter than the night sky surface brightness. For LSB studies, one should carefully take into account the surface brightness level of the night sky, which varies from place to place from about 20 to 23 mag arcsec^{-2} in B band at different places. Disney (1976) famously quoted that "*galaxies are like icebergs and what is seen above the sky background may be no reliable measure of what lies underneath*". This realisation lead researchers to look for more and more LSBs in the following years.

Figure 2.2 clearly illustrates that after dedicated searches for LSBs, indeed there is a large population of galaxies much fainter than the Freeman (1970) value. The number density of LSBs remains flat down

[1] Although, for high redshift sources there is also an additional cosmological dimming factor that needs to be taken care of where $\mu \propto 1/(1+z)^4$, causing objects to appear fainter than their intrinsic brightness. However, in my work, I focus mainly on low redshift sources where this effect is minimal.

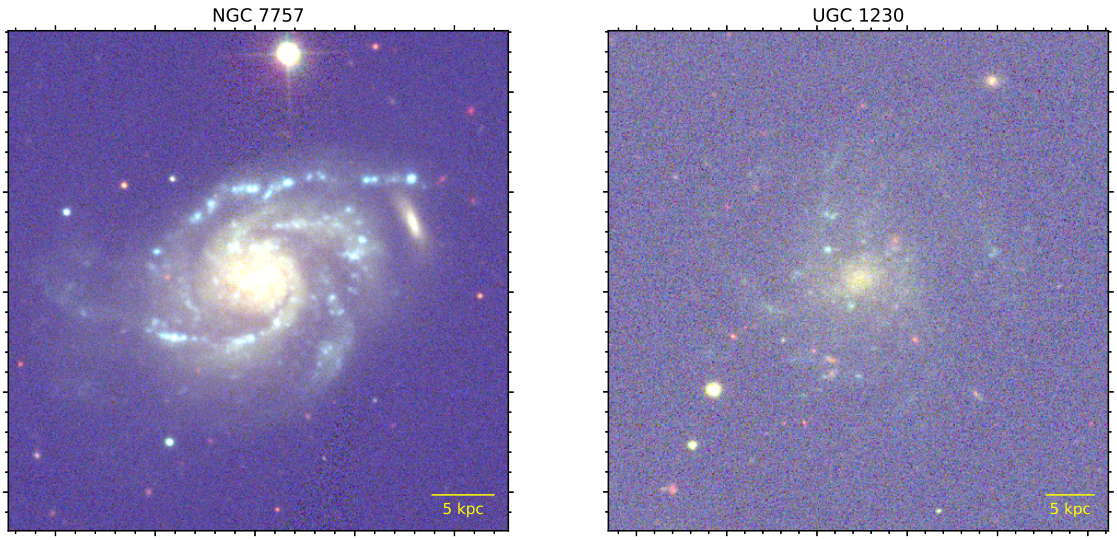

Figure 2.1.: Comparison of a high and low surface brightness galaxy NGC 7757 (left) and UGC 1230 (right), respectively. These galaxies are about the same distance and span roughly the same physical diameter with a network of spiral structures, but differ mostly in their surface brightness (McGaugh 2021).

to surface brightness levels as low as 25 mag arcsec^{-2}. Both observations and simulations reveal that LSBs constitute a large population comparable to or even more than the normal high surface brightness galaxies (HSBs), making them crucial for the field of extra-galactic astrophysics.

2.2. Significance of LSBs

As mentioned in Sect. 2.1, LSBs constitute a large population of galaxies in the universe. In terms of number, LSBs might account for about 50% or more of the total population of all the galaxies in the universe (O'Neil & Bothun 2000), and a stellar-mass/luminosity contribution of about 10% (based on Horizon-AGN simulations from Martin et al. 2019). Therefore, it is of utmost importance for us to identify and study them in detail. Our current picture of the universe, which is predominantly based on the information from brighter galaxies, can be biased without considering the LSB population. They could challenge our current understanding of the galaxy formation and evolution scenarios.

The abundance of LSBs has various implications on galaxy studies, as well as in a cosmological context. The large population of LSBs steepens the faint-end slope of the galaxy luminosity function (Sabatini et al. 2003). This is a crucial component in the current ΛCDM framework of galaxy formation and dark matter models. The infamous "missing satellites" problem of the ΛCDM models is another relevant issue. The theoretical prediction of satellite galaxies from dark matter simulations are largely abundant compared to the observed satellite galaxies in the Local Group, where they appear to be missing (Klypin et al. 1999). LSBs could act as a test-bed in resolving this issue. The inclusion of baryonic physics in recent simulations, limiting the star formation in smaller haloes, similar to LSBs, have largely alleviated this issue (Wetzel et al. 2016).

Another interesting feature of LSBs is their low stellar and other baryonic matter density. Although LSBs are generally found to be rich in gas, their gas surface densities are about a factor 3 lower than normal HSB galaxies (de Blok et al. 1996). The presence of these low-density gas regions leads to the low star formation rates found in LSBs. Star formation rates in galaxies are heavily influenced by a threshold

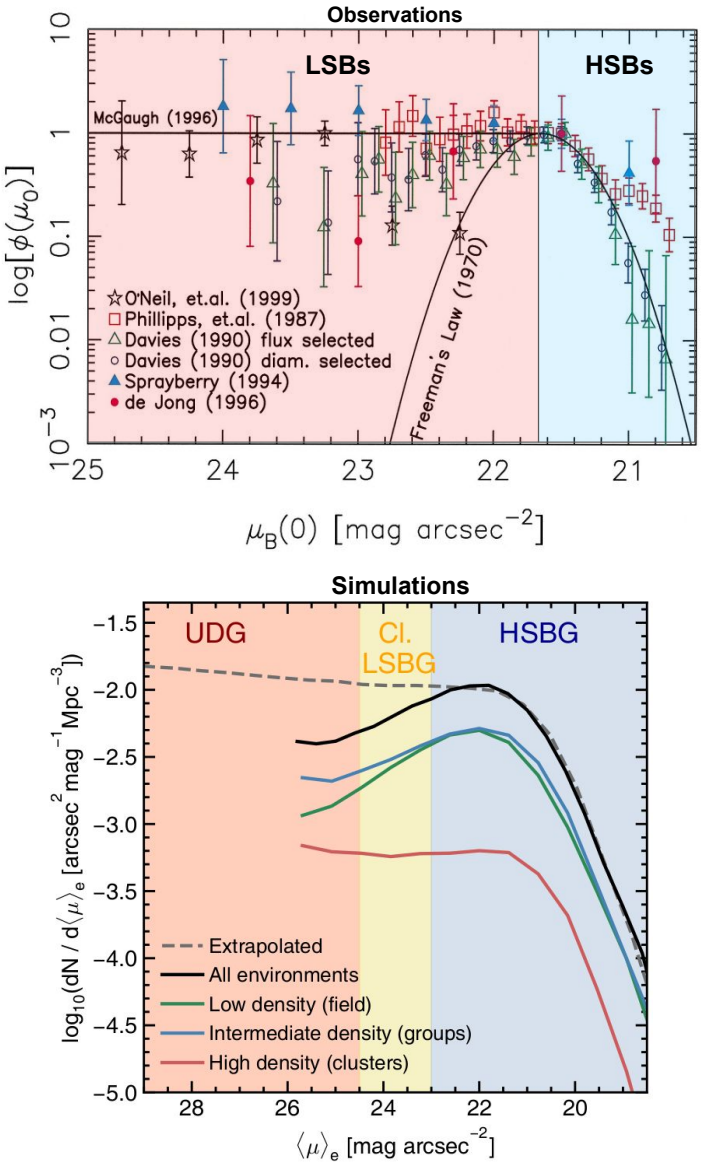

Figure 2.2.: *Top*: The observed number density of galaxies as a function of their central surface brightness (O'Neil & Bothun 2000). The Gaussian-like distribution in black solid line shows the expected behaviour from Freeman (1970), which neglects surface-brightness selection effects. The horizontal solid black line below the Freeman (1970) peak value shows the observed distribution after applying volumetric corrections and selection effects (McGaugh 1996). The blue and red shaded regions shows separation of LSBs and HSBs, respectively, based on the Freeman (1970) value. *Bottom*: Simulation results from Martin et al. (2019) depicting a similar plot with the number density of galaxies (separated as UDGs, classical LSBs and HSBs) as a function of their average surface brightness within the effective radii. The solid lines show the variation among different environments, and the dashed line is the trend when the resolution of the simulations are extrapolated from 10^8 $M_\odot$ to 10^7 $M_\odot$.

of gas density (Kennicutt 1989), below which widespread star formation do not occur (although local gas instabilities can at times lead to a very low amount of star formation). The gas surface densities found in LSBs are close to this critical density where star formation will be very minimal (Impey & Bothun 1997). Therefore, LSBs can be a perfect laboratory for the study of star formation activity in low-density regimes (Boissier et al. 2008; Wyder et al. 2009; Bigiel et al. 2010). The universality of the star formation threshold and its dependence on other factors like the environment still needs to be tested.

LSBs are also generally considered to be dominated by dark matter (de Blok & McGaugh 1997). Therefore, the low-density regime of LSBs can also be used as a tool for probing the dark matter distribution within them where there is only a minimal contribution from the baryonic matter. The "core-cusp" problem of the dark matter models can be tested using LSBs (de Blok 2010). The steep/cuspy inner dark matter profiles predicted by the simulations are in violation of the observed flat/core like profile in the central regions of low mass galaxies. Resolving this anomaly will help us in a better understanding of dark matter physics.

It is also necessary for us to understand the potential role of LSBs at high redshifts where most of them may be missing from our current observations. Disseau et al. (2017) found the presence of a significant number of galaxies with extended sizes with respect to their mass, up to $z \sim 0.5$. Later Martin et al. (2019) suggested that LSBs originate from the same progenitors as HSBs at $z > 2$. In their scenario, a fraction of the galaxies among them formed stars more rapidly at earlier epochs, creating higher rates of supernovae feedbacks that flattened their profiles to form LSBs. Such an early formation scenario for LSBs could only be tested with deeper and high redshift observations from future surveys, that will detect LSBs in large numbers. Only then our catalogue of galaxies will be closer to completion.

2.3. LSB definitions and sub-populations

LSB galaxies span a wide range of sizes, masses, and morphology from the largest existing galaxies down to the more common dwarfs. The conventional Hubble classification of galaxies would fail to separate LSBs (McGaugh et al. 1995) from other galaxies, making them an interesting population that requires further attention to understand what separates them from regular galaxies.

The LSB population is divided into various sub-groups based on different definitions in the literature. As discussed Sect. 2.1, still now we do not have a clear definition of what an LSB galaxy is. Classically, LSBs are defined to be galaxies with a central disk surface brightness clearly below the Freeman (1970) value of 21.65 mag arcsec^{-2}, as can be seen in Fig. 2.2. Another criterion now generally followed is that LSBs are arbitrarily categorised as the galaxies with μ_0 values below the typical sky surface brightness level of ~23 mag arcsec^{-2}.

Sprayberry et al. (1995) put forward another classification of LSBs based on the disk scale length and central surface brightness of the disk component. According to this criteria, a diffuse extended disk or in other words a giant LSB galaxy can be defined using a "diffuseness index" given as $\mu_{0,B} - 5\log r_s > 27$, where r_s is the disk scale length of a galaxy in kpc. Giant Low Surface Brightness (GLSB) galaxies are an extreme case of LSBs, having a very extended low surface brightness disk, with scale lengths ranging from 10 to 50 kpc (Bothun et al. 1987) and rich in gas content ($M_{HI} \sim 10^{10}\, M_\odot$; Matthews et al. 2001). Sprayberry et al. (1995) observed that all the GLSB galaxies known at the time followed the diffuseness relation (see Fig. 2.3).

Apart from the classical and giant LSBs, in recent years a new class of LSBs emerged, known as the Ultra-diffuse galaxies (UDGs). UDGs are galaxies as large as Milky Way in size with effective radii (R_e) ranging from 1-5 kpc, but extremely faint ($\mu_0 > 24$ mag arcsec^{-2}) in terms of luminosity, similar to dwarf galaxies (van Dokkum et al. 2015). See Fig. 2.3 for the location UDGs in the $\mu_0 - r_s$ plane.

There are also other definitions for LSBs existing in the literature. For instance, Lim et al. (2020) recently put forward a new selection criterion for LSBs based on identifying "outlier" sources in galaxy scaling relationships (see Fig. 2.4). According to this definition, LSBs are identified when their physical properties significantly differ from the general population of galaxies observed, in one or more scaling

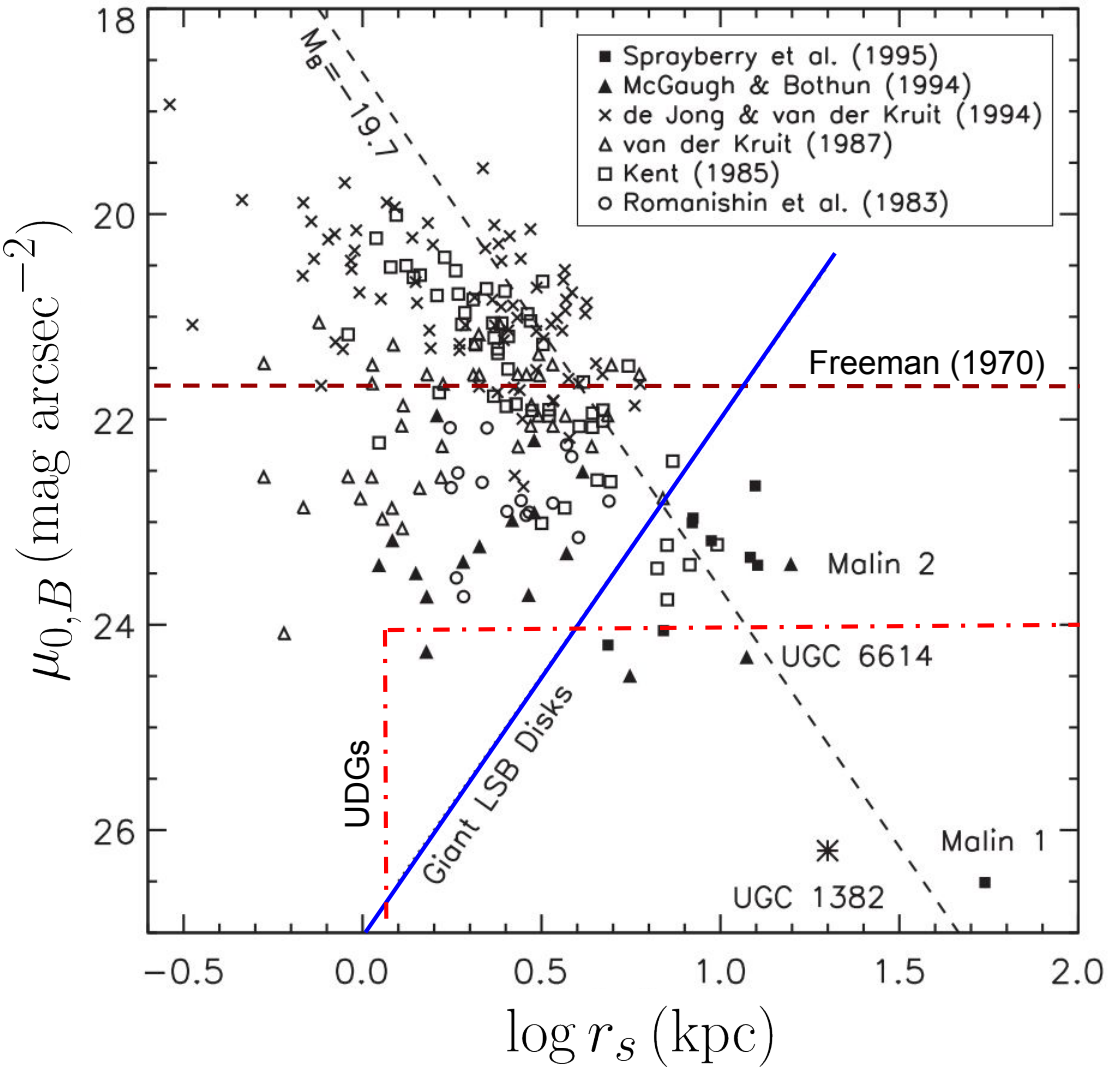

Figure 2.3.: Selection criteria of LSB galaxies with central disk surface brightness as a function of disk scale length (Hagen et al. 2016). The horizontal brown dashed marks the Freeman (1970) surface brightness value. The blue solid line is the division between normal and giant LSB galaxies from Sprayberry et al. (1995). The red dot-dashed box marks the selection of ultra-diffuse galaxies from van Dokkum et al. (2015), corresponding to an effective radius $R_e > 1.5$ kpc and $\mu_0 > 24$ mag arcsec^{-2}. The dashed black line represents a constant disk luminosity of $M_B = -19.7$ (corresponding to an $L_\star$ disk). This plot is based on Hagen et al. (2016).

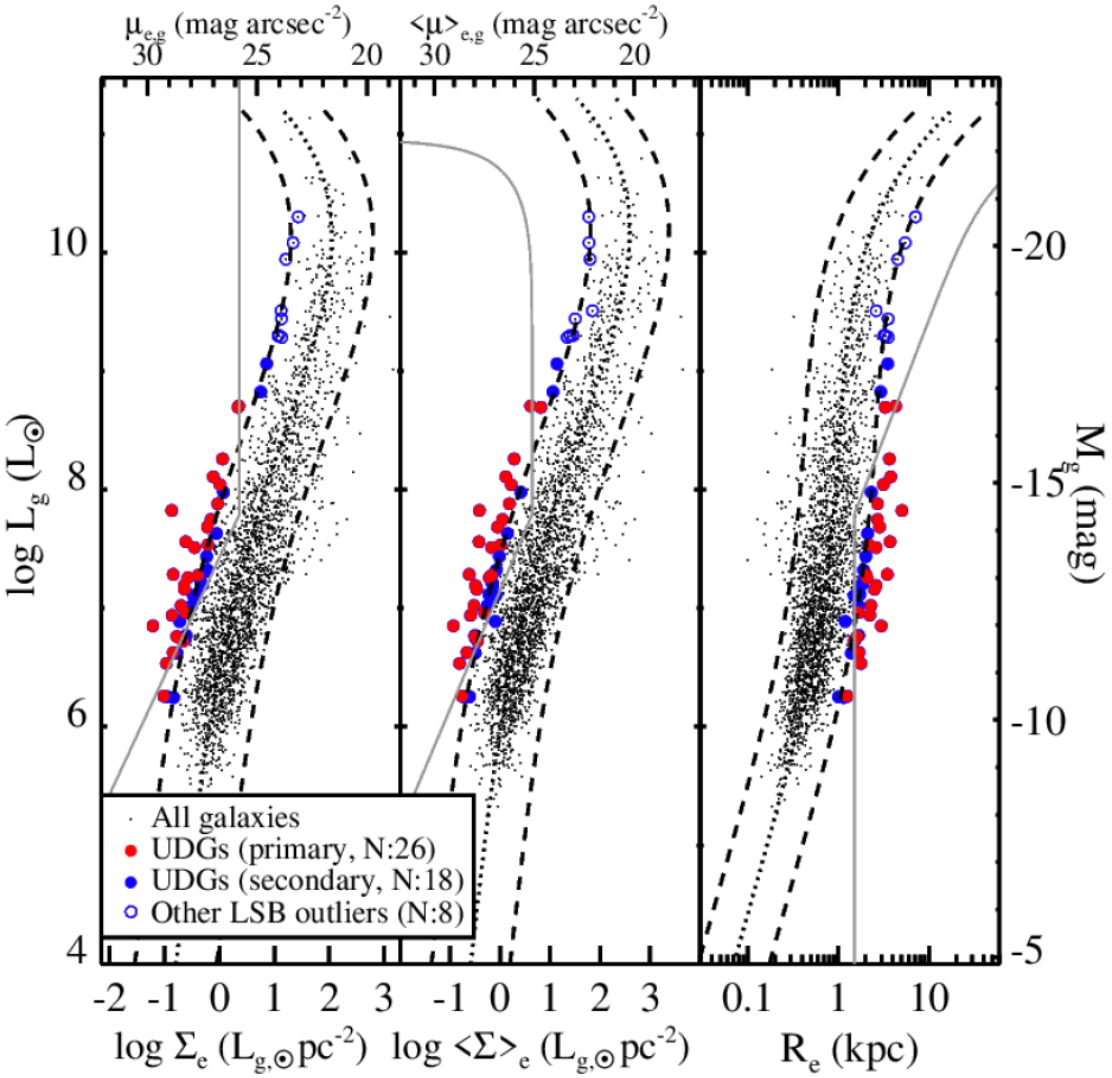

Figure 2.4.: Scaling relationships (in the *g*-band) between luminosity, effective radius and surface brightness, and mean effective surface brightness for galaxies in the Virgo cluster denoted as small black points (Lim et al. 2020). The dotted and dashed curves show the mean scaling relations and their 2.5σ confidence limits, respectively. The blue and red circles show the 2.5σ outliers in one or more scaling relationships. The gray solid curve in each panel shows the UDG definitions adopted by van Dokkum et al. (2015).

relationships. Figure 2.4 shows that many of the outlier galaxies obtained from the selection of Lim et al. (2020) overlap with the UDG definition of van Dokkum et al. (2015) discussed above. Lim et al. (2020) selection also has the advantage that it avoids the use of an arbitrary limiting value of the effective radius, and it removes few galaxies that are close to regular dwarfs.

Yet another type of definition for LSBs exists in the literature when it comes to large scale simulations. Since the LSB population also contain low mass diffuse galaxies, simulations that are often limited by their resolutions, select LSBs by putting a certain mass threshold apart from the classical surface brightness selection. For instance, Martin et al. (2019) studied the population of LSBs using Horizon-AGN simulations considering the LSB population with an average surface brightness fainter than 23 mag arcsec^{-2} but a total mass above $\sim 10^8$ $M_\odot$ (see bottom panel of Fig. 2.2).

Looking at the various definitions discussed above for LSBs, it is clear that one should be cautious about the choice of their LSB definition before undergoing any study on this population. In my work, I will be focusing on the population of giant LSBs and UDGs by combining various definitions discussed in the literature. However, we should also keep in mind that there might not be such an artificial difference between LSBs and "normal" galaxies as obtained from various definitions. The main difference lies where we draw the line separating them.

2.4. A new interest in the recent years

In the recent years, it became possible for astronomers to obtain deeper observations allowing us to study LSBs with a new perspective (e.g. owing to instruments like CFHT Megacam, Subaru Suprime-Cam, the "Dragonfly" Telescope, MUSE).

The class of GLSB galaxies were studied in many recent works (Galaz et al. 2015; Boissier et al. 2016; Hagen et al. 2016; Zhu et al. 2018; Saburova et al. 2021; Saha et al. 2021), trying to understand the properties of these giant objects. They put forward several scenarios for the GLSB galaxy formation (e.g. merger events, gas accretion by HSB galaxies, large angular momentum halo). A detailed description and history of this population of galaxies is given in Chapters 3 and 4.

UDGs are the other class of objects that attracted a lot of attention in the past few years. In fact, the very term "Ultra-Diffuse Galaxies" was coined by van Dokkum et al. (2015), in which the authors observed an abundance of extended diffuse LSB galaxies in the Coma cluster using deep imaging from the Dragonfly telescope. This was the beginning of a new interest in the population of LSB galaxies. However, UDG-like galaxies are not new to astronomers. Very large LSBs like the GLSBs have been known to exist for several decades (Sandage & Binggeli 1984; Bothun et al. 1987; Pickering et al. 1997). But the recent interest was fuelled by their high abundance, combined with their existence in a variety of environments (Koda et al. 2015; van Dokkum et al. 2015; Leisman et al. 2017; Román & Trujillo 2017; Prole et al. 2019). The discovery of UDGs adds to the already large population of LSBs discussed in Sect. 2.2, consistent with observations and theoretical predictions. However, the formation of UDGs is still debated.

There are several proposed formation scenarios for UDGs. van Dokkum et al. (2015) suggests that UDGs could be failed $L_\star$ galaxies residing in Milky Way-like haloes that have experienced in the past a truncation in their star formation history. Another scenario considers UDGs as "puffed-up dwarf" galaxies whose stellar and gas components were puffed up by environmental interactions (e.g. tidal encounters, ram-pressure stripping) or supernovae feedback within themselves (Baushev 2018; Di Cintio et al. 2019). Amorisco & Loeb (2016) suggests UDGs are formed in dwarf-sized haloes with higher than average initial angular momentum. This implies that UDG formation may not uniquely be connected to the environment or internal feedback processes. However, every physical process should leave an imprint on the properties of the UDGs we observe. It is up to us to carefully identify them and pinpoint the exact reasons behind the high prevalence of UDGs. For this purpose, I investigated a population of UDGs and other LSBs in this work, discussed in detail in Chapters 5, 6 and 7.

Part II.

Giant Low Surface Brightness Galaxies

3. The Mysterious case of Malin 1

Summary

3.1 A peek into the past . . . 45
3.2 A new spectroscopic study . . . 47
3.2.1 Source of Data . . . 48
3.2.2 Data reduction . . . 48
3.2.2.1 Correction for instrumental errors . . . 50
3.2.2.2 Spectral Extraction . . . 51
3.2.3 Measurements . . . 55
3.2.3.1 Emission line fitting . . . 55
3.2.3.2 Measurement of rotational velocity . . . 55
3.2.4 Results . . . 58
3.2.4.1 Rotation curve . . . 58
3.2.4.2 Star formation rate surface density . . . 58
3.2.4.3 Dust attenuation . . . 61
3.2.4.4 Metal abundance . . . 62
3.2.4.5 Presence of active galactic nucleus (AGN) . . . 62
3.2.4.6 Malin 1 along the cosmic web . . . 65
3.2.5 A new mass model for Malin 1 . . . 65
3.2.6 Conclusions . . . 69

3.1. A peek into the past

Serendipitous discoveries are not at all new to science. Several groundbreaking discoveries in science are actually like that (e.g. discovery of Penicillin, Radioactivity, X-ray, Cosmic Microwave background, expansion of the universe, and many more). The galaxy Malin 1 (shown in Fig. 3.1) is probably one such example where a serendipitous discovery shed light on the existence of a peculiar galaxy.

Malin 1 was accidentally discovered as a background galaxy during a systematic survey of the Virgo cluster region designed to detect extremely low surface brightness galaxies (Bothun et al. 1987)[1]. Malin 1 is one of the most unusual galaxies known to date.

It has the largest radial extent of any known spiral galaxy, with a low surface brightness disk extending out to ~120 kpc (Moore & Parker 2006) and a central disk surface brightness of $\mu_{0,V} \approx 25.5$ mag arcsec^{-2} (Impey & Bothun 1997). This makes Malin 1 an archetype of the class of GLSB galaxies.

A simple illustration of the extremely low surface brightness nature of Malin 1 is shown in Fig. 3.1. In the V-band CCD image of Malin 1 taken after its discovery[2] (Bothun et al. 1987), we can hardly see some faint network of diffuse structures around the galaxy. However, in the recent images from NGVS using the Canada France Hawaii Telescope (CFHT) Megacam (Ferrarese et al. 2012), there is a clear and prominent disc of faint spiral arms around Malin 1 (see also Galaz et al. 2015). Despite the very faint surface brightness of its disk, Malin 1 is a massive galaxy with a total optical luminosity of

[1] The galaxy was named after David Malin, who took the first image of the galaxy.

[2] Malin 1 was originally discovered on an electronically amplified photographic plate image (see Fig. 1 of Bothun et al. 1987).

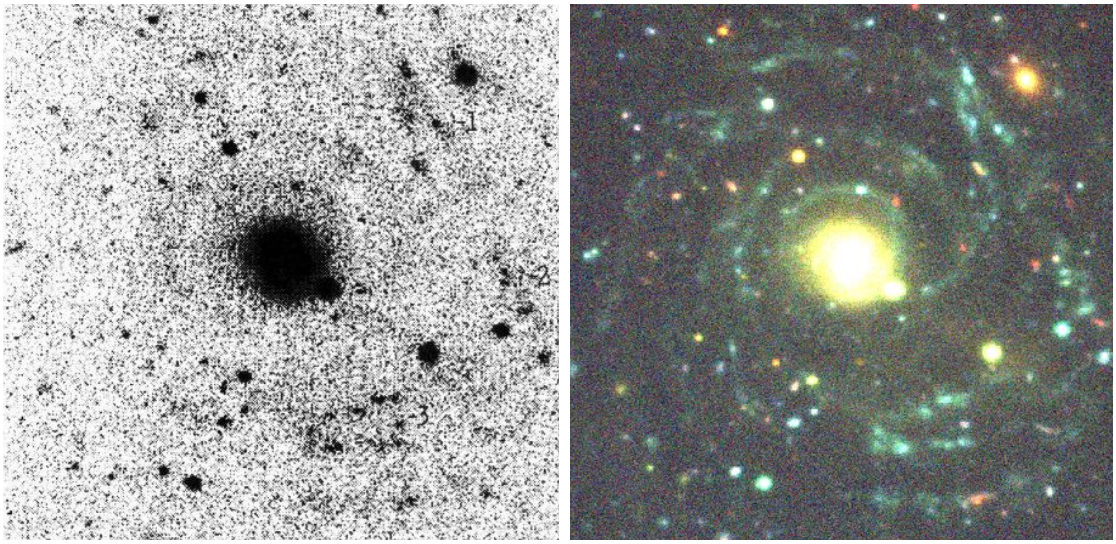

Figure 3.1.: *Left*: V-band greyscale image of Malin 1 from Bothun et al. (1987) discovery paper. *Right*: u, g and i-band colour image of Malin 1 from Boissier et al. (2016), using the Next Generation Virgo Cluster Survey (NGVS; Ferrarese et al. 2012). The sides of both the above images extend up to ~150 kpc.

$M_V \approx -22.9$ mag (Pickering et al. 1997). It is an extremely gas rich galaxy with an H I mass of $\sim 6 \times 10^{10}$ $M_\odot$ (Pickering et al. 1997; Matthews et al. 2001).

An analysis of a Hubble Space Telescope I-band image by Barth (2007) suggests that Malin 1 has a normal barred inner spiral disc embedded in a huge diffuse LSB envelope. This also makes it similar to the galaxies with an extended Ultraviolet (XUV) disc found in 30% of nearby galaxies (Thilker et al. 2007). Malin 1 is thus a perfect laboratory to study star formation activity in low-density regimes. It is the most extreme case of a range of objects, including GLSB and XUV galaxies. However, due to the observational limitations set by the extremely low surface brightness disk of Malin 1, we lack high quality spectroscopic and photometric data for this source. It remains a significant challenge to understand the physical processes behind the formation and stability of the disk of Malin 1, which is at least five times larger than our own galaxy Milky Way.

Lelli et al. (2010) re-visited H I observations from Pickering et al. (1997) to derive a rotation curve and H I velocity map for the disk of Malin 1. Despite the relatively poor angular resolution of $\sim 21''$ of the data, they observed a steep rise in the rotation curve of Malin 1 ($V_{\rm max}$ up to 250 km s^{-1}). This is typical of a High Surface Brightness (HSB) galaxy, and contrary to the expectation that LSB galaxies have a slowly rising rotation curve dominated by dark matter (DM) at all radii (Verheijen & Tully 1999). Lelli et al. (2010) concluded that GLSB galaxies like Malin 1 have a double structure with an inner HSB early-type spiral galaxy embedded in an outer extended LSB disk, similar to the observation of Barth (2007).

Reshetnikov et al. (2010) studied the stellar kinematics of the inner part ($r \leq 15$ kpc) of Malin 1 and its nearby small companion galaxy Malin 1B (located at a distance of 14 kpc from the centre of Malin 1). For this purpose, they used a single long-slit spectroscopic data obtained with the 6m telescope of the Special Astrophysical Observatory of Russian Academy of Sciences. In this work, they observed that the stellar kinematics of both the galaxies show some signs of possible interaction, which could probably explain some of the morphological features of Malin 1's central region (e.g. a two-armed spiral structure, a bar). On the large scale environment of Malin 1 and the formation of its extended disc, Reshetnikov et al. (2010) also identified another possible bygone intruder galax. SDSS J123708.91+142253.2, located

at ~ 350 kpc from Malin 1, has a similar central velocity as Malin 1. With the data available at the time, they couldn't exclude the possibility of a collisional past of Malin 1 with this source.

The mystery of the giant LSB disk of Malin 1 continued to encourage more and more researchers to look for answers. Galaz et al. (2015) obtained deep optical images (g and r-bands) of Malin 1 from the 6.5m Magellan/Clay telescope in Chile. This enabled the first time to observe the striking faint morphological features, including the spiral arms of Malin 1 with high visual contrast compared to the previous images. These new images revealed various stellar clumps and streams in the spiral arms of Malin 1 at a very low luminosity and mass surface density.

Later on, Boissier et al. (2016) studied the stellar populations of the giant disk of Malin 1 (shown in Fig. 3.1) using a multi-wavelength set of photometric data (u, g, i, z, FUV and NUV-bands) obtained from the NGVS and GUViCS surveys (Boselli et al. 2011; Ferrarese et al. 2012). The surface brightness and colour profiles in comparison with stellar population models suggested that Malin 1 had a long and quiet star-formation history ranging from 0.1-3 Gyr at different regions of the spiral arm. Their models indicated that Malin 1 probably has an exceptionally large angular momentum spin parameter ($\lambda \sim 0.6$), about 20 times larger than for the Milky Way. This still leaves an open question about the formation of such an enormous low-density structure, surviving billions of years of evolution.

Zhu et al. (2018) recently published a work based on the 100 Mpc cube IllustrisTNG simulation, where they observe the formation of a galaxy analogous to Malin 1. The observed properties of Malin 1 (stellar mass, gas mass, radial extend) match well with the galaxy formed in the simulation. Using this work, they propose a formation scenario for the extremely low surface brightness disc of Malin 1. Looking back at the history of the Malin 1 like galaxy in their simulation, they observed that the large extended disc of the galaxy was formed due to the cooling of hot halo gas triggered by the merger of two intruding galaxies a few billion years ago. The galaxies merged with the central Malin 1 like progenitor, brought in an extensive gas reservoir, along with the cooled halo gas to form the large disc of the Malin 1 like galaxy observed in the simulation. The simulation results also show that the extended disc was formed only after $z = 0.3$ (~ 3.5 Gyr ago). This is well consistent with the observation Boissier et al. (2016) that the faint spiral arms of Malin 1 contain star complexes with age in the range of 0.1 to 3 Gyr. According to the scenario proposed by Zhu et al. (2018), the formation of Malin 1 like galaxies is rare (they observe only one such galaxy in a cube of 100 Mpc !) but well feasible within the current framework of galaxy formation scenarios.

Several other works were also published recently based on the formation of Malin 1 and other GLSB galaxies. Saburova et al. (2021) performed a study on a sample of 7 GLSB galaxies, including Malin 1, to investigate the formation mechanism of GLSBs. They proposed that there could be three significant scenarios resulting in the formation of GLSB galaxies. The proposed scenarios involve HSB galaxies accreting gas to form massive LSB disks, GLSBs formed from large angular momentum DM haloes and major merger events that bring in an extensive reservoir of gas leading to the formation of GLSBs. Saha et al. (2021) also recently published a study on the central region of Malin 1 using UVIT data. They observed recent star formation in the central bar region of Malin 1 (within 14 kpc). This recent star formation in the centre could indicate that the companion galaxy Malin 1B is interacting with Malin 1 to trigger star formation in the central region, consistent with the observation from Reshetnikov et al. (2010).

However, to pinpoint the several proposed evolution histories of GLSBs, we need to obtain larger samples and data for this class of galaxies in the future.

Table 3.1 provides various physical parameters of Malin 1 taken from the literature discussed above.

3.2. A new spectroscopic study

The history of Malin 1 discussed in Sect. 3.1 clearly shows the mysterious nature of this galaxy. Although many dedicated works were carried out in the past, the formation of Malin 1 remains elusive to researchers. This is mainly because of the lack of high-quality data, especially spectroscopic data, obtained for Malin 1. This motivated me to work on a new set of spectroscopic data of Malin 1 to

Table 3.1.: Properties of Malin 1

Property	Value	References
R.A. (J2000)	$12^h\ 36^m\ 59.350^s$	1
Dec. (J2000)	$+14°\ 19'\ 49.32''$	1
Morphological type	S0/a	2
Redshift	0.0826 ± 0.0017	3
V_{sys}	24766.7 ± 4.0 km s^{-1}	3
Inclination angle	$38° \pm 3°$	3
D_L	377 ± 8 Mpc	3
M_{HI} ($10^{10}\ M_\odot$)	6.7 ± 1.0	3,6
$\mu_{0,V}$	25.5 mag arcsec^{-2}	4
M_V	-22.9 ± 0.4 mag	5
Radius of LSB disc	130 kpc	7
Global SFR	$< 2\ M_\odot\ yr^{-1}$	7

References: (1) NASA/IPAC Extragalactic Database (NED); (2) Barth (2007); (3) Lelli et al. (2010); (4) Impey & Bothun (1997); (5) Pickering et al. (1997); (6) Matthews et al. (2001); (7) Boissier et al. (2016).

explore and better understand the nature of this galaxy. I present here a summary of the work I published in Junais et al. (2020).

3.2.1. Source of Data

The spectroscopic data of Malin 1 used in this work were obtained by my collaborator Barry F. Madore (Carnegie Observatories) from the Inamori-Magellan Areal Camera and Spectrograph (IMACS) installed on the 6.5 m Magellan-Baade telescope at Las Campanas Observatory, Chile. Two runs of observation occurred in 2016 and 2019, where Malin 1 was observed in a long slit mode with slit widths of 2.5″ and 1.2″, respectively. The detailed specifications of the two observations are given in Table 3.2.

In the 2016 observation, four slit positions were observed (shown in Fig. 3.2) with an exposure time of 3×1200 seconds per slit position. The large width of the slit was chosen to optimise the chance of detecting H II regions within the slit. The orientation of the slits was selected based on UV images from Boissier et al. (2008), allowing the slits to pass through many UV blobs. Each of the slits was oriented at a position angle (PA) of 39.95° to the North. The initial slit position passes through the galaxy centre. The second and third slits were placed parallel to the initial slit by a shift of 2.5″ towards the West. The fourth slit was placed about 50″ towards the East of the initial slit, allowing it to pass through distant UV blobs and a deeper exposure time of 6×1200 seconds. However, unfortunately, we couldn't detect any useful signal in that position.

3.2.2. Data reduction

The raw spectroscopic data obtained from the observation must be processed and corrected for various instrumental errors before extracting scientific information. The data reduction process was carried out using the `Pyraf` Python package by following standard IRAF procedures from Massey et al. (1992) and Massey (1997).

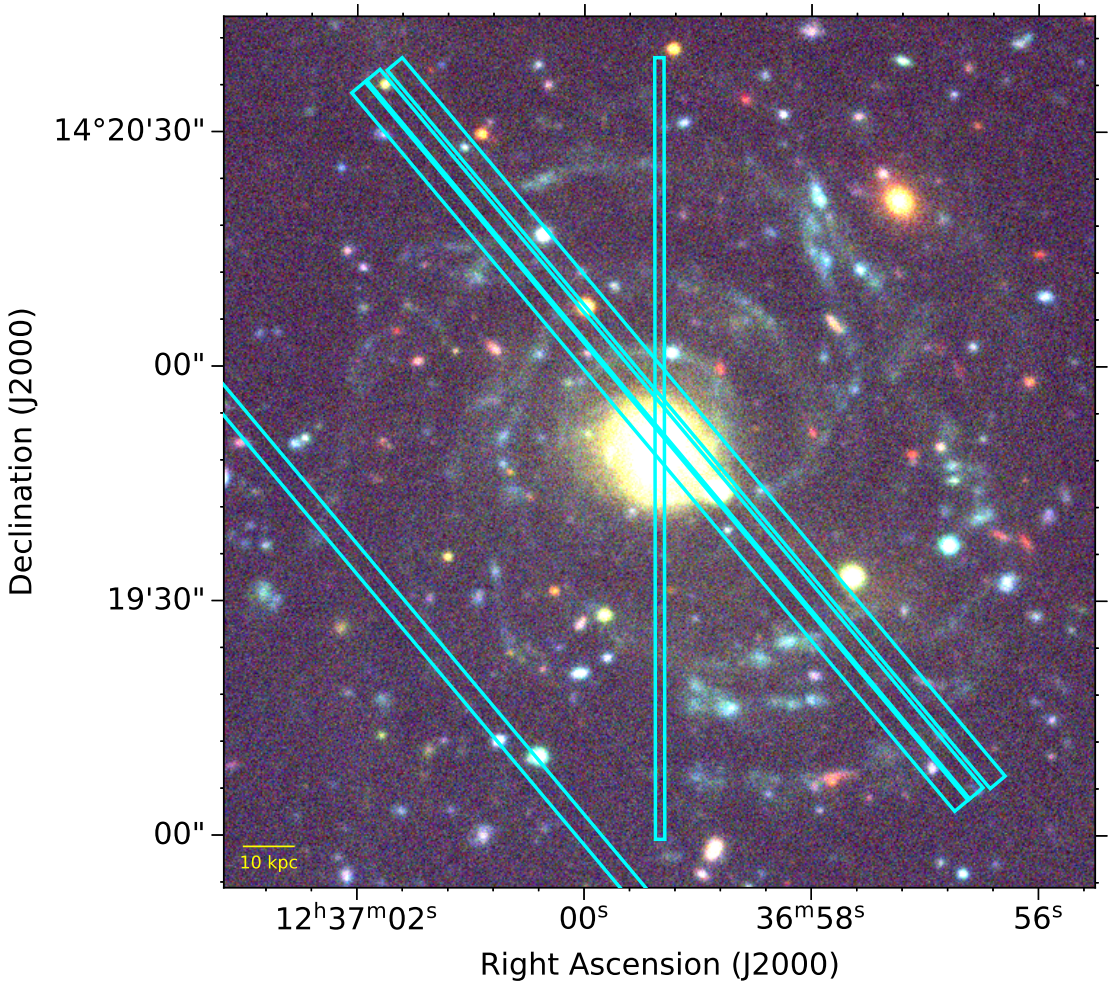

Figure 3.2.: Slit positions of our observations (shown as blue rectangles) superposed over the NGVS image of Malin 1. The tilted slits and the vertical slit are from the 2016 and 2019 observations, respectively.

Table 3.2.: IMACS Magellan instrument specifications and observation log.

Property	Value	
	2016 Observation	2019 Observation
Imaging	f/4 Camera	f/4 Camera
Field of View	$15.4' \times 15.4'$	$15.4' \times 15.4'$
CCD	8K × 8K pixels	8K pixels
CCD Pixel Scale	$0.111''$ per pixel	$0.111''$ per pixel
Airmass	1.4	1.4
Average seeing	$1''$	$1''$
Grating	600 lines/mm	600 lines/mm
Grating angle	10.86°	9.71°
Dispersion	0.378 Å/pixel	0.378 Å/pixel
Slit width	$2.5''$	$1.2''$
Wavelength Range	4250 - 7380 Å	3650 - 6770 Å
Spectral Resolution	850	1000
Number of slit positions	4	1
Slit position angle[†]	39.95°	0°
Exposure time (per slit position)	3 × 1200 seconds	2 × 1200 seconds

[†] Slit position angle is defined with respect to the North.

The data reduction process consisted of two significant steps: i) correction for instrumental errors and 2) extraction of the spectra. These steps are discussed more in detail here.

3.2.2.1. Correction for instrumental errors

Instrumental or systematic errors are an integral part of a majority of scientific observations. Therefore, identifying and removing them correctly is crucial for any data set before using them for scientific analysis. I applied the following basic corrections to the raw spectroscopic data to make it free from instrumental errors.

- **Bias correction :** Generally, there is a zero error or bias value associated with every image captured by a CCD detector. The standard way to correct this bias is to use the several zero exposures images of the source taken during the night of observations and combine them using their median value to produce a master bias image. This master bias image (shown in Fig. 3.3) is then subtracted from the raw image to make the bias correction.
- **Flat Field correction :** There could be some variations in the response and light sensitivity of every pixel in a CCD detector, leading to some non-uniform patterns in the images they record. To correct this effect, I used images of a flat field (uniformly illuminated the slit with a white lamp which emits equally in all wavelengths) taken during the observation, average and normalised them to map the sensitivity variations across the CCD. The bias subtracted raw images are divided by the normalised master flat-field (shown in Fig. 3.3) to make the flat field correction. Both the bias and flat-field corrections were done using the `ccdproc` task in IRAF.
- **Eliminate cosmic rays :** Normally, cosmic rays do not interact with anything, but 1 in a billion incident particles could interact with the CCD and produce imperfections in the data by inducing

tremendous values in few pixels. This will result in some tiny bright spots in the image (shown in the top panel of Fig. 3.3). In my case, these abnormally high pixel values were eliminated by combining the multiple exposures of the same slit. This correction was done using the IRAF task `imcombine`.

$$\text{Reduced Image} = \frac{\text{Raw Image - Bias}}{\text{Flat Field - Bias}} + \text{Cosmic ray correction} \tag{3.1}$$

A portion of the reduced image even after the bias, flat field and cosmic ray correction using the relation from Eqn. 3.1, still possess a small artefact on the bottom left corner of the CCD (see bottom panel of Fig. 3.3). This is probably due to some reflections from a bright background star. Since I couldn't remove this artefact, its presence was carefully noted during my further steps of data reduction and analysis.

3.2.2.2. Spectral Extraction

Once my data was corrected for the CCD imperfections, the next step was to extract scientific spectra out of it. The spectral extraction process was done using the standard IRAF task `apall`.

An extraction aperture size of 9 pixels (corresponding to $1''$) was chosen for all the spectra, due to the minimum observable size limit set by the atmospheric seeing. For the 2016 and 2019 observations with different slit widths, this corresponds to aperture sizes of $1'' \times 2.5''$ and $1'' \times 1.2''$, respectively.

For each aperture, I also chose a global sky background subtraction window to eliminate skylines from the extracted spectra. This sky background was chosen far from each aperture to make sure that no signal corresponding to the source is subtracted. For the CCD chip 1 (shown in Fig. 3.3), this sky subtraction window was set outside the artefact region found on the chip, to eliminate any possibilities of overestimation of the sky background.

For each slit position, I started placing apertures at the peak of emission, and moved outwards in both directions with an increment of $1''$ for each aperture, until no signal was measured. For instance, in the 2D spectrum shown in the bottom panel of Fig. 3.3, the initial aperture was placed on the peak of the bright horizontal line corresponding to the centre of Malin 1 and moved outwards vertically along both sides until no more signal (above 2σ) was obtained in the extracted spectrum. This procedure led to the extraction of 15 spectra from the central region of Malin 1 (11 in the 2016 data and 4 in the 2019 data).

I continued this procedure towards the outer parts of Malin 1, but the signal was too weak, except for a region at $\sim 16''$ from Malin 1 centre in the 2016 data. In this region, close to a compact source visible in the broad-band images of Malin 1, I obtained a spectrum above the noise level (after re-binning the spectrum by a factor of 3). This region also overlaps with FUV GALEX images (Boissier et al. 2016) and archival UVIT UV emission.

The above spectral extraction procedures resulted in a total of 16 spectra for Malin 1. All the regions where I extracted a spectrum is shown in Fig. 3.4.

After the successful extraction of the spectra, a calibration procedure also needs to be performed for converting the spectra from pixel units to wavelength and flux units. This is discussed in the following sections.

Wavelength Calibration

I performed a wavelength calibration on the extracted spectra of Malin 1 using a standard HeNeAr calibration lamp spectra taken during the observations. I manually identified the spectral lines of the extracted spectra with that of the HeNeAr spectral lines to obtain a dispersion relation of the wavelength as a function of pixel positions in the CCD. IRAF tasks `identify` and `dispcor` were used for this wavelength calibration procedure.

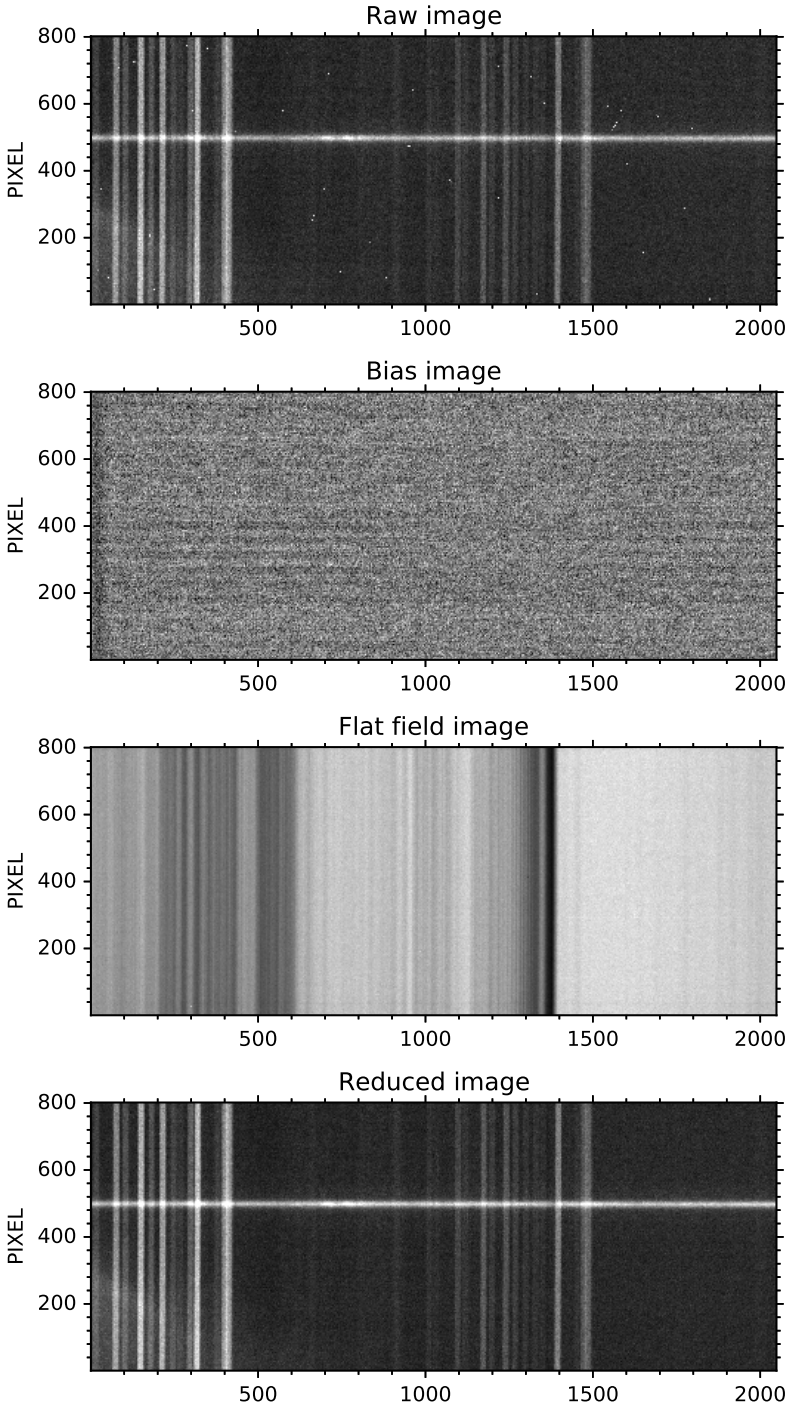

Figure 3.3.: Malin 1 2D spectra of the CCD chip 1 (6600 - 7380 Å) obtained in the 2016 observations. The raw image, master bias image, master flat field image and the final reduced image (including cosmic ray correction) are shown in the images from top to bottom, respectively. The vertical and horizontal axes are respectively the spatial and spectral directions. In the bottom reduced image, the bright horizontal line passing through $y \approx 500$ pixel is the central part of Malin 1. The bright vertical lines are skylines. A relatively bright blob at $(x, y) \approx (750, 500)$ is the position of the Hα line in Malin 1.

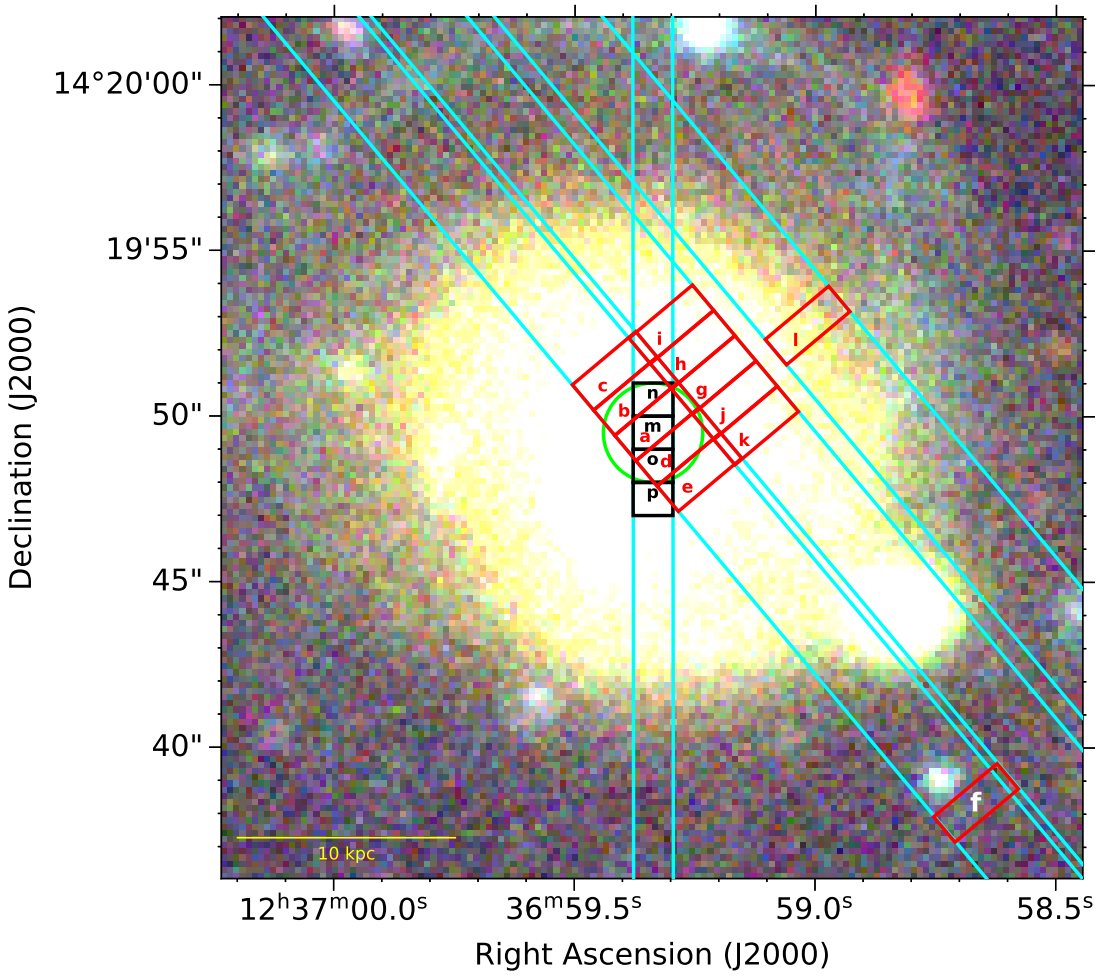

Figure 3.4.: Positions of the 16 apertures in which we could extract a spectrum. The 2016 and 2019 observations are denoted as red and black regions, respectively, along with their designated region names. The regions are named in the order in which I extracted the spectrum beginning from the center of each slit and then moving outwards in both directions. There is a small overlap of 0.1″ in slits one and two caused due to the shifting of the slits during the 2016 observation. This overlap, however, is negligible compared to the size of apertures studied in this work. The green circular region indicated in the centre is the location of an SDSS spectrum of Malin 1 with an aperture of 3″ diameter.

Flux Calibration

The last step in the data reduction process was carried out by a flux calibration of the Malin 1 spectra using a standard reference star spectrum taken during the observation. For the 2016 data, the observed reference star was *LTT 3218*. However, I did not perform a flux calibration for the 2019 data, since this observation was carried out without a proper reference star.

Flux calibration initially consists of extracting the reference star spectrum and comparing it with the

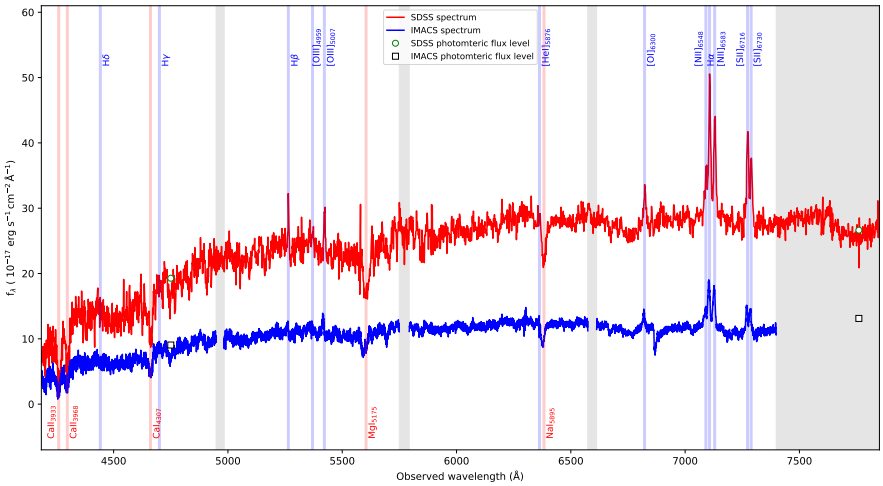

Figure 3.5.: Central region spectra of Malin 1. The blue curve is the spectrum I extracted in the central $1'' \times 2.5''$ aperture (region *a* in Fig. 3.4). The red curve is the SDSS spectrum of Malin 1, extracted within a circular optical fibre of diameter $3''$ (shown as a green circle in Fig. 3.4). The green open circles and black open squares indicate the photometric flux levels obtained within the SDSS and my aperture, respectively, using the NGVS *g* and *i* band photometric images of Malin 1. The grey shaded area represents the region outside the wavelength coverage of observations used in this work. The blue and red vertical shaded regions indicate the main identified emission and absorption lines.

tabulated flux values for the given star in standard reference star directories. An extinction correction based on the airmass (*LTT 3218* was observed at an airmass of 1.011) of the observation, along with an IRAF standard extinction correction applied to produce a flux calibrated spectra of the reference star. This flux calibrated spectrum of the standard star is used as a reference for all the further flux calibration processes of the obtained Malin 1 spectra. IRAF tasks `standard`, `sensfunc` and `calibrate` were used for the flux calibration procedure.

The final scientific spectra of Malin 1 was obtained after doing all the extraction and calibration processes discussed above. I was able to extract a total of 16 spectra, corresponding to different regions of the galaxy, including a region relatively far from the centre of Malin 1 at a distance of ~$16''$.

Comparison to the SDSS Spectrum

To check the consistency and correctness of the extraction procedures I followed, I made a comparison of the spectrum I extracted for the centre of Malin 1 with that of the SDSS spectrum (DR12) in the central $3''$ region of the galaxy (shown in Fig. 3.5).

The entire range of both spectra is consistent in terms of the line positions and features. However, we need to note that the flux levels in both spectra are different due to the difference in the aperture sizes of both the data (SDSS spectrum have a larger aperture size of $3''$ in diameter compared to the $1'' \times 2.5''$ aperture from this work. This captures more flux in the SDSS aperture). This difference is expected and I verified it using the photometric flux levels of the same apertures (SDSS aperture and mine) from the NGVS *g* and *i*-band images of Malin 1. The continuum flux levels in both spectra are also found to be consistent with respect to their aperture sizes (see Fig. 3.5). The emission lines observed in both

the data are also very similar. Therefore, hereupon for my further analysis, I concentrate on these emission lines with a special focus on the Hα and [O II] lines which were the strongest among those in the observed wavelength range (Hα for the 2016 observation and [O II] for the 2019 ones). For simplicity, from now on I indifferently refer to the 2016 and 2019 observations as to the Hα and [O II] ones.

3.2.3. Measurements

The spectra obtained for Malin 1 after all the data reduction processes needs to analysed to extract scientific information from it. The initial step in this direction was to perform an emission line fitting for identified key emission lines. This is discussed in the following section.

3.2.3.1. Emission line fitting

I performed an emission line fitting of the Hα and [O II] lines using the Python `leastsq` routine on a Gaussian line profile to obtain the peak wavelength and flux of the lines.

The overlapping lines (Hα and the [N II]$_{6548}$, [N II]$_{6583}$ doublet; and the [O II]$_{3727}$, [O II]$_{3729}$ doublet) were fitted simultaneously. I also applied various constraints on the emission lines during the fitting procedure. This includes a fixed line ratio for the [N II] and [O II] doublets ([N II]$_{6583}$ / [N II]$_{6548}$ = 2.96 adopted from Ludwig et al. (2012); [O II]$_{3729}$ / [O II]$_{3727}$ = 0.58 from Comparat et al. 2016). The separations between the lines were fixed using their rest-frame wavelengths along with an additional line separation taking into account the redshift of Malin 1 (given in Table 3.1) where $\Delta\lambda_{obs} = \Delta\lambda_{rest}\,(1+z)$. I also performed a spectral re-binning by a factor of 3 for a few of the spectra affected by a considerably weaker signal that are at the limit of the detection (regions *f*, *l* and *p* from Fig. 3.4).

The error bars associated with each quantity (peak wavelength and line flux) was separately measured (apart from the formal error obtained from the `leastsq`). For this purpose, I implemented a Monte Carlo chain of 10000 by adding a random noise (with the same standard deviation as the noise in the spectrum) in the initially fitted spectra.

The results of the emission line fitting are given in Fig. 3.6 and Table 3.3.

3.2.3.2. Measurement of rotational velocity

The observed shift in the wavelength of the Hα and [O II] emission lines (given in Table 3.3) from their respective rest-frame wavelengths can be used to measure the line of sight velocity ($V_{l.o.s}$) of the observed region with respect to the rest frame. The rest-frame wavelengths of Hα and [O II]$_{3727}$ lines are 6562.8 Å and 3726.04 Å, respectively. Using these values, the line of sight velocity of a region is given as:

$$V_{l.o.s} = \left(\frac{\lambda_{obs} - \lambda_{rest}}{\lambda_{rest}}\right) c \tag{3.2}$$

where λ_{obs} and λ_{rest} are the observed and rest-frame wavelength of a line, respectively. c is the speed of light.

Using Eqn. 3.2 along with the Hα peak wavelength for the region *given in Table 3.3*, we can measure the line of sight velocity of the centre of Malin 1. This gives, $V^{a}_{l.o.s} = 24726 \pm 4$ km s^{-1}. This is consistent with the systemic velocity (V_{sys}) of Malin 1 from Lelli et al. (2010) using H I observations (see Table 3.1). Therefore, for comparison purposes, we adopt the global systemic velocity of Malin 1 from Lelli et al. (2010).

Before the measurement of the rotational velocity in the plane of the galaxy, we also need to de-project the radius of the observed region (with respect to Malin 1 center) on the sky plane to the galaxy plane. Teuben (2002) gives the following transformation:

$$R_g = R_s \sqrt{\cos^2\phi + \frac{\sin^2\phi}{\cos^2 i}} \tag{3.3}$$

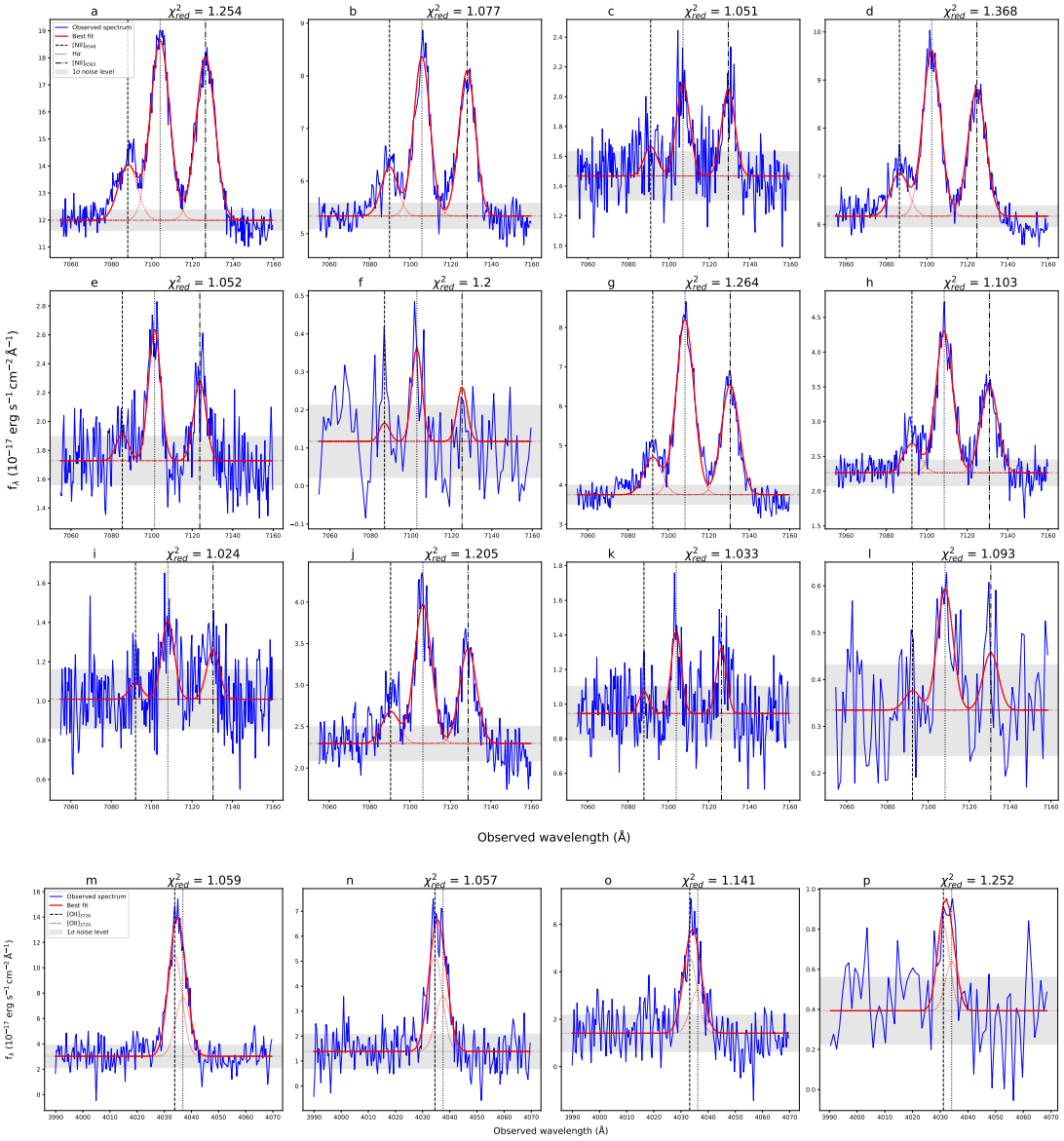

Figure 3.6.: Hα and [O II] spectra extracted from 16 different regions of Malin 1 (12 Hα spectra in the top three rows and 4 [O II] spectra in the fourth row). The solid red curve is the best fit along with its decomposition in a single Gaussian shown as thin red dotted lines. The grey dashed line and shaded region indicate the continuum level obtained from the fitting with the 1σ noise level. The black dashed, dotted, and dot-dashed vertical lines indicate the positions of the [N II]$_{6548}$, Hα and [N II]$_{6583}$ emission lines, respectively, for the three top rows. The dashed and dotted lines in the bottom row show the position of the two components of the [O II] doublet. The region name and the reduced χ^2 are indicated on top of each panel.

Region name	Radius (kpc)	Peak wavelength $\lambda_{H\alpha}$ or $\lambda_{[OII]_{3727}}$ (Å)	Velocity V_{rot} (km s^{-1})	Flux Hα	Flux [N II]$_{6583}$	Flux Hβ	Flux [O III]$_{5007}$
(1)	(2)	(3)	(4)	(5)	(6)	(7)	(8)
a	0.58 ± 0.38	7104.07 ± 0.08	-53 ± 54	78.3 ± 1.5	71.4 ± 1.6	10.8 ± 1.2	25.7 ± 1.7
b	2.00 ± 0.37	7105.77 ± 0.09	80 ± 23	30.5 ± 0.9	27.9 ± 0.9	4.7 ± 0.7	...
c	3.70 ± 0.40	7107.04 ± 0.27	197 ± 39	5.2 ± 0.6	4.8 ± 0.6	...	1.7 ± 0.5
d	1.64 ± 0.48	7102.38 ± 0.09	408 ± 173	37.8 ± 0.9	29.1 ± 0.9	7.0 ± 0.9	12.4 ± 0.9
e	3.33 ± 0.46	7101.37 ± 0.22	420 ± 87	7.0 ± 0.6	4.2 ± 0.5	3.5 ± 1.1	2.7 ± 0.6
f*	25.9 ± 0.43	7102.93 ± 0.88	189 ± 91	1.6 ± 0.5	1.0 ± 0.5	...	...
g	4.53 ± 0.20	7108.22 ± 0.08	393 ± 24	48.9 ± 1.0	30.7 ± 0.9	11.2 ± 0.6	9.1 ± 0.7
h	4.56 ± 0.18	7108.62 ± 0.13	308 ± 13	21.2 ± 0.7	13.0 ± 0.7	3.1 ± 0.6	3.5 ± 0.6
i	5.21 ± 0.14	7108.02 ± 0.47	228 ± 33	3.2 ± 0.5	2.0 ± 0.5	...	1.9 ± 0.5
j	5.12 ± 0.19	7106.38 ± 0.17	367 ± 54	17.7 ± 0.8	12.1 ± 0.8	3.5 ± 0.8	5.6 ± 0.7
k	6.16 ± 0.17	7103.89 ± 0.33	-1092 ± 692	3.0 ± 0.5	2.4 ± 0.4	...	...
l*	10.51 ± 0.27	7108.20 ± 1.08	489 ± 155	2.5 ± 0.7	1.2 ± 0.8	...	1.7 ± 0.4
m	0.00 ± 0.64	4033.85 ± 0.11	23 ± 13	...	...	...	...
n	1.56 ± 0.13	4034.52 ± 0.18	104 ± 23	...	...	...	...
o	1.56 ± 0.13	4033.20 ± 0.24	55 ± 29	...	...	...	...
p*	3.11 ± 0.07	4031.14 ± 0.67	304 ± 81	...	...	...	...

Table 3.3.: Measured data for Malin 1 from the 2016 and 2019 observations. (1) Name of the spectral extraction region. The * symbol indicates spectra that I re-binned for the analysis. (2) Radius in the galaxy plane. (3) Hα or [O II]$_{3727}$ observed wavelength. (4) Rotational velocity in the plane of the galaxy. (5-8) Observed flux of Hα, [N II]$_{6583}$, H$_\beta$, and [O III]$_{5007}$ emission lines, respectively, within the $1'' \times 2.5''$ regions. The flux units are in 10^{-17} erg s^{-1} cm^{-2}.

$$\cos\theta = \frac{R_s}{R_g}\cos\phi \tag{3.4}$$

where R_g and R_s are the radius of the observed region on the galaxy plane and sky plane, respectively. The angle i is the inclination angle of Malin (see Table 3.1). Angles ϕ and θ are respectively the azimuthal angles on the sky and galaxy plane.

Combining Eqn. 3.2, 3.3 and 3.4, one can easily find the rotational velocity of a region on the plane of the galaxy, given as:

$$V_{rot} = \frac{V_{l.o.s} - V_{sys}}{\sin i \cos\theta} \tag{3.5}$$

The measured rotational velocities for all the regions are given in Table 3.3.

3.2.4. Results

3.2.4.1. Rotation curve

The analysis of the rotation curve of a galaxy is of utmost importance in understanding the dynamics and underlying mass distribution, especially the DM distribution, within a galaxy. The rise of rotation curve for LSB galaxies which are generally considered to be DM dominated (de Blok & McGaugh 1997), is important in understanding the differences they possess with their HSB counterparts.

Using the measurements discussed in the previous section, I extracted a rotation curve for Malin 1 from the observed wavelength shift in the Hα and [O II]$_{3727}$ emission at different regions of the galaxy (shown in Fig. 3.7).

I observed a steep rise in the rotational velocity for the inner regions of Malin 1 (inside ~10 kpc) up to ~350 km s^{-1} (with, however, some spread between 200 and 400 km s^{-1} around a radius of 5 kpc), and a subsequent decline to reach the plateau observed on large scales consistent with H I from Lelli et al. (2010). Both the Hα and [O II] velocities in our data follow a similar trend and are consistent with each other. A steep inner rise of the rotation curve is typical for an HSB system. For Malin 1, it is the first time to observe this behaviour, unlike the slowly rising rotation curve predicted by Pickering et al. (1997) or the poorly resolved inner rotation curve from Lelli et al. (2010) using H I data. In Sect. 3.2.5 I discuss a new mass model based on this rotation curve.

3.2.4.2. Star formation rate surface density

The presence of Hα emission line is a good indicator of star formation activity in a galaxy (Boissier 2013b). I use the Hα emission line fluxes observed for Malin 1 (given in Table 3.3) to estimate the star formation rate surface density ($\Sigma_{\rm SFR}$) at different regions of the galaxy.

Boissier (2013b) gives the following relation for the conversion of Hα to star formation rate (SFR):

$$\mathrm{SFR}\,(M_\odot\, yr^{-1}) = 5.1\times10^{-42}\, L_{H\alpha}\,(\mathrm{erg}\, s^{-1}) \tag{3.6}$$

Using Eqn. 3.6, along with the area of our measured apertures (our apertures cover several kpc), the estimated star formation rate surface density for different regions of Malin 1 is given in Fig. 3.8.

The variation of $\Sigma_{\rm SFR}$ in Malin 1 in comparison to the values from González Delgado et al. (2016) and Bigiel et al. (2010) shows some interesting results. For comparison purposes, the profiles shown in Fig. 3.8 are normalised to the effective radius (R_e). I estimated the R_e of Malin 1 to be equal to 2.6″ (3.9 kpc), calculated within 20″ of the centre of the galaxy I-band profiles of Barth (2007). I adopted this limit so that the comparison is based on the "inner" galaxy at the centre of Malin 1 as described by Barth (2007), not the extended disk, as we believe that the data from González Delgado et al. (2016) (using CALIFA survey data from SDSS) better correspond to this inner galaxy.

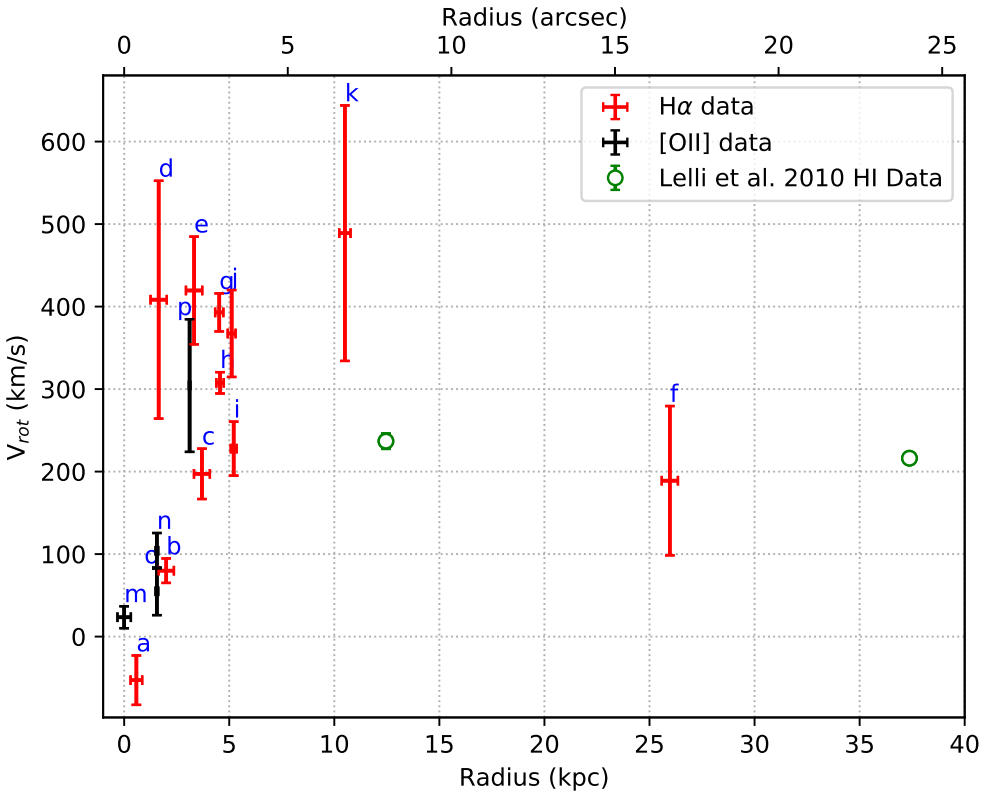

Figure 3.7.: Rotation curve of Malin 1, projected on the plane of the galaxy. The red and black points indicate the Hα and [O II] data, respectively. The green open circle shows Lelli et al. (2010) H I data points in the same radial range. The region name of each point is indicated with blue letters.

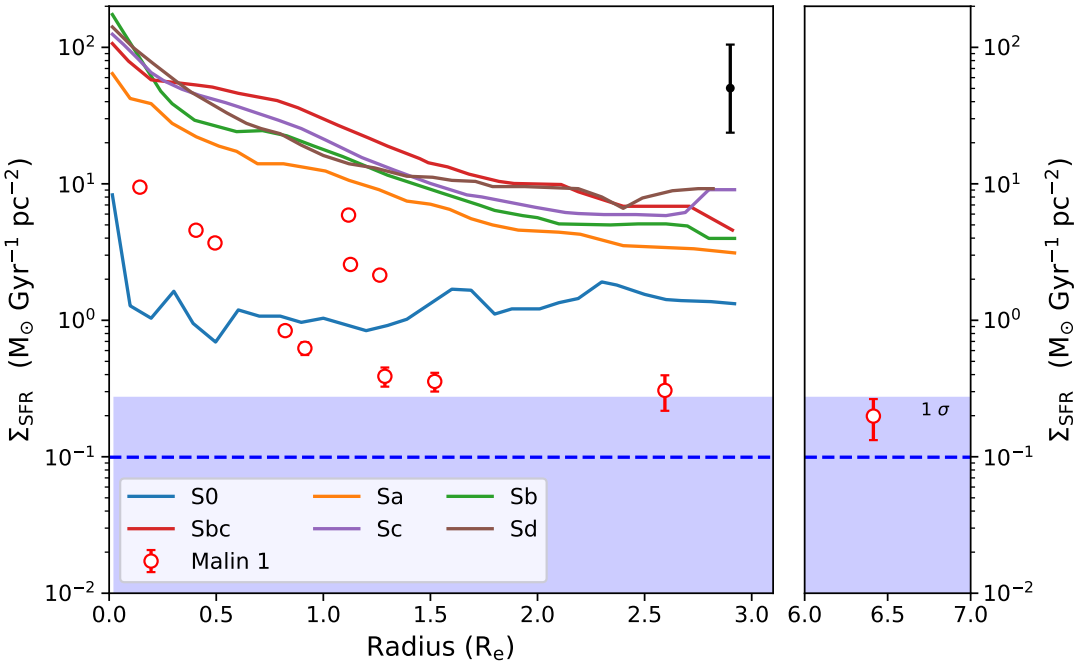

Figure 3.8.: Radial profiles (in units of effective radius) of the star formation rate surface density of Malin 1 in comparison with different morphology of spiral galaxies from González Delgado et al. (2016) (shown as solid curves). The red open circles show the estimated Σ_{SFR} for Malin 1 using Hα data. The blue dashed line indicates the mean level of Σ_{SFR} in the extended disc of spiral galaxies from Bigiel et al. (2010) with a 1σ level of dispersion (blue shaded region). The error bar in black indicates the typical dispersion among galaxies provided by González Delgado et al. (2016) around each solid curve.

From Fig. 3.8, we can see that the central region of Malin 1 (within $\sim 1.5\,R_e$) behaves as an intermediate between an S0/Sa early-type spiral. This is also consistent with the observation from Barth (2007) discussed in Sect. 3.1.

The Σ_{SFR} values in the extended disk of Malin 1 ($> 1.5\,R_e$) is similar to the levels found in the extended disk of XUV and spiral galaxies (Bigiel et al. 2010). However, considering that these observed data points only correspond to a few regions of Malin 1, it is hard to draw any conclusion on the global variation of Σ_{SFR} within the galaxy. Nevertheless, these observations can be still considered as an order of magnitude estimate of the star formation rate surface density in Malin 1.

3.2.4.3. Dust attenuation

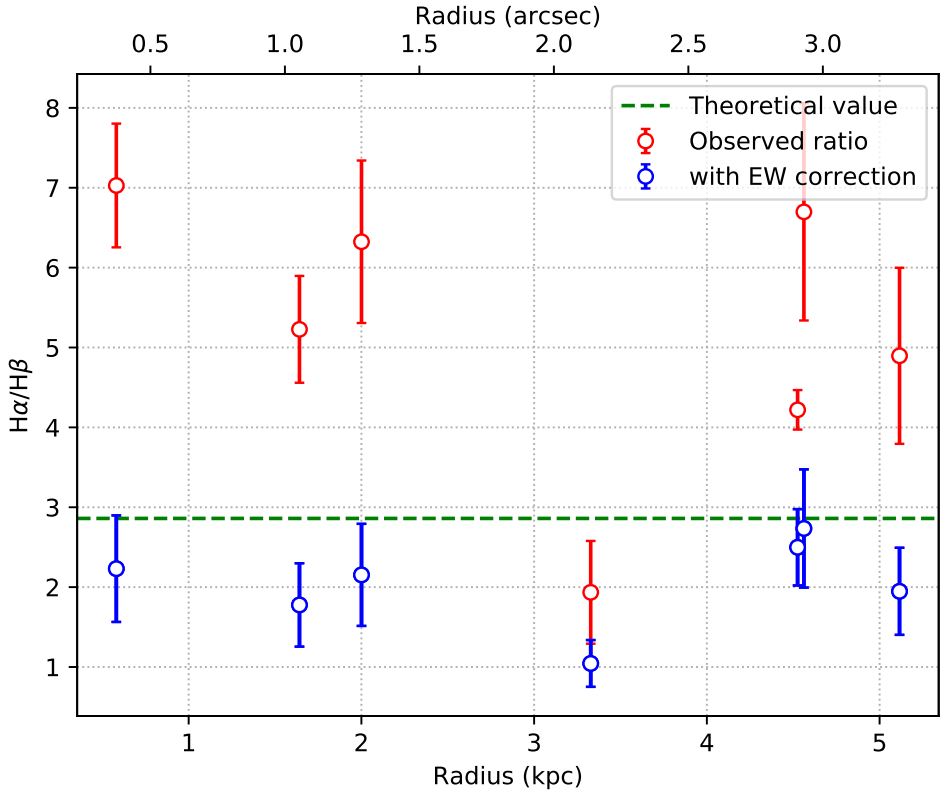

Figure 3.9.: The Balmer ratio for the eight different regions in Malin 1. The red and blue open circles show the observed and equivalent width corrected values, respectively. The green dashed line marks the theoretical value of 2.86 in the absence of dust.

Low surface brightness galaxies are generally considered to have low amounts of dust (Hinz et al. 2007; Rahman et al. 2007). In order to investigate this in the case of Malin 1, I used the observed Hα and Hβ fluxes given in Table. 3.3.

The effect of dust attenuation in a region can be indirectly probed using the Balmer ratio (Hα /Hβ). Hβ emission being on the shorter wavelength end of the spectrum, relative to Hα, is attenuated more by the dust content leading to higher Balmer ratios than the typical theoretical value for Hα /Hβ = 2.86 for a Case B recombination, in the absence of dust (Osterbrock 1974). However, the Balmer ratio is

also affected by the underlying stellar absorption. Since the data used in this work lack the spectral resolution to measure the underlying stellar absorption, I applied a standard equivalent width (EW) correction of 1.3 Å and 2.5 Å to the Hα and Hβ fluxes, respectively, from the literature (Moustakas et al. 2010; Gavazzi et al. 2011).

Fig. 3.9 shows the observed Balmer ratios in the eight regions of Malin 1. The Balmer ratio for the majority of the regions after EW corrections is close to the theoretical value (within 3σ), except for one region at about 3.3 kpc which is systematically below the theoretical value. This could be probably due to an uncertainty in the applied EW corrections. In any case, all the values indicate a low amount of dust in Malin 1. Moreover, the non-detection of Malin 1 in far-infrared by *Herschel* and *Spitzer* also point towards the same conclusion (Boissier et al. 2016).

3.2.4.4. Metal abundance

For a large majority of star-forming regions in galaxies, the metal abundance is mainly estimated using some empirical methods based on the relative intensities of strong, easily observable emission lines. Although abundances derived in this way could have considerable uncertainties, still they are capable of providing a general trend in abundance followed by a large fraction of galaxies (Denicoló et al. 2002). The [N II]$_{6583}$ /Hα ratio (also known as the N2 calibrator) is one such good estimator for metal abundance. Pettini & Pagel (2004) gives the following relation for the conversion of [N II]$_{6583}$ /Hα flux ratio in to Oxygen abundance:

$$12 + \log(O/H) = 8.90 + 0.57 \times \log \frac{[NII]_{6583}}{H\alpha} \tag{3.7}$$

Using the observed Hα and [N II]$_{6583}$ flux values for different regions of Malin 1 given in Table. 3.3 and Eqn. 3.7, I estimated the abundance in Malin 1. This is shown in Fig. 3.10.

Pettini & Pagel (2004) calibration points to metallicities about 0.15 dex above solar (or almost solar while using the improved calibration of Marino et al. (2013)) for the inner regions of Malin 1. In the extended disk, the uncertainty in the flux ratios due to weak signal makes it hard to draw reliable conclusions on metallicity. However, the high value of metallicity in the very central region of Malin 1 may not be realistic as the line ratios could be affected by the presence of an Active Galactic Nuclei (AGN) as discussed in Sect. 3.2.4.5.

3.2.4.5. Presence of active galactic nucleus (AGN)

Although Active Galactic Nuclei (AGN) are generally not seen in LSBs, a significant fraction of bulge-dominated GLSBs does show AGN activity (Sprayberry et al. 1995; Galaz et al. 2011). Similary, Malin 1 also appears to have an active nuclei. Barth (2007) classified Malin 1 as a LINER nucleus galaxy with an [N II]$_{6583}$ /Hα flux ratio of 0.85. This is close to the flux ratio of [N II]$_{6583}$ /Hα = 0.91 ± 0.06, I measured in the centre of Malin 1. Subramanian et al. (2016) also gives a similar classification for Malin 1, placing it in the category of a LINER and composite nuclei using the Malin 1 SDSS spectrum.

Figure 3.11 shows an emission line diagnostic diagram (commonly known as BPT diagrams, Baldwin et al. 1981; Kewley et al. 2006) for Malin 1 in comparison to other samples of LSB and HSB galaxies. The [N II]$_{6583}$ /Hα and [O III]$_{5007}$/Hβ flux ratios measured in the centre would place Malin 1 on the borderline of LINER-Seyfert classification. A sample of LSBs from Subramanian et al. (2016) is also located in a similar place as Malin 1 in this diagram. The flux ratios from the other detected regions (six regions in addition to the nucleus) lie in the starburst region but close to the starburst-AGN demarcation line. The photo-ionisation models of Kewley et al. (2001) shown in Fig. 3.11, also shows that the inner regions of Malin 1 may have a large metallicity. This is consistent with the oxygen abundance in Malin 1, discussed in Sect. 3.2.4.4.

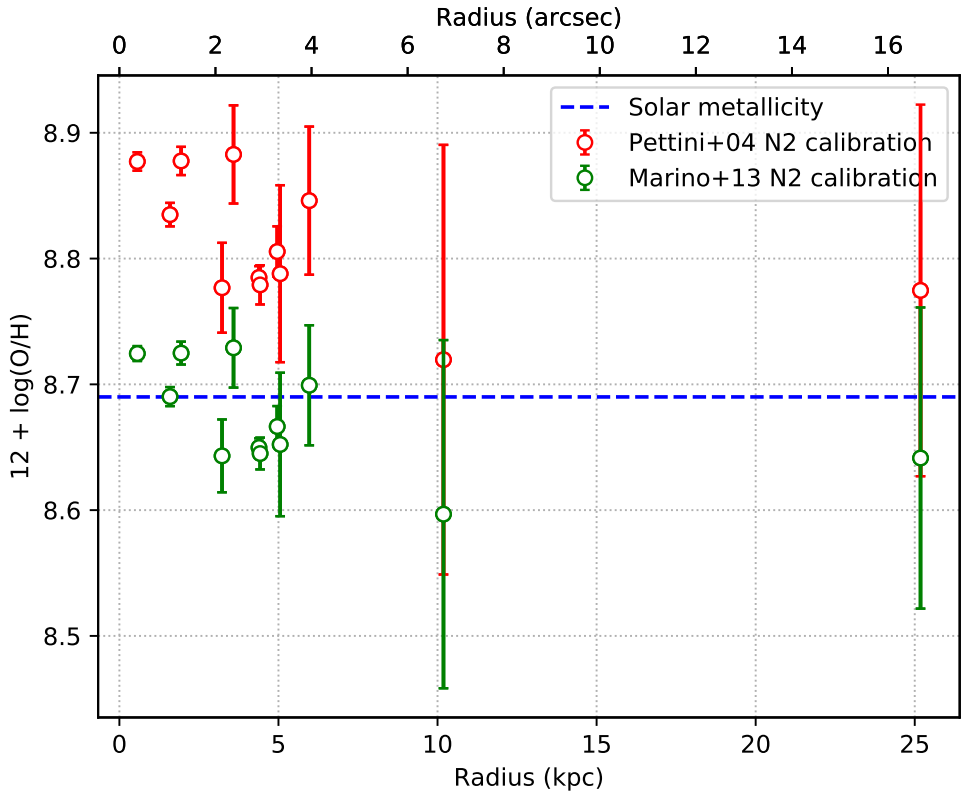

Figure 3.10.: Oxygen abundance measured for different regions of Malin 1. The red and blue open circles are the calibrations using Pettini & Pagel (2004) and Marino et al. (2013), respectively. The blue dashed line is the solar oxygen abundance value.

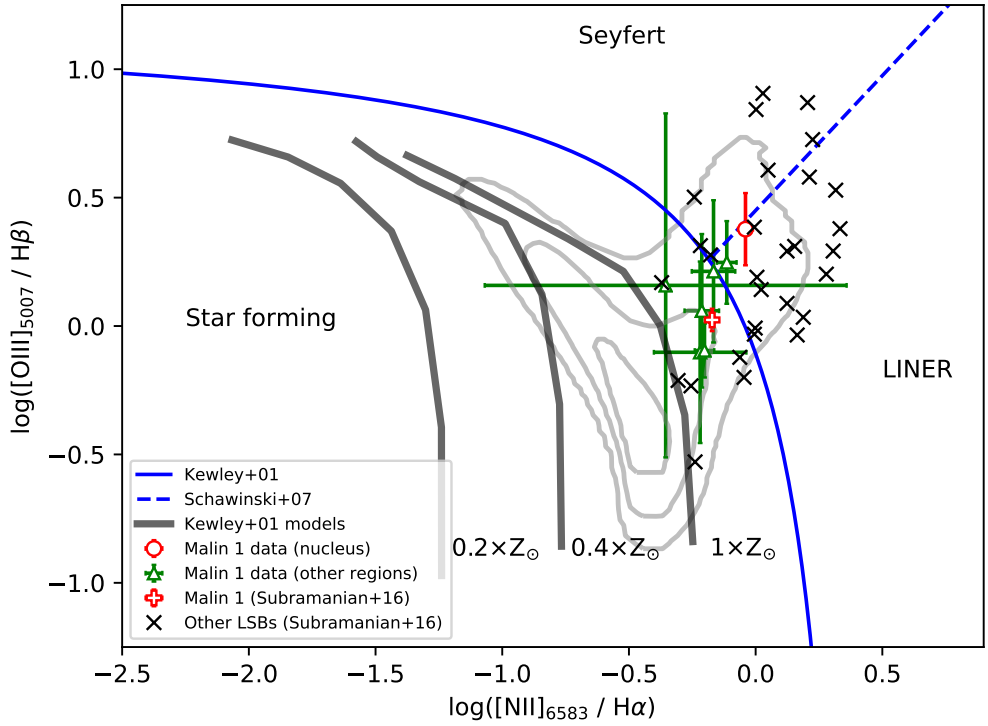

Figure 3.11.: Line diagnostic BPT diagram with $\log([\mathrm{N\,II}]_{6583}/\mathrm{H}\alpha)$ vs. $\log([\mathrm{O\,III}]_{5007}/\mathrm{H}\beta)$. The red circle and the green triangles respectively indicate the data points of Malin 1 for the nucleus and other detected regions in this work. The red plus and black crosses are the LSB sample from Subramanian et al. (2016), including Malin 1. The blue solid and dashed lines are defined by Kewley et al. (2001) and Schawinski et al. (2007), respectively, for the separation of AGN from star-forming regions. The grey contours show the distribution of a random sample of nuclear spectra of SDSS galaxies in the redshift range 0.01–1 and stellar mass 10^9-10^{11} (Boselli et al. 2018c). The black solid thick lines show the expected behaviour of star-forming regions as derived from the photo-ionisation models of Kewley et al. (2001) for three different metallicities (0.2, 0.4, 1 $Z_\odot$).

3.2.4.6. Malin 1 along the cosmic web

The environment of galaxies plays a major role in their evolution. This motivates one to investigate whether the environment of Malin 1 has something to do with its extreme nature and the very LSB giant disk. We used the SDSS-BOSS data in combination with the DISPERSE code to identify the filaments and mass density along the cosmic galaxy distribution (Sousbie 2011), shown in Fig. 3.12. Malin 1 appears to be in a rather low-density environment at a distance of about 10 Mpc from the edge of its closest filament. This relatively low density but proximity to a filament could account for the stability and richness of its extremely huge gaseous disk, similar to an observation from Reshetnikov et al. (2010).

3.2.5. A new mass model for Malin 1

In Sect. 3.2.4.1, I obtained a new rotation curve for Malin 1 using the Hα and [O II] emission lines. These rotation curves (shown in Fig. 3.7) contains some interesting features where for the first time we observe a very steep rise of rotational velocity values in the inner regions of Malin 1. This clearly demands a further investigation to understand the kinematics of this galaxy.

Mass models are a crucial tool in determining the kinematics and mass distribution of galaxies. Therefore, I teamed up with my collaborators Philippe Amram and Benôit Epinat to perform a mass modelling for Malin 1 based on this new rotation curve.

The total circular velocity components within a disc galaxy given by:

$$V_{\rm cir}(r) = \sqrt{V_{\rm disc}^2 + V_{\rm bulge}^2 + V_{\rm gas}^2 + V_{\rm halo}^2} \tag{3.8}$$

where $V_{\rm cir}$ is the circular velocity of the galaxy as a function of radius. $V_{\rm disc}$, $V_{\rm bulge}$, $V_{\rm gas}$, and $V_{\rm halo}$ are the stellar disc, stellar bulge, gas and DM halo velocity components, respectively.

The gas velocity component is taken from the H I measurements of Lelli et al. (2010). For the stellar disc and bulge velocity components, I used the HST I-band photometry from Barth (2007), by decomposing it into bulge, bar and disc components.

The light profile was decomposed into a Sérsic bulge, bar and a broken exponential disc component, following procedures from Barbosa et al. (2015). The decomposed light profile is shown in Fig. 3.13. The obtained decomposition is also consistent with the decomposition from Barth (2007). Malin 1 appears to have a double disk component which I mimicked here using a broken exponential disk. However, a choice of broken exponential disk over a double exponential disk won't affect my further analysis. In the mass modelling, the bulge component is taken from the decomposition and the effective "disc" component is taken as all the remaining light after removing the bulge.

The surface brightness profiles after the decomposition needs to be converted in to stellar mass profiles in order to obtain the velocity components. For this purpose, I used a standard mass-to-light-ratio-color relation from Taylor et al. (2011). Thus, a polynomial fit to the radial variation of $g-i$ color (from NGVS images) in Malin 1 gives the following i-band mass-to-light-ratio (in solar units):

$$\frac{M_\star}{L_i}(r) = 1.69 - 0.0986r + 0.0025r^2 - 0.0000208r^3 \tag{3.9}$$

Equation 3.9 is only valid for a radial range of $1'' < r < 40''$. For the very inner region and the extended disk, I adopted a constant $M_\star/L_i$ ratio of 3.765 and 0.379, respectively, obtained from the colour profile. The mass-to-light ratio and the stellar surface brightness profiles were then used to find the disk and bulge velocity components (assuming a thin disk geometry for the disk and spherical geometry for the bulge). For the disk and bulge velocity components, we also applied a correction for the beam smearing effect before using them in the modelling model (Epinat et al. 2010). The beam smearing effect caused due to the mixing of regions with different velocity contributions systematically flattens the observed velocity where there is a sharp gradient. In the inner regions of Malin 1, this was carefully taken into account in the modelling following procedures from Epinat et al. (2010).

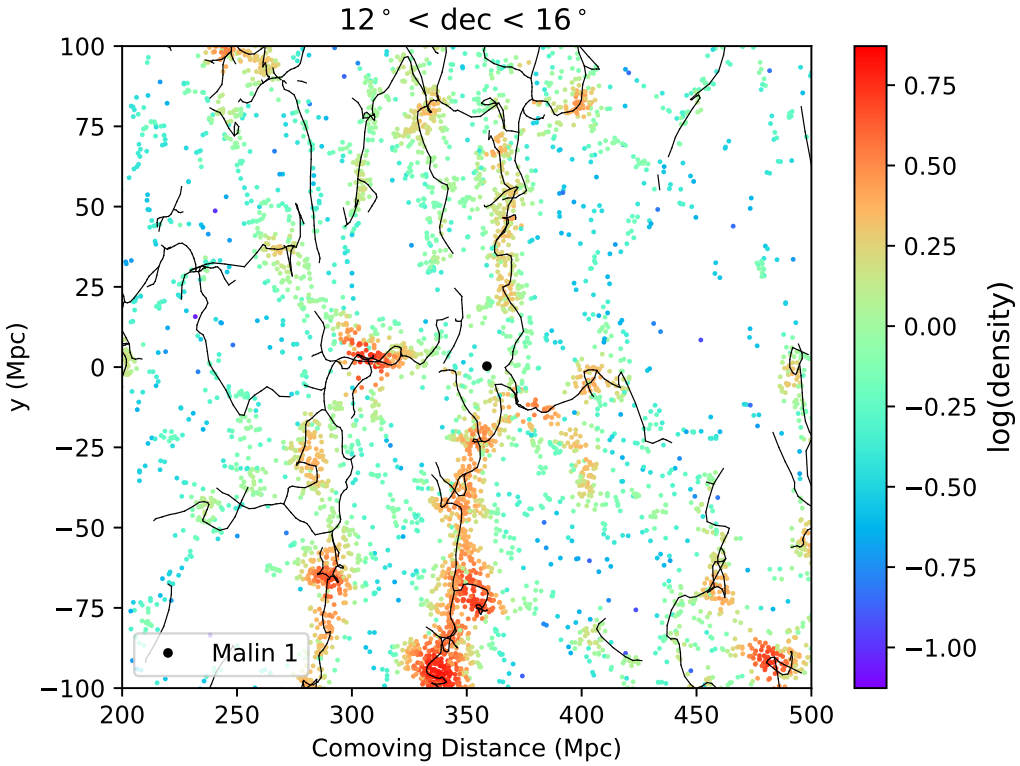

Figure 3.12.: Distribution of galaxies along the cosmic web. The black circle in the center of the plot shows the location of Malin 1. The horizontal and vertical axes correspond to the projection of the redshift ($0.02 \leq z \leq 0.15$) and right ascension ($150^\circ \leq \alpha(J2000) \leq 230^\circ$) in Cartesian coordinates. The declination range of $12^\circ < \delta\,(J2000) < 16^\circ$ is projected onto the plane. The black solid lines are the filaments identified using the DISPERSE code (Sousbie 2011). The galaxies are colour-coded as a function of the 3D density within a 5 Mpc radius of each galaxy (density is shown in the colour bar with an arbitrary unit).

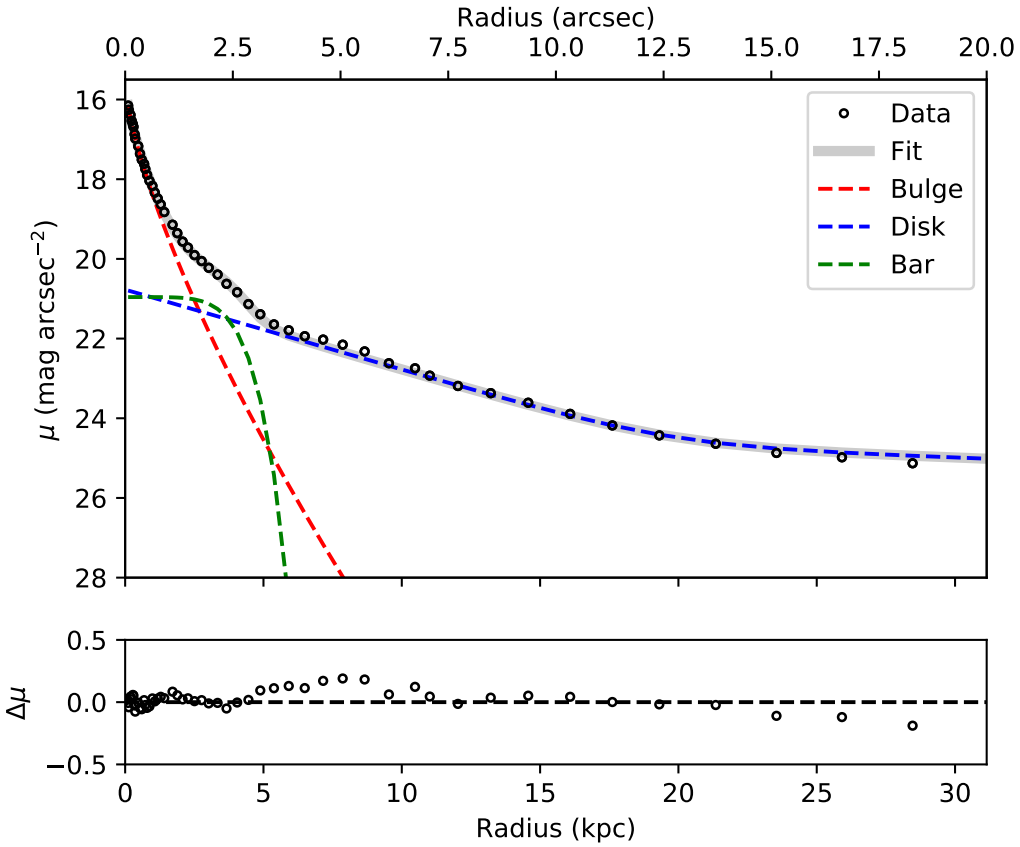

Figure 3.13.: Malin 1 I-band surface brightness profile decomposition. The bottom panel of the plot represents the difference between the observed surface brightness distribution and the model fit shown in the top panel.

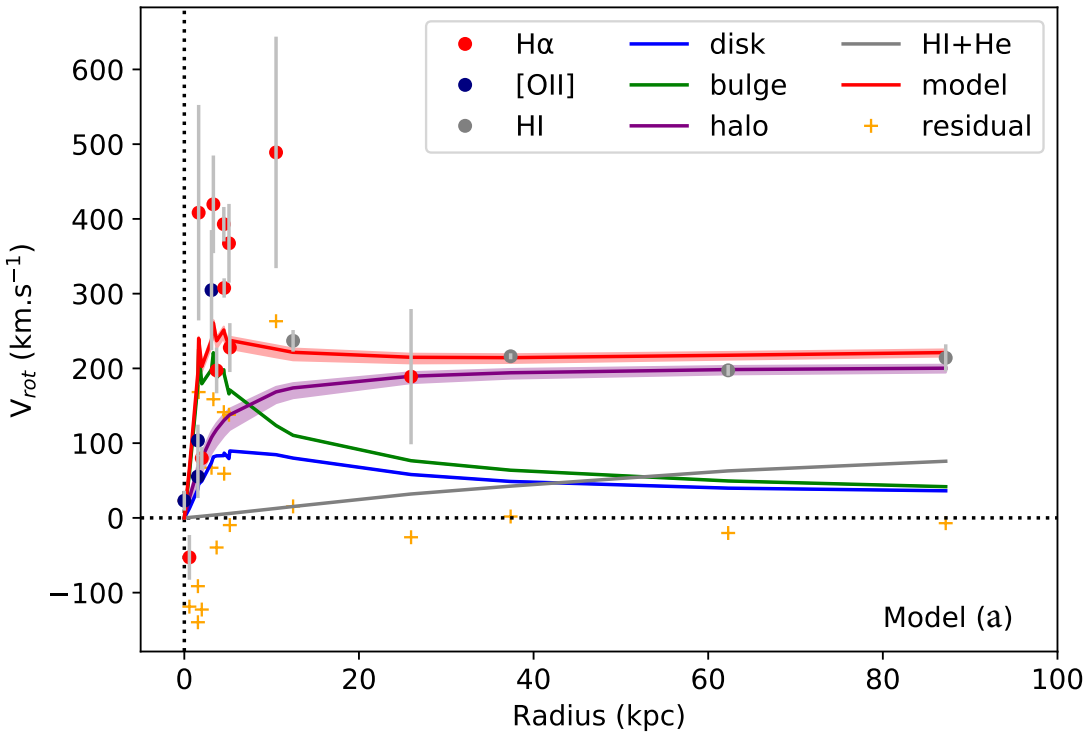

Figure 3.14.: Rotation curve of Malin 1 with the results from the mass modelling. The red solid line is the quadratic sum of the gas, disc, bulge, and DM halo components obtained as the best fit model. The shaded area around the model components are the confidence leveld from best fit χ^2 value ($\chi^2_{min} \approx 13$). The orange crosses represent the difference between the observed rotation velocities and the model for each point of the RC.

The final component in the rotation velocity (given in Eqn. 3.8) is the contribution from the DM halo. We assumed a DM halo with an iso-density core profile from Kent (1986) given as following:

$$V_{\rm halo}(r) = \sqrt{2}\sigma \times \sqrt{\left(1 - \frac{R_c}{r} \arctan \frac{r}{R_c}\right)}. \tag{3.10}$$

where the halo velocity contribution ($V_{\rm halo}$) depends on two free parameters, R_c and σ, the halo core radius and the velocity dispersion, respectively. The mass modelling was performed by varying these two parameters to find the best fit matching the observed rotational velocity. Figure 3.14 shows the result of our mass modelling. The central region of Malin 1 is dominated by baryons, with the extended disc dominated by DM ($R_c \sim 130$ km s^{-1}; $\sigma \sim 3$ kpc; $M_{halo} = 6 \times 10^{11}\, M_\odot$). However, our models couldn't explain the largest rotational velocity values observed in the centre. This could be attributed to the relatively poor resolution of our data, along with some assumptions on the geometry of Malin 1 disc (e.g., uncertainty in inclination, non-circular velocity components due to a bar). Nevertheless, the results from our models indicate that kinematically Malin 1 is an interesting source with a steep rising rotation curve in the observations, which could probably be explained only using high observational data in the future (e.g., IFU).

3.2.6. Conclusions

The spectroscopic study of the GLSB galaxy Malin 1 allowed me to obtain the following results:

- A complete data reduction process of raw long-slit spectroscopic data of Malin 1 yielded a set of spectra from 16 different regions of the galaxy. ,
- I extracted a new rotation curve for Malin 1 using Hα and [O II] emission lines, up to a radial extend of ~26 kpc.
- For the first time we observe a steep rise in the inner rotation curve of Malin 1 (within $r < 10$ kpc) up to ~350 km s^{-1} (with large dispersion). This is typical of an HSB galaxy, contrary to what is observed for LSB galaxies in general.
- I estimated the SFR surface density of Malin 1 in different regions at various radii, using the observed Hα emission line flux. The Σ_{SFR} within the inner regions of Malin 1 is consistent with an S0/Sa early-type spiral. The region detected at ~26 kpc from the centre of Malin 1 has a Σ_{SFR} close to the level found in the extended disc of spiral galaxies.
- An analysis of the line ratios indicates a very low amount of dust attenuation within Malin 1 (consistent with previous works in the infrared) and a relatively high metallicity in the inner regions. The line ratios in the centre are also consistent with the previous classification of Malin 1 with a LINER/Seyfert nucleus.
- A mass modelling based on the new rotation curve indicates that Malin 1 is dominated by baryons in the central region with a massive dark matter halo in the extended disk.
- The best fit from the mass modelling poorly fits the largest velocities observed in the centre. This could be due to a poor resolution of the data and uncertainty in the assumed geometry of Malin 1.

This work allows us to provide new constraints on Malin 1. However, the results from this study clearly illustrate that we need higher quality observational data for studying this galaxy more in detail. The mysterious case of Malin 1 will not be solved until then.

4. The family of giant LSBs

Summary

4.1 A history of what we know about GLSB galaxies . . . 70
4.2 A sample of GLSBs . . . 71
4.2.1 Followup spectroscopy and photometry . . . 73
4.2.1.1 IMACS-Magellan observations . . . 73
4.2.1.2 UVIT observations . . . 73
4.2.1.3 Malin 1 MUSE proposal . . . 76
4.2.1.4 Hα filter for Malin 1 . . . 76
4.3 Perspectives . . . 78

4.1. A history of what we know about GLSB galaxies

In Sect. 2.3, I briefly discussed the basic definitions of the class of GLSB galaxies along with a detailed description of the work done on Malin 1, the most extreme case of GLSB galaxy currently known, in Sect. 3.1.

Apart from Malin 1, many other GLSBs were also discovered over the past few decades (although they are not as extreme as Malin 1). Two years after the discovery of Malin 1, Bothun et al. (1990) discovered another GLSB galaxy, Malin 2, with features similar to Malin 1. This discovery opened a new window to the search for GLSBs where the accidental discovery of Malin 1 was not anymore an isolated case. Later, Hoffman et al. (1992) suggested that massive galaxies like Malin 1 and Malin 2 are rare, contributing only to a small fraction of the mass in the universe. Their analytical models of structure formation also indicated that the formation of these GLSB galaxies are largely environment-dependent, where they form in low-density void environments with large extended haloes. Both Malin 1 and Malin 2, located in relatively isolated environments, are consistent with this scenario.

In the following years, more GLSBs were discovered and investigated in detail. Sprayberry et al. (1995) studied a sample of 8 GLSBs and observed that they tend to have larger scale lengths and H I mass reservoirs than normal spirals. The colours and absorption line features in the central bulge regions of their sample also showed close similarities to the stellar population of HSB galaxies. Later Pickering et al. (1997) studied the kinematics of a sample of 4 GLSBs, observing a slowly rising rotation curve for these sources, indicating that GLSBs may be dominated by DM.

Matthews et al. (2001) re-visited a sample of 16 GLSBs (most of them already studied in past works, except for three sources) with better quality H I observations. Their observations indicated that GLSBs in general have H I masses $> 10^{10}$ $M_{\odot}$. With the increasing interest in GLSBs over the years, Noguchi (2001) proposed another scenario for the formation of GLSBs. According to this, GLSBs are formed due to the dynamical evolution of normal spirals during the formation of a bar, inducing non-circular motions and radial mixing of the disc resulting in a faint extended disk. Since many observed GLSBs tend to have a central bar and HSB-like structure, this scenario is quite feasible.

Most of the GLSB observations until this time were based on H I measurements due to the extreme gas-rich nature of these sources. Then Rahman et al. (2007) investigated the infrared properties of three GLSBs, including Malin 1, using *Spitzer* observations. Their observations revealed that all the three GLSB sources contain poly-aromatic hydrocarbon (PAH) molecules in their central region. At the same time, the extended disk was undetected in infrared for two of them, including Malin 1. Moreover, the

estimated dust-to-gas ratio of all their sources was found to be less than $10^{-3} - 10^{-2}$, indicating that LSB galaxies, in general, have a very low amount of dust.

Later, Mapelli et al. (2008) put forward another formation scenario for GLSBs where they can be formed as a final product of the dynamical evolution of collisional ring galaxies. According to this scenario, a progenitor ring galaxy formed due to collisions undergoes an expansion of its ring to create a faint extended disc with properties observed in GLSBs.

After various works on GLSBs in H I and infrared over the years, Boissier et al. (2008) assembled a sample of 18 LSB galaxies, ranging from dwarfs to giants LSBs, using UV data from GALEX. The derived star formation efficiencies (SFE) of their sample indicated that LSBs tend to have a lower SFE than HSB galaxies. Moreover, their analysis also found indications that LSBs might have a star formation history characterized by bursts followed by quiescent phases. This observation is also consistent with the collisional scenario proposed by Mapelli et al. (2008), which can lead to a burst of star formation.

The family of GLSBs continued to attract attention. Lelli et al. (2010) re-visited the H I kinematics of two GLSBs (including Malin 1), followed by the works of Pickering et al. (1997) and Matthews et al. (2001). They obtained a new rotation curve for these sources and observed a steep rise in the rotational velocity, contrary to the observation and prediction of a slowly rising rotation curve from Pickering et al. (1997) and Mapelli et al. (2008), respectively. Their analysis indicated that GLSB galaxies have a double structure, with a central HSB-like galaxy dominated by baryons and an outer LSB disk dominated by dark matter. Similar to this observation, Hagen et al. (2016) identified a new GLSB galaxy, UGC 1382, which was previously classified as a passive elliptical galaxy. They found that UGC 1382, like other GLSBs, studied in the literature, resides in a low-density environment and contains a two-component structure with an HSB disk surrounded by an extended LSB disk.

Mishra et al. (2017) performed a detailed analysis of a sample of 7 GLSBs from the literature using new H I observations and archival UV data. Their study revealed that the H I in all these galaxies extends roughly twice the optical radius, with total dynamical masses in the range of $10^{11} - 10^{12}$ $M_{\odot}$. The rotational velocities of the sample, too, showed an extensive range from ~ 200 to 400 km s^{-1}. Moreover, the UV properties of the sample also showed signs of star formation bursts and the presence of rings, consistent with the observation from Boissier et al. (2008) and formation scenario from Mapelli et al. (2008). Later, Saburova et al. (2021) performed yet another detailed study of a sample of 7 GLSBs using new long-slit spectroscopic data for a few and archival data for the rest of the sources. They concluded that there could be several possible formation scenarios for GLSB galaxies. This includes major merger events, gas accretion, or extended dark matter haloes.

The literature on GLSB galaxies shows that they were a pretty hot topic over the past few decades. However, apart from a lot of H I observations, we still lack high-quality spectroscopic and photometric data for these sources. In terms of numbers too, only a few GLSBs were identified and studied until now. Either the family of GLSBs is intrinsically small, or we are yet to discover more of them. A promising step towards identifying more GLSBs can be seen in an ongoing work by Ramya et al. (in preparation) using the SDSS galaxy catalogue from Meert et al. (2015, 2016). They systematically identified a sample of ~250 GLSBs from this catalogue following Sprayberry et al. (1995) GLSB criterion. This would increase the known GLSB population from few tens to few hundreds. Moreover, identifying a possible relation with XUV galaxies and GLSBs in future works will also potentially increase the GLSB galaxy population to more significant numbers.

4.2. A sample of GLSBs

As a step forward to better understand GLSBs, I recently assembled a sample of known GLSBs to collect more spectroscopic and photometric data for these giant sources. The selected sample consists of 21 GLSBs, with at least existing H I and GALEX UV data (although for six sources, there is only shallow UV coverage).

	Name	RA (deg)	DEC (deg)	Distance (Mpc)	$\log M_{HI}$ ($M_\odot$)	References
1	UGC 00568	13.787	-1.046	181.0	10.25	1,2
2	UGC 1382	28.671	-0.143	80.0	10.23	3
3	UGC 1378	29.080	73.283	38.8	10.08	4
4	UGC 1752	34.087	24.888	241.0	10.85	2
5	UGC 1922	36.941	28.209	150.0	10.51	4
6	PGC 135657	40.046	-1.774	176.0	10.20	2
7	UGC 2936	60.701	1.966	51.5	9.85	4
8	UGC 4422	126.925	21.479	63.4	10.17	4
9	NGC 2770	137.390	33.124	25.8	9.76	2
10	PGC 135754	159.365	2.089	287.8	10.06	1
11	Malin 2	159.969	20.847	183.2	10.52	1
12	UGC 6614	174.812	17.144	83.3	10.42	4
13	Malin 1	189.247	14.330	329.0	10.66	1
14	PGC 45080	195.817	1.469	162.5	9.99	2
15	UGC 9024	211.669	22.070	30.6	9.40	2
16	NGC 5533	214.032	35.344	54.3	10.48	5,6
17	NGC 5905	228.847	55.517	52.2	10.15	5,7
18	F530-1	316.887	26.450	194.6	10.27	1
19	F533-3	334.305	25.213	172.5	10.24	1
20	NGC 7589	349.565	0.261	120.7	10.01	1
21	PGC 71626	352.635	-2.463	135.9	10.23	1

Table 4.1.: Sample of H I and UV selected GLSB galaxies from the literature. References: (1) Boissier et al. (2008), (2) Matthews et al. (2001), (3) Hagen et al. (2016), (4) Mishra et al. (2017), (5) Sprayberry et al. (1995), (6) Noordermeer et al. (2005), (7) van Moorsel (1982)

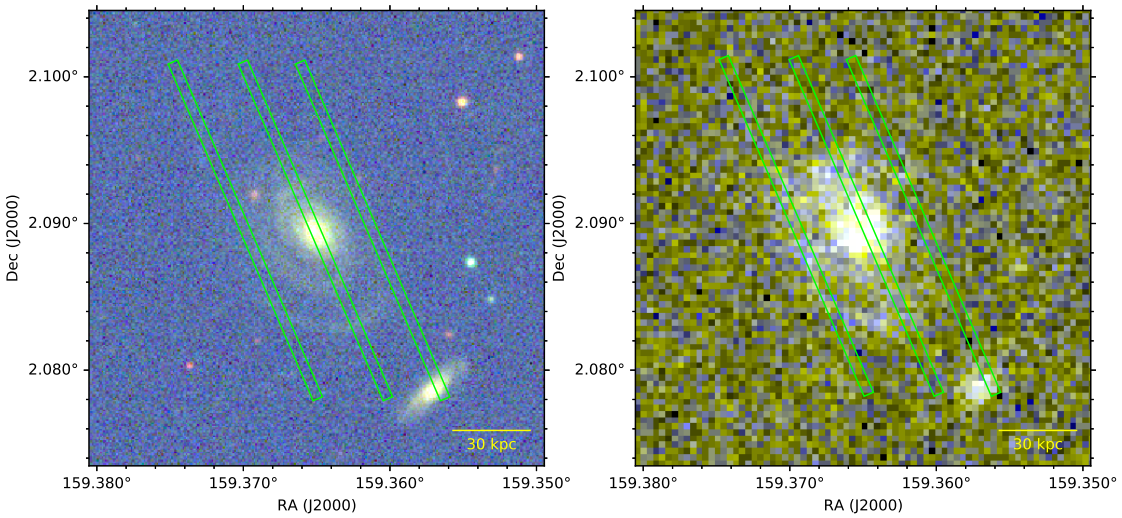

Figure 4.1.: GLSB galaxy PGC 135754 in optical and UV. Left panel is the SDSS *u*, *g* and *i*-band colour composite image. The right panel is the GALEX NUV and FUV colour image. The green boxes show the three observed IMACS Magellan long slit positions for this source, with a slit width of 2.5″.

4.2.1. Followup spectroscopy and photometry

I use the sample of GLSBs given in Table 4.1 as a basis for planning current and future follow-up observations, listed in the following sub-sections.

4.2.1.1. IMACS-Magellan observations

Initially, I proposed a sub-sample of GLSB sources from the sample given in Table 4.1 for a program of spectroscopic observation using the IMACS Magellan spectrograph (only 9 out of 21 sources are observable using IMACS). This is done in collaboration with our colleague Barry Madore from Carnegie Observatory, who has guaranteed observation time with the instrument.

In a May 2019 observation, I already obtained optical spectroscopic data for two sources from the sample, including Malin 1 and another GLSB galaxy, PGC 135754. A detailed analysis of the Malin 1 data from this observation is discussed in Sect. 3.2.1.

For PGC 135754, the spectroscopic data reduction is not yet performed to extract the spectra and carry out the analysis as I did in the case of Malin 1.

Similar data for the rest of the sample is expected in future observing runs. I plan to get complementary spectroscopic and photometric data with matching resolution for the entire sample.

4.2.1.2. UVIT observations

Apart from the proposed spectroscopic observations discussed above, recently, I also submitted an accepted proposal for the observation of another GLSB source from the sample (UGC 6614) and an XUV galaxy (NGC 1042) using the Ultraviolet Imaging Telescope (UVIT; Kumar et al. 2012). UVIT, a successor of GALEX, has an improved imaging quality in UV with a resolution of ~1.8″, almost three times better than the GALEX resolution of ~6″. The resolution of UVIT also matches the slit widths of our spectroscopic observations.

Figure 4.2 clearly illustrates that UVIT achieves a better spatial resolution than GALEX, allowing pinpointing UV emission regions more precisely (and a resolution similar to the 2.5″ slit width of the

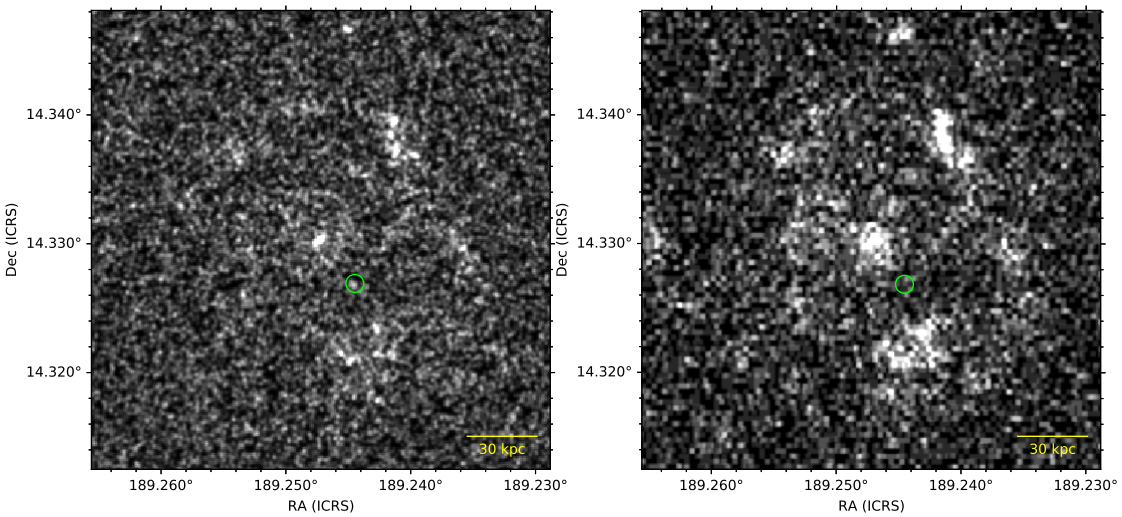

Figure 4.2.: An example of the performance of UVIT compared to GALEX for Malin 1 (UVIT archival FUV image in the left and GALEX FUV image in the right). The green circle indicates the compact region in the extended disk of Malin 1 (~26 kpc away from the galaxy center) with Hα detection in the spectroscopic data discussed in Chapter 3.

Malin 1 spectroscopic data). The spiral-arm system is also easier to identify in the UVIT image as some small and faint regions were lost in GALEX due to the PSF dilution (see Fig. 4.2). The UVIT archival data of Malin 1 (before it was published recently in Saha et al. 2021) have allowed us to see that an H II region found in the extended disk matches the position of UV emission (what was not possible at GALEX resolution).

I thus proposed to observe UGC 6614 and NGC 1042 using the FUV mode of UVIT. This will identify the recent star-forming regions of these galaxies (FUV is sensitive to star formation on a time scale of 100 Myr) and study the star formation properties in their low-density environment.

Although UGC 6614 and NGC 1042 were observed using GALEX, their resolution does not allow a proper comparison to the spectroscopic data I plan to acquire. Moreover, for NGC 1042, there is already existing MUSE data in the central region, with sub-arcsecond resolution. For a comparison to the spectroscopic data, UVIT could significantly improve this situation with its high resolution and bring more constraints on the SFR history of these galaxies.

Figures 4.3 show the GALEX UV and optical images of the galaxies I proposed for the UVIT observation. Although the UVIT resolution of 1.8″ is not enough to resolve individual molecular clouds, studies of star formation in galaxies can be done on scales of several 100 pc to obtain the statistical behaviour of star-forming regions (Boissier et al. 2007; Bigiel et al. 2008; Shi et al. 2018; Dey et al. 2019). Especially, the UVIT resolution will be sufficient to measure the Hα /UV ratio on matching scales. Deviations from standard Hα /UV ratio can indicate time-variations of the SFR history on short time-scales (Boselli et al. 2009). The relative numbers of blue UV regions observed from UVIT and those bright in Hα can be used to test the universality of the IMF, similar to what was done for the outer disk of the XUV galaxy M83 in Koda et al. (2012). New UVIT observations of UGC 6614 and NGC 1042 will be of great help in this study. The UV data with high spatial resolution will further motivate spectroscopic observations for these sources in the future.

In a November 2020 observation run of UVIT, I obtained an initial set of the proposed FUV data for UGC 6614 and NGC 1042, shown in Fig. 4.4. Although the current observed exposure is shallower than GALEX, we clearly see UV clumps at similar position as in the GALEX images, but with an improved

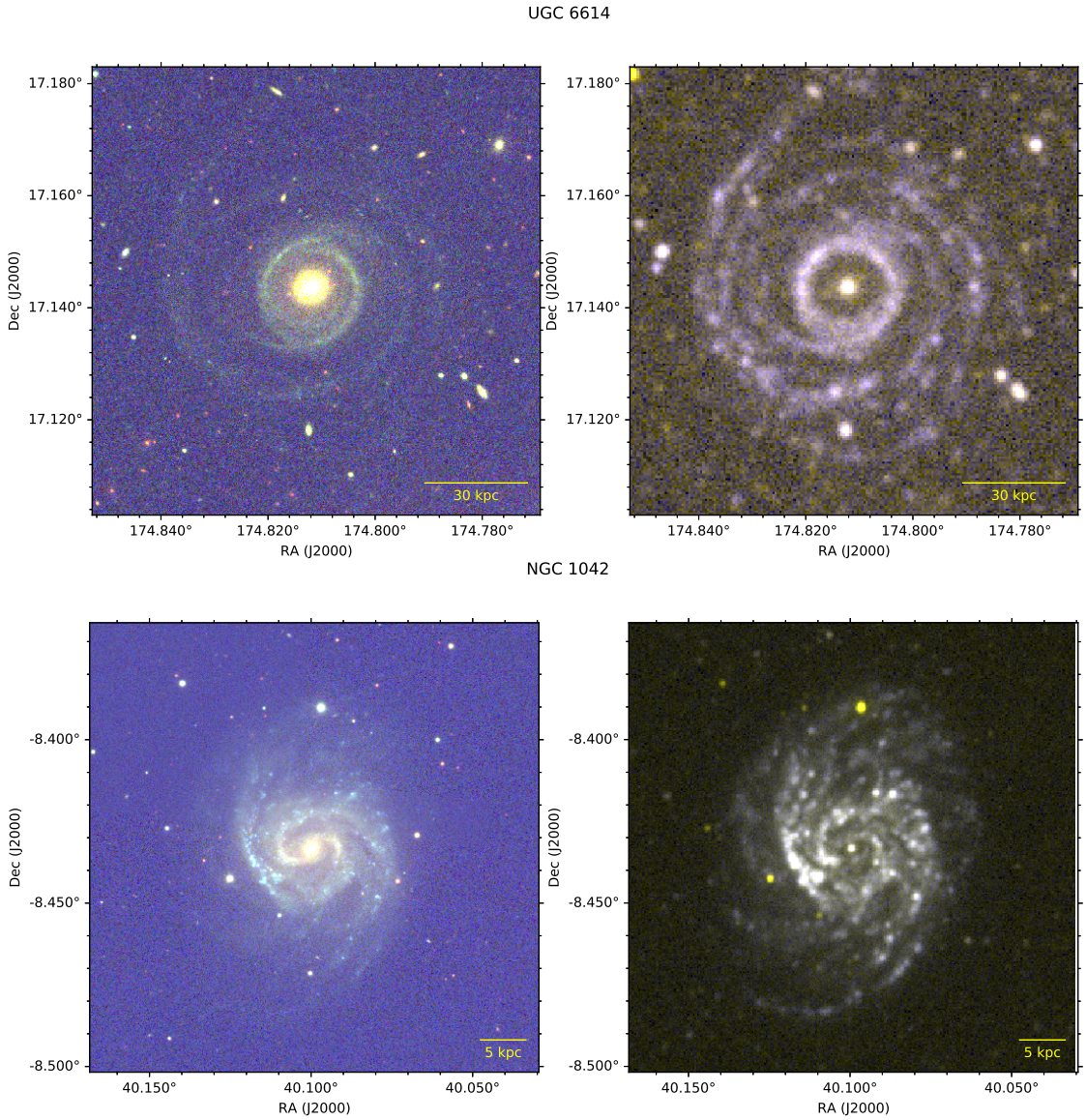

Figure 4.3.: GLSB galaxy UGC 6614 (top panel) and XUV galaxy NGC 1042 (bottom panel) in optical and UV. Left panels show the SDSS *u*, *g* and *i* band colour image and the right panel with the GALEX FUV and NUV colour image.

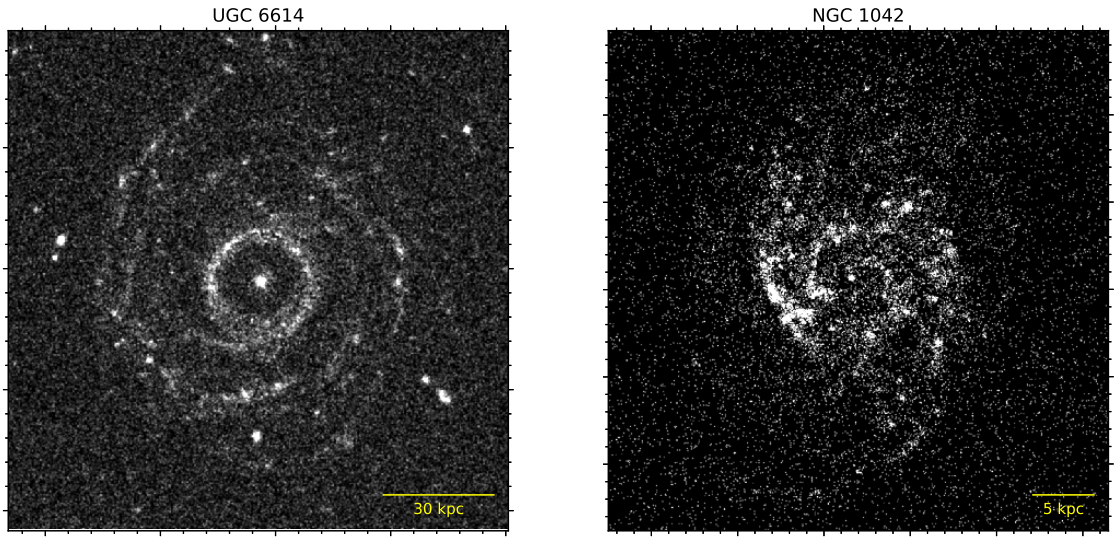

Figure 4.4.: Preliminary UVIT FUV images obtained for UGC 6614 and NGC 1042.

resolution. The observations are still going on, and the final data will be available by the end of the year.

4.2.1.3. Malin 1 MUSE proposal

The spectroscopic study of Malin 1 from Junais et al. (2020) illustrated the crucial need for a further follow up of Malin 1 using a powerful instrument like MUSE IFU. For this purpose, we submitted a proposal to observe Malin 1 with MUSE (PI-Gaspar Galaz; with myself as a Co-I). The proposal was accepted in a rank B category for observation in the cycle of 2020. However, due to various technical difficulties caused by the global Covid-19 pandemic, the proposal had to be re-submitted and accepted for the MUSE 2021 cycle.

Fig. 4.5 shows the four MUSE pointings covering a field of $2'$, we proposed for the Malin 1 observation. With its exquisite imaging quality, MUSE will resolve the Balmer lines and velocity field in the gigantic disk of Malin 1. Once observed, this will be the first time to study the 3D kinematics and star formation activity of this mysterious galaxy. An analysis of the velocity field, Balmer lines and metal lines obtained from this data will bring crucial constraints on various aspects of Malin 1, including its formation, dust, stellar population and dark matter content. This might even change our understanding of the whole family of GLSBs.

The 2021 observation cycle of MUSE is in progress, and Malin 1 was observed for the first time in April 2021. One out of the four proposed fields was observed in this run. A preliminary analysis of the data from this run illustrates that there is prominent Hα emission over large parts of the spiral arms in Malin 1, coinciding with the UV emission and extending out to very far distances from the galaxy centre. Another interesting observation from this data is an apparent double nucleated structure in the velocity field obtained from the Malin 1 centre. If not an artefact, this feature could be crucial in understanding the formation history of Malin 1. These double nucleated central velocity components could also explain the steep rise in the inner rotation curve of Malin 1 I observed in Junais et al. (2020). However, considering the preliminary nature of this data, it is hard to conclude now. Once the observations are complete, we expect to perform a detailed analysis of Malin 1 MUSE data.

4.2.1.4. Hα filter for Malin 1

In addition to the long-slit spectroscopy and MUSE IFU observations of Malin 1, I am also a Co-I in a grant obtained from my laboratory (LAM) to buy a narrow-band (NB) Hα filter at the redshift of Malin

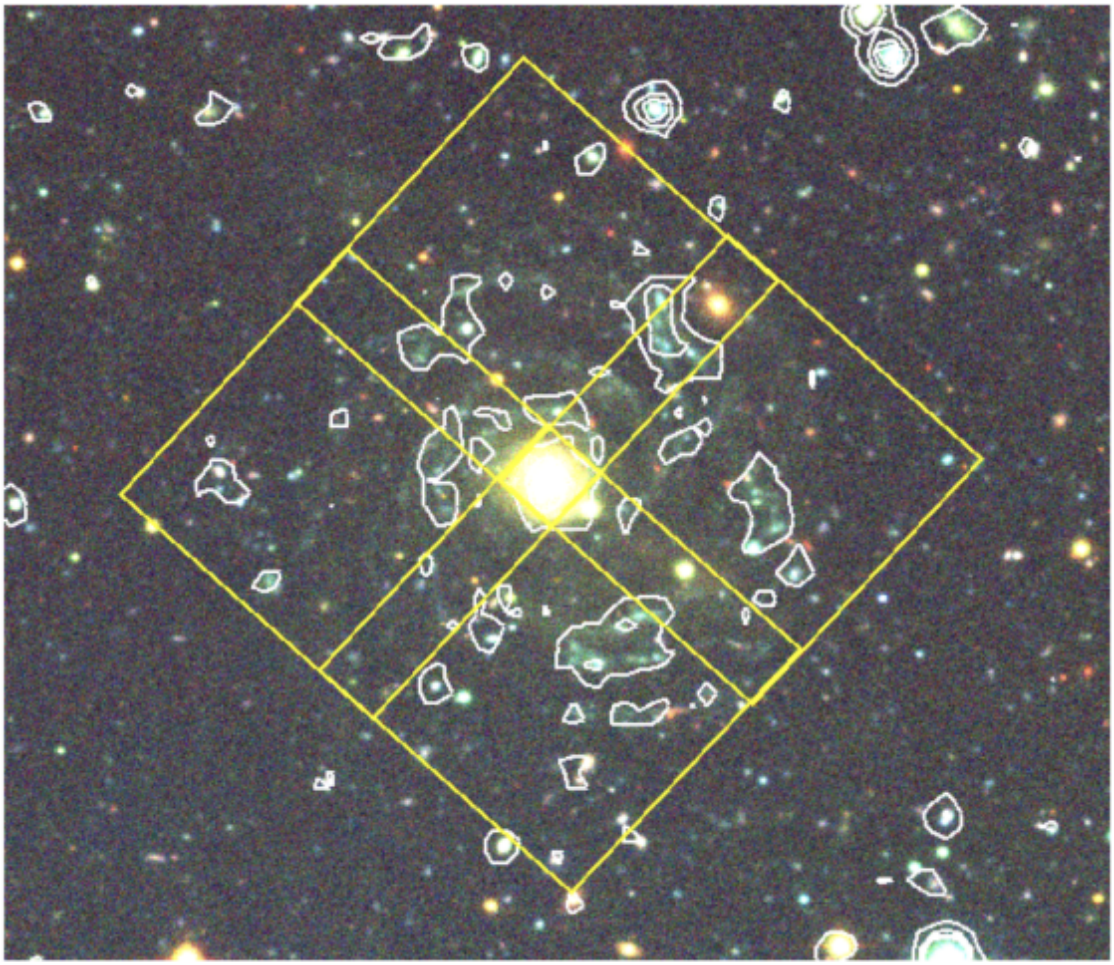

Figure 4.5.: Proposed MUSE fields for Malin 1 observation, overlaid on the NGVS image. The four yellow square boxes are the MUSE fields each with a $1' \times 1'$ coverage. The white contours are GALEX UV data from Boissier et al. (2016).

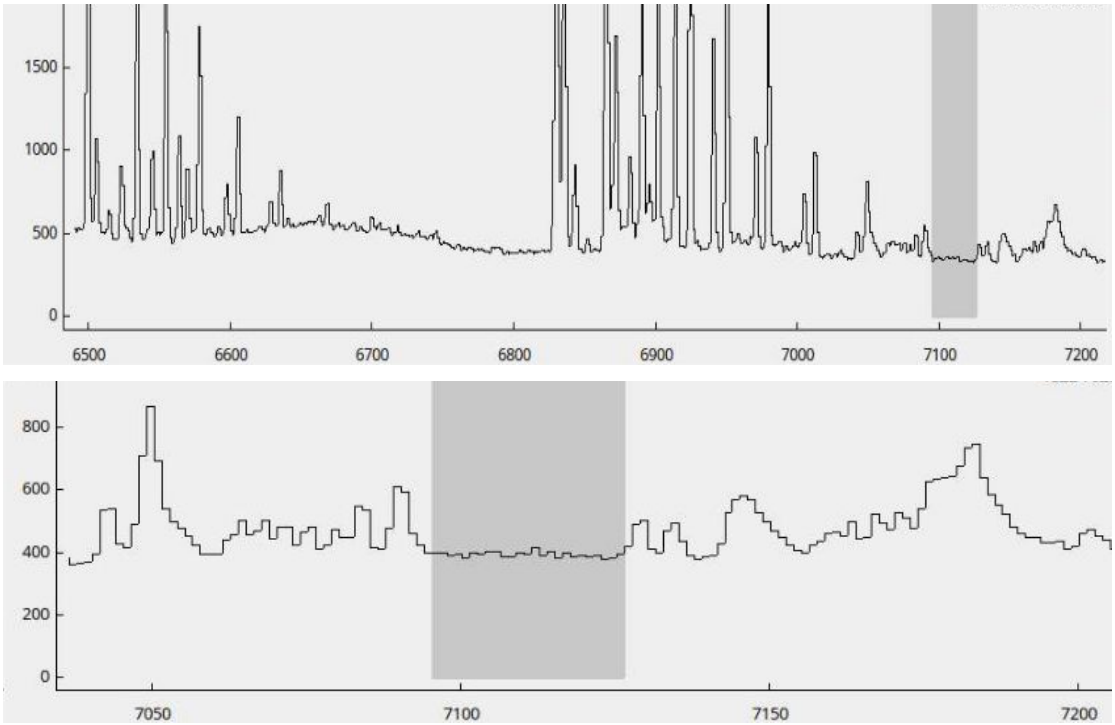

Figure 4.6.: Position of the narrow-band Hα filter for Malin 1 (in grey shaded area). The top and bottom panels show the sky background observed with MUSE. Note that very few skylines are found in the range 7090-7127 Å.

1, covering a wavelength range of 7090-7127 Å(see Fig. 4.6). Due to the high radial velocity of Malin 1, currently, no other NB filters are available at this range. We planned to use this filter to obtain deep NB Hα imaging and Fabry-Perot kinematics of Malin 1 (this project was started before acceptance of the Malin 1 MUSE proposal). Observations will be done by my collaborators Philippe Amram and Benoit Epinat, who have guaranteed observation time at various instruments (e.g. Observatoire de Haute-Provence, France; Southern Astrophysical Research Telescope, Chile). Once observed, such data could be used to map the Hα emission within the entire disc of the galaxy, in comparison with the work from Junais et al. (2020), and also to perform various analyses similar to those discussed in the previous sections (e.g. Hα /UV ratio, velocity map). The filter will also be useful to study the star formation rate and the kinematics of group galaxies at a redshift range $0.4 < z < 1$, using [O II] , [O III] and Hβ lines.

4.3. Perspectives

Giant low surface brightness galaxies are indeed fascinating objects. In the recent years, we have opened a window for the observation of these sources with great details. Using the expertise I acquired during my thesis research, I plan to continue working on the topic of GLSBs. A few of the possible projects are listed below.

– In the context of the Malin 1 MUSE observation, for which I am a co-I, I will propose to focus my contribution in the analysis of the Hα emission map. This will enable us to study the star formation rate in the disk of Malin 1, in comparison with Junais et al. (2020) and also with the UVIT data in hand. These data can also be used to answer other numerous science questions. For instance, the Hα /UV ratio can be used to test the universality of the IMF and stochasticity.

The Balmer ratio will be used to determine the amount of dust extinction since LSBs, in general, are considered to have a very low amount of dust (Hinz et al. 2007), but this has to be studied at high spatial resolution. The kinematics retrieved from the Hα line map will be investigated to characterise the dynamics of the gas around the galaxy (e.g. disturbed gas profile, presence of bars). This will give crucial clues to the formation of the system.

– I will analyse my sample of GLSBs with the data already in hand, and I will also pursue new observations. A similar study as performed in the case of Malin 1 (Junais et al. 2020), will be extended to this larger sample of GLSBs. This will enable me to study the nature and formation of GLSBs, which is still debated (e.g. rotating discs in large haloes, late gas accretion, results of past interactions).

– I plan to compare GLSBs to the recently discovered phenomenon of XUV disk galaxies (Thilker et al. 2007), with extended diffuse disks characterised in UV but not systematically in optical, found around otherwise “normal” galaxies. This would establish a link between the big disks in GLSBs, and the disks outside "normal" galaxies that have XUV disk. For this work, I will make use of the sample of XUV galaxies observed with Hyper Suprime-Cam (with collaborator Jin Koda at Stony Brook University, New York), or future observations of the CASTLE project (Lombardo et al. 2020) in which I am involved.

– I also proposed possible observations with the upcoming BlueMUSE instrument at VLT (Richard et al. 2019). BlueMUSE, with its larger FoV and higher spectral resolution compared to MUSE, will revolutionise the study of the low surface brightness universe.

– As a long-term plan for studying GLSB galaxies in detail, I will propose a larger project to identify and catalogue new GLSB sources hiding from our plain sight. This will include data mining of various existing and future deep, blind surveys (e.g. NGVS, GUViCs, LSST, SKA). I will also use the full capabilities of instruments like MUSE and ALMA by proposing more observation time for the identified GLSB candidates. Using all the spectro-photometric data in hand (and the more data I acquire in the future), it will be possible to uncover the truths behind the family of GLSBs.

Part III.

Ultra Diffuse Galaxies

5. A new sample of LSBs in the Virgo cluster

Summary

5.1 Context . . . 81
5.2 Data . . . 83
5.2.1 NGVS . . . 83
5.2.1.1 The NGVS catalogue . . . 83
5.2.2 GUViCS . . . 84
5.2.3 VESTIGE . . . 84
5.3 Sample selection . . . 84
5.4 Measurements . . . 94
5.4.1 Creation of stamps . . . 94
5.4.2 Preparation of masks and further processing of the stamps . . . 95
5.4.3 Background sky measurements . . . 96
5.4.4 Extraction of surface brightness profiles . . . 96
5.4.5 Surface brightness profile decomposition . . . 98
5.4.6 New determination of effective radii . . . 102
5.4.7 Integrated magnitudes . . . 102
5.5 Preliminary analysis . . . 111
5.5.1 Colour distribution . . . 111
5.5.2 Gradient in colour . . . 111
5.5.3 Colour-Magnitude Diagram . . . 111
5.6 A sub-sample: cross-correlation with H I from ALFALFA . . . 115
5.7 Conclusions . . . 115

5.1. Context

The Virgo cluster is one of the richest clusters of galaxies in the nearby Universe. With thousands of member galaxies of all morphological types lying at nearly a typical distance of 16.5 Mpc (Mei et al. 2007; Blakeslee et al. 2009), the Virgo cluster is a prime candidate for deep, blind surveys at all wavelengths (see Fig. 5.1). The richness of its cluster environment and the multitude of available data play a key role in the study of galaxy formation and evolution in dense environments. Owing to the depth of recent surveys like the NGVS (Next Generation Virgo cluster Survey; Ferrarese et al. 2012, VESTIGE (Virgo Environmental Survey Tracing Ionised Gas Emission; Boselli et al. 2018a), and GUViCS (GALEX Ultraviolet Virgo Cluster Survey; Boselli et al. 2011), we can now study very low surface brightness objects in great detail at unprecedented depths. Therefore, the Virgo cluster can be considered a perfect laboratory for studying LSB galaxies, which are also found in large numbers in cluster environments.

In this work, I study a sample of LSBs in the Virgo cluster, using a multi-wavelength set of photometric data from the NGVS, GUViCS and VESTIGE surveys in optical, UV and Hα narrow-band, respectively. This work aims to study the role of cluster environment in shaping the evolution of LSBs. The data analyses performed and obtained results are discussed in further sections.

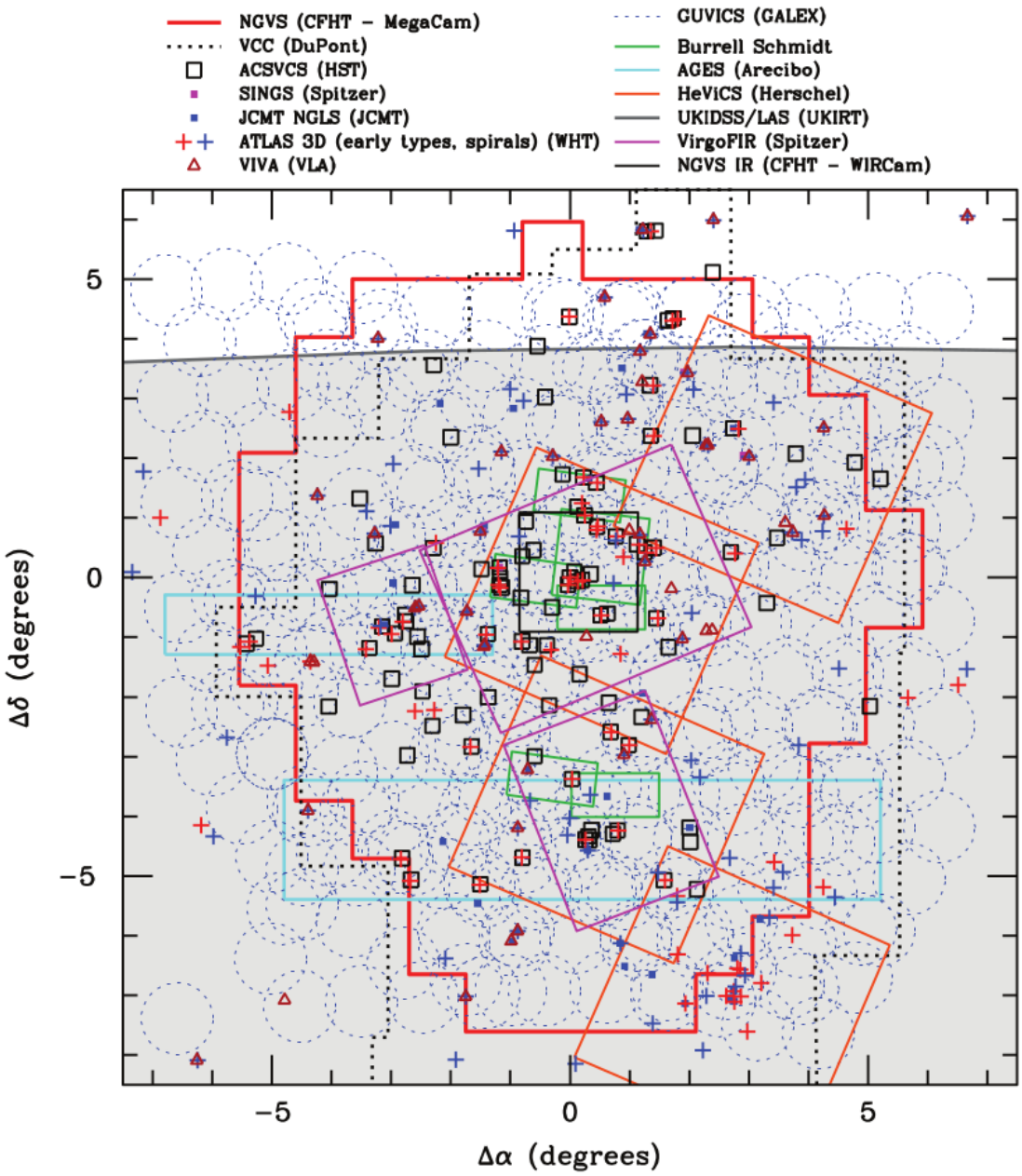

Figure 5.1.: Multi-wavelength surveys of the Virgo cluster. The different surveys are indicated in the legend at the top of the figure. This work utilises the data from the NGVS, VESTIGE (same coverage area as NGVS) and GUViCS surveys, discussed in detail in the Sect. 5.2. The image is centered around the brightest cluster elliptical galaxy M87 (α, δ [$J2000$] = 187.706°, +12.391°). Image credits: Ferrarese et al. (2012).

Survey	Filter	Central wavelength (Å)	FWHM
GUViCS	FUV	1524	~5″
GUViCS	NUV	2309	~5″
NGVS	u	3811	0.88″
NGVS	g	4862	0.80″
VESTIGE	r	6258	0.65″
VESTIGE	Hα	6591	0.64″
NGVS	i	7552	0.54″
NGVS	z	8871	0.75″

Table 5.1.: Filters and resolution of the data from NGVS (Ferrarese et al. 2012), GUViCS (Boselli et al. 2011) and VESTIGE (Boselli et al. 2018a) used in this work.

5.2. Data

5.2.1. NGVS

The NGVS (Ferrarese et al. 2012) is a deep broad-band imaging survey of the Virgo cluster in the u, g, r, i, z-bands[1], carried out with the MegaCam instrument on the 3.6m Canada-France-Hawaii Telescope (CFHT). The survey spans an area of 104 deg^2 (see Fig. 5.1), using 117 distinct MegaCam pointings each of 1° field of view. NGVS covers the whole Virgo cluster region from its core to one virial radius of the Virgo A and Virgo B subclusters ($R_{vir,A}$ = 1.55 Mpc; $R_{vir,B}$ = 0.96 Mpc), which are centred on M87 and M49, respectively. The NGVS images were processed with the Elixir-LSB pipeline optimised for the recovery of low surface brightness features, reaching a surface brightness limit of $\mu_g \sim 29$ mag arcsec^{-2} (2σ above the mean sky level; Ferrarese et al. 2012). The survey has a typical full-width-half-maximum (FWHM) resolution of 0.54″ in i-band and ~0.8″ in the other bands (see Table. 5.1). Full details on the survey, including observations and data processing, are discussed in Ferrarese et al. (2012).

5.2.1.1. The NGVS catalogue

Using the deep data covering the entire Virgo cluster, the NGVS team identified and catalogued the cluster members to produce the most up to date catalogue of the Virgo cluster (Ferrarese et al. 2020). The initial source identifications for the catalogue were performed using multiple SExtractor (Bertin & Arnouts 1996) runs followed by a THELI `automask` procedure (Erben et al. 2005, 2009) on the NGVS g-band images. Prior to object detection, this procedure had masks avoiding any contaminating foreground stars, globular clusters, and stellar haloes in the field to ease the source identification process. Later, the structural parameters and photometry of each source were measured using Galfit (Peng et al. 2002). The final catalogue was prepared after a visual inspection of the initially identified sources to remove clear false detections.

For each source, NGVS also estimated the cluster membership probabilities designated into three categories as a `certain`, `likely` or `possible` member. NGVS used a rigorous algorithm involving multiple 'distance indicators' to compute the probability that a given galaxy is a member of the cluster. This process utilises several scaling relationships (magnitudes, colors and Galfit structural parameters), photometric redshift estimates and visual inspections to confidently identify potential Virgo cluster

[1]NGVS r-band has coverage only over a small area of ~4 deg^2 in the core region of Virgo, centred around M87. Therefore in this work, I use the r-band from the VESTIGE survey covering the whole cluster.

members. The final NGVS catalogue after all these processes consist of a total of 3689 galaxies, out of which 1483 are already in the standard Virgo Cluster Catalogue (VCC; Binggeli et al. 1985). A detailed description of the catalogue is discussed in Ferrarese et al. (2020).

The NGVS catalogue is used as a basis for my LSB galaxy sample selection and analysis discussed in the Sections 5.3 and 5.4. In my selection, I only used the sources with `certain` and `likely` cluster membership flag from NGVS, to avoid any contamination. For reference, the mean membership probabilities for the class of `certain` and `likely` members are $84 \pm 23\%$ and $77 \pm 21\%$, respectively (Lim et al. 2020). Therefore, in confidence with the cluster memberships assigned by NGVS, throughout this work we assume that all the galaxies in the NGVS catalogue are at the distance of the Virgo cluster (16.5 Mpc). This is particularly important in the case of LSBs where distance estimation using spectroscopy are extremely challenging.

5.2.2. GUViCS

GUViCS (Boselli et al. 2011) is a blind survey of the Virgo cluster using the GALEX far-UV (FUV) and near-UV (NUV) observations. GUViCS combine data from the GALEX All-Sky Imaging Survey (AIS), typically with an exposure of 100s, Medium Imaging Survey (MIS) with deeper exposure times of at least 1500s (Morrissey et al. 2005) and dedicated observations of the Virgo cluster (Boselli et al. 2011). With the GALEX field of view of $\sim$1.2° and a resolution of $\sim$5″, GUViCS covers almost the entire Virgo cluster region with multiple overlapping exposures (see Fig. 5.1 for the GUViCS coverage). However, there are a few gaps in the survey coverage, as shown in Fig. 5.1, due to bright stars in the field hindering observations.

5.2.3. VESTIGE

VESTIGE is a blind Hα narrow-band (NB), and broad-band r imaging survey of the Virgo cluster carried out with MegaCam at the CFHT (Boselli et al. 2018a). It is designed to cover an area of 104 deg^2 in the Virgo cluster (the same area as that of NGVS; see Fig. 5.1).

The Hα NB filter of VESTIGE covers a wavelength range of $6538 < \lambda < 6644$ Å with a central wavelength 6591 Å and filter width of 106 Å. It includes the Hα line and the two nearby [N II] emission lines at λ6548 and 6583 Å. Hereafter I refer to the Hα+[N II] contribution simply as Hα, unless otherwise stated.

Currently, the survey covers $\sim$40% of the designed area at full depth (exposure of 7200s in Hα) with observations of high imaging quality (resolution of $\sim$0.6″; see Table. 5.1). The depth and extremely high image quality of the survey make it perfectly suitable for studying the effects of the environment on the star formation process in galaxies down to scales of $\sim$100 pc, since Hα is a perfect tracer of star formation on short timescales. Moreover, the Hα filter is optimal to detect the line emission of galaxies at the redshift of the Virgo cluster with a typical recessional velocity of $-500 \leq cz \leq 3000$ km s^{-1}. In the case of detection, VESTIGE also confirms the Virgo membership provided by the NGVS.

The line sensitivity limit of the survey is $f(\mathrm{H}\alpha) \sim 4 \times 10^{-17}$ erg s^{-1} cm^{-2} (5σ detection limit) for point sources and $\Sigma(H\alpha) \sim 2 \times 10^{-18}$ erg s^{-1} cm^{-2} arcsec^{-2} (1σ detection limit at 3″ resolution) for extended sources. The contribution of the stellar continuum emission in the NB Hα filter is determined and removed using a combination of the VESTIGE r-band and NGVS g-band images, as described in Boselli et al. (2019).

5.3. Sample selection

Since the goal of this work to study a population of LSB galaxies in the Virgo cluster, I identified and created a sample of LSBs using the NGVS catalogue. For this purpose, I combined definitions of LSBs from the literature discussed in Sect. 2.3. This is done to produce the largest possible sample of LSBs by

avoiding the selection biases associated with the choice of a particular LSB definition. This will also allow me to study the potential effect of selection bias when applying one specific selection or another.

The sample selection was performed using the Galfit g-band central surface brightness and effective radius for each source given in the NGVS catalogue. The choice of g-band for sample selection stems from the fact that it is the deepest among the NGVS bands, and is one among the most commonly used filters for UDG selection (van Dokkum et al. 2015; Lim et al. 2020). Moreover, g-band also has a larger survey coverage than, for instance, the r-band (although r-band follows more closely the mass distribution than g-band).

Fig. 5.2 and Fig. 5.3 show the distribution of the selected sample in the $\mu_0 - r_s$ plane and sky plane, respectively. The sample consists of a total 150 LSBs, including "diffuse" galaxies following Sprayberry et al. (1995), UDGs based on the van Dokkum et al. (2015) definition and outlier galaxies from Lim et al. (2020). Among the 150 selected sources, 125 galaxies satisfy the UDG definition, 51 follow the diffuseness criteria and 52 belongs to the Outlier definition, where many of them also overlaps with different definitions. From hereupon, I will be addressing these three sub-groups as Diffuse, UDG and Outlier sources, unless stated otherwise.

From Fig. 5.2 we can note that many of the selected sources are indeed overlapping among the diffuse, UDG and outlier categories. However, the selection creates clear differences. For instance, many outliers have relatively high surface brightness. But I chose to keep all of them in my sample for the sake of completeness in selection. At a later stage, this initial sample of 150 sources will be visually inspected to remove any suspicious detection, which will be discussed in Sect. 5.4.

Table 5.2 gives the selected sample with their physical parameters provided by the NGVS catalogue (from Galfit measurements). For few sources (9 out of 150; ID - 1318, 1389, 1435, 1459, 1529, 2409, 2568, 2635, 3578), there were no Galfit measurements in the NGVS catalogue (Galfit failed to converge in these sources due to residual artefacts or bright foreground stars in the field). Therefore, to be consistent with the rest of the sample, I performed a Galfit structural decomposition on these sources after masking any artefacts in the field (see Sect. 5.4.2 for the details on the masks used), which helped Galfit to converge. The initial guess values I used for the Galfit were taken from the isophotal fit parameters in the NGVS catalogue (NGVS provides structural parameters of a source obtained from different methods like Galfit and isophotal analysis; Ferrarese et al. 2020). In this way, I obtained Galfit structural parameters of the entire sample as given in Table 5.2.

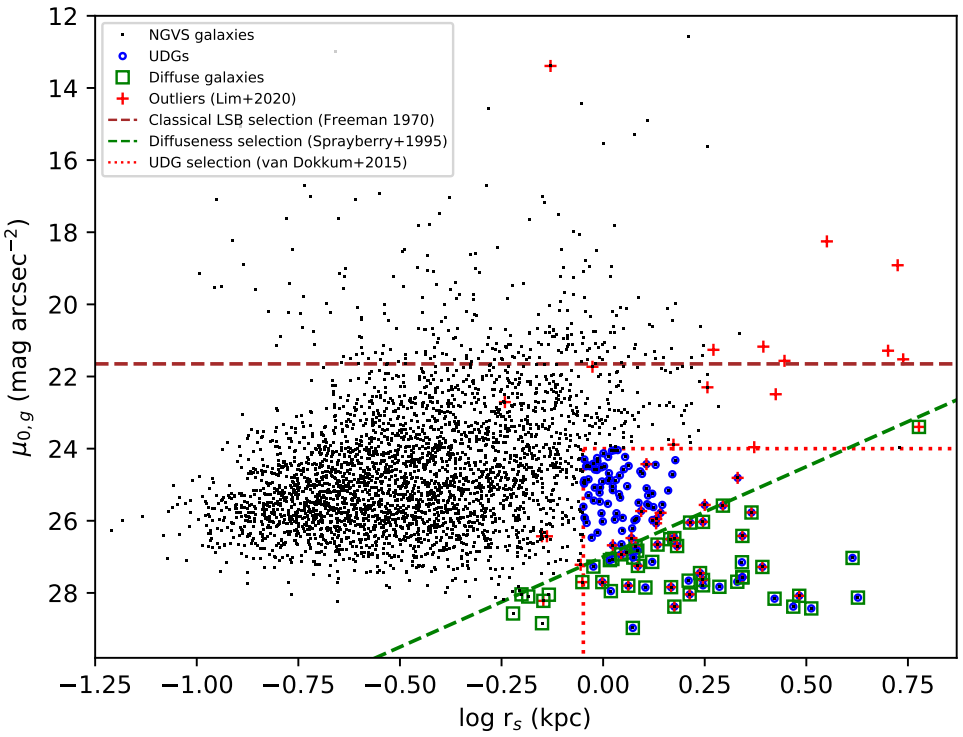

Figure 5.2.: Selected sample of 150 LSBs from the NGVS catalogue. The black dots are all the galaxies in the NGVS catalogue. The blue circles, red crosses and green squares are the UDGs, diffuse galaxies and the outliers, respectively based on various selection criteria (discussed in Sect. 2.3 and Fig. 2.3). The brown horizontal dashed line is the classical Freeman (1970) value. The green dashed line shows the Sprayberry et al. (1995) diffuseness selection. The red dotted box is the UDG selection criteria from van Dokkum et al. (2015). The disc scale length values are obtained by converting the R_e values given in Table 5.2, where $r_s = R_e/1.678$ assuming an exponential disc (Peng et al. 2002).

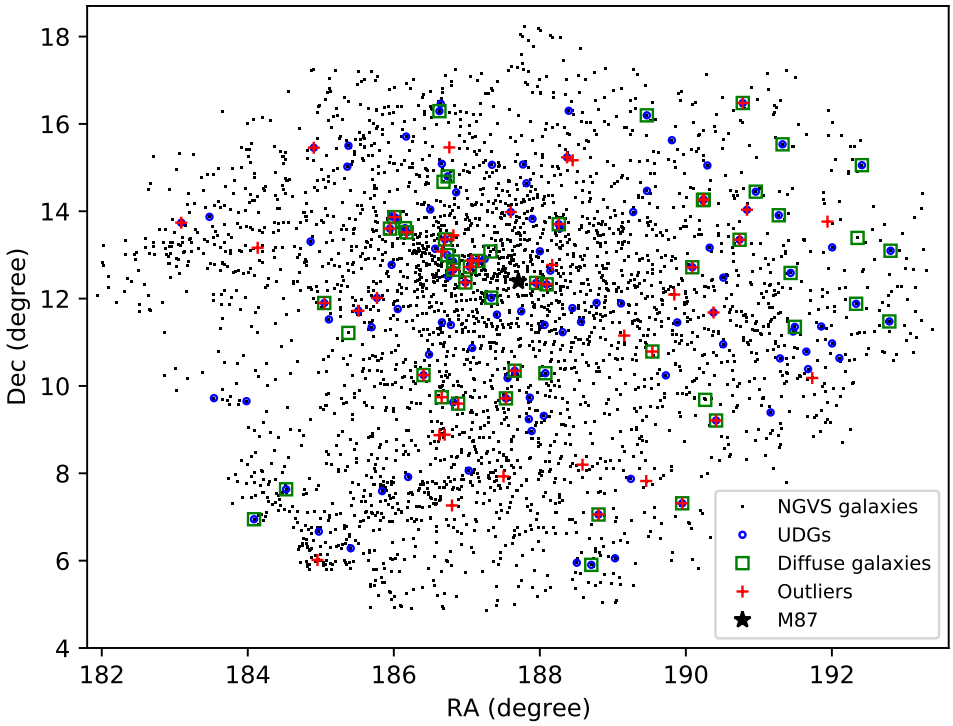

Figure 5.3.: On sky distribution of the selected sample of LSBs. The symbols are same Fig. 5.2. The black star symbol in the centre marks the position of M87.

Table 5.2.: Properties of the selected sample from the NGVS catalogue. (1) Source ID based on the position in the NGVS catalogue. (2) Name of the source in NGVS. (3-4) Coordinates of the source in J2000. (5) g-band magnitude (6) Effective radius of the source. (7) Axis ratio. (8) Position angle. (9) g-band central surface brightness. (10) Foreground galactic extinction from Schlegel et al. (1998). (11) Selection flag based on the LSB definition where the flags 1,2, and 3 corresponds to UDG, Diffuse and Outlier sources, respectively. All the parameters given in this table are taken from the NGVS catalogue, except for the 9 sources where I performed Galfit myself.

ID	NGVS name	RA (deg)	DEC (deg)	g (mag)	$R_{e,g}$ (kpc)	q	P.A (deg)	$\mu_{0,g}$ (mag arcsec^{-2})	E (B-V) (mag)	Flag
(1)	(2)	(3)	(4)	(5)	(6)	(7)	(8)	(9)	(10)	(11)
67	NGVSJ12:12:21.23+13:44:16.6	183.088	13.738	17.76	2.29	0.77	-37.44	26.07	0.033	1,3
103	NGVSJ12:13:54.12+13:52:21.3	183.475	13.873	16.33	2.55	0.62	-45.63	24.32	0.03	1
110	NGVSJ12:14:08.88+09:43:15.7	183.537	9.721	17.62	1.94	0.52	38.98	25.04	0.016	1
186	NGVSJ12:15:55.76+09:39:04.1	183.982	9.651	16.97	2.51	0.6	-79.74	24.71	0.018	1
213	NGVSJ12:16:20.63+06:56:52.9	184.086	6.948	18.46	2.98	1.0	-34.98	27.79	0.021	1,2
227	NGVSJ12:16:32.59+13:09:51.3	184.136	13.164	16.78	3.99	0.3	65.29	23.96	0.03	3
321	NGVSJ12:18:05.98+07:38:02.6	184.525	7.634	18.93	1.79	0.78	71.5	27.06	0.019	1,2
405	NGVSJ12:19:26.37+13:18:27.4	184.86	13.308	16.77	1.7	0.66	-16.6	24.49	0.041	1
421	NGVSJ12:19:36.96+15:27:16.8	184.904	15.455	16.61	3.01	0.81	81.84	25.56	0.023	1,3
435	NGVSJ12:19:49.20+06:00:53.8	184.955	6.015	13.0	1.26	0.82	-61.23	13.39	0.021	3
444	NGVSJ12:19:53.47+06:39:56.9	184.973	6.666	16.74	1.68	0.9	57.35	24.91	0.021	1
466	NGVSJ12:20:11.38+11:53:56.5	185.047	11.899	19.78	1.94	0.51	87.17	26.88	0.028	1,2,3
495	NGVSJ12:20:26.70+11:31:24.7	185.111	11.524	17.86	1.64	0.69	86.73	24.35	0.033	1
583	NGVSJ12:21:27.21+15:01:16.0	185.363	15.021	17.12	1.75	0.53	53.04	24.68	0.033	1
588	NGVSJ12:21:30.60+11:12:51.1	185.378	11.214	21.96	1.02	0.53	85.85	28.57	0.034	2
590	NGVSJ12:21:30.88+15:30:04.9	185.379	15.501	17.56	2.2	0.7	-39.03	25.58	0.023	1
604	NGVSJ12:21:38.40+06:16:59.7	185.41	6.283	18.71	1.69	0.76	-13.77	26.02	0.02	1
646	NGVSJ12:22:03.58+11:43:17.5	185.515	11.722	18.34	1.79	1.0	88.31	26.68	0.029	1,3
743	NGVSJ12:22:47.06+11:20:40.6	185.696	11.345	17.28	1.87	0.7	-56.38	25.36	0.026	1
796	NGVSJ12:23:04.59+12:00:53.4	185.77	12.016	17.25	2.1	1.0	40.36	25.73	0.028	1,3
833	NGVSJ12:23:21.46+07:35:30.4	185.839	7.592	17.1	1.91	0.59	81.73	24.57	0.023	1
892	NGVSJ12:23:47.33+13:36:08.3	185.947	13.602	18.61	2.04	0.72	-4.76	26.7	0.047	1,2,3
904	NGVSJ12:23:52.61+13:52:57.6	185.969	13.883	16.78	1.7	0.95	-47.25	24.13	0.038	1

Table 5.2 Continued..

ID	NGVS name	RA	DEC	g	$R_{e,g}$	q	P.A	$\mu_{0,g}$	E (B-V)	Flag
		(deg)	(deg)	(mag)	(kpc)		(deg)	(mag arcsec^{-2})	(mag)	
(1)	(2)	(3)	(4)	(5)	(6)	(7)	(8)	(9)	(10)	(11)
906	NGVSJ12:23:52.90+12:46:23.1	185.97	12.773	17.58	1.64	0.94	-46.92	24.59	0.04	1
935	NGVSJ12:24:01.84+13:51:56.4	186.008	13.866	18.39	2.98	0.77	-35.93	27.64	0.038	1,2,3
952	NGVSJ12:24:08.52+13:49:59.6	186.035	13.833	18.82	1.89	0.49	-82.58	26.28	0.037	1
964	NGVSJ12:24:13.00+11:45:41.5	186.054	11.762	17.55	1.79	0.95	14.74	25.15	0.038	1
1008	NGVSJ12:24:36.61+13:36:45.2	186.153	13.613	19.65	1.6	0.62	69.75	27.27	0.04	1,2
1013	NGVSJ12:24:40.41+15:42:36.0	186.168	15.71	17.49	1.74	0.77	-8.41	24.23	0.024	1
1017	NGVSJ12:24:42.06+13:31:00.6	186.175	13.517	17.6	2.98	0.76	-1.61	26.03	0.042	1,2,3
1027	NGVSJ12:24:47.07+07:54:57.6	186.196	7.916	18.31	1.56	0.62	-27.28	25.29	0.024	1
1160	NGVSJ12:25:37.61+10:14:58.6	186.407	10.25	16.96	2.77	0.95	21.24	26.05	0.028	1,2,3
1214	NGVSJ12:25:55.79+10:43:13.2	186.482	10.72	18.55	1.52	0.71	-10.55	25.91	0.032	1
1227	NGVSJ12:25:59.76+14:02:22.6	186.499	14.04	17.36	1.76	0.72	-16.26	24.84	0.048	1
1271	NGVSJ12:26:16.00+13:08:32.0	186.567	13.142	18.39	2.0	0.51	37.83	26.21	0.029	1
1318	NGVSJ12:26:29.90+08:52:19.9	186.625	8.872	13.1	3.17	0.95	29.35	21.26	0.025	3
1314	NGVSJ12:26:30.00+16:17:31.0	186.625	16.292	20.51	2.15	0.25	0.18	27.85	0.024	1,2
1335	NGVSJ12:26:34.33+16:27:51.0	186.643	16.464	19.04	1.59	0.71	81.24	26.47	0.023	1
1346	NGVSJ12:26:37.41+09:44:32.0	186.656	9.742	20.7	1.21	0.9	-28.4	28.22	0.024	2,3
1349	NGVSJ12:26:37.97+15:05:07.6	186.658	15.085	17.7	1.62	0.82	-32.15	25.08	0.033	1
1352	NGVSJ12:26:38.25+13:04:44.2	186.659	13.079	19.45	0.97	0.81	-70.36	22.71	0.029	3
1354	NGVSJ12:26:38.26+11:27:22.5	186.659	11.456	18.59	2.24	0.43	-36.15	25.98	0.035	1
1372	NGVSJ12:26:43.48+14:40:23.9	186.681	14.673	21.62	1.11	0.56	66.21	28.1	0.035	2
1389	NGVSJ12:26:47.23+08:53:04.6	186.697	8.885	12.45	4.2	0.97	54.3	21.17	0.029	3
1397	NGVSJ12:26:48.36+13:21:17.7	186.702	13.355	19.1	2.06	0.78	-77.18	27.25	0.026	1,2,3
1416	NGVSJ12:26:55.95+12:59:40.0	186.733	12.994	18.14	3.62	0.9	71.26	27.69	0.027	1,2
1424	NGVSJ12:26:57.00+14:47:52.5	186.738	14.798	19.1	2.06	0.49	51.69	26.83	0.034	1,2
1429	NGVSJ12:26:59.05+12:30:20.5	186.746	12.506	16.62	1.84	0.77	55.89	24.04	0.028	1
1435	NGVSJ12:27:02.54+15:27:41.3	186.761	15.461	11.77	6.02	0.75	16.23	18.25	0.024	3
1436	NGVSJ12:27:02.60+12:34:47.1	186.761	12.58	18.43	2.05	0.61	56.07	25.95	0.03	1
1450	NGVSJ12:27:07.58+11:23:49.2	186.782	11.397	18.65	1.68	0.64	24.81	25.79	0.035	1
1459	NGVSJ12:27:11.29+07:15:46.9	186.797	7.263	12.16	9.28	0.86	-6.98	21.52	0.03	3
1473	NGVSJ12:27:15.01+12:50:55.9	186.813	12.849	18.02	7.18	0.26	86.84	28.13	0.029	1,2

Table 5.2 Continued..

ID	NGVS name	RA	DEC	g	$R_{e,g}$	q	P.A	$\mu_{0,g}$	E (B-V)	Flag
		(deg)	(deg)	(mag)	(kpc)		(deg)	(mag arcsec^{-2})	(mag)	
(1)	(2)	(3)	(4)	(5)	(6)	(7)	(8)	(9)	(10)	(11)
1474	NGVSJ12:27:15.30+09:37:35.7	186.814	9.627	17.63	1.66	0.99	-77.24	25.22	0.024	1
1476	NGVSJ12:27:15.46+12:39:41.4	186.814	12.662	17.77	2.48	0.68	0.05	26.51	0.03	1,2,3
1479	NGVSJ12:27:15.75+13:26:56.1	186.816	13.449	19.42	1.23	0.83	11.46	26.43	0.025	3
1506	NGVSJ12:27:25.07+14:26:01.0	186.854	14.434	17.31	1.62	0.89	85.79	24.58	0.043	1
1529	NGVSJ12:27:31.55+09:35:44.3	186.881	9.596	13.88	10.15	0.78	-20.5	23.4	0.022	2,3
1593	NGVSJ12:27:55.22+12:22:09.5	186.98	12.369	16.16	3.93	0.78	41.59	25.77	0.027	1,2,3
1620	NGVSJ12:28:06.26+08:03:43.7	187.026	8.062	18.38	1.66	0.7	66.56	25.47	0.022	1
1633	NGVSJ12:28:10.07+12:43:29.4	187.042	12.725	18.36	2.93	0.73	88.93	27.45	0.024	1,2,3
1653	NGVSJ12:28:15.85+12:52:12.0	187.066	12.87	19.07	2.35	0.57	-74.87	25.78	0.022	1,3
1656	NGVSJ12:28:17.60+10:52:07.1	187.073	10.869	17.46	2.09	0.56	-85.15	24.63	0.029	1
1719	NGVSJ12:28:37.88+12:51:42.0	187.158	12.862	19.17	2.49	0.59	-63.21	27.84	0.02	1,2,3
1782	NGVSJ12:28:58.84+12:54:28.8	187.245	12.908	17.28	1.85	0.83	-7.98	25.26	0.02	1
1832	NGVSJ12:29:17.55+13:04:42.6	187.323	13.079	21.07	1.07	0.64	10.66	28.04	0.023	2
1837	NGVSJ12:29:20.27+12:01:16.4	187.334	12.021	18.25	3.28	0.71	59.26	27.83	0.026	1,2
1846	NGVSJ12:29:22.72+15:03:49.4	187.345	15.064	17.99	2.07	0.71	-30.32	25.5	0.034	1
1896	NGVSJ12:29:39.06+11:38:00.3	187.413	11.633	16.7	2.11	0.79	42.18	24.7	0.036	1
1968	NGVSJ12:30:00.61+07:55:45.8	187.503	7.929	14.46	3.06	0.67	-1.25	22.3	0.022	3
1993	NGVSJ12:30:08.68+09:42:56.2	187.536	9.716	17.09	3.73	0.58	88.39	26.42	0.021	1,2,3
2006	NGVSJ12:30:14.01+10:10:49.7	187.558	10.18	16.71	1.64	0.96	-40.8	24.26	0.026	1
2046	NGVSJ12:30:24.43+13:58:54.5	187.602	13.982	15.93	3.63	0.98	19.74	24.81	0.036	1,3
2079	NGVSJ12:30:37.30+10:20:53.0	187.655	10.348	17.45	4.18	0.79	-60.49	27.28	0.034	1,2,3
2143	NGVSJ12:30:58.81+11:42:30.8	187.745	11.709	17.17	1.86	0.61	41.9	24.74	0.031	1
2156	NGVSJ12:31:04.78+15:04:13.2	187.77	15.07	17.18	1.74	0.89	-18.0	24.89	0.029	1
2178	NGVSJ12:31:16.10+14:38:28.7	187.817	14.641	18.68	1.54	0.52	25.96	26.06	0.034	1
2200	NGVSJ12:31:23.84+09:14:25.5	187.849	9.24	18.77	1.64	0.68	28.72	26.33	0.019	1
2205	NGVSJ12:31:27.11+09:44:00.5	187.863	9.733	17.19	2.28	0.36	72.24	24.45	0.019	1
2227	NGVSJ12:31:33.09+08:58:02.9	187.888	8.967	17.9	1.74	0.69	-4.05	25.53	0.017	1
2237	NGVSJ12:31:35.84+13:49:28.2	187.899	13.824	17.22	2.19	0.76	53.29	25.3	0.034	1
2269	NGVSJ12:31:48.01+12:21:33.1	187.95	12.359	19.87	2.77	0.31	71.84	28.04	0.024	1,2,3
2301	NGVSJ12:32:00.19+13:04:55.4	188.001	13.082	16.91	1.6	0.65	0.68	24.42	0.028	1

Table 5.2 Continued..

ID	NGVS name	RA	DEC	g	$R_{e,g}$	q	P.A	$\mu_{0,g}$	E (B-V)	Flag
		(deg)	(deg)	(mag)	(kpc)		(deg)	(mag arcsec^{-2})	(mag)	
(1)	(2)	(3)	(4)	(5)	(6)	(7)	(8)	(9)	(10)	(11)
2343	NGVSJ12:32:12.92+09:18:56.7	188.054	9.315	17.33	2.18	0.9	-14.17	25.54	0.021	1
2351	NGVSJ12:32:15.43+11:23:52.6	188.064	11.398	19.21	1.61	0.64	13.93	25.44	0.057	1
2355	NGVSJ12:32:18.20+10:17:29.0	188.076	10.291	15.89	6.97	0.85	-55.0	27.03	0.032	1,2
2365	NGVSJ12:32:22.52+12:19:32.1	188.094	12.326	18.16	5.15	0.5	89.1	28.08	0.028	1,2,3
2394	NGVSJ12:32:34.71+12:38:21.1	188.145	12.639	17.17	2.37	0.86	26.66	25.56	0.026	1
2409	NGVSJ12:32:40.80+12:46:16.1	188.17	12.771	13.55	4.51	0.8	85.4	22.49	0.026	3
2458	NGVSJ12:33:02.20+13:42:14.0	188.259	13.704	20.03	2.54	0.49	-65.27	28.38	0.036	1,2,3
2473	NGVSJ12:33:06.81+13:36:38.4	188.278	13.611	19.47	1.53	0.46	88.32	25.94	0.035	1
2499	NGVSJ12:33:15.05+11:13:49.6	188.313	11.23	18.39	1.54	0.85	-3.2	24.49	0.053	1
2531	NGVSJ12:33:29.59+15:14:02.8	188.373	15.234	17.51	2.29	0.9	35.97	25.95	0.033	1,3
2542	NGVSJ12:33:35.06+16:18:00.7	188.396	16.3	17.62	2.17	0.62	-27.69	25.1	0.028	1
2563	NGVSJ12:33:47.06+11:46:53.8	188.446	11.782	17.49	1.68	0.91	-35.64	24.52	0.041	1
2568	NGVSJ12:33:47.95+15:10:05.7	188.45	15.168	12.89	4.74	0.75	26.39	21.57	0.04	3
2592	NGVSJ12:34:01.54+05:57:10.0	188.506	5.953	17.67	1.52	0.73	17.13	24.93	0.022	1
2621	NGVSJ12:34:15.55+11:28:00.8	188.565	11.467	17.91	2.02	0.82	-52.14	25.99	0.036	1
2635	NGVSJ12:34:20.31+08:11:52.6	188.585	8.198	10.3	8.52	0.75	10.76	21.28	0.019	3
2690	NGVSJ12:34:49.20+05:54:13.4	188.705	5.904	19.39	2.01	0.46	63.37	27.02	0.02	1,2
2717	NGVSJ12:35:06.59+11:54:02.3	188.777	11.901	17.3	1.57	0.73	-22.67	24.49	0.044	1
2731	NGVSJ12:35:12.86+07:03:22.4	188.804	7.056	18.09	3.73	0.86	33.87	27.57	0.02	1,2,3
2829	NGVSJ12:36:07.14+06:03:14.7	189.03	6.054	17.05	1.96	0.46	-1.97	24.48	0.02	1
2863	NGVSJ12:36:27.14+11:53:19.2	189.113	11.889	17.39	1.52	0.75	-74.09	24.97	0.045	1
2887	NGVSJ12:36:37.40+11:09:13.1	189.156	11.154	16.4	2.52	0.84	-67.59	23.89	0.031	3
2918	NGVSJ12:36:59.28+07:52:22.5	189.247	7.872	18.27	1.52	0.64	2.17	24.88	0.023	1
2928	NGVSJ12:37:06.81+13:58:54.0	189.278	13.982	17.13	2.45	0.54	77.81	25.16	0.052	1
2999	NGVSJ12:37:49.73+07:49:23.1	189.457	7.823	19.5	1.49	1.0	-37.31	27.22	0.023	3
3004	NGVSJ12:37:51.81+16:11:45.7	189.466	16.196	18.41	4.48	0.8	-71.16	28.16	0.034	1,2
3005	NGVSJ12:37:52.19+14:28:02.1	189.467	14.467	17.29	1.52	0.75	82.49	24.3	0.026	1
3032	NGVSJ12:38:09.93+10:47:17.6	189.541	10.788	20.66	1.51	0.69	24.37	27.7	0.021	2,3
3088	NGVSJ12:38:54.29+10:14:31.6	189.726	10.242	17.0	2.24	0.81	-88.57	25.25	0.02	1
3103	NGVSJ12:39:14.07+15:37:36.1	189.809	15.627	16.53	1.78	0.7	10.15	24.06	0.034	1

Table 5.2 Continued..

ID	NGVS name	RA	DEC	g	$R_{e,g}$	q	P.A	$\mu_{0,g}$	E (B-V)	Flag
		(deg)	(deg)	(mag)	(kpc)		(deg)	(mag arcsec^{-2})	(mag)	
(1)	(2)	(3)	(4)	(5)	(6)	(7)	(8)	(9)	(10)	(11)
3116	NGVSJ12:39:21.99+12:05:34.6	189.842	12.093	20.76	1.2	0.7	73.36	26.43	0.045	3
3128	NGVSJ12:39:31.78+11:27:15.3	189.882	11.454	17.94	2.04	0.76	75.42	25.97	0.034	1
3146	NGVSJ12:39:48.00+07:18:47.2	189.95	7.313	18.12	2.54	0.64	-61.81	26.48	0.024	1,2,3
3190	NGVSJ12:40:21.21+12:43:02.8	190.088	12.717	18.23	2.58	0.58	88.38	26.7	0.04	1,2,3
3225	NGVSJ12:40:56.41+14:15:16.3	190.235	14.255	19.46	1.88	0.74	-39.45	26.93	0.038	1,2,3
3233	NGVSJ12:40:58.86+14:15:57.6	190.245	14.266	19.5	1.69	0.85	5.14	27.7	0.037	1,2,3
3240	NGVSJ12:41:03.65+09:40:54.5	190.265	9.682	21.17	1.25	0.69	-45.69	28.05	0.017	2
3245	NGVSJ12:41:10.74+15:02:57.3	190.295	15.049	17.26	1.67	0.85	-67.22	25.07	0.039	1
3254	NGVSJ12:41:18.14+13:09:56.9	190.326	13.166	17.61	1.55	0.52	-2.69	24.46	0.029	1
3265	NGVSJ12:41:30.86+11:40:55.8	190.379	11.682	18.58	2.17	0.48	71.21	24.43	0.033	1,3
3272	NGVSJ12:41:39.34+09:12:30.5	190.414	9.208	16.29	3.34	0.82	67.42	25.58	0.02	1,2,3
3297	NGVSJ12:42:02.67+10:57:11.3	190.511	10.953	17.66	1.83	0.93	-74.78	25.79	0.022	1
3300	NGVSJ12:42:03.23+12:28:48.1	190.513	12.48	17.48	1.82	0.72	20.86	24.87	0.035	1
3356	NGVSJ12:42:56.59+13:20:49.4	190.736	13.347	18.29	2.31	0.65	86.74	26.66	0.025	1,2,3
3365	NGVSJ12:43:07.09+16:28:42.0	190.78	16.478	19.38	1.95	0.74	-81.73	27.8	0.021	1,2,3
3379	NGVSJ12:43:20.88+14:02:02.9	190.837	14.034	18.77	1.99	0.7	66.98	26.48	0.027	1,3
3404	NGVSJ12:43:49.88+14:26:54.0	190.958	14.448	19.12	2.75	0.39	-26.43	27.66	0.028	1,2
3451	NGVSJ12:44:38.62+09:23:34.9	191.161	9.393	19.16	1.88	0.54	51.12	26.65	0.024	1
3477	NGVSJ12:45:05.47+13:54:28.4	191.273	13.908	18.15	4.98	0.57	-27.84	28.38	0.024	1,2
3481	NGVSJ12:45:09.71+10:37:49.5	191.29	10.63	16.8	1.81	0.86	10.46	24.04	0.024	1
3492	NGVSJ12:45:17.82+15:31:56.1	191.324	15.532	18.31	3.73	0.66	-64.29	27.56	0.028	1,2
3516	NGVSJ12:45:44.41+12:35:14.3	191.435	12.587	18.78	5.51	0.35	-88.73	28.43	0.024	1,2
3520	NGVSJ12:45:52.39+11:14:45.9	191.468	11.246	16.81	1.92	0.79	82.04	24.23	0.033	1
3523	NGVSJ12:45:58.25+11:21:12.0	191.493	11.353	20.0	1.77	0.58	59.8	27.95	0.031	1,2
3539	NGVSJ12:46:36.06+10:47:07.5	191.65	10.785	17.39	1.56	0.95	-59.48	24.85	0.028	1
3543	NGVSJ12:46:41.73+10:23:10.4	191.674	10.386	17.5	1.79	0.86	61.67	25.05	0.025	1
3548	NGVSJ12:46:55.48+10:10:56.7	191.731	10.182	15.64	1.6	0.33	75.54	21.73	0.032	3
3561	NGVSJ12:47:24.87+11:21:40.7	191.854	11.361	18.18	1.81	0.78	75.82	25.97	0.029	1
3578	NGVSJ12:47:45.58+13:45:46.2	191.94	13.763	10.69	8.99	0.81	-15.66	18.92	0.023	3
3589	NGVSJ12:48:00.60+10:58:23.5	192.002	10.973	17.67	2.25	0.49	66.56	25.62	0.039	1

Table 5.2 Continued..

ID	NGVS name	RA	DEC	g	$R_{e,g}$	q	PA	$\mu_{0,g}$	E (B-V)	Flag
		(deg)	(deg)	(mag)	(kpc)		(deg)	(mag arcsec^{-2})	(mag)	
(1)	(2)	(3)	(4)	(5)	(6)	(7)	(8)	(9)	(10)	(11)
3590	NGVSJ12:48:00.89+13:10:20.8	192.004	13.172	17.84	1.52	0.95	81.3	25.61	0.027	1
3599	NGVSJ12:48:24.73+10:38:17.1	192.103	10.638	18.11	1.89	0.57	-78.73	25.92	0.028	1
3626	NGVSJ12:49:19.72+11:52:54.2	192.332	11.882	20.77	2.01	0.48	27.55	28.97	0.035	1,2
3628	NGVSJ12:49:24.40+13:23:22.3	192.352	13.39	21.31	1.2	0.82	-6.98	28.84	0.031	2
3633	NGVSJ12:49:38.67+15:03:16.6	192.411	15.055	19.16	1.76	0.72	-82.5	27.09	0.029	1,2
3659	NGVSJ12:51:08.90+11:28:36.4	192.787	11.477	18.8	3.72	0.43	-81.85	27.15	0.051	1,2
3661	NGVSJ12:51:12.85+13:05:45.1	192.804	13.096	19.61	2.24	0.59	-78.91	27.14	0.034	1,2

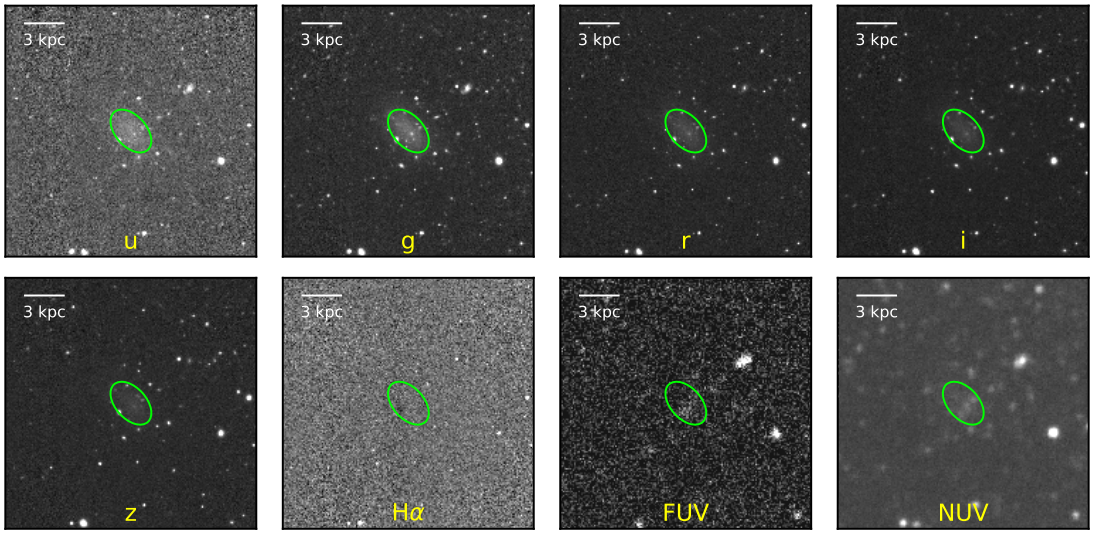

Figure 5.4.: An example of the stamps created for the source ID 2143 (see Table. 5.2). The name of the bands is given in yellow below each panel. The green ellipse shows the effective radius and position angle of the galaxy from the NGVS catalogue.

5.4. Measurements

After the selection of a sample of 150 LSBs discussed in Sect. 5.3, the next obvious step is to extract more information on them using all the data in hand. In the following sub-sections, I discuss the preparation of the available data and perform scientific measurements on the entire sample.

5.4.1. Creation of stamps

Initially, I collected the photometric data from all the surveys (u, g, r, i, z, Hα, FUV and NUV bands) to create a separate stamp for all the sources in each band. This procedure was done using the `Montage` tool in Python (Jacob et al. 2010), which co-adds the multiple exposures of the same source to a single stamp. Especially in the case of the UV images from GUViCS, where the GALEX AIS and MIS fields have multiple overlapping coverages as seen in Fig. 5.1, co-adding the exposures help to create a deeper image of the source. This is also useful in combining the partial coverage of few sources along the edge of specific fields in the NGVS, VESTIGE or GUViCS images.

In this way, I created stamps for each source in 8 photometric bands to make 1200 stamps for the 150 sources in the sample. The size of each stamp, centred around the source, was arbitrarily chosen so that it has size ten times the effective radius of the galaxy given in the NGVS catalogue. For comparison purposes, all the stamps, including the UV images (with GALEX pixels of $1.5''$), were projected onto a pixel scale of the NGVS and VESTIGE images (with pixels of $0.187''$).

Figure 5.4 shows an example of the stamps created for a single source.

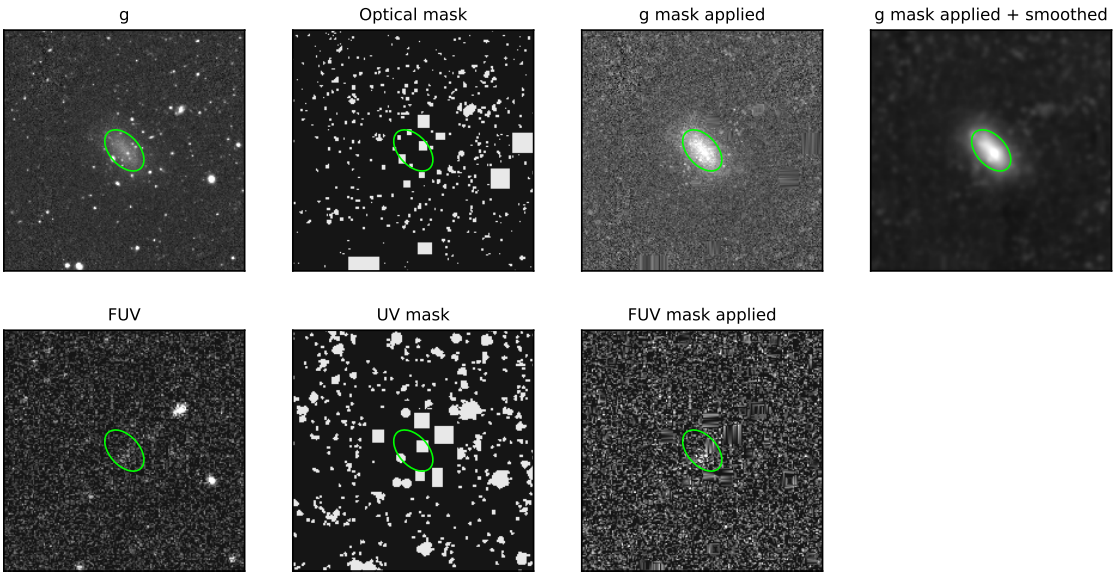

Figure 5.5.: An illustration of the cleaning of the stamps using the optical and UV masks for the source 2143. From left to right in the top panels are the *g*-band stamp, optical mask, cleaned *g*-band stamp after applying the mask and the *g*-band cleaned image smoothed at the resolution of GALEX, respectively. Similarly, the bottom panels are the FUV stamp, UV mask and the cleaned FUV mask after applying the UV mask.

5.4.2. Preparation of masks and further processing of the stamps

After creating stamps for the sample and before proceeding with the photometric measurements, I needed to clean the stamps from foreground or background sources contaminating the field of my sources of interest. For this purpose, I used the masks provided by the NGVS team (Ferrarese et al. 2020). For all the galaxies in the catalogue, NGVS masks artefacts, foreground stars, stellar halos, background galaxies, as well as globular clusters in the field of the galaxy. Using the NGVS masks as a reference, I manually inspected and edited them to remove any residual artefacts and faint stars. For the UV images, I created a separate mask after smoothing the NGVS masks to the GALEX point source resolution of $5''$. The UV masks were also manually edited to remove any background source not masked in the NGVS masks. This procedure gave two kinds of masks for each source: an optical mask and a UV mask.

After preparing the optical and UV masks, I used them to clean the stamps I created in the previous step. This was done by the IRAF `fixpix` procedure, when provided with a stamp and the corresponding mask, linearly interpolates the masked region in the stamp with that of the unmasked regions to produce a stamp cleaned of any background sources, as shown in Fig. 5.5. For the NGVS and VESTIGE images with a higher resolution than the UV images, for comparison purposes, I also made a version of the cleaned stamps convoluted with a Gaussian kernel to match the GALEX resolution of $5''$. The photometric measurements discussed in Sect. 5.4.3 and 5.4.4 will be done on these cleaned stamps (both high and low resolution, which hereupon I refer to as HR and LR stamps).

5.4.3. Background sky measurements

Once the stamps are cleaned of any background sources, they are ready to carry out quantitative photometric measurements. The first one in this step is an estimation of the background sky level around each of my sources. The mean and dispersion in the sky level are crucial for disentangling the light from my source of interest from any contamination from the sky.

I measured the local and global sky variations around each of my sources following the procedure from Gil de Paz et al. (2005). This was done by initially placing several equidistant and equal-sized "skyboxes" vertically and horizontally around each source, as shown in Fig. 5.6. The boxes were arbitrarily placed at a distance of $3R_e$ from the source to be far any of its light and also not too far to reach the stamp edges. I checked that on average a variation in the placement of the boxes from $3R_e$ to $4R_e$ from the source has a negligible effect of $< 2\%$ on the sky level measurements. The size of each box was also fixed so that they are large enough to make an independent statistically significant sky measurement and, simultaneously, sufficient to place a total of 24 similar boxes around a source without any overlap. I visually inspected all these boxes and moved/removed them if any problem or artefact within them could affect the sky measurements.

These boxes were used as sky estimation apertures to measure statistics to get a mean sky level and dispersion from all the boxes. Following Gil de Paz et al. (2005) (see their Eqn. 4), I combined the mean and standard deviation of each of the skyboxes to get an estimate of the global sky uncertainty at any point within the field of the galaxy, as shown in Eqn. 5.1.

$$\sigma_{\rm global} = \sqrt{\frac{<\sigma^2_{sky}>}{N_{\rm data}} + \max\left(\sigma^2_{<sky>} - \frac{<\sigma^2_{sky}>}{N_{\rm box}}, 0\right)} \tag{5.1}$$

Here $<\sigma_{sky}>$ and $\sigma_{<sky>}$ corresponds to the mean of standard deviations and the standard deviation of the mean sky values measured in each of the skyboxes, respectively. The former term in Eqn. 5.1 gives the local pixel-level variation in the sky, whereas the latter term concerns the large scale variation or gradients in the sky. $N_{\rm box}$ is the number of pixels in each of the skyboxes and $N_{\rm data}$ is the number of pixels where a photometric measurement is performed (for instance, in case of surface brightness measurements, this is the number of pixels in an isophote). These sky uncertainty values were measured for both the HR and LR stamps of a source using Eqn. 5.1, and will be used later in the surface brightness profile measurements discussed in Sect. 5.4.4.

5.4.4. Extraction of surface brightness profiles

After the preparation of the data discussed in the previous sections, my sample was ready to carry out surface brightness profile measurements, which is crucial for studying the photometric properties of these galaxies.

The surface brightness profile measurements were performed using the `Ellipse` task in the `Photutils` python package (Bradley et al. 2019). This procedure measures the average flux along elliptical isophotes on the stamp of each galaxy. The isophotes are placed concentrically around the sources (see Fig. 5.6) at different radii, by fixing few geometrical parameters of the galaxy (central coordinates, position angle and axis ratio) as given in Table. 5.2 from the NGVS catalogue. The choice of concentric elliptical isophotes (rather than trying to fit the geometrical parameters in each band) was made to be consistent with previous studies (Muñoz-Mateos et al. 2011; Boissier et al. 2016). Using the same isophotes while performing measurements on various sets of images is better in order to compare them later (e.g. magnitudes and colours in different photometric bands will be measured using the same apertures).

The average flux at each radii is converted to the surface brightness units using the following relation:

$$\mu_r = -2.5\log(F_r) + {\rm ZP} + 5\log\left({\rm arcsec\,pixel}^{-1}\right) \tag{5.2}$$

where μ_r is the surface brightness (in units of mag arcsec^{-2}) at radius r. F_r is the corresponding

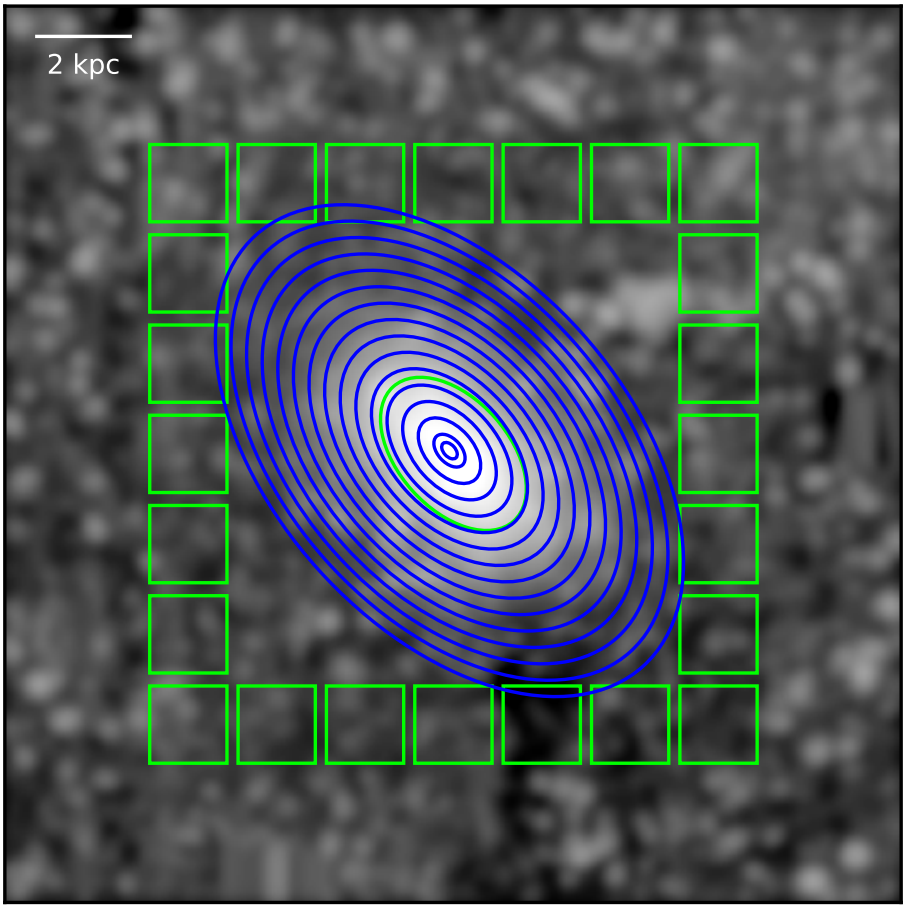

Figure 5.6.: The sky measurement boxes (green squares) and ellipses (in blue) used for the surface brightness profile measurements of the source 2143. The image is *g*-band smoothed image same as shown in Fig. 5.5, with different contrast.

flux at that radius, in units of number counts. ZP is the photometric zero-point corresponding to the data used to convert the magnitude into AB units. For the NGVS and VESTIGE data, ZP = 30 (Ferrarese et al. 2012; Boselli et al. 2018a), whereas for the GUViCS FUV and NUV data, ZP is 18.82 and 20.08 (Morrissey et al. 2005), respectively. The final term in Eqn. 5.2 converts the magnitudes to the surface brightness. For the data used in this work, this conversion scale is 0.187 arcsec pixel^{-1}. Using Eqn. 5.2 on the `Ellipse` isophotal measurements gives the radial surface brightness profiles of each source in all the photometric bands. Later, I applied a foreground galactic extinction correction for these profiles using the E($B-V$) value given in Table. 5.2 and adopting a Cardelli et al. (1989) extinction curve. I assumed there was no internal extinction in these galaxies, as it is generally found in low surface brightness galaxies (Hinz et al. 2007; Rahman et al. 2007). The profiles were also corrected for the galaxy inclination by de-projecting them to a face-on value using their corresponding axis ratios from Table. 5.2.

Fig. 5.7 shows an example of the measured profiles (both HR and LR profiles) for galaxy 2143. The galaxy is close to an exponential disk in *u, g, r, i, z* and NUV bands. There is only an upper limit in FUV. In Hα, the HR profiles show a faint central detection. However, it vanishes in the smoothed LR profiles where there is only an upper limit in Hα.

5.4.5. Surface brightness profile decomposition

The first in analysing the surface brightness profiles obtained as described up to now is to decompose the profiles into various galaxy components (e.g. disk, bulge). I performed a two-component decomposition of all the profiles into a Sérsic central component and an exponential disk, using the `Profit` python routine developed by Barbosa et al. (2015). The fitting algorithm performs a weighted $\chi 2$ minimisation procedure, with a Gaussian PSF (corresponding to the FWHM of the data given in Table 5.1) convoluted with the model light profiles.

For the Sérsic component, the Sérsic index (n) was fixed to $n = 4$ corresponding to a de Vaucouleurs profile. The effective radius and surface brightness at effective radius for each source from the NGVS catalogue was provided as an initial guess for the Sérsic component. Similarly, for the exponential disk, the scale length and central surface brightness were also given as an initial guess for the fitting (disk scale length guess was obtained from the R_e value with a conversion factor of 1.678; Peng et al. 2002).

In this way, I fitted the surface brightness profiles in each band for both the HR and LR profiles. For the majority of the sources in the sample, this procedure provided a very good quality decomposition fit, as can be seen from the example in Fig. 5.7. However, for few sources with failed fits, the initial guess parameters had to be manually adjusted to obtain better fitting results.

The HR profiles decomposition in optical and Hα helps to identify the presence of a central component (if present). In contrast, the LR profiles give the overall distribution of light in the galaxy at a lower resolution, with the additional UV bands. For the remaining part of this work, I will be using only the relatively standard *g*-band decomposition results in HR, where we have deeper data.

The distribution of some of the parameters derived in the surface brightness profile decomposition is shown in Fig. 5.8. Most of the sources in the sample are predominantly dominated by disks without any bright central component (~90% of the galaxies in the sample have a central component to the disk light ratio lower than 0.1). The distribution of the central disk surface brightness values extends to as faint as 28 mag arcsec^{-2}, almost identical to the distribution of the NGVS values. However, a few sources have a central component brighter than the disk, with a spiral or elliptical nature. These sources mainly belong to the outlier sources. The distribution of the disk lengths from the decomposition also shows that majority of the sample have disk scale lengths larger than one kpc (which corresponds to an effective radius of 1.678 kpc), consistent with the population of UDGs from the sample selection.

A manual inspection followed the above decomposition procedure to check the quality of the extracted surface brightness profiles and fits. Sources that are marginally detected as well as having failed decomposition were identified in this step. There were 15 such sources (10 percent of the total sample) that I removed from my sample at this stage (see Fig. 5.9). The sample size is now reduced to 135 galaxies.

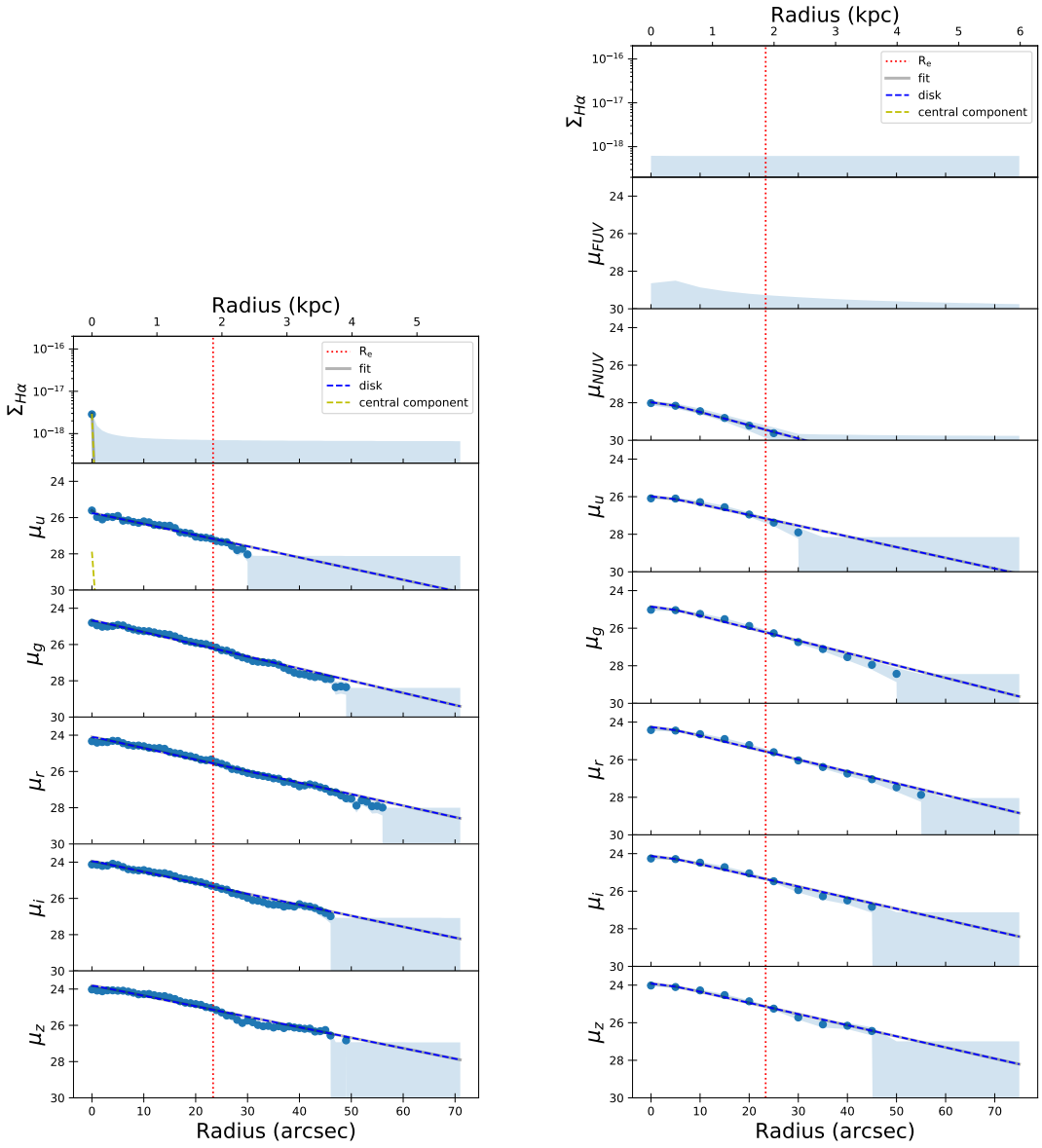

(a) High resolution profiles

(b) Low resolution profiles

Figure 5.7.: Radial surface brightness profiles of galaxy 2143 measured in eight bands, shown as blue filled dots. The surface brightness units are in mag arcsec^{-2} for all the bands except for Hα which is in erg s^{-1} cm^{-2} arcsec^{-2}. The blue shaded area marks the 1σ error (for data points) and upper limits (3σ). The vertical red dotted line gives g-band effective radius of the galaxy from Table. 5.2. The grey line, blue dashed line and yellow dashed line are the best fit, disk component and the central component, respectively, obtained from the surface brightness decomposition procedure discussed in Sect. 5.4.5. The profiles shown here are not corrected for the galaxy inclination and Milky Way foreground galactic extinction.

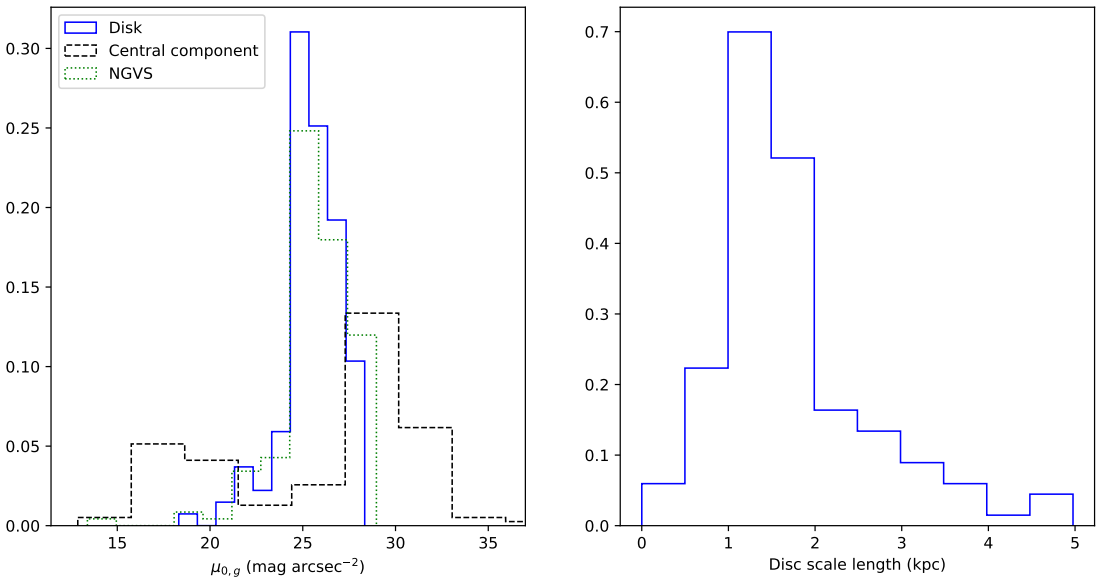

Figure 5.8.: *Left:* Distribution of the g-band central surface brightness from the decomposition results. The solid blue line and the black dashed lines are the $\mu_{0,g}$ distribution corresponding to the exponential disk and Sérsic central component, respectively. The green dotted distribution is the $\mu_{0,g}$ from the NGVS catalogue (as given in Table 5.2). *Right:* The corresponding distribution of the disk scale lengths obtained from the surface brightness decomposition.

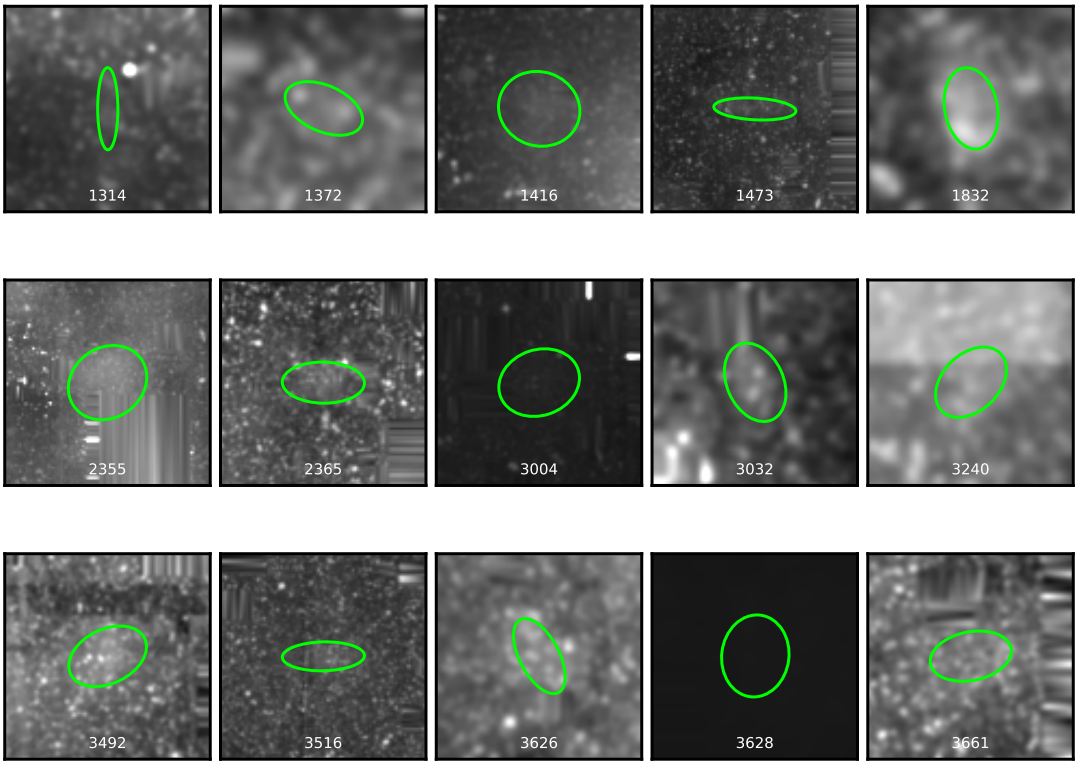

Figure 5.9.: The *g*-band mask applied and smoothed images of the 15 sources that were removed from the sample after manual inspection of their surface brightness profiles. The green ellipse shows the effective radius and position angle of the sources identified in the NGVS catalogue. These sources have either only upper limits or suspicious detections close to the sky level in their *g*-band surface brightness profile.

After the profile extraction, decomposition and manual inspections, the profiles are in a good state to proceed further with the analysis.

5.4.6. New determination of effective radii

After the validation of the radial surface brightness profiles discussed in Sect. 5.4.5, I made a new determination of R_e of the galaxies in my sample, apart from the values given by the NGVS catalogue. This was necessary so that the R_e would be consistent with the profiles I measured, in a slightly different way than that of the NGVS. Moreover, considering the effective radius is one of the main parameters used in my sample selection, one needs to be confident of those values, irrespective of the method of measurements adopted by me and NGVS.

I measured the g-band R_e of my sample (135 sources now) by numerically integrating their total light until the last observed radius in the surface brightness profile corrected for inclination, as shown in Eqn. 5.3 (where q is the axis ratio of a galaxy, given in Table 5.2). The R_e corresponds to the radius at which the integrated light reaches half of its total value ($L_{\rm tot}/2$).

$$L_{\rm tot} = \int_0^{r_{\rm last}} 10^{-0.4\mu(r)}\, q\, 2\pi r\, dr \tag{5.3}$$

Figure 5.10 (top panel) shows the comparison of the effective radii after the above measurement with that of the values from the NGVS. Although both the values are close to each other, on average, the R_e from my measurements seems to be slightly lower than the NGVS values. This is due to the difference in the measurement procedures, where I integrated the light profiles until the last observed radius, whereas the NGVS R_e measurements are based on extrapolated Sérsic fits. Moreover, the distribution of the UDG sub-sample (blue open circles in Fig. 5.10) also shows an interesting difference. Although the initial selection of the UDG sample was made based on the van Dokkum et al. (2015) limit of $R_e > 1.5$ kpc, a portion of the newly determined R_e of the same UDGs falls below this selection limit, potentially classifying them as non-UDGs (but the majority of the UDGs still fall above this limit or overlaps with the "diffuse" or "outlier" classifications). This illustrates that an arbitrary size selection of UDGs generally done in the literature depends highly on the measurements' method. One needs to keep in mind that a specific measurement can classify a source as UDG, whereas a different measurement approach of the same quantity can fail.

In recent works, Chamba et al. (2020) and Trujillo et al. (2020) suggests that R_e measures the concentration of light within a galaxy and thus does not capture the physical size of a galaxy, leading to a misleading interpretation of size, especially in the case of diffuse sources like LSBs and UDGs. They put forward a new physically motivated measurement of a galaxy size called the R_1 radius (the radius at which the stellar mass surface density of a galaxy reaches 1 $M_\odot$ pc^{-2}, which is a proxy for the location of the gas density threshold for star formation). This captures the intuitive definition of a physical size which is related to the edge or boundary of a galaxy. One should note that a size estimator like R_1 or other isophotal estimators like R_{25} or Holmberg Radius ($R_{\rm H}$) will be more meaningful than R_e, if one is focused on studying the physical size of a galaxy (especially for LSBs). However, in this work, the R_e is only used as a parameter for the LSB sample selection, consistently with the LSB definitions in the literature. Moreover, as can be seen in Sect. 5.4.5, most of the galaxies in my sample do not have a strong central concentration affecting the size estimation of the LSB component. Therefore, I chose to keep all sources from the current sample for further measurements in this work.

5.4.7. Integrated magnitudes

The integrated photometric measurements on the sample were done using the elliptical isophotes discussed in Sect. 5.4.4, obtained for the surface brightness profile measurements. For each source, I integrated the total flux in a photometric band until the last observed radius in the g-band. This was done to keep a uniform measurement aperture for all the bands (which I will use together for colour

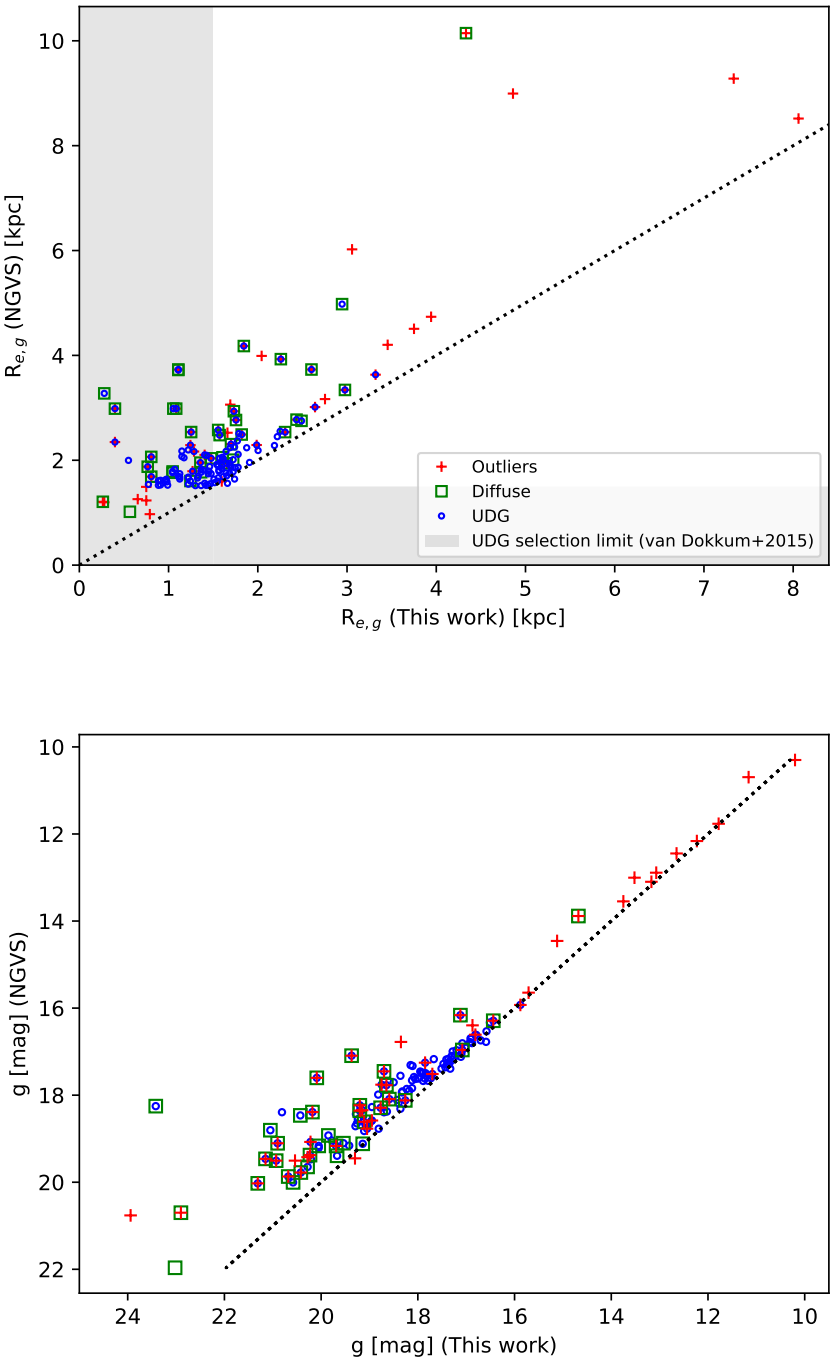

Figure 5.10.: Comparison of the newly determined g-band effective radii (top panel) and magnitudes (bottom panel) of the sample with the initial values from the NGVS catalogue. Different sub-samples (UDGs, Diffuse and Outliers) are marked with circles, squares and crosses, respectively (similar to Fig. 5.2). The grey shaded area in the top panel marks the region below the UDG selection limit of $R_{e,g}$ = 1.5 kpc (van Dokkum et al. 2015). The blacked dotted lines give a one-to-one relation.

estimates in the later stages), and the g-band being the deepest ensures that all the flux from the source will be within the last observed radii of g-band. Table 5.3 gives the measured magnitudes and fluxes of the sample. Most of the sources are well detected in the optical bands (u, g, r, i, z), whereas in Hα and UV bands, there are primarily upper limits, which is still quite helpful in constraining their properties.

Figure 5.10 (bottom panel) compares the measured magnitudes in g-band with that of the values from NGVS. For all the sources, except for the faintest sources ($g < 20$ mag), both the measurements agree. In the faintest sources, the magnitudes I measured seem to be systematically lower than the NGVS ones, similar to the measurements of effective radii discussed in the previous section. For sources close to the limit of the sky, there is significant uncertainty and the possibility of over or under-estimation of these measured quantities.

Table 5.3.: Photometric measurements of the sample. Column details: (1) ID of the source. (2-6) *u*, *g*, *r*, *i* and *z*-band magnitudes. (7) VESTIGE Hα flux. (8-9) GALEX *NUV* and *FUV* magnitudes. The upper limits (3σ) in the broad-band magnitudes and in the Hα fluxes are denoted with > and < symbols, respectively. The sources with no coverage in the VESTIGE Hα or *r*-band are marked with the "−" symbol. All the magnitudes and flux values were measured within an aperture of the last *g*-band observed radius and corrected for Galactic extinction.

ID	*u* (mag)	*g* (mag)	*r* (mag)	*i* (mag)	*z* (mag)	Hα Flux (10^{-15} erg s^{-1} cm^{-2})	*NUV* (mag)	*FUV* (mag)
(1)	(2)	(3)	(4)	(5)	(6)	(7)	(8)	(9)
67	19.71 ± 0.36	18.73 ± 0.24	–	18.05 ± 0.2	18.06 ± 0.36	–	> 21.59	> 21.09
103	17.5 ± 0.11	16.51 ± 0.08	–	15.85 ± 0.08	15.87 ± 0.14	–	19.86 ± 0.26	> 20.86
110	18.82 ± 0.08	17.85 ± 0.1	–	17.13 ± 0.07	17.05 ± 0.13	–	> 20.29	> 19.76
186	17.88 ± 0.21	17.19 ± 0.13	–	16.94 ± 0.14	> 16.52	–	18.71 ± 0.08	18.84 ± 0.15
213	> 20.91	20.42 ± 0.18	–	19.68 ± 0.38	> 18.72	–	> 21.53	> 22.15
227	> 18.98	18.34 ± 0.15	17.71 ± 0.15	17.52 ± 0.29	17.48 ± 0.29	< 1.63	> 21.87	> 21.96
321	20.61 ± 0.37	19.83 ± 0.24	–	19.24 ± 0.28	> 19.12	–	> 21.22	> 21.89
405	17.37 ± 0.08	16.59 ± 0.05	16.26 ± 0.12	16.07 ± 0.16	16.01 ± 0.22	< 4.02	18.54 ± 0.12	18.71 ± 0.22
421	17.7 ± 0.2	16.8 ± 0.15	> 15.9	16.33 ± 0.15	16.37 ± 0.17	< 27.56	> 19.42	> 19.94
435	14.88 ± 0.12	13.51 ± 0.06	–	12.53 ± 0.06	12.23 ± 0.06	–	18.51 ± 0.13	> 20.31
444	17.29 ± 0.17	16.7 ± 0.07	16.36 ± 0.34	16.44 ± 0.08	16.35 ± 0.14	< 23.78	18.17 ± 0.07	18.35 ± 0.05
466	> 20.99	20.4 ± 0.22	> 19.84	> 19.08	> 18.31	< 0.77	> 20.93	> 21.19
495	19.45 ± 0.21	18.23 ± 0.07	17.64 ± 0.1	17.66 ± 0.16	17.42 ± 0.21	< 0.79	> 21.39	> 21.54
583	18.08 ± 0.12	17.1 ± 0.08	16.67 ± 0.05	16.56 ± 0.08	16.42 ± 0.18	< 2.19	19.77 ± 0.17	20.33 ± 0.15
588	> 22.97	22.99 ± 0.26	> 22.84	> 22.12	> 21.01	< 0.11	> 23.99	> 24.03
590	19.37 ± 0.33	18.35 ± 0.17	17.7 ± 0.08	17.58 ± 0.08	17.48 ± 0.06	< 2.15	> 21.72	> 22.33
604	20.18 ± 0.2	19.28 ± 0.12	–	18.63 ± 0.23	> 18.06	–	> 21.54	> 20.17
646	20.36 ± 0.32	19.13 ± 0.21	18.65 ± 0.24	> 18.1	> 17.92	< 0.8	> 21.8	> 21.84
743	18.35 ± 0.08	17.35 ± 0.08	16.96 ± 0.05	16.68 ± 0.14	16.51 ± 0.16	< 1.46	20.2 ± 0.3	> 21.17
796	> 18.89	17.84 ± 0.14	17.2 ± 0.11	17.06 ± 0.11	16.96 ± 0.12	< 1.71	> 20.72	> 21.06
833	18.42 ± 0.12	17.3 ± 0.07	16.61 ± 0.08	16.47 ± 0.05	16.24 ± 0.08	< 6.31	> 20.69	> 21.52

Table 5.3 Continued..

ID	u (mag)	g (mag)	r (mag)	i (mag)	z (mag)	Hα Flux (10^{-15} erg s^{-1} cm^{-2})	*NUV* (mag)	*FUV* (mag)
(1)	(2)	(3)	(4)	(5)	(6)	(7)	(8)	(9)
892	> 19.93	19.1 ± 0.15	18.5 ± 0.18	18.15 ± 0.26	18.06 ± 0.18	< 2.11	–	–
904	18.07 ± 0.15	16.92 ± 0.05	16.34 ± 0.06	16.07 ± 0.06	15.9 ± 0.08	< 2.78	–	–
906	> 19.18	18.07 ± 0.12	17.5 ± 0.14	17.24 ± 0.12	17.14 ± 0.14	< 0.86	> 21.47	> 21.78
935	> 20.61	20.13 ± 0.32	19.55 ± 0.32	> 19.32	> 19.01	< 0.75	–	–
952	20.13 ± 0.33	19.1 ± 0.15	18.56 ± 0.18	18.42 ± 0.16	18.21 ± 0.35	< 1.31	–	–
964	19.06 ± 0.36	17.82 ± 0.08	17.21 ± 0.11	16.65 ± 0.31	16.92 ± 0.32	< 1.66	> 20.73	> 20.98
1008	> 20.89	20.27 ± 0.16	19.47 ± 0.2	19.08 ± 0.32	> 19.27	< 0.82	> 21.82	> 21.64
1013	19.03 ± 0.06	17.92 ± 0.05	17.34 ± 0.05	17.1 ± 0.06	17.15 ± 0.09	< 2.17	> 20.06	> 22.08
1017	21.26 ± 0.35	20.08 ± 0.12	19.6 ± 0.14	19.3 ± 0.1	19.18 ± 0.18	< 0.15	> 23.34	> 23.3
1027	19.21 ± 0.21	18.36 ± 0.1	17.81 ± 0.12	17.74 ± 0.2	> 17.69	< 1.71	20.43 ± 0.28	> 20.72
1160	18.29 ± 0.23	17.07 ± 0.12	16.57 ± 0.15	16.34 ± 0.16	16.42 ± 0.32	< 4.62	> 19.72	> 19.65
1214	20.26 ± 0.14	19.23 ± 0.16	18.6 ± 0.14	18.54 ± 0.18	> 18.14	< 0.53	> 21.78	> 20.99
1227	18.56 ± 0.3	17.43 ± 0.06	16.8 ± 0.08	16.65 ± 0.13	16.74 ± 0.3	< 4.57	> 19.71	–
1271	> 21.96	20.77 ± 0.3	20.07 ± 0.19	19.88 ± 0.36	> 19.65	< 0.13	> 23.25	> 24.31
1318	13.99 ± 0.05	13.17 ± 0.05	12.69 ± 0.05	12.49 ± 0.05	12.33 ± 0.05	114.87 ± 2.3	15.28 ± 0.05	15.65 ± 0.05
1335	> 20.45	19.77 ± 0.16	19.26 ± 0.16	18.99 ± 0.14	18.66 ± 0.3	< 1.43	> 22.41	> 22.9
1346	23.56 ± 0.3	22.88 ± 0.2	22.2 ± 0.18	21.9 ± 0.27	> 21.51	< 0.03	> 24.15	> 24.15
1349	> 19.11	18.48 ± 0.18	17.87 ± 0.19	17.76 ± 0.14	17.62 ± 0.24	< 1.5	> 21.7	> 22.82
1352	20.36 ± 0.18	19.29 ± 0.14	18.65 ± 0.14	18.48 ± 0.16	18.26 ± 0.18	< 0.48	> 21.84	> 21.94
1354	19.9 ± 0.24	18.96 ± 0.14	18.36 ± 0.22	18.25 ± 0.15	18.32 ± 0.26	< 1.27	> 22.1	> 21.24
1389	13.43 ± 0.05	12.65 ± 0.05	12.21 ± 0.05	12.04 ± 0.05	11.91 ± 0.05	202.41 ± 8.5	14.63 ± 0.05	14.93 ± 0.05
1397	> 21.21	20.87 ± 0.25	20.4 ± 0.18	> 19.41	> 17.31	< 0.6	> 22.74	> 23.33
1424	> 20.66	19.53 ± 0.15	18.99 ± 0.26	18.99 ± 0.27	> 18.73	< 1.75	> 21.51	> 21.8
1429	17.61 ± 0.18	16.78 ± 0.08	16.14 ± 0.05	16.05 ± 0.06	15.84 ± 0.11	< 2.23	20.03 ± 0.14	> 20.64
1435	13.05 ± 0.05	11.78 ± 0.05	11.09 ± 0.05	10.84 ± 0.05	10.54 ± 0.07	< 107.7	16.69 ± 0.17	> 18.42
1436	20.24 ± 0.29	19.26 ± 0.2	18.66 ± 0.26	18.64 ± 0.26	18.58 ± 0.34	< 0.75	> 22.15	> 22.63

Table 5.3 Continued..

ID	u	g	r	i	z	Hα Flux	NUV	FUV
	(mag)	(mag)	(mag)	(mag)	(mag)	(10^{-15} erg s^{-1} cm^{-2})	(mag)	(mag)
(1)	(2)	(3)	(4)	(5)	(6)	(7)	(8)	(9)
1450	> 19.97	19.26 ± 0.12	18.72 ± 0.18	18.61 ± 0.18	18.18 ± 0.33	< 0.79	> 22.05	> 22.05
1459	12.93 ± 0.18	12.22 ± 0.1	11.92 ± 0.08	> 11.59	11.06 ± 0.1	422.89 ± 41.44	14.78 ± 0.08	15.07 ± 0.22
1474	19.12 ± 0.25	18.04 ± 0.18	17.54 ± 0.22	17.27 ± 0.26	17.07 ± 0.26	< 1.17	> 20.48	> 20.97
1476	> 19.74	18.61 ± 0.26	18.03 ± 0.22	17.81 ± 0.32	17.5 ± 0.37	< 1.09	> 21.7	> 22.03
1479	21.34 ± 0.18	20.26 ± 0.18	19.69 ± 0.23	19.58 ± 0.36	19.46 ± 0.34	< 0.34	> 22.68	> 22.53
1506	19.19 ± 0.24	18.14 ± 0.16	17.5 ± 0.18	17.27 ± 0.21	17.2 ± 0.29	< 1.03	> 21.94	> 21.04
1529	15.56 ± 0.11	14.68 ± 0.06	14.22 ± 0.07	14.04 ± 0.12	13.9 ± 0.29	< 27.56	17.96 ± 0.28	> 19.05
1593	> 17.94	17.1 ± 0.21	16.48 ± 0.1	16.45 ± 0.21	16.36 ± 0.34	< 3.98	> 20.93	> 20.82
1620	19.76 ± 0.34	18.64 ± 0.1	17.98 ± 0.13	17.79 ± 0.15	17.7 ± 0.34	< 2.44	> 20.5	> 21.63
1633	20.22 ± 0.34	19.18 ± 0.2	18.57 ± 0.21	> 18.37	> 17.23	< 1.0	> 21.32	> 21.84
1653	21.39 ± 0.08	20.22 ± 0.06	19.59 ± 0.05	19.46 ± 0.08	19.35 ± 0.1	< 0.09	23.9 ± 0.25	> 24.66
1656	18.81 ± 0.3	17.94 ± 0.13	17.39 ± 0.12	17.25 ± 0.13	17.04 ± 0.18	< 1.66	> 20.88	> 20.39
1719	> 20.38	19.66 ± 0.26	> 19.21	> 18.92	> 18.59	< 1.37	> 21.6	> 22.47
1782	18.5 ± 0.18	17.47 ± 0.06	16.92 ± 0.1	16.75 ± 0.17	16.76 ± 0.32	< 4.83	> 20.26	> 20.92
1837	> 23.9	23.37 ± 0.33	22.67 ± 0.26	22.0 ± 0.16	22.12 ± 0.27	< 0.03	> 25.75	> 25.85
1846	> 18.88	18.8 ± 0.18	18.3 ± 0.16	18.03 ± 0.1	17.71 ± 0.13	< 0.98	> 21.55	> 22.49
1896	18.03 ± 0.11	16.91 ± 0.07	16.26 ± 0.05	16.18 ± 0.07	16.02 ± 0.12	< 2.86	20.68 ± 0.26	> 20.95
1968	15.93 ± 0.06	15.11 ± 0.12	14.7 ± 0.16	14.64 ± 0.21	14.5 ± 0.26	< 7.8	17.78 ± 0.18	> 18.73
1993	> 19.2	19.33 ± 0.3	> 19.36	18.93 ± 0.15	17.43 ± 0.21	< 0.44	> 22.29	> 21.96
2006	18.07 ± 0.15	16.9 ± 0.05	16.25 ± 0.05	16.07 ± 0.08	15.73 ± 0.3	< 4.09	> 19.67	–
2046	17.07 ± 0.24	15.88 ± 0.1	15.28 ± 0.14	15.03 ± 0.12	14.85 ± 0.14	< 17.55	> 18.73	> 19.72
2079	> 19.48	18.67 ± 0.26	18.05 ± 0.12	17.78 ± 0.28	> 17.62	< 1.79	> 20.95	20.34 ± 0.24
2143	18.44 ± 0.24	17.37 ± 0.06	16.69 ± 0.05	16.54 ± 0.11	16.32 ± 0.1	< 2.97	> 20.63	> 21.08
2156	18.44 ± 0.12	17.41 ± 0.07	16.71 ± 0.08	16.49 ± 0.13	16.3 ± 0.13	< 2.66	> 20.03	> 19.31
2178	19.91 ± 0.3	19.06 ± 0.2	18.46 ± 0.06	18.37 ± 0.16	18.28 ± 0.21	< 0.89	> 21.4	> 20.29
2200	19.39 ± 0.22	18.8 ± 0.14	18.32 ± 0.16	18.26 ± 0.18	18.16 ± 0.29	< 2.19	> 20.6	> 20.16

Table 5.3 Continued..

ID	u (mag)	g (mag)	r (mag)	i (mag)	z (mag)	Hα Flux (10^{-15} erg s^{-1} cm^{-2})	*NUV* (mag)	*FUV* (mag)
(1)	(2)	(3)	(4)	(5)	(6)	(7)	(8)	(9)
2205	18.39 ± 0.21	17.28 ± 0.06	16.67 ± 0.08	16.53 ± 0.12	16.36 ± 0.18	< 2.99	> 20.11	–
2227	19.44 ± 0.18	18.18 ± 0.08	17.66 ± 0.12	17.52 ± 0.2	17.39 ± 0.21	< 1.74	> 20.65	> 21.67
2237	18.38 ± 0.18	17.34 ± 0.1	16.8 ± 0.11	16.57 ± 0.14	16.4 ± 0.2	< 5.45	> 19.53	> 20.07
2269	> 21.67	20.66 ± 0.21	19.92 ± 0.22	> 19.69	> 19.41	< 0.85	> 22.54	> 22.82
2301	18.0 ± 0.13	17.02 ± 0.05	16.52 ± 0.07	16.3 ± 0.08	16.09 ± 0.08	< 3.28	20.31 ± 0.3	> 21.15
2343	> 18.87	18.1 ± 0.18	17.62 ± 0.16	17.48 ± 0.12	> 17.41	< 2.21	> 21.7	> 22.16
2351	21.13 ± 0.26	20.04 ± 0.16	19.48 ± 0.18	19.37 ± 0.26	> 19.15	< 0.35	> 23.09	> 22.64
2394	18.74 ± 0.16	17.67 ± 0.09	17.05 ± 0.11	16.93 ± 0.2	16.74 ± 0.3	< 2.27	> 20.78	> 21.12
2409	14.97 ± 0.08	13.75 ± 0.05	13.16 ± 0.05	12.91 ± 0.05	12.72 ± 0.06	< 44.08	17.7 ± 0.22	> 18.59
2458	> 22.07	21.28 ± 0.25	20.49 ± 0.33	> 20.21	> 18.76	< 1.0	> 22.46	> 22.52
2473	21.04 ± 0.09	20.2 ± 0.12	19.62 ± 0.12	19.47 ± 0.16	> 19.39	< 0.25	> 22.82	> 22.32
2499	19.79 ± 0.1	18.7 ± 0.1	18.08 ± 0.11	18.0 ± 0.12	17.95 ± 0.19	< 0.71	> 22.29	> 21.54
2531	18.77 ± 0.21	17.7 ± 0.1	17.05 ± 0.1	16.86 ± 0.12	16.7 ± 0.15	< 3.73	> 19.87	> 18.68
2542	18.94 ± 0.08	17.98 ± 0.11	–	17.34 ± 0.15	> 17.22	–	> 20.33	> 20.59
2563	> 18.88	17.89 ± 0.08	17.29 ± 0.08	17.12 ± 0.08	17.11 ± 0.24	< 2.0	> 21.25	> 20.09
2568	13.69 ± 0.11	13.07 ± 0.05	12.65 ± 0.05	12.59 ± 0.05	12.42 ± 0.08	166.04 ± 4.65	14.62 ± 0.05	14.97 ± 0.05
2592	18.7 ± 0.18	17.78 ± 0.1	–	17.21 ± 0.2	> 16.47	–	20.1 ± 0.25	> 20.77
2621	> 18.74	18.32 ± 0.1	17.51 ± 0.12	17.43 ± 0.18	17.44 ± 0.3	< 1.87	> 20.54	> 19.95
2635	11.13 ± 0.05	10.2 ± 0.05	9.66 ± 0.05	9.48 ± 0.05	9.25 ± 0.05	2052.22 ± 41.04	12.67 ± 0.05	13.08 ± 0.05
2690	20.94 ± 0.34	19.67 ± 0.12	–	> 18.82	> 18.64	–	> 20.97	> 20.39
2717	18.47 ± 0.14	17.38 ± 0.06	16.74 ± 0.08	16.52 ± 0.08	16.47 ± 0.11	< 2.03	> 20.76	> 20.55
2731	> 19.14	18.58 ± 0.2	17.82 ± 0.34	> 17.62	> 17.48	< 11.07	> 20.23	> 20.3
2829	18.19 ± 0.11	17.1 ± 0.06	–	16.38 ± 0.12	16.16 ± 0.16	–	> 19.25	> 19.99
2863	18.73 ± 0.15	17.51 ± 0.07	16.9 ± 0.05	16.71 ± 0.07	16.62 ± 0.2	< 1.32	> 21.43	> 20.65
2887	18.07 ± 0.17	16.87 ± 0.1	16.2 ± 0.07	16.08 ± 0.11	16.0 ± 0.1	< 3.8	> 20.64	> 20.59
2918	> 19.91	18.94 ± 0.15	18.42 ± 0.22	18.25 ± 0.14	17.94 ± 0.36	< 0.82	> 21.97	> 22.13

Table 5.3 Continued..

ID	u (mag)	g (mag)	r (mag)	i (mag)	z (mag)	Hα Flux (10^{-15} erg s^{-1} cm^{-2})	*NUV* (mag)	*FUV* (mag)
(1)	(2)	(3)	(4)	(5)	(6)	(7)	(8)	(9)
2928	18.53 ± 0.13	17.24 ± 0.08	16.52 ± 0.14	16.48 ± 0.09	16.36 ± 0.15	< 4.41	> 20.49	> 20.63
2999	21.46 ± 0.32	20.51 ± 0.25	19.97 ± 0.18	19.9 ± 0.16	> 19.55	< 0.63	> 22.02	> 22.01
3005	18.46 ± 0.11	17.4 ± 0.05	16.82 ± 0.08	16.67 ± 0.06	16.62 ± 0.1	< 6.73	> 20.44	> 21.16
3088	> 18.17	17.28 ± 0.08	16.94 ± 0.12	16.6 ± 0.13	16.36 ± 0.19	< 5.4	> 19.9	> 20.33
3103	17.73 ± 0.1	16.58 ± 0.05	16.05 ± 0.1	15.87 ± 0.07	15.74 ± 0.1	< 13.07	> 19.79	> 20.18
3116	> 24.41	23.9 ± 0.32	> 23.23	> 22.15	> 21.46	< 0.03	> 25.87	> 25.01
3128	19.42 ± 0.1	18.32 ± 0.14	17.8 ± 0.08	17.66 ± 0.15	17.6 ± 0.16	< 2.09	> 20.93	> 20.74
3146	> 18.89	18.25 ± 0.16	17.22 ± 0.18	17.48 ± 0.22	> 17.03	< 13.56	> 20.29	> 19.85
3190	> 19.61	19.17 ± 0.26	18.58 ± 0.29	18.48 ± 0.29	> 17.16	< 1.65	> 21.8	> 20.84
3225	> 21.09	21.12 ± 0.25	> 20.34	> 20.12	> 19.71	< 0.94	> 23.08	> 22.64
3233	> 21.67	20.9 ± 0.25	20.17 ± 0.32	> 19.9	> 19.74	< 0.94	> 22.95	> 22.17
3245	18.47 ± 0.08	17.37 ± 0.05	–	16.69 ± 0.1	16.55 ± 0.15	–	> 20.28	> 18.19
3254	18.92 ± 0.14	17.73 ± 0.06	17.1 ± 0.06	17.04 ± 0.08	16.89 ± 0.15	< 1.39	> 20.81	> 19.52
3265	19.92 ± 0.11	18.95 ± 0.06	18.32 ± 0.1	18.26 ± 0.14	18.16 ± 0.29	< 1.79	> 21.64	> 21.59
3272	17.46 ± 0.34	16.44 ± 0.11	15.66 ± 0.18	15.51 ± 0.14	15.5 ± 0.16	< 32.83	> 19.06	> 18.69
3297	19.26 ± 0.3	18.11 ± 0.15	17.45 ± 0.07	17.39 ± 0.08	17.28 ± 0.12	< 1.56	> 20.0	> 20.11
3300	18.96 ± 0.16	17.92 ± 0.11	17.38 ± 0.16	17.26 ± 0.14	17.41 ± 0.36	< 1.21	> 20.72	> 20.59
3356	> 19.75	18.76 ± 0.14	18.24 ± 0.12	18.24 ± 0.18	17.89 ± 0.29	< 2.01	> 20.85	> 19.49
3365	> 20.15	20.2 ± 0.29	–	> 19.51	> 18.11	–	> 21.31	> 22.16
3379	20.02 ± 0.22	19.04 ± 0.16	> 18.21	> 18.39	> 17.45	< 2.99	> 21.27	> 20.78
3404	> 19.75	19.12 ± 0.19	–	18.62 ± 0.24	> 18.03	–	> 21.17	> 20.97
3451	> 20.24	19.4 ± 0.22	> 18.43	18.8 ± 0.24	> 17.6	< 5.97	> 21.86	–
3477	> 15.87	> 16.58	> 14.91	> 15.86	> 14.87	< 91.25	> 17.47	–
3481	> 18.28	16.88 ± 0.05	16.12 ± 0.05	16.02 ± 0.07	15.72 ± 0.16	< 7.52	> 19.68	> 19.62
3520	18.23 ± 0.14	17.08 ± 0.1	16.44 ± 0.08	16.26 ± 0.1	15.96 ± 0.18	< 4.25	> 20.43	> 20.49
3523	> 20.5	20.54 ± 0.28	19.76 ± 0.37	> 19.2	> 18.84	< 0.83	> 21.31	> 21.48

Table 5.3 Continued..

ID	u	g	r	i	z	Hα Flux	NUV	FUV
	(mag)	(mag)	(mag)	(mag)	(mag)	(10^{-15} erg s^{-1} cm^{-2})	(mag)	(mag)
(1)	(2)	(3)	(4)	(5)	(6)	(7)	(8)	(9)
3539	> 18.27	17.32 ± 0.12	16.64 ± 0.08	16.38 ± 0.18	16.2 ± 0.2	< 4.88	> 19.11	> 19.97
3543	18.6 ± 0.2	17.84 ± 0.12	17.49 ± 0.13	17.51 ± 0.2	17.29 ± 0.28	< 2.73	20.1 ± 0.2	> 20.66
3548	16.91 ± 0.05	15.71 ± 0.05	–	14.85 ± 0.05	14.71 ± 0.05	–	19.93 ± 0.25	> 20.82
3561	19.58 ± 0.18	18.4 ± 0.11	17.59 ± 0.13	17.42 ± 0.28	> 17.12	< 1.98	> 20.77	> 21.05
3578	12.16 ± 0.12	11.16 ± 0.05	10.57 ± 0.05	10.32 ± 0.05	10.09 ± 0.05	492.29 ± 51.2	–	–
3589	18.48 ± 0.16	17.88 ± 0.17	17.7 ± 0.16	17.74 ± 0.24	> 17.88	< 3.6	19.57 ± 0.08	19.84 ± 0.06
3590	19.19 ± 0.21	18.12 ± 0.1	17.44 ± 0.08	17.24 ± 0.1	17.1 ± 0.18	< 2.23	> 21.01	–
3599	> 19.14	18.42 ± 0.15	17.9 ± 0.18	17.64 ± 0.18	17.58 ± 0.18	< 2.71	> 21.16	> 21.41
3633	> 20.69	20.03 ± 0.19	–	19.27 ± 0.17	> 19.2	–	> 21.94	> 21.58
3659	> 20.9	21.0 ± 0.32	> 20.34	20.12 ± 0.28	> 19.51	< 1.1	> 22.84	> 22.9

5.5. Preliminary analysis

Results from the photometric measurements of the sample presented above give the global properties of these galaxies. In the following subsections, I discuss few such properties and compare them with similar results from the literature. These are only the preliminary results from an ongoing work (Junais et al. in preparation), which I plan to complete by the end of my thesis (September 2021).

5.5.1. Colour distribution

Figure 5.11 shows the distribution of the measured $g-i$ colour of the sample from Table 5.3. We can see that the distribution of the UDG sub-population peaks at $g-i = 0.72 \pm 0.17$ mag, corresponding to the range commonly found for red UDGs in clusters (van der Burg et al. 2016). For the Diffuse and Outlier sub-population of the sample, only a handful of sources have detected $g-i$ colours, making it hard to draw any conclusion on them.

In a recent work, Tanoglidis et al. (2021) studied an extensive sample of LSBs obtained from the Dark Energy Survey covering an area of ~5000 deg^2 on the Southern hemisphere. The $g-i$ colour distribution of their sample was found to bimodal, with a red and blue population of LSBs. A similar distribution was also found by Greco et al. (2018) on another sample of LSBs obtained from Subaru Hyper Suprime-Cam data. Figure 5.11 shows the separation of red and blue LSBs from Tanoglidis et al. (2021) at $g-i = 0.6$ mag. The distribution of my sample compared to this lies mostly on the red end of the LSB population, with only very few sources having bluer colours similar to those commonly found in group environments (Prole et al. 2019).

5.5.2. Gradient in colour

I investigated the dependence of the measured colours with respect to the spatial distribution of the galaxies in the cluster. Figure 5.12 shows the variation of the $g-i$ and $u-r$ colours of the sample with respect to the distance of each source from the Virgo cluster centre. There is a small indication of a gradient in colour (more prominent in $u-r$ than in $g-i$), where redder sources are located more towards the cluster centre, whereas bluer sources are towards the periphery. This visual impression was indeed verified by an error-weighted least-square fitting of the sample. The best-fit lines obtained are:

$$\begin{aligned} g-i &= 0.8 - 0.03\, D_{\rm cluster} \\ u-r &= 1.8 - 0.25\, D_{\rm cluster} \end{aligned} \tag{5.4}$$

where $D_{\rm cluster}$ is the projected distance of the galaxy from the cluster centre in Mpc. Considering the large scatter in the colours, the observed gradients are minimal. Nevertheless, from Fig. 5.12 we can observe that the galaxies with the most bluer colours in the sample are located only beyond a distance of ~0.75 Mpc from the cluster centre, indicating a role of the cluster environment in shaping the evolution of these galaxies. This is also similar to the colour gradient observed by Román & Trujillo (2017), where UDGs with bluer colours tend to reside in low-density cluster regions.

5.5.3. Colour-Magnitude Diagram

Colour-magnitude diagrams are an excellent tool to study galaxy properties. Figure 5.13 shows the colour-magnitude diagram of my sample with respect to the NUV and r-band magnitudes. NUV being a good tracer of recent star formation and r-band related to the old stellar population, the $NUV-r$ colour acts as a proxy for the specific star formation rate in galaxies. From Fig. 5.13, we can see that majority of the sources in my sample are non-detected in UV with only an upper limit in the $NUV-r$ colour. Still, this provides strong constraints on the recent star formation rates within these sources. The sample mainly lies along with the population of the low-mass quiescent red sequence of galaxies, as defined by Singh et al. (2019).

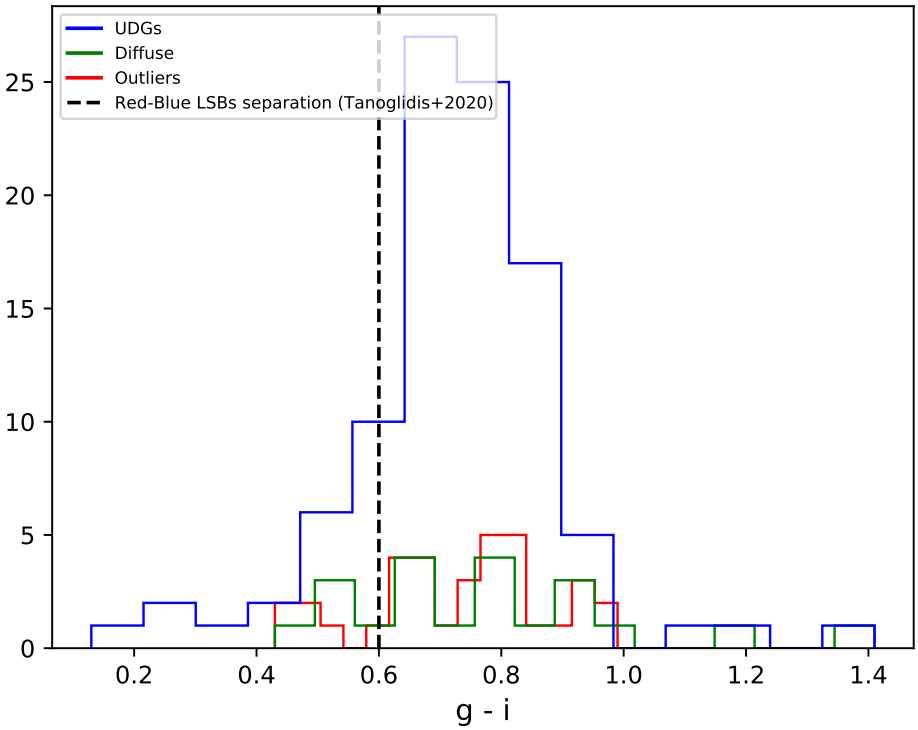

Figure 5.11.: $g - i$ colour distribution of the sample. The blue, green and red solid lines show the UDGs, Diffuse and Outlier sub-samples. Sources with only upper-limits on the colour are removed from this distribution. The black dashed line marks the separation of red and blue LSBs from the Dark Energy Survey (DES; Tanoglidis et al. 2021).

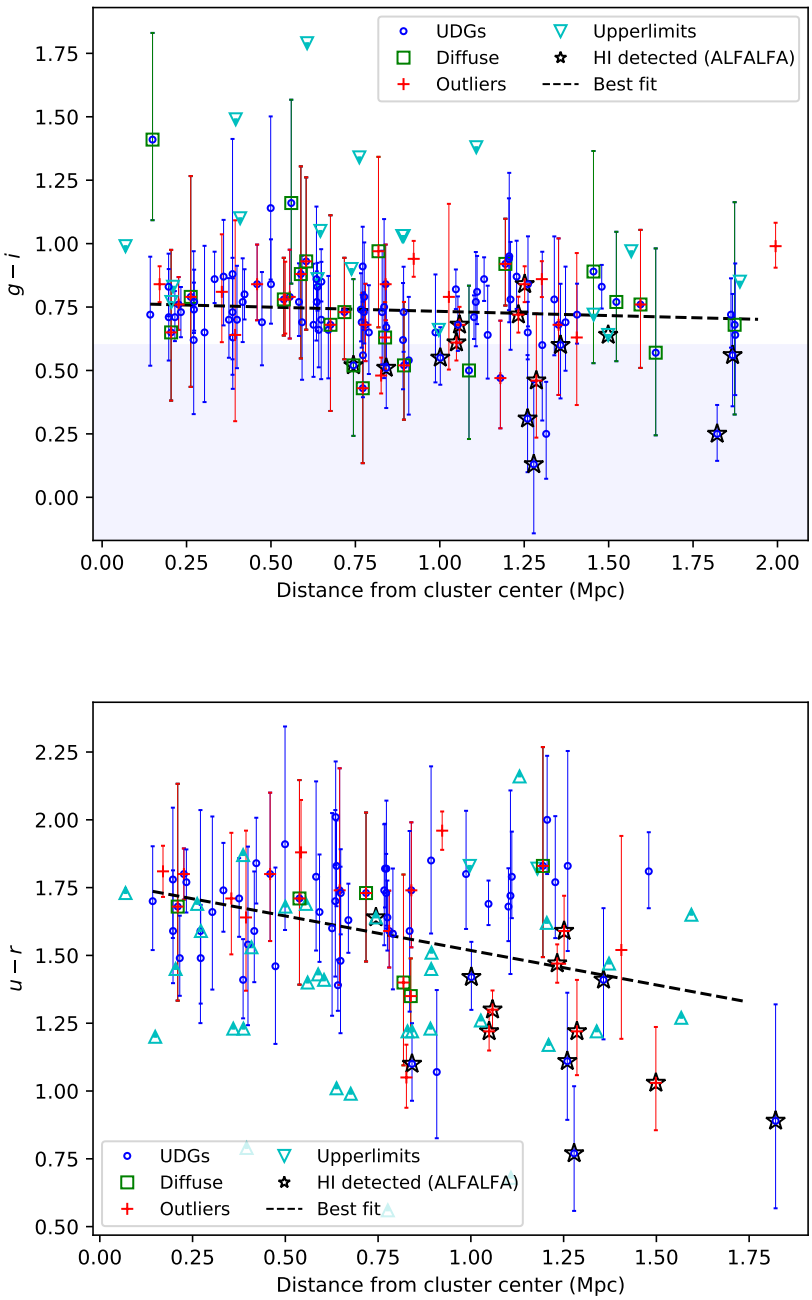

Figure 5.12.: $g-i$ (top panel) and $u-r$ (bottom panel) colour distribution of the sample as a function of their distance from the Virgo cluster centre (distance from M87). The UDGs, Diffuse and Outlier sub-sumples are marked with the open blue circles, green squares and red crosses, respectively. The upper-limits in color are shown as open triangles. The black dashed lines are the error-weighted best-fit line obtained for each distribution. The blue shaded region in the top panel marks the region of blue LSBs with $g-i<0.6$ mag (Greco et al. 2018; Tanoglidis et al. 2021). The black star symbols are the sources with H I detection in ALFALFA survey (see Sect. 5.6).

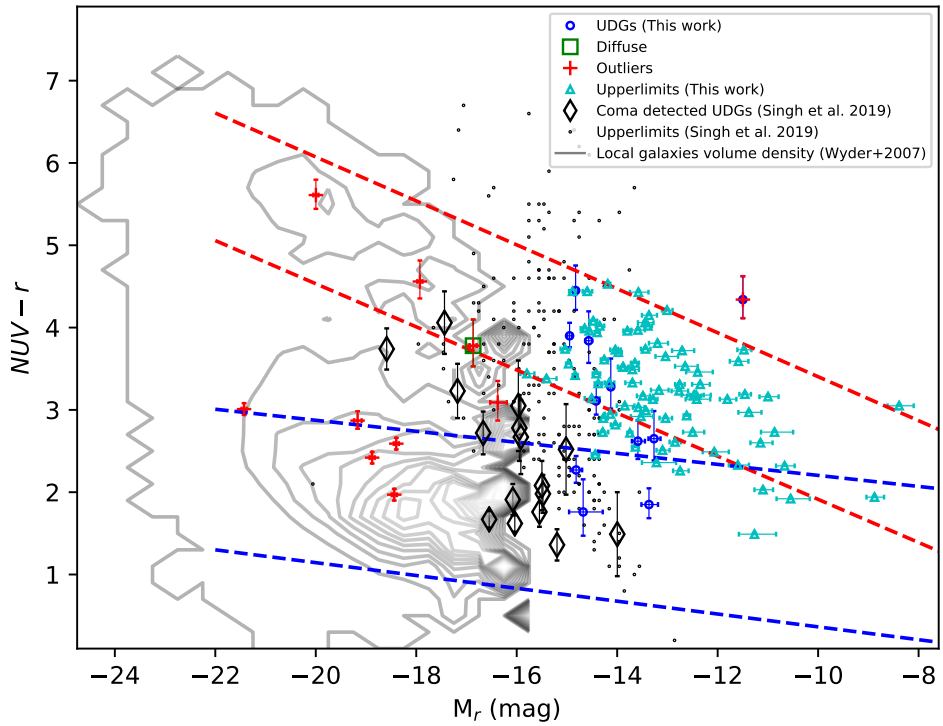

Figure 5.13.: $NUV - r$ versus r-band absolute magnitude colour-magnitude-diagram. The symbols for the sample are the same as Fig. 5.12. The black diamond symbols and tiny dots are the detected Coma cluster UDGs and upper limits, respectively from Singh et al. (2019), along with a separation of red and blue sequence galaxies from their sample (shown as red and blue dashed lines). The grey iso-density contours represent the volume density of local galaxies from Wyder et al. (2007).

For the few regions detected in NUV, the UDG and the outlier sub-populations contain both red and blue sources. However, the Outlier sources generally seem to be on the massive end of the colour-magnitude diagram, close to the local population of galaxies from Wyder et al. (2007).

I compared these results with the work from Singh et al. (2019) on a population of UDGs in the Coma cluster. They also obtained a similar result where most of their UDGs were undetected in NUV, with few detections lying along the blue sequence (see Fig. 5.13). This is not surprising, considering UDGs in clusters are predominantly redder. Moreover, the galaxies in my sample extend to much fainter, low mass galaxies, than the UDG sample of Singh et al. (2019), owing to the higher depth of the NGVS data and the proximity of the Virgo cluster.

5.6. A sub-sample: cross-correlation with H I from ALFALFA

The Arecibo Legacy Fast ALFA (ALFALFA; Haynes et al. 2018) survey is a blind extragalactic H I survey covering a wide area of the sky up to ~7000 deg^2. The high sensitivity and sky coverage of ALFALFA makes it suitable for providing the H I content of a cosmologically significant sample of ~ 31500 extragalactic sources.

To investigate the amount of H I gas in the sample of LSBs I study, I made a crossmatch of the ALFALFA H I catalogue with the sources in my sample. A total of 14 sources were identified with ALFALFA counterparts within a beam size of ~3.5′ (the original beam size of ALFALFA survey is 3.8′ × 3.3′) and corresponding to the Virgo distance of 16.5 Mpc. Table 5.4 and Fig. 5.14 show this sub-sample of LSBs with ALFALFA H I detection.

The H I content of the 14 identified sources ranges from $7.3 < \log M_{HI} < 9.6$ solar masses. Five out of them with large H I content are spirals belonging to the Outlier sub-population (AGC 7537, 7546, 7557, 7727 and 7965 from Table 5.4). The rest of the sources belongs to the UDG population with H I detection either on-source or offset from the galaxy (7 out of the 9 UDGs have H I detection outside their effective radii). This is particularly interesting when the existence of H I bearing UDGs are largely observed in many recent works (Leisman et al. 2017; Janowiecki et al. 2019; Prole et al. 2019). Moreover, from Fig. 5.12 we can see that the H I detected sources from my sample are all predominantly blue and located far from the cluster centre ($D_{\rm cluster} > 0.75$ Mpc). This point towards environmental effects (e.g. ram-pressure stripping) that shape the evolution of these galaxies. Such effects will be discussed in more detail in Chapter 6 and 7. One particularly interesting source was identified (AGC 226178 from Table 5.4) during the inspection of my sample of LSBs, which shows clear indications of a tail of star-forming regions with an H I cloud found in the vicinity of a UDG (ID 3543). I dedicate Chapter 7 for a detailed study on this system.

5.7. Conclusions

The main outline of the work presented in this chapter is as follows:

- Using a multi-wavelength set of data obtained from different Virgo cluster surveys, I created a sample of 135 low surface brightness galaxies. The sample includes various LSB sub-populations (UDGs, Diffuse galaxies and Outliers) based on different selection criteria existing in the literature.
- I performed photometric measurements on the sample to obtain radial surface brightness profiles, sizes, magnitudes and colours for each source.
- Comparing the effective radii (R_e) of the galaxies I measured with that of the initial values from the NGVS catalogue reveals that for very faint sources, the measured R_e differ from each other. This will impact the UDG selection criteria generally used in the literature, which uses an arbitrary cut on the R_e, which can lead to over-estimation or under-estimation of the UDG population. The combination of various LSB selection criteria as used in this work will be helpful in such cases.
- The distribution of optical colours in the sample indicates that the LSBs in my sample, especially the UDG sub-population, are predominantly red, consistent with what generally found for UDGs in clusters.
- There is also an indication of a slight colour gradient in the sample with respect to the distance from the cluster centre. Galaxies towards the edge of the cluster are bluer than the rest of the population, similar to the population of blue UDGs found in groups, suggesting environmental effects.

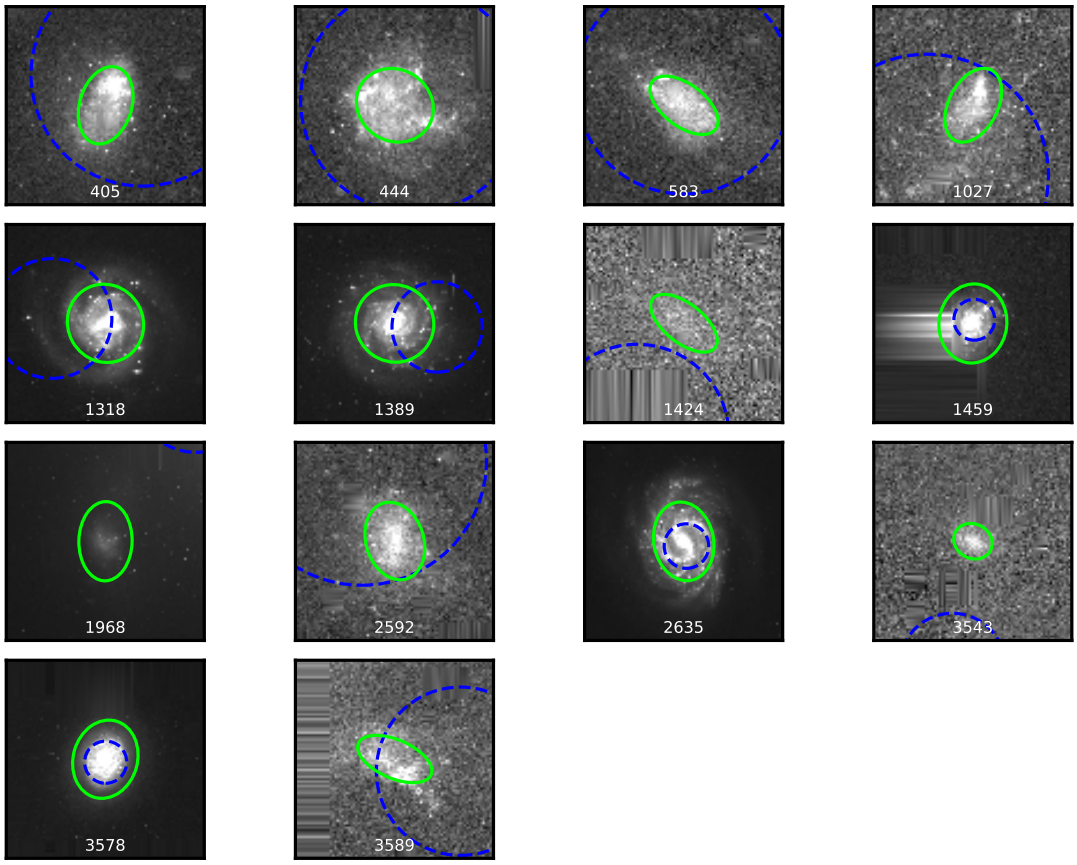

Figure 5.14.: Sub-sample of LSBs with ALFALFA H I detection is given in Table 5.4. The greyscale images are the NGVS g-band mask applied images. The green ellipse shows the effective radius and position angle of the galaxy from the NGVS catalogue. The blue dashed circles marks the position of the ALFALFA H I centroid. For illustrative purpose, here, the ALFALFA centroid is depicted with a size of $1'$ (diameter of the blue dashed circles), unlike the original ALFALFA beam of $\sim 3.5'$ which covers a larger extend.

ID	AGC ID	Distance (Mpc)	$\log M_{HI}$ ($M_\odot$)	Offset
(1)	(2)	(3)	(4)	(5)
405	220366	16.70 ± 1.30	7.95 ± 0.08	1.22
444	220383	16.50 ± 1.20	8.26 ± 0.07	0.49
583	220435	16.70 ± 1.30	7.59 ± 0.09	0.5
1027	227889	16.60 ± 4.30	7.30 ± 0.23	2.12
1318*	7537	16.40 ± 1.20	9.01 ± 0.08	1.35
1389*	7546	16.40 ± 1.20	9.12 ± 0.08	1.08
1424	220597	16.70 ± 1.20	7.70 ± 0.08	3.09
1459*	7557	16.40 ± 1.30	9.22 ± 0.08	0.1
1968	227874	16.60 ± 4.30	7.89 ± 0.23	4.45
2592	223873	16.50 ± 1.20	7.44 ± 0.08	2.21
2635*	7727	14.80 ± 1.50	9.57 ± 0.10	0.14
3543	226178	16.50 ± 2.30	7.60 ± 0.13	6.39
3578*	7965	16.70 ± 1.20	8.74 ± 0.08	0.07
3589	221026	16.70 ± 1.20	8.57 ± 0.08	1.7

Table 5.4.: Sub-sample of LSBs at the distance of Virgo cluster with H I detection in the ALFALFA survey (Haynes et al. 2018). Column details: (1) Name of the source from my LSB sample (spiral galaxies are marked with $\star$ symbol); (2) Arecibo General Catalogue (AGC) ID; (3) Distance of the source based on ALFALFA H I measurements; (4) H I mass; (5) Offset of the ALFALFA beam centroid with respect to the NGVS coordinate of the source. This offset is normalised with the effective radius of the galaxy given in Table 5.2 (an offset > 1 indicates that the H I centroid is outside the effective radius of the galaxy).

- Around 10% of sources in the sample have associated counterparts with H I measurements. More interestingly, all of these H I detected sources are located towards the edge of the cluster and have bluer colours. Combining the colour gradients with these H I detection raises an essential question on the role of cluster environment in shaping the evolution of LSBs in my sample.

6. Galaxy evolution modelling

Summary

6.1 The framework of the models . . . 119
6.1.1 Main ingredients of the Milky Way model . . . 119
6.1.2 Extension to other disk galaxies . . . 120
6.1.3 Modelling the effect of ram-pressure stripping . . . 121
6.2 Grid of parameters . . . 122
6.3 Fitting of models . . . 123
6.4 Results . . . 124
6.4.1 Distribution of V_C, λ and t_{rps} . . . 124
6.4.2 Colour and t_{rps} gradient . . . 127
6.4.3 Evolution of gas mass, stellar mass and star formation rate . . . 127
6.5 Conclusions . . . 129

6.1. The framework of the models

In this chapter, I describe the main ingredients and results of the chemo-spectrophotometric models I used to analyse the observed multi-wavelength profiles of the sample of LSB galaxies discussed in Chapter 5. Initially, these models were developed and calibrated to reproduce several observed properties of the Milky Way (Boissier & Prantzos 1999). Then they were generalised to other disk galaxies of different sizes and masses using several scaling relations based on the ΛCDM disk formation scenario (Boissier & Prantzos 2000). Later, Boselli et al. (2006) introduced in the same approach the effect of ram-pressure stripping on disk galaxies to reproduce several observed properties of galaxies in the cluster environment (Boselli et al. 2008a,b, 2014).

In the Sections 6.1.1, 6.1.2 and 6.1.3, I discuss the basic formalism used for the construction of the models.

6.1.1. Main ingredients of the Milky Way model

Boissier & Prantzos (1999) modelled the Milky Way (MW) disk as several independently evolving concentric rings which are gradually built up by the accretion of primordial gas. Despite the assumption of independently evolving zones, the model is successful in reproducing the main observed properties of the MW. Models including radial transfer were also developed in recent years, especially to reproduce the dispersion in the properties of the MW disk (Kubryk et al. 2015). However, the simplicity and success of the Boissier & Prantzos (2000) models motivate us to use them in this work.

The chemical evolution of each zone in Boissier & Prantzos (1999) models is determined by two key ingredients, the star formation rate (SFR) and the gas infall rate, assuming a Kroupa (2001) IMF[1].

In the models, the SFR surface density at each radius and time, $\Sigma_{SFR}(t,r)$, is given by a modulated Schmidt-type law proportional to the local gas surface density $\Sigma_g(t,r)$ as follows:

[1]The original models were made using Kroupa et al. (1993) IMF, but in this work, we use the more recent Kroupa (2001) IMF.

$$\Sigma_{SFR}(t,r) = \alpha \Sigma_g(t,r)^n V(r) r^{-1} \tag{6.1}$$

where $V(r)$ is the circular velocity at radius r. The term $V(r)r^{-1}$ takes into account the variation of the SFR in disk galaxies as a result of the frequency of the periodic passage of spiral density waves that induce star formation (Wyse & Silk 1989). However, some other theories also produce similar dynamical factors affecting the SFR (Boissier 2013b, and references therein). The coefficient α was originally fixed to $\alpha = 0.00364$ in order to reproduce the current local gas fraction in the solar neighbourhood, and $n = 1.5$ was chosen to reproduce radial trends. Later, Boissier et al. (2003) empirically determined $\alpha = 0.00263$ and $n = 1.48$ from a sample of nearby galaxies. In this work, we adopt these values.

The gas infall rate is assumed to be exponentially decreasing in time, i.e.

$$f(t,r) = A(r) \exp^{-t/\tau(r)} \tag{6.2}$$

with the gas accretion timescale $\tau(r)$ increasing with radius, from $\tau(r = 1\,kpc) = 1$ Gyr to $\tau(r = 17\,kpc) = 15$ Gyr, allowing the inside-out formation of the disks. At $r = 8$ kpc, τ is set to be equal to 7 Gyr to reproduce the metallicity distribution of the G-dwarf stars in the solar neighbourhood. The coefficient $A(r)$ is constructed in such a way that the total integrated gas infall rate from time $t = 0$ to the current time $t = 13.5$ Gyr, reproduces the observed total mass profile of the MW disk.

The disk scale length and central mass surface density of the MW disk is fixed from the observations as $R_{d,MW} = 2.6$ kpc and $\Sigma_{0,MW} = 1150\,M_\odot$ pc^{-2}, respectively.

With the following basic framework discussed above, Boissier & Prantzos (1999) showed that these models successfully reproduce the observables in the solar neighbourhood, as well as various other properties of the MW disk, including the radial profile of the gas surface density, gas-phase oxygen abundance, SFR and photometric profiles at different bands.

6.1.2. Extension to other disk galaxies

Following the success of the Boissier & Prantzos (1999) MW model, Boissier & Prantzos (2000) extended them to other disk galaxies in general, using scaling relations from Mo et al. (1998) based on the ΛCDM galaxy disk formation scenario. According to this scenario, primordial density fluctuations creates DM haloes of mass M and baryonic gas condenses within them to form discs of maximum circular velocity V_C. The halo mass and circular velocity are related by,

$$V_C^3 = 10GH(z)M \tag{6.3}$$

where $H(z)$ is the Hubble parameter at redshift z of the halo formation, and G is the universal gravitational constant.

To obtain the mass of the disk (M_d), it is assumed that the disk mass is a fraction of the halo mass, where

$$M_d = m_d M. \tag{6.4}$$

For an exponential disk, with surface density profile given by

$$\Sigma(r) = \Sigma_0 \exp^{-r/R_d} \tag{6.5}$$

the disc mass is given by

$$M_d = 2\pi\Sigma_0 R_d^2 \tag{6.6}$$

where Σ_0 and R_d are the central surface density and scalelength, respectively. Combining Eqns. (6.3), (6.4) and (6.6), one can relate the parameters Σ_0 and R_d to the circular velocity of the disc V_C. However, mass is not the only quantity determining the properties of halo, there is also their angular momentum. This quantity is introduced as the spin parameter λ, related to the halo mass M through

$$\lambda = J|E|^{1/2}G^{-1}M^{-5/2} \tag{6.7}$$

where the total energy of the halo is given by

$$E = -\frac{MV_C^2}{2}. \tag{6.8}$$

Finally, assuming that the angular momentum of the disk (J_d) is a fraction j_d of that of the halo, we get:

$$J = 2M_d V_C R_d / j_d \tag{6.9}$$

Using Eqns. (6.3 to 6.9), the disk parameters Σ_0 and R_d can be now uniquely expressed in terms of the V_C and λ as:

$$R_d = \frac{1}{10\sqrt{2}}\lambda V_C \left(\frac{j_d}{m_d}\right) H(z)^{-1} \tag{6.10}$$

and

$$\Sigma_0 = \frac{10}{\pi G} m_d \lambda^{-2} V_C \left(\frac{j_d}{m_d}\right)^{-2} H(z) \tag{6.11}$$

In the framework of the models, it is assumed that m_d and j_d are constants with a ratio $j_d/m_d = 1$, implying that the specific angular momentum of the disk and halo are equal. This assumption is necessary to reproduce the disk properties from observations. Moreover, the effects of the formation time of the disc arising through the term $H(z)$ in Eqns. (6.10) and (6.11) are also neglected. In these models, the history of the galaxies is instead set by the infall temporal dependence. The infall may occur at different times, and the "formation" may be defined in various ways (e.g. epoch the first star appear, epoch half of the stars were formed). Here we assume all the galaxies start their star formation history at the same given time ($t = 0$), a few hundred Myr after the big bang up to an age now of $t = 13.5$ Gyr. Under the these observationally motivated assumptions, the parameters Σ_0 and R_d of any disk galaxy can be obtained from the corresponding MW values as follows:

$$R_d = R_{d,MW}\frac{V_C}{V_{C,MW}}\left(\frac{\lambda}{\lambda_{MW}}\right) \tag{6.12}$$

$$\Sigma_0 = \Sigma_{0,MW}\frac{V_C}{V_{C,MW}}\left(\frac{\lambda}{\lambda_{MW}}\right)^{-2} \tag{6.13}$$

where $V_{C,MW} = 220$ km s^{-1} and $\lambda_{MW} = 0.03$ (Boissier & Prantzos 2000).

By the construction of these models, any unperturbed disk galaxy can be easily modelled using only two free parameters, V_C and λ, to reproduce their observed properties. However, this requires several underlying assumptions where we adopt a universal star formation law and gas infall by generalising the MW properties to all the disk galaxies. Indeed many works show that these simple assumptions with 2 parameters are sufficient to reproduce the properties of various samples of galaxies as demonstrated by Boissier et al. (2003) and Muñoz-Mateos et al. (2011).

6.1.3. Modelling the effect of ram-pressure stripping

Boselli et al. (2006) modified the chemical and spectrophotometric evolution models for unperturbed galaxies discussed in Sect. 6.1.1 and 6.1.2, to implement the effect of ram-pressure stripping (RPS) experienced by galaxies in dense cluster environments. With the addition of RPS, Boselli et al. (2006) successfully reproduced the properties of anaemic and dwarf galaxies located in the Virgo Cluster.

The RPS scenario is modelled based on Vollmer et al. (2001), where a galaxy is modelled as crossing the intergalactic medium (IGM) of a cluster in an elliptical orbit. The galaxy experiences a ram-pressure

exerted by the IGM, which varies with time following a Gaussian profile, where the peak of ram-pressure is at $t = t_{rps}$ when the galaxy crosses the dense cluster core at the highest velocity. The models assume that the gas in the galaxy is removed at a rate of $\epsilon\Sigma_{gas}/\Sigma_{potential}$, which is proportional to the galaxy gas column density at any given time but is modulated by the potential of the galaxy, measured by the total (baryonic) local density. ϵ is linked to the RPS efficiency and follows a similar Gaussian with a maximum value ϵ_0 at the peak time t_{rps}, assuming that the current age of the galaxy is 13.5 Gyr. This time variation of ϵ is chosen to mimic the variation of RPS obtained by Vollmer et al. (2001). This simplified but physically motivated scenario allows one to easily model the gas removal from a galaxy experiencing ram-pressure using only two free parameters (t_{rps} and ϵ_0). However, to further reduce the number of free parameters, and to reproduce the properties of an originally anaemic galaxy, Boselli et al. (2006) fixed the peak efficiency as $\epsilon_0 = 1.2\,M_\odot$ kpc^{-2} yr^{-1} (which was later adopted in Boselli et al. 2008a), and the average FWHM of the Gaussian variation to be ≃150 Myr, similar to Vollmer et al. (2001). The fact that the ϵ_0 and the Gaussian FWHM are fixed is clearly an over-simplification of the problem. Indeed these parameters should depend on the precise orbit within the cluster. However, it is chosen to explore a large grid of models for the other parameters, within reasonable computational time, discussed in Sect. 6.2. Moreover, in Junais et al. (2021) we also investigated the possible effect of a variation in the ϵ_0 and FWHM values and found that it changed very little the conclusion (e.g. t_{rps}, V_C and λ were modified by less than 0.1 Gyr, 2 km s^{-1} and 0.01, respectively; see Sect. 7.3)

Therefore, a perturbed disk galaxy undergoing RPS can be modelled using only three free parameters, V_C, λ and t_{rps}, which will be the basis of the modelling of LSB galaxies in the Virgo cluster discussed in this work.

6.2. Grid of parameters

The original models from Boissier & Prantzos (2000) consisted of a grid of 25 models with V_C ranging from 80 – 360 km s^{-1} with a spacing $\Delta V_C = 70$ km s^{-1} and λ values from 0.01 – 0.09 with $\Delta\lambda = 0.02$. Later Boissier et al. (2003) extended them to larger spin values ($\lambda = 0.15$ and 0.21) to reproduce the properties of LSB galaxies. Then Muñoz-Mateos et al. (2011) used a finer grid of models with V_C values ranging from 130 to 250 km s^{-1} in steps of 10 km s^{-1}, and a few extra values 40, 80, 290 and 360 km s^{-1}. For spin parameter, they adopted an interval of $0.02 \leq \lambda \leq 0.09$ in steps of 0.01, along with few extra values of $\lambda = 0.10$, 0.15 and 0.20 to take in to account the LSB population found by Boissier et al. (2003). The RPS model Boselli et al. (2006) was done using one typical spin ($\lambda = 0.05$).

However, a large grid including both LSBs (i.e., very large spins) and RPS has not been computed so far. For the study of the sample of LSBs in Virgo cluster discussed in this work, we prepared a very large grid with the same models, but covering a vast range of spin, velocity and RPS parameters as shown in Table. 6.1. Three types of grids were prepared: coarse, fine and hyperfine grids. The coarse grid covers the parameter space of both the HSB and LSB galaxies, but with a larger spacing among each model. The large extend of λ and V_C values in this grid are motivated from the work of Boissier et al. (2016) on the extended disk of Malin 1, where they obtained the values of spin and velocity of Malin 1 up to 0.6 and 600 km s^{-1}, respectively. The t_{rps} values for all the grids were chosen such that the models include RPS events ranging from very distant past ($t_{rps} = 8$ Gyr) to the future ($t_{rps} = 13.6$ Gyr), where the current age assumed to be $t_{rps} = 13.5$ Gyr.

Considering the LSB nature of the galaxies in my sample, their physical parameters mainly lie in the low velocity extended spin regime (Boissier et al. 2003). Therefore, we created a fine resolution grid within our coarse grid to precisely model the most probable parameter range for the sample ($V_C = 20$ to 220 km s^{-1} with $\Delta V_C = 2$ km s^{-1}; $\lambda = 0.01$ to 0.40 with $\Delta\lambda = 0.01$). This fine grid was later extended to a hyper-fine grid with $\Delta t_{rps} = 0.01$ Gyr for the very recent RPS values (t_{rps} from 13.4 to 13.6 Gyr) where the gas removal due to RPS is closely connected to the detection in Hα with a short timescale of 10 Myr. Moreover, for all the grids (coarse, fine and hyper-fine) we also included models without RPS, to account for sources that haven't experienced RPS events. In this way, we assembled our entire grid with a total of 310550 models to study my sample of LSBs (see Table. 6.1 for the details on the grid).

Grid type	V_C (km s^{-1})		λ		t_{rps} (Gyr)	
	Range	ΔV_C	Range	$\Delta\lambda$	Range	Δt_{rps}
Coarse	20 – 600	20	0.01 – 0.80	0.1	8.0 – 13.5	0.5
Fine	20 – 220	2	0.01 – 0.40	0.01	8.0 – 13.6	0.1
Hyper-fine	20 – 220	2	0.01 – 0.40	0.01	13.40 – 13.60	0.01

Table 6.1.: Grids of V_C, λ and t_{rps} values used for the modelling in this work. For the three different types of grids, the range and corresponding spacing of each parameter are provided as separate columns. Apart from the models with RPS, all the grids also include models without RPS.

Most of the models used in this work were prepared by Samuel Boissier, as it is his expertise from the development of the original models in Boissier & Prantzos (1999) and Boissier & Prantzos (2000). However, I also used the code to independently check the results and make some tests on the variation of properties in different models. The model runs for the entire grid were computationally time-consuming where the outputs from all the models (e.g. surface brightness profiles, gas mass, stellar mass, metallicity) were created over the course of few months. This is also another reason for the choice of different types of grids with an uneven resolution, to limit the computation time required for the whole process. Once all the model runs were completed, I used them to compare with the observed surface brightness profiles of my sample to find the best fit model matching the observations. This is discussed in Sect. 6.3.

6.3. Fitting of models

To find the best model for each source in my sample, I performed a χ^2 fitting procedure of the observed surface brightness profiles from Chapter 5 with that of the surface brightness profiles from the models. For each source, a total χ^2 value was computed by comparing the observed profiles with a model in all the 8 photometric bands, until the last observed radius ($> 3\sigma$). This is given in Eqn. 6.14.

$$\chi^2 = \sum_{b=1}^{b=8} \sum_{r=1}^{r=r_{\rm last}} \left(\frac{\mu_{b,\rm obs}(r) - \mu_{b,\rm model}(r)}{\sigma_{b,\rm obs}(r)} \right)^2 \tag{6.14}$$

The χ^2 computation was done adopting a minimum error of 0.05 mag in the surface brightness profiles to take into account systematic uncertainties associated with the models (e.g., IMF, stellar tracks, stellar libraries). Any model violating the 3σ upper limits of the photometry was also rejected. However, here I also allowed a maximum tolerance of 0.1 mag above the 3σ upper limit to avoid rejecting a good model that only marginally violates one upper limit. Modifying this tolerance within a range of a few tenths of dex changes the best-fit parameters within their error bars.

The top panel of Fig. 6.1 shows an example of the χ^2 distribution obtained for the source ID 2143. The model corresponding to the minimum χ^2 value (χ^2_{min}) from this distribution gives the best-fit model. The 3σ uncertainty associated with the best-fit model parameters are also computed from this distribution following Avni (1976). In this way, I obtained the best fit models for all the sources and their corresponding uncertainties. Moreover, I also estimated the goodness of the fitting procedure by the reduced χ^2 values given as:

$$\chi^2_{\rm reduced} = \frac{\chi^2}{N_{\rm data} - 3} \tag{6.15}$$

where $N_{\rm data}$ is the total number of data points used for the χ^2 computation of a 3 parameter model

fit. The bottom panel of Fig. 6.1 show the distribution of the $\chi^2_{\rm reduced}$ for the full sample. The majority of the sample (~ 76%) have $\chi^2_{\rm reduced} < 5$, indicating a reasonable fit. For few sources (mainly among the Outlier and Diffuse sub-populations) with a very high or low number of data points, the fitting procedure leads to poor fits. This could be due to several reasons. Some of the Outliers have indeed non-disk surface brightness profiles (elliptical type or spirals with strong central components), leading to the failure of the models which were designed for discs. On the other hand, sources with profiles close to the sky level with very few data points also lead to poor fits. However, the quality of all the fits is reflected in the uncertainties computed for each of them, given in Table 6.2.

Figure 6.2 shows the surface brightness profiles of the source ID 2143 along with the best fit model given by $V_C = 58 \pm 2$ km s^{-1}, $\lambda = 0.09 \pm 0.01$ and $t_{rps} = 11.80 \pm 0.1$ Gyr. All the observed bands and upper limits are very well fitted by these models, except for NUV, where the best model slightly under predicts the NUV flux by ~ 0.5 mag. This could be attributed to the choice of IMF or the assumed RPS efficiency parameters to which NUV is sensitive. For the Hα and FUV, the best models respect well the observed upper limits. From these results, it is evident that only an extended low mass galaxy that had undergone an RPS event ~ 1.7 Gyr ago could reproduce the observed properties of this galaxy. The same models in the absence of an RPS event (shown as the green dashed line in Fig. 6.2) is well above the observed levels in all the bands.

6.4. Results

The detailed results from the model fitting for the full sample are given in Table 6.2. In this section, I analyse these results and the predictions from the models to investigate more on the nature of my sample. This is part of ongoing work (Junais et al. in preparation), where I will discuss the results more in detail.

6.4.1. Distribution of V_C, λ and t_{rps}

Figure 6.3 shows the distribution of the model parameters V_C, λ and t_{rps} obtained from the modelling of the sample. The uncertainties associated with these parameters (shown in Table 6.2) were also taken into account for this distribution. This was done using a Monte Carlo simulation of 10000 chains where I created pseudo sources corresponding to each source in my sample, with random parameter values generated based on a normal distribution around the best fit value and uncertainty.

The V_C distribution from Fig. 6.3 peaks along the range of low mass galaxies with a median velocity value of $V_{C,med} = 56$ km s^{-1}. The large velocity end of this distribution ($V_C > 100$ km s^{-1}) comprises very few sources, mostly among the Outlier sub-population.

On the other hand, the spin distribution indicates that the majority of the sources have large extended spins with a median value of $\lambda_{med} = 0.13$. This is consistent with the typical spins needed for LSB galaxies (Boissier et al. 2003). The very large spin tail ($\lambda > 0.4$) seen in this distribution is a resultant of the sources with poor fits and large uncertainties.

In the case of the t_{rps} distribution, almost all of the sources in the sample have undergone an RPS event in their lifetime (except for two sources - ID 3365 and 3477 from Table 6.2, having the best fit without RPS), peaking at a median t_{rps} value of 12.09 Gyr. This indicates that, although some sources are undergoing recent RPS events, the Virgo cluster LSBs on average experienced significant RPS events ~ 1.4 Gyr ago. This strong effect of the cluster environment in the past shaped the evolution of the sources in my sample and the properties we observe now.

In terms of the sub-populations (UDGs, Diffuse and Outliers), there is no evident difference in the V_C, λ or t_{rps} distributions among any of them, except Diffuse sources on average, have larger spins, what probably comes from their definition.

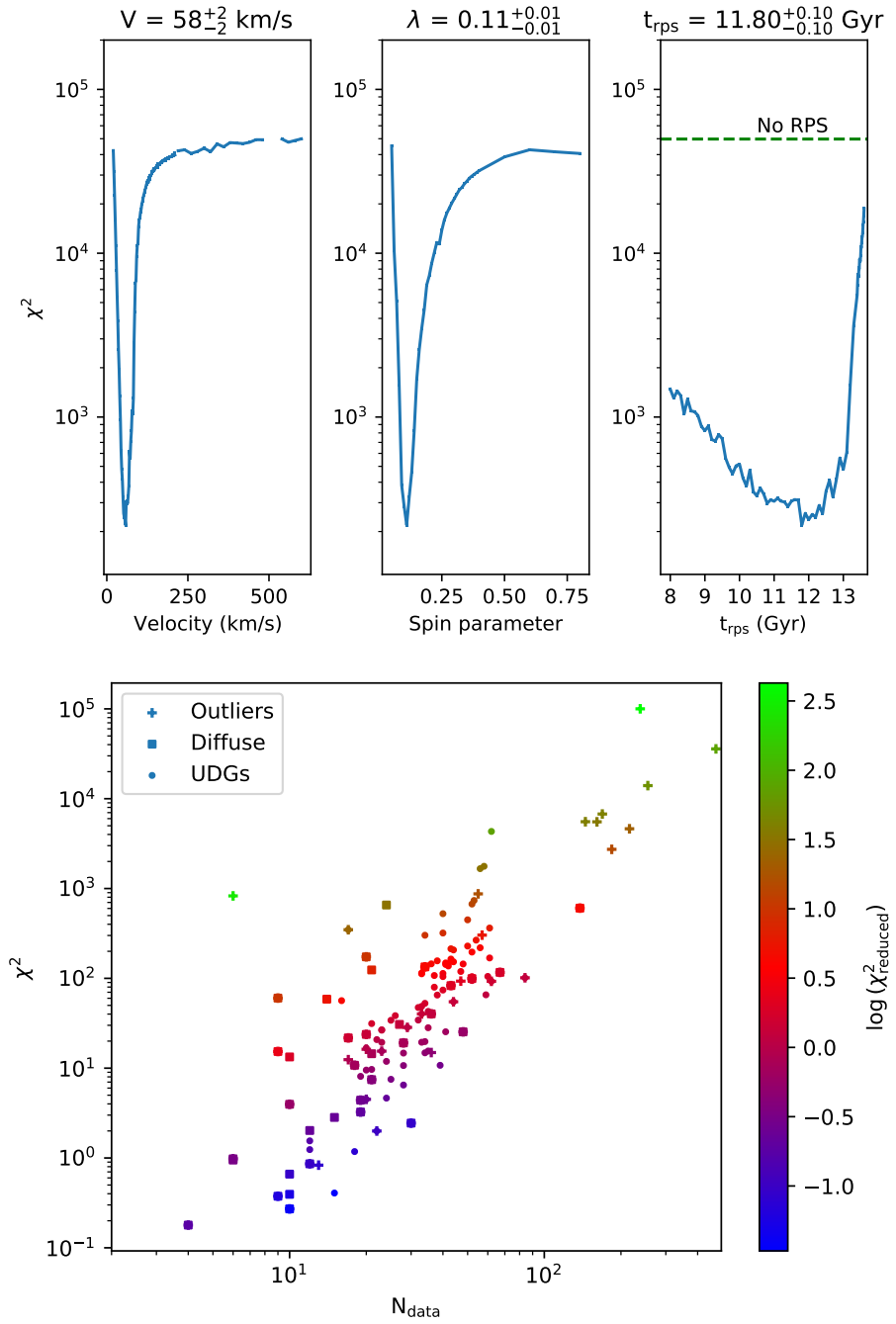

Figure 6.1.: *Top*: An example of χ^2 distribution for the determination of the best model parameters (V_C, λ, t_{rps}) for the source ID 2143. The best-fit parameters are given in the upper part of each panel. The given confidence limits (3σ) in each parameter are obtained following Avni (1976). The green horizontal dashed line in the right panel marks the χ^2 value corresponding to a model without RPS, keeping the same values of V_C and λ as in the best-fit model. *Bottom*: The χ^2 values of the full sample as a function of the total number of data used in the χ^2 computation. The colour bar shows the goodness of the fit indicated by the reduced χ^2 value for each source.

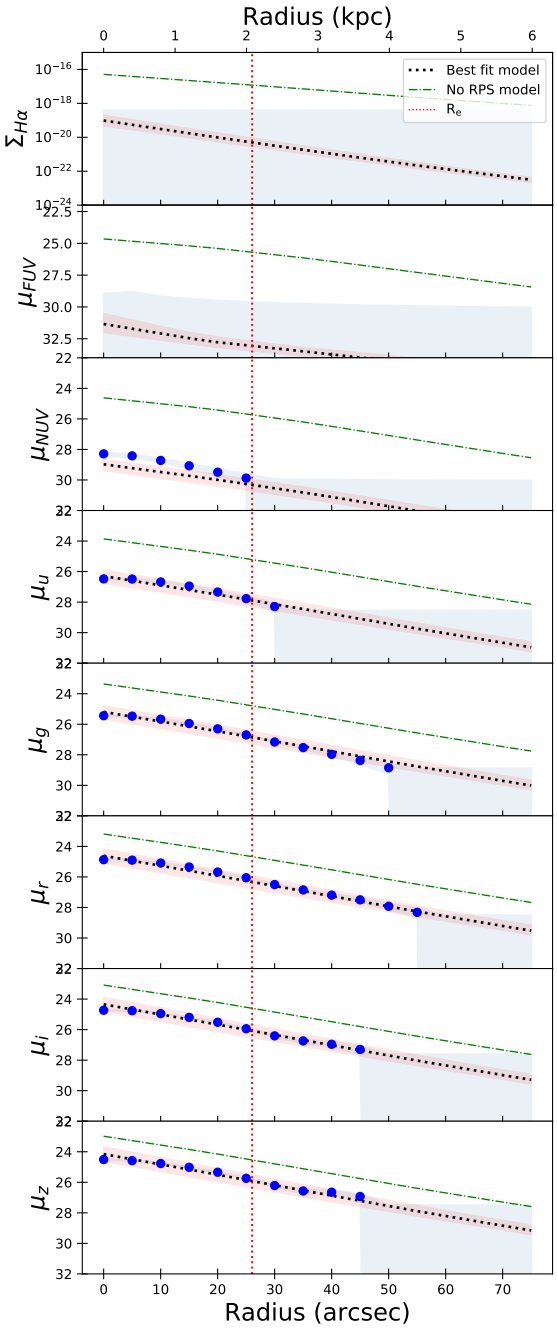

Figure 6.2.: Radial surface-brightness profiles of source ID 2143 with best fit models. The surface brightness units are in mag arcsec^{-2} for all the bands except for Hα which is in erg s^{-1} cm^{-2} arcsec^{-2}. The blue shaded area marks the 1σ error (for data points) and upper limits (3σ). The black dotted line indicates the best-fit model described in Sect. 6.3 for a ram-pressure stripped galaxy ($V_C = 58 \pm 2$ km s^{-1}, $\lambda = 0.09 \pm 0.01$ and $t_{rps} = 11.80 \pm 0.10$ Gyr), with the red shaded area as the 3σ confidence level of the best fit model. The green dot-dashed line shows the same model for an unperturbed system (without RPS). The vertical red dotted line gives the g-band effective radius I measured for the galaxy.

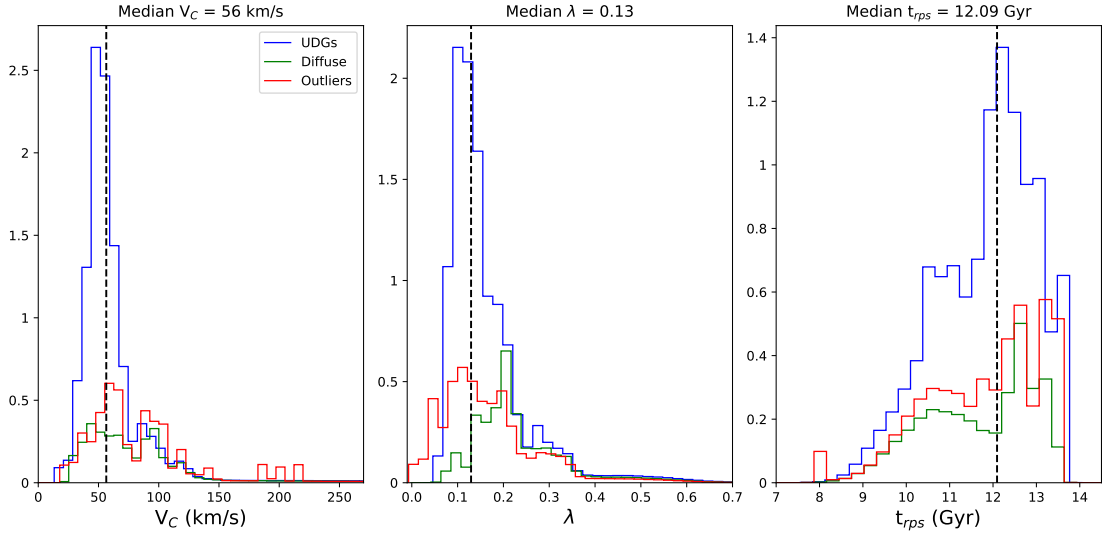

Figure 6.3.: The distribution of the V_C, λ and t_{rps} parameters from the best fit models, done after redistributing them within their uncertainties (see Sect. 6.4.1). The blue, green and red lines correspond to the UDG, Diffuse and Outlier sub-populations, respectively. The vertical black dashed lines show the median values corresponding to each parameter in the entire sample.

6.4.2. Colour and t_{rps} gradient

After obtaining the results from the modelling, I investigated the presence of any gradient in the model parameters, similar to the distance-colour gradient discussed in Sect. 5.5.2. Figure 6.4 shows the correlation of the observed $g-i$ colour and t_{rps} values from the models. Sources with $t_{rps} > 13.0$ Gyr seems to have bluer colours than the rest of the sample. This result is a trend between t_{rps} and the cluster centric distance too. Only the galaxies that are far from the centre of the cluster (> 0.75 Mpc, which is about half the virial radius of the Virgo cluster) have experienced RPS at very recent times ($t_{rps} \sim 13.5$ Gyr). This illustrates that the relatively low-density environment in the periphery of the cluster is sufficient to affect low mass extended galaxies entering the cluster. In the centre, the galaxies have already experienced RPS at an earlier epoch. This is similar to the trend we observed in Chapter 5, where galaxies towards the edge of the cluster centre having bluer colours and detection in H I from the ALFALFA survey.

6.4.3. Evolution of gas mass, stellar mass and star formation rate

A few of the several interesting outputs from the models are the estimate of the gas mass, stellar mass and star formation rate of the sample. The model gives predictions on these quantities for a galaxy with and without experiencing RPS. This can be considered as a proxy for the state of a galaxy both before and after undergoing an RPS event. Figure 6.5 shows the distribution of these quantities.

The gas mass of the sample had undergone a tremendous change due to the RPS events. All the sources in the sample were rich in gas content before the RPS, with a median gas mass of $\sim 10^9$ $M_\odot$. However, the RPS had completely transformed them to a gas-poor state by removing around 3 orders of magnitude of the gas mass to reach a median gas mass of $\sim 10^6$ $M_\odot$ after the RPS. A similar evolution is observed in the case of SFR too. Initially, before the RPS, all the galaxies in the sample were star-forming

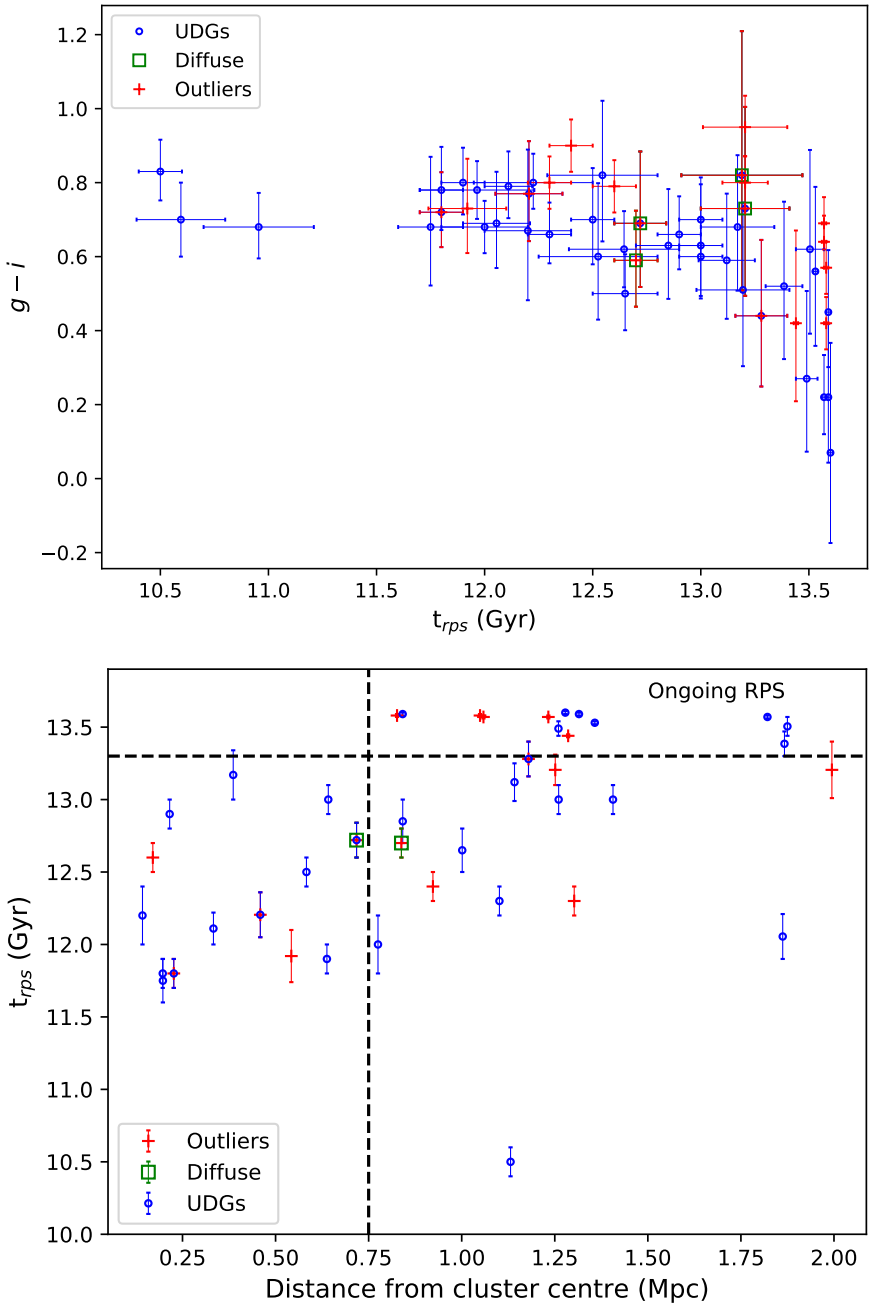

Figure 6.4.: *Top*: Observed $g-i$ colour as a function of the t_{rps} value from the models. *Bottom*: The t_{rps} values with respect to the distance from the cluster centre. Sources with only upper limits in $g-i$ and those with t_{rps} uncertainty >0.3 Gyr are eliminated from these plots. The black dashed lines marks the region of ongoing RPS ($t_{rps}>13.3$ Gyr) beyond a distance of 0.75 Mpc from the cluster centre.

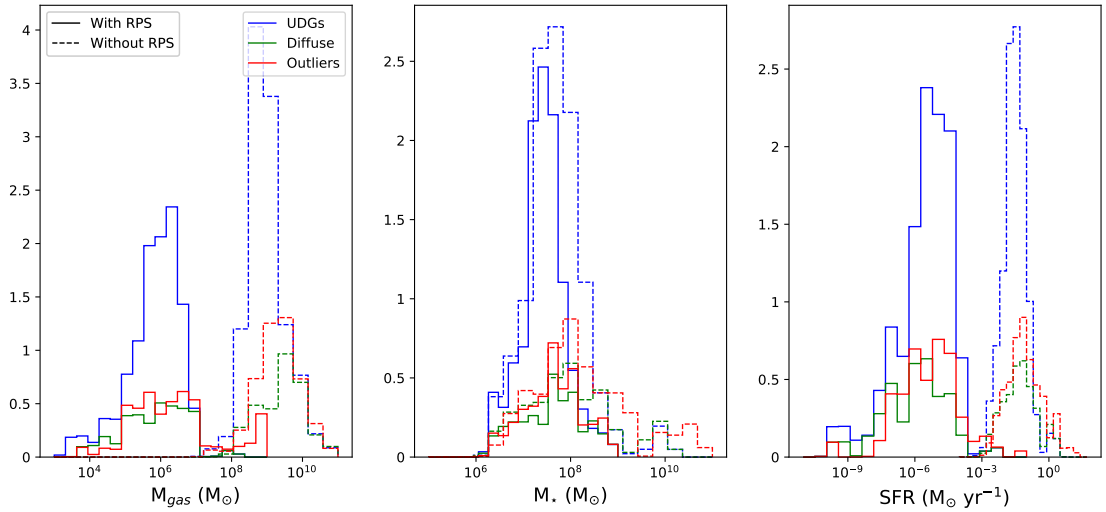

Figure 6.5.: Distribution of the gas mass, stellar mass and SFR of the sample obtained from the models, after redistributing them within their uncertainties as discussed in Sect. 6.4.1. The dashed lines and solid lines show the values before and after the RPS event, respectively.

with SFR levels similar to normal galaxies for their mass. Then the RPS completely quenches them to form a population of quiescent red galaxies. In the case of stellar mass, the RPS had an almost negligible effect on the global stellar mass of the population. This is quite expected in an RPS scenario. The trend of evolution of these quantities is similar for all three LSB sub-populations studied here, although very few Outliers even after the RPS have a large gas reservoir.

The prediction from the models discussed here on various key parameters of a galaxy population will be useful for future works on LSBs in different environments (both high-density cluster and low-density group environments). Moreover, the quantities observed and predicted in this work can be considered as a testbed for future surveys (e.g. LSST, SKA) that will observe LSBs in large numbers. For instance, with the recent SKA-pathfinder WALLABY survey (Koribalski et al. 2020), the H I gas reservoirs in Virgo cluster galaxies will be detectable down to a gas mass of 5×10^6 $M_\odot$. This indicates that based on my analysis a large portion of LSBs in my sample will still be undetected in H I (see Fig. 6.5), but indeed a few sources will be above this limit where we can observationally constrain their gas content. Such measurements will also be a further verification of the results obtained in this work.

6.5. Conclusions

The main outline of the work presented in this chapter are as follows:

- I used a set of chemo-spectrophotometric galaxy evolution models including the environmental effect of ram-pressure stripping on my sample of LSBs from the Virgo cluster. The simplicity of this model allows one to reproduce the observed properties of the disc of any galaxy using only three free parameters: the circular velocity (V_C), halo spin (λ) and the ram-pressure stripping time (t_{rps}).
- I generated a large grid of models with V_C, λ and t_{rps} values ranging from dwarf to extremely massive galaxies and compact to highly extended sources.

- I compared the observed photometric properties of the sample with the models by a χ^2 minimisation procedure to find the best fit model for each galaxy.
- The results from the modelling indicates that the LSBs in my sample are predominantly low mass ($V_C \sim 56$ km s^{-1}) but extended galaxies ($\lambda \sim 0.13$), consistent with what typically found in LSBs/UDGs in the literature.
- The distribution of the t_{rps} values from the models shows an interesting result. Almost all of the galaxies in my sample had undergone strong RPS events in the past, on an average of ~1.5 Gyr ago. However, few sources are experiencing ongoing RPS events.
- A comparison of the observed $g-i$ colour with the respect to the t_{rps} values from the models indicate that galaxies that had undergone very recent or ongoing RPS have bluer colours. A similar trend is observed for their cluster centric distance. Galaxies towards the edge of the cluster (> half the virial radius) have very recent or ongoing RPS events, while galaxies near the cluster centre experienced RPS in the past.
- The gas mass, stellar mass and SFR predictions from the models provide another interesting result. The galaxies in my sample before experiencing the RPS were gas-rich star-forming sources who had almost all of their gas content ripped off due to the RPS forming the quiescent galaxies we observe now. However, the RPS did not have any noticeable effect on the overall stellar mass of the population.
- The constraints from my modelling of the LSB sample from the Virgo cluster will be critically tested by the detection and study of LSBs in various future surveys.

Table 6.2.: Properties of the best RPS models, and the model with the same spin and velocity but without RPS. Column details: (1) Name of the source; (2-4) Best fit model t_{rps}, λ and V_C values; (5-8) Stellar-mass, gas mass, SFR and gas-phase metallicity from the best fit model; (9-12) Same quantities in the absence of RPS. The uncertainties given in the RPS models are from the confidence limits in t_{rps}, λ and V_C parameters. For the non-RPS models, the uncertainties are from the error in λ and V_C alone. The $\star$ symbol indicates a best-fit model without RPS.

ID	Best fit model							Model without RPS			
	t_{rps} (Gyr)	λ	V_C (km s^{-1})	$\log M_\star$ ($M_\odot$)	$\log M_{gas}$ ($M_\odot$)	$\log SFR$ ($M_\odot$ yr^{-1})	Z_{gas} ($Z_\odot$)	$\log M_\star$ ($M_\odot$)	$\log M_{gas}$ ($M_\odot$)	$\log SFR$ ($M_\odot$ yr^{-1})	Z_{gas} ($Z_\odot$)
(1)	(2)	(3)	(4)	(5)	(6)	(7)	(8)	(9)	(10)	(11)	(12)
67	10.86 ± 2.40	0.17 ± 0.06	63 ± 21	7.13 ± 0.75	5.65 ± 0.15	-6.04 ± 0.24	0.32 ± 0.03	7.66 ± 0.30	8.99 ± 0.49	-1.54 ± 0.26	0.18 ± 0.07
103	13.00 ± 0.10	0.13 ± 0.01	58 ± 2	7.63 ± 0.02	5.91 ± 0.09	-5.48 ± 0.22	0.47 ± 0.04	7.76 ± 0.00	8.93 ± 0.05	-1.44 ± 0.01	0.23 ± 0.03
110	13.00 ± 0.10	0.15 ± 0.01	48 ± 2	7.18 ± 0.03	5.46 ± 0.08	-6.19 ± 0.19	0.34 ± 0.02	7.33 ± 0.01	8.69 ± 0.06	-1.82 ± 0.00	0.16 ± 0.01
186	13.59 ± 0.01	0.17 ± 0.01	50 ± 2	7.27 ± 0.01	6.35 ± 0.47	-4.20 ± 0.52	0.36 ± 0.03	7.29 ± 0.01	8.75 ± 0.05	-1.87 ± 0.02	0.12 ± 0.01
213	10.80 ± 2.80	0.21 ± 0.12	65 ± 40	6.80 ± 1.20	5.64 ± 0.89	-5.39 ± 1.15	0.27 ± 0.08	7.38 ± 0.62	8.81 ± 0.94	-1.81 ± 0.55	0.17 ± 0.10
227	10.19 ± 1.11	0.12 ± 0.02	60 ± 6	7.27 ± 0.23	6.24 ± 0.12	-5.01 ± 0.12	0.47 ± 0.03	7.81 ± 0.11	8.97 ± 0.14	-1.40 ± 0.10	0.28 ± 0.06
321	12.59 ± 1.01	0.32 ± 0.10	86 ± 53	7.16 ± 1.16	4.58 ± 0.54	-8.25 ± 1.02	0.18 ± 0.06	7.42 ± 0.94	9.17 ± 0.91	-1.81 ± 0.81	0.07 ± 0.01
405	13.59 ± 0.01	0.14 ± 0.01	42 ± 2	7.13 ± 0.02	6.35 ± 0.35	-3.99 ± 0.37	0.45 ± 0.06	7.16 ± 0.01	8.51 ± 0.07	-1.98 ± 0.02	0.16 ± 0.01
421	13.28 ± 0.12	0.18 ± 0.01	65 ± 3	7.58 ± 0.03	5.04 ± 0.48	-7.15 ± 0.85	0.30 ± 0.04	7.66 ± 0.01	9.11 ± 0.07	-1.53 ± 0.01	0.12 ± 0.02
435	13.21 ± 0.20	0.01 ± 0.01	140 ± 10	10.00 ± 0.08	8.31 ± 0.17	-0.87 ± 0.05	7.00 ± 0.43	10.00 ± 0.08	9.09 ± 0.33	-0.20 ± 0.20	3.97 ± 0.64
444	13.57 ± 0.01	0.12 ± 0.01	44 ± 2	7.34 ± 0.00	6.15 ± 0.26	-4.23 ± 0.28	0.63 ± 0.09	7.37 ± 0.01	8.57 ± 0.06	-1.80 ± 0.00	0.22 ± 0.03
466	12.08 ± 1.40	0.20 ± 0.04	34 ± 9	6.21 ± 0.53	4.15 ± 0.50	-8.40 ± 1.24	0.20 ± 0.08	6.56 ± 0.22	8.24 ± 0.35	-2.56 ± 0.21	0.08 ± 0.03
495	12.63 ± 0.36	0.10 ± 0.01	37 ± 3	7.07 ± 0.07	5.58 ± 0.12	-5.50 ± 0.36	0.59 ± 0.11	7.28 ± 0.00	8.33 ± 0.12	-1.87 ± 0.02	0.31 ± 0.07
583	12.65 ± 0.15	0.12 ± 0.01	52 ± 2	7.44 ± 0.02	5.99 ± 0.06	-5.25 ± 0.17	0.49 ± 0.05	7.64 ± 0.00	8.79 ± 0.05	-1.55 ± 0.01	0.25 ± 0.03
588	10.80 ± 2.80	0.43 ± 0.36	259 ± 219	8.14 ± 1.82	5.04 ± 1.48	-7.54 ± 2.54	0.38 ± 0.30	8.17 ± 1.80	9.95 ± 1.55	-1.27 ± 1.50	0.27 ± 0.25
590	11.39 ± 1.69	0.13 ± 0.02	60 ± 11	7.41 ± 0.49	6.00 ± 0.04	-5.33 ± 0.14	0.43 ± 0.02	7.82 ± 0.18	8.98 ± 0.25	-1.38 ± 0.16	0.24 ± 0.05
604	13.51 ± 0.07	0.19 ± 0.01	34 ± 2	6.51 ± 0.07	3.34 ± 0.08	-9.76 ± 0.10	0.16 ± 0.03	6.57 ± 0.05	8.25 ± 0.07	-2.55 ± 0.04	0.08 ± 0.00
646	10.59 ± 2.59	0.15 ± 0.05	71 ± 31	7.29 ± 1.01	5.96 ± 0.55	-5.25 ± 0.57	0.40 ± 0.03	7.87 ± 0.51	9.07 ± 0.63	-1.36 ± 0.44	0.23 ± 0.06
743	13.00 ± 0.10	0.13 ± 0.01	46 ± 2	7.23 ± 0.03	5.53 ± 0.08	-5.95 ± 0.21	0.41 ± 0.04	7.37 ± 0.01	8.63 ± 0.06	-1.78 ± 0.01	0.20 ± 0.02
796	10.90 ± 1.53	0.11 ± 0.01	65 ± 10	7.59 ± 0.41	6.43 ± 0.20	-4.65 ± 0.12	0.55 ± 0.02	8.05 ± 0.15	9.07 ± 0.20	-1.17 ± 0.14	0.32 ± 0.04
833	10.84 ± 0.86	0.10 ± 0.01	62 ± 6	7.59 ± 0.23	6.51 ± 0.13	-4.40 ± 0.08	0.66 ± 0.02	8.05 ± 0.09	8.99 ± 0.13	-1.17 ± 0.09	0.39 ± 0.04
892	10.58 ± 0.78	0.15 ± 0.03	74 ± 12	7.52 ± 0.27	6.46 ± 0.18	-4.93 ± 0.07	0.41 ± 0.04	8.06 ± 0.12	9.23 ± 0.23	-1.19 ± 0.10	0.23 ± 0.05
904	12.22 ± 0.28	0.08 ± 0.01	51 ± 3	7.67 ± 0.04	6.36 ± 0.04	-4.33 ± 0.18	0.90 ± 0.13	7.90 ± 0.02	8.72 ± 0.09	-1.31 ± 0.02	0.50 ± 0.08
906	11.91 ± 0.90	0.08 ± 0.01	42 ± 6	7.26 ± 0.29	5.87 ± 0.17	-5.02 ± 0.27	0.73 ± 0.10	7.54 ± 0.18	8.49 ± 0.23	-1.63 ± 0.16	0.41 ± 0.08
935	10.80 ± 2.80	0.48 ± 0.33	317 ± 283	7.95 ± 2.35	5.77 ± 1.04	-6.28 ± 0.86	0.23 ± 0.03	8.55 ± 1.78	10.02 ± 1.77	-0.91 ± 1.45	0.11 ± 0.03
952	11.76 ± 1.25	0.17 ± 0.03	52 ± 8	7.00 ± 0.38	5.57 ± 0.07	-6.12 ± 0.24	0.31 ± 0.03	7.36 ± 0.16	8.81 ± 0.23	-1.82 ± 0.14	0.13 ± 0.03
964	11.06 ± 0.87	0.11 ± 0.01	58 ± 7	7.45 ± 0.28	6.34 ± 0.16	-4.70 ± 0.12	0.56 ± 0.01	7.91 ± 0.13	8.93 ± 0.15	-1.31 ± 0.11	0.32 ± 0.02
1008	12.57 ± 0.97	0.23 ± 0.02	41 ± 12	6.42 ± 0.62	3.95 ± 0.72	-8.77 ± 1.28	0.18 ± 0.06	6.68 ± 0.40	8.47 ± 0.39	-2.44 ± 0.38	0.06 ± 0.00
1013	11.96 ± 0.27	0.08 ± 0.01	42 ± 2	7.29 ± 0.03	6.08 ± 0.04	-4.68 ± 0.17	0.79 ± 0.12	7.61 ± 0.02	8.48 ± 0.08	-1.58 ± 0.01	0.45 ± 0.08
1017	11.06 ± 2.16	0.09 ± 0.04	30 ± 9	6.58 ± 0.54	5.26 ± 0.15	-5.89 ± 0.52	0.69 ± 0.26	7.07 ± 0.13	8.02 ± 0.43	-2.07 ± 0.15	0.42 ± 0.22
1027	13.53 ± 0.01	0.15 ± 0.01	34 ± 2	6.72 ± 0.04	3.43 ± 0.06	-9.23 ± 0.01	0.21 ± 0.02	6.77 ± 0.04	8.25 ± 0.07	-2.35 ± 0.03	0.12 ± 0.01

Table 6.2 Continued..

ID	Best fit model							Model without RPS			
	t_{rps} (Gyr)	λ	V_C (km s^{-1})	$\log M_\star$ ($M_\odot$)	$\log M_{gas}$ ($M_\odot$)	$\log SFR$ ($M_\odot$ yr^{-1})	Z_{gas} ($Z_\odot$)	$\log M_\star$ ($M_\odot$)	$\log M_{gas}$ ($M_\odot$)	$\log SFR$ ($M_\odot$ yr^{-1})	Z_{gas} ($Z_\odot$)
(1)	(2)	(3)	(4)	(5)	(6)	(7)	(8)	(9)	(10)	(11)	(12)
1160	12.72 ± 0.12	0.16 ± 0.01	64 ± 2	7.57 ± 0.02	6.08 ± 0.04	-5.46 ± 0.12	0.38 ± 0.03	7.75 ± 0.00	9.08 ± 0.04	-1.44 ± 0.00	0.16 ± 0.01
1214	11.05 ± 1.84	0.13 ± 0.03	52 ± 11	7.10 ± 0.50	5.82 ± 0.15	-5.54 ± 0.08	0.41 ± 0.04	7.57 ± 0.19	8.79 ± 0.29	-1.61 ± 0.16	0.23 ± 0.06
1227	12.50 ± 0.10	0.10 ± 0.01	46 ± 2	7.36 ± 0.02	5.97 ± 0.03	-5.05 ± 0.16	0.60 ± 0.08	7.59 ± 0.01	8.62 ± 0.06	-1.59 ± 0.01	0.32 ± 0.05
1271	10.66 ± 2.66	0.21 ± 0.11	94 ± 59	7.35 ± 1.35	5.83 ± 0.72	-5.62 ± 0.66	0.33 ± 0.04	7.93 ± 0.82	9.28 ± 0.98	-1.34 ± 0.68	0.17 ± 0.06
1318	13.57 ± 0.01	0.05 ± 0.01	88 ± 2	9.03 ± 0.05	8.57 ± 0.09	-0.90 ± 0.02	2.51 ± 0.42	9.06 ± 0.06	9.29 ± 0.09	-0.40 ± 0.01	1.27 ± 0.22
1335	10.59 ± 2.59	0.15 ± 0.04	53 ± 16	6.90 ± 0.82	5.64 ± 0.41	-5.75 ± 0.41	0.35 ± 0.03	7.51 ± 0.30	8.79 ± 0.41	-1.68 ± 0.28	0.18 ± 0.04
1346	12.20 ± 1.40	0.14 ± 0.07	38 ± 18	6.67 ± 0.71	5.85 ± 0.92	-5.06 ± 1.20	0.45 ± 0.16	6.98 ± 0.42	8.23 ± 0.72	-2.17 ± 0.40	0.23 ± 0.13
1349	10.49 ± 2.41	0.12 ± 0.03	58 ± 16	7.23 ± 0.74	5.98 ± 0.36	-5.27 ± 0.26	0.46 ± 0.03	7.82 ± 0.30	8.87 ± 0.38	-1.39 ± 0.26	0.28 ± 0.07
1352	10.42 ± 2.42	0.09 ± 0.03	44 ± 15	6.99 ± 0.73	5.78 ± 0.40	-5.04 ± 0.24	0.65 ± 0.11	7.58 ± 0.30	8.49 ± 0.49	-1.61 ± 0.28	0.42 ± 0.15
1354	12.69 ± 0.42	0.17 ± 0.01	43 ± 3	6.81 ± 0.12	5.23 ± 0.15	-6.62 ± 0.31	0.28 ± 0.03	7.02 ± 0.06	8.55 ± 0.09	-2.13 ± 0.05	0.10 ± 0.01
1389	13.58 ± 0.01	0.05 ± 0.01	102 ± 2	9.28 ± 0.05	8.86 ± 0.10	-0.64 ± 0.02	2.58 ± 0.42	9.29 ± 0.06	9.47 ± 0.09	-0.23 ± 0.01	1.39 ± 0.24
1397	10.80 ± 2.80	0.22 ± 0.12	61 ± 33	6.71 ± 1.08	5.55 ± 0.78	-5.60 ± 1.02	0.26 ± 0.05	7.30 ± 0.51	8.78 ± 0.81	-1.89 ± 0.44	0.15 ± 0.09
1424	12.78 ± 0.34	0.21 ± 0.02	42 ± 5	6.65 ± 0.19	5.07 ± 0.10	-7.06 ± 0.24	0.23 ± 0.03	6.86 ± 0.11	8.55 ± 0.15	-2.28 ± 0.10	0.07 ± 0.01
1429	12.45 ± 0.36	0.09 ± 0.01	56 ± 2	7.77 ± 0.03	6.39 ± 0.11	-4.45 ± 0.27	0.80 ± 0.11	7.98 ± 0.02	8.86 ± 0.06	-1.24 ± 0.02	0.44 ± 0.07
1435	12.40 ± 0.10	0.09 ± 0.01	116 ± 2	9.04 ± 0.04	7.69 ± 0.10	-2.78 ± 0.27	1.49 ± 0.27	9.19 ± 0.04	9.78 ± 0.04	-0.24 ± 0.02	0.78 ± 0.11
1436	11.25 ± 1.88	0.16 ± 0.04	50 ± 13	6.86 ± 0.58	5.47 ± 0.12	-6.21 ± 0.16	0.31 ± 0.02	7.36 ± 0.21	8.73 ± 0.35	-1.81 ± 0.19	0.15 ± 0.05
1450	11.13 ± 1.68	0.13 ± 0.02	47 ± 9	6.90 ± 0.52	5.66 ± 0.21	-5.79 ± 0.13	0.37 ± 0.01	7.38 ± 0.20	8.64 ± 0.26	-1.78 ± 0.18	0.20 ± 0.04
1459	8.10 ± 0.10	0.05 ± 0.01	184 ± 2	9.95 ± 0.09	8.93 ± 0.02	-0.80 ± 0.12	4.56 ± 0.77	10.19 ± 0.04	10.10 ± 0.10	0.35 ± 0.03	2.18 ± 0.32
1474	11.44 ± 1.57	0.11 ± 0.02	55 ± 13	7.39 ± 0.56	6.04 ± 0.19	-5.07 ± 0.04	0.53 ± 0.03	7.80 ± 0.28	8.83 ± 0.34	-1.41 ± 0.25	0.30 ± 0.05
1476	10.53 ± 2.53	0.21 ± 0.09	109 ± 50	7.84 ± 0.97	6.54 ± 0.54	-4.82 ± 0.44	0.34 ± 0.02	8.38 ± 0.50	9.64 ± 0.66	-0.93 ± 0.40	0.21 ± 0.07
1479	12.89 ± 0.60	0.13 ± 0.06	48 ± 25	7.18 ± 0.64	4.95 ± 0.46	-6.83 ± 1.29	0.49 ± 0.23	7.34 ± 0.51	8.51 ± 0.77	-1.83 ± 0.48	0.27 ± 0.14
1506	10.15 ± 1.84	0.09 ± 0.01	61 ± 12	7.60 ± 0.52	6.53 ± 0.32	-4.18 ± 0.23	0.84 ± 0.05	8.17 ± 0.19	8.96 ± 0.27	-1.09 ± 0.17	0.53 ± 0.07
1529	12.70 ± 0.10	0.13 ± 0.01	98 ± 2	8.51 ± 0.01	6.98 ± 0.06	-4.12 ± 0.16	0.69 ± 0.07	8.65 ± 0.02	9.62 ± 0.04	-0.66 ± 0.02	0.37 ± 0.04
1593	12.39 ± 0.35	0.19 ± 0.02	91 ± 6	8.03 ± 0.09	6.61 ± 0.06	-4.93 ± 0.18	0.39 ± 0.04	8.24 ± 0.04	9.55 ± 0.09	-1.03 ± 0.03	0.17 ± 0.03
1620	12.13 ± 0.97	0.11 ± 0.02	39 ± 5	6.94 ± 0.24	5.54 ± 0.18	-5.78 ± 0.40	0.48 ± 0.08	7.24 ± 0.06	8.39 ± 0.19	-1.91 ± 0.05	0.25 ± 0.06
1633	10.64 ± 2.64	0.19 ± 0.07	69 ± 29	7.08 ± 0.96	5.56 ± 0.33	-6.37 ± 0.45	0.28 ± 0.01	7.64 ± 0.44	9.05 ± 0.60	-1.55 ± 0.37	0.15 ± 0.05
1653	11.80 ± 0.10	0.06 ± 0.01	20 ± 2	6.35 ± 0.07	5.18 ± 0.07	-5.43 ± 0.25	0.88 ± 0.19	6.73 ± 0.06	7.56 ± 0.08	-2.42 ± 0.05	0.49 ± 0.11
1656	11.98 ± 1.08	0.12 ± 0.02	50 ± 6	7.29 ± 0.29	5.77 ± 0.16	-5.47 ± 0.36	0.47 ± 0.07	7.54 ± 0.16	8.75 ± 0.19	-1.65 ± 0.15	0.24 ± 0.05
1719	13.08 ± 0.38	0.48 ± 0.27	190 ± 134	8.17 ± 1.06	6.40 ± 0.80	-6.20 ± 0.37	0.23 ± 0.04	8.29 ± 0.99	9.94 ± 1.03	-1.12 ± 0.73	0.07 ± 0.02
1782	11.75 ± 0.15	0.11 ± 0.01	56 ± 2	7.49 ± 0.01	6.30 ± 0.02	-4.74 ± 0.12	0.57 ± 0.05	7.83 ± 0.01	8.88 ± 0.05	-1.37 ± 0.01	0.31 ± 0.04
1837	10.62 ± 2.61	0.26 ± 0.14	97 ± 61	7.24 ± 1.33	5.71 ± 0.67	-5.87 ± 0.61	0.27 ± 0.02	7.84 ± 0.80	9.29 ± 0.99	-1.43 ± 0.66	0.15 ± 0.06
1846	10.40 ± 2.00	0.12 ± 0.03	57 ± 13	7.21 ± 0.58	6.10 ± 0.35	-4.88 ± 0.39	0.52 ± 0.04	7.88 ± 0.29	8.87 ± 0.31	-1.33 ± 0.26	0.32 ± 0.09
1896	10.96 ± 0.26	0.09 ± 0.01	67 ± 3	7.85 ± 0.03	6.77 ± 0.01	-3.95 ± 0.13	0.84 ± 0.11	8.29 ± 0.01	9.07 ± 0.07	-0.98 ± 0.02	0.50 ± 0.07
1968	13.44 ± 0.01	0.08 ± 0.01	58 ± 2	8.08 ± 0.04	5.57 ± 0.27	-5.22 ± 0.55	1.43 ± 0.30	8.11 ± 0.03	8.89 ± 0.06	-1.12 ± 0.02	0.55 ± 0.10
1993	9.70 ± 1.80	0.23 ± 0.04	119 ± 13	7.99 ± 0.35	6.93 ± 0.18	-4.59 ± 0.18	0.31 ± 0.02	8.63 ± 0.14	9.89 ± 0.15	-0.70 ± 0.12	0.17 ± 0.03
2006	11.90 ± 0.10	0.08 ± 0.01	54 ± 2	7.72 ± 0.02	6.50 ± 0.04	-4.15 ± 0.19	0.93 ± 0.16	8.01 ± 0.03	8.79 ± 0.06	-1.22 ± 0.02	0.52 ± 0.09
2046	12.21 ± 0.15	0.14 ± 0.01	87 ± 2	8.19 ± 0.01	6.85 ± 0.05	-4.32 ± 0.14	0.56 ± 0.04	8.41 ± 0.01	9.48 ± 0.04	-0.87 ± 0.02	0.29 ± 0.03

Table 6.2 Continued..

ID	Best fit model							Model without RPS			
	t_{rps} (Gyr)	λ	V_C (km s^{-1})	$\log M_\star$ ($M_\odot$)	$\log M_{gas}$ ($M_\odot$)	$\log SFR$ ($M_\odot$ yr^{-1})	Z_{gas} ($Z_\odot$)	$\log M_\star$ ($M_\odot$)	$\log M_{gas}$ ($M_\odot$)	$\log SFR$ ($M_\odot$ yr^{-1})	Z_{gas} ($Z_\odot$)
(1)	(2)	(3)	(4)	(5)	(6)	(7)	(8)	(9)	(10)	(11)	(12)
2079	13.19 ± 0.28	0.34 ± 0.04	99 ± 9	7.79 ± 0.11	5.40 ± 0.60	−7.45 ± 1.21	0.17 ± 0.06	7.90 ± 0.08	9.65 ± 0.11	−1.36 ± 0.06	0.07 ± 0.01
2143	11.80 ± 0.10	0.11 ± 0.01	58 ± 2	7.56 ± 0.00	6.36 ± 0.02	−4.67 ± 0.12	0.59 ± 0.06	7.89 ± 0.01	8.92 ± 0.05	−1.32 ± 0.01	0.32 ± 0.04
2156	11.44 ± 0.86	0.10 ± 0.01	56 ± 6	7.51 ± 0.25	6.34 ± 0.11	−4.66 ± 0.08	0.64 ± 0.02	7.89 ± 0.11	8.86 ± 0.14	−1.32 ± 0.10	0.36 ± 0.04
2178	11.76 ± 1.67	0.16 ± 0.03	54 ± 10	7.08 ± 0.47	4.98 ± 0.64	−7.04 ± 1.24	0.30 ± 0.05	7.42 ± 0.19	8.83 ± 0.25	−1.75 ± 0.17	0.15 ± 0.04
2200	13.20 ± 0.21	0.19 ± 0.02	42 ± 2	6.80 ± 0.03	4.40 ± 0.68	−8.03 ± 1.21	0.22 ± 0.05	6.90 ± 0.03	8.53 ± 0.06	−2.23 ± 0.03	0.09 ± 0.01
2205	12.26 ± 0.56	0.12 ± 0.01	58 ± 4	7.53 ± 0.11	6.21 ± 0.13	−5.04 ± 0.27	0.50 ± 0.06	7.83 ± 0.05	8.94 ± 0.10	−1.37 ± 0.05	0.26 ± 0.04
2227	12.32 ± 0.52	0.13 ± 0.01	46 ± 4	7.10 ± 0.18	5.70 ± 0.04	−5.64 ± 0.10	0.42 ± 0.02	7.37 ± 0.07	8.63 ± 0.12	−1.79 ± 0.07	0.20 ± 0.01
2237	12.10 ± 0.55	0.12 ± 0.01	58 ± 4	7.54 ± 0.14	6.27 ± 0.07	−4.98 ± 0.19	0.50 ± 0.05	7.83 ± 0.05	8.96 ± 0.12	−1.37 ± 0.05	0.26 ± 0.04
2269	9.94 ± 1.34	0.30 ± 0.06	97 ± 20	7.34 ± 0.48	6.29 ± 0.33	−5.80 ± 0.25	0.22 ± 0.01	7.95 ± 0.20	9.61 ± 0.27	−1.31 ± 0.16	0.08 ± 0.01
2301	12.90 ± 0.10	0.10 ± 0.01	46 ± 2	7.44 ± 0.01	5.83 ± 0.07	−5.27 ± 0.21	0.60 ± 0.08	7.59 ± 0.01	8.62 ± 0.06	−1.59 ± 0.01	0.32 ± 0.05
2343	11.40 ± 1.60	0.11 ± 0.03	49 ± 11	7.18 ± 0.45	5.84 ± 0.07	−5.32 ± 0.24	0.53 ± 0.10	7.60 ± 0.15	8.66 ± 0.32	−1.58 ± 0.14	0.30 ± 0.10
2351	12.38 ± 0.77	0.14 ± 0.03	30 ± 4	6.37 ± 0.22	4.78 ± 0.22	−6.88 ± 0.55	0.33 ± 0.07	6.66 ± 0.06	8.07 ± 0.19	−2.45 ± 0.06	0.14 ± 0.04
2394	12.20 ± 0.20	0.13 ± 0.01	54 ± 2	7.39 ± 0.07	6.10 ± 0.02	−5.18 ± 0.08	0.46 ± 0.03	7.67 ± 0.03	8.87 ± 0.07	−1.52 ± 0.03	0.23 ± 0.02
2409	12.60 ± 0.10	0.10 ± 0.01	100 ± 2	8.73 ± 0.02	7.27 ± 0.09	−3.45 ± 0.22	1.06 ± 0.15	8.87 ± 0.03	9.61 ± 0.04	−0.48 ± 0.03	0.58 ± 0.08
2458	10.73 ± 2.73	0.26 ± 0.15	81 ± 56	6.69 ± 1.27	5.35 ± 0.79	−6.36 ± 0.64	0.24 ± 0.04	7.34 ± 0.74	8.88 ± 1.00	−1.87 ± 0.64	0.12 ± 0.06
2473	13.17 ± 0.17	0.15 ± 0.01	28 ± 2	6.30 ± 0.07	4.23 ± 0.31	−7.83 ± 0.57	0.26 ± 0.03	6.43 ± 0.03	7.99 ± 0.09	−2.67 ± 0.03	0.10 ± 0.01
2499	12.84 ± 0.64	0.14 ± 0.09	48 ± 20	7.24 ± 0.31	5.04 ± 0.73	−6.66 ± 2.11	0.73 ± 0.56	7.40 ± 0.20	8.55 ± 0.65	−1.76 ± 0.16	0.40 ± 0.31
2531	10.84 ± 1.46	0.12 ± 0.01	62 ± 8	7.50 ± 0.39	6.35 ± 0.21	−4.69 ± 0.17	0.54 ± 0.02	7.98 ± 0.13	9.02 ± 0.19	−1.24 ± 0.12	0.31 ± 0.04
2542	13.12 ± 0.13	0.15 ± 0.01	46 ± 2	7.13 ± 0.05	5.27 ± 0.13	−6.45 ± 0.27	0.33 ± 0.02	7.27 ± 0.01	8.64 ± 0.06	−1.90 ± 0.02	0.15 ± 0.01
2563	11.97 ± 0.58	0.09 ± 0.01	43 ± 3	7.28 ± 0.17	6.00 ± 0.04	−4.90 ± 0.11	0.67 ± 0.06	7.59 ± 0.07	8.54 ± 0.13	−1.60 ± 0.06	0.37 ± 0.05
2568	13.58 ± 0.01	0.07 ± 0.01	101 ± 3	9.10 ± 0.02	8.80 ± 0.11	−0.85 ± 0.03	1.98 ± 0.33	9.11 ± 0.03	9.55 ± 0.07	−0.31 ± 0.01	0.97 ± 0.15
2592	13.38 ± 0.09	0.14 ± 0.01	41 ± 4	7.12 ± 0.08	4.31 ± 0.41	−7.77 ± 0.81	0.38 ± 0.09	7.20 ± 0.05	8.51 ± 0.13	−1.95 ± 0.06	0.17 ± 0.03
2621	12.54 ± 0.26	0.14 ± 0.01	48 ± 2	7.16 ± 0.05	5.73 ± 0.06	−5.73 ± 0.16	0.39 ± 0.03	7.39 ± 0.01	8.69 ± 0.06	−1.78 ± 0.01	0.17 ± 0.01
2635	13.57 ± 0.01	0.04 ± 0.01	218 ± 2	10.50 ± 0.03	9.36 ± 0.25	−0.17 ± 0.28	4.92 ± 0.44	10.50 ± 0.03	10.14 ± 0.16	0.44 ± 0.06	3.04 ± 0.52
2690	13.08 ± 0.32	0.21 ± 0.01	33 ± 5	6.27 ± 0.27	3.99 ± 0.47	−8.69 ± 0.97	0.17 ± 0.03	6.41 ± 0.21	8.20 ± 0.20	−2.69 ± 0.20	0.06 ± 0.00
2717	12.11 ± 0.11	0.09 ± 0.01	48 ± 2	7.45 ± 0.00	6.20 ± 0.03	−4.67 ± 0.16	0.72 ± 0.10	7.73 ± 0.02	8.66 ± 0.07	−1.46 ± 0.01	0.40 ± 0.07
2731	12.74 ± 0.71	0.28 ± 0.06	68 ± 22	7.12 ± 0.54	5.00 ± 0.43	−7.77 ± 1.09	0.19 ± 0.06	7.32 ± 0.38	9.09 ± 0.44	−1.87 ± 0.33	0.06 ± 0.01
2829	12.05 ± 0.15	0.11 ± 0.01	58 ± 2	7.60 ± 0.01	6.35 ± 0.03	−4.69 ± 0.14	0.59 ± 0.07	7.89 ± 0.01	8.92 ± 0.05	−1.32 ± 0.01	0.32 ± 0.04
2863	11.04 ± 0.76	0.10 ± 0.01	57 ± 5	7.48 ± 0.20	6.38 ± 0.10	−4.57 ± 0.05	0.64 ± 0.03	7.92 ± 0.08	8.88 ± 0.12	−1.29 ± 0.07	0.37 ± 0.04
2887	11.92 ± 0.18	0.09 ± 0.01	58 ± 2	7.77 ± 0.03	6.54 ± 0.02	−4.22 ± 0.14	0.81 ± 0.10	8.06 ± 0.02	8.92 ± 0.08	−1.17 ± 0.01	0.46 ± 0.07
2918	10.73 ± 2.74	0.13 ± 0.06	45 ± 17	6.74 ± 0.76	4.83 ± 0.62	−7.17 ± 1.37	0.39 ± 0.17	7.32 ± 0.24	8.49 ± 0.55	−1.85 ± 0.23	0.28 ± 0.15
2928	10.59 ± 0.21	0.11 ± 0.01	68 ± 2	7.66 ± 0.01	6.60 ± 0.01	−4.37 ± 0.11	0.60 ± 0.06	8.16 ± 0.01	9.13 ± 0.05	−1.09 ± 0.02	0.36 ± 0.05
2999	11.41 ± 1.81	0.17 ± 0.04	42 ± 10	6.54 ± 0.54	5.09 ± 0.09	−6.79 ± 0.39	0.28 ± 0.04	7.01 ± 0.17	8.48 ± 0.33	−2.12 ± 0.16	0.12 ± 0.05
3005	12.00 ± 0.20	0.09 ± 0.01	48 ± 2	7.43 ± 0.02	6.20 ± 0.03	−4.66 ± 0.16	0.72 ± 0.10	7.73 ± 0.02	8.66 ± 0.07	−1.46 ± 0.01	0.40 ± 0.07
3088	12.85 ± 0.15	0.13 ± 0.01	50 ± 2	7.35 ± 0.03	5.76 ± 0.08	−5.64 ± 0.21	0.43 ± 0.04	7.52 ± 0.00	8.74 ± 0.06	−1.66 ± 0.00	0.21 ± 0.03
3103	12.30 ± 0.10	0.09 ± 0.01	56 ± 2	7.75 ± 0.01	6.43 ± 0.05	−4.38 ± 0.18	0.80 ± 0.11	7.98 ± 0.02	8.86 ± 0.06	−1.24 ± 0.02	0.44 ± 0.07
3116	10.80 ± 2.80	0.11 ± 0.10	298 ± 220	9.18 ± 2.03	7.92 ± 1.69	−3.06 ± 2.40	4.04 ± 3.77	9.61 ± 1.62	10.04 ± 1.69	0.04 ± 1.28	1.73 ± 1.58

Table 6.2 Continued..

ID	Best fit model							Model without RPS			
	t_{rps} (Gyr)	λ	V_C (km s^{-1})	$\log M_\star$ ($M_\odot$)	$\log M_{gas}$ ($M_\odot$)	$\log SFR$ ($M_\odot$ yr^{-1})	Z_{gas} ($Z_\odot$)	$\log M_\star$ ($M_\odot$)	$\log M_{gas}$ ($M_\odot$)	$\log SFR$ ($M_\odot$ yr^{-1})	Z_{gas} ($Z_\odot$)
(1)	(2)	(3)	(4)	(5)	(6)	(7)	(8)	(9)	(10)	(11)	(12)
3128	12.52 ± 0.28	0.14 ± 0.01	49 ± 3	7.15 ± 0.08	5.72 ± 0.08	-5.76 ± 0.20	0.38 ± 0.04	7.37 ± 0.05	8.72 ± 0.08	-1.80 ± 0.03	0.17 ± 0.02
3146	13.21 ± 0.21	0.21 ± 0.01	55 ± 3	7.17 ± 0.09	4.74 ± 0.60	-7.70 ± 1.07	0.22 ± 0.03	7.28 ± 0.05	8.88 ± 0.07	-1.89 ± 0.03	0.08 ± 0.00
3190	10.80 ± 2.80	0.27 ± 0.14	99 ± 51	7.34 ± 0.98	5.60 ± 0.48	-7.15 ± 1.19	0.21 ± 0.07	7.90 ± 0.46	9.38 ± 0.69	-1.36 ± 0.36	0.14 ± 0.07
3225	10.80 ± 2.80	0.33 ± 0.21	125 ± 93	7.35 ± 1.65	4.49 ± 1.17	-8.39 ± 1.65	0.18 ± 0.08	7.68 ± 1.32	9.39 ± 1.25	-1.63 ± 1.12	0.11 ± 0.06
3233	10.80 ± 2.80	0.23 ± 0.10	97 ± 73	7.00 ± 1.89	6.27 ± 2.01	-4.90 ± 2.67	0.29 ± 0.07	7.62 ± 1.28	9.08 ± 1.30	-1.65 ± 1.12	0.10 ± 0.02
3245	12.65 ± 0.26	0.11 ± 0.01	46 ± 2	7.31 ± 0.05	5.85 ± 0.09	-5.34 ± 0.23	0.52 ± 0.05	7.52 ± 0.00	8.62 ± 0.06	-1.66 ± 0.00	0.27 ± 0.03
3254	11.98 ± 0.32	0.10 ± 0.01	47 ± 3	7.31 ± 0.07	6.06 ± 0.02	-4.93 ± 0.10	0.60 ± 0.06	7.61 ± 0.03	8.64 ± 0.09	-1.57 ± 0.03	0.33 ± 0.04
3265	12.19 ± 0.56	0.12 ± 0.01	37 ± 4	6.86 ± 0.18	5.58 ± 0.06	-5.74 ± 0.18	0.45 ± 0.05	7.17 ± 0.06	8.37 ± 0.14	-1.98 ± 0.06	0.22 ± 0.04
3272	11.21 ± 1.04	0.14 ± 0.01	87 ± 8	8.02 ± 0.26	6.84 ± 0.11	-4.33 ± 0.06	0.52 ± 0.02	8.40 ± 0.10	9.48 ± 0.12	-0.88 ± 0.08	0.29 ± 0.01
3297	11.90 ± 1.14	0.10 ± 0.01	47 ± 7	7.24 ± 0.33	5.83 ± 0.05	-5.26 ± 0.17	0.54 ± 0.04	7.57 ± 0.13	8.64 ± 0.20	-1.61 ± 0.11	0.30 ± 0.05
3300	12.42 ± 0.38	0.12 ± 0.01	45 ± 3	7.19 ± 0.15	5.76 ± 0.06	-5.49 ± 0.13	0.46 ± 0.03	7.44 ± 0.08	8.62 ± 0.12	-1.73 ± 0.07	0.23 ± 0.02
3356	12.47 ± 0.67	0.18 ± 0.02	49 ± 4	7.00 ± 0.18	5.37 ± 0.26	-6.48 ± 0.52	0.29 ± 0.04	7.20 ± 0.08	8.75 ± 0.11	-1.95 ± 0.07	0.11 ± 0.02
3365	*	0.34 ± 0.04	47 ± 11	6.55 ± 0.32	3.72 ± 0.32	-9.86 ± 0.28	0.08 ± 0.00	6.58 ± 0.32	8.65 ± 0.33	-2.56 ± 0.29	0.03 ± 0.00
3379	12.67 ± 0.75	0.20 ± 0.01	49 ± 11	6.86 ± 0.50	4.68 ± 0.47	-7.70 ± 0.93	0.24 ± 0.04	7.08 ± 0.33	8.70 ± 0.30	-2.07 ± 0.30	0.08 ± 0.00
3404	12.65 ± 0.81	0.32 ± 0.07	64 ± 19	6.93 ± 0.47	4.99 ± 0.53	-7.99 ± 1.10	0.17 ± 0.07	7.16 ± 0.29	9.03 ± 0.38	-2.02 ± 0.25	0.05 ± 0.01
3451	10.71 ± 2.71	0.19 ± 0.06	56 ± 20	6.75 ± 0.92	4.91 ± 0.41	-7.57 ± 0.89	0.22 ± 0.03	7.35 ± 0.37	8.83 ± 0.51	-1.82 ± 0.33	0.12 ± 0.04
3477	*	0.67 ± 0.04	140 ± 2	7.71 ± 0.07	4.89 ± 0.07	-8.92 ± 0.04	0.10 ± 0.00	7.75 ± 0.07	9.86 ± 0.08	-1.57 ± 0.05	0.03 ± 0.00
3481	10.50 ± 0.10	0.07 ± 0.01	58 ± 2	7.73 ± 0.04	6.70 ± 0.06	-3.75 ± 0.25	1.17 ± 0.27	8.22 ± 0.04	8.87 ± 0.07	-1.05 ± 0.02	0.67 ± 0.12
3520	11.49 ± 1.09	0.09 ± 0.01	59 ± 6	7.74 ± 0.26	6.50 ± 0.05	-4.30 ± 0.06	0.78 ± 0.03	8.09 ± 0.09	8.94 ± 0.14	-1.15 ± 0.08	0.46 ± 0.05
3523	10.80 ± 2.80	0.47 ± 0.33	281 ± 257	7.59 ± 2.55	5.45 ± 1.27	-6.38 ± 1.36	0.21 ± 0.02	8.21 ± 1.93	9.72 ± 1.93	-1.21 ± 1.61	0.12 ± 0.02
3539	10.38 ± 1.73	0.10 ± 0.01	69 ± 13	7.74 ± 0.49	6.64 ± 0.30	-4.17 ± 0.21	0.72 ± 0.03	8.27 ± 0.19	9.10 ± 0.26	-1.00 ± 0.17	0.46 ± 0.07
3543	13.49 ± 0.05	0.15 ± 0.01	43 ± 3	7.11 ± 0.07	3.83 ± 0.06	-8.62 ± 0.06	0.28 ± 0.04	7.14 ± 0.06	8.55 ± 0.10	-2.00 ± 0.05	0.14 ± 0.01
3548	12.30 ± 0.10	0.08 ± 0.01	64 ± 2	8.06 ± 0.02	6.76 ± 0.07	-3.85 ± 0.23	1.06 ± 0.19	8.29 ± 0.03	9.02 ± 0.06	-0.98 ± 0.02	0.58 ± 0.10
3561	9.20 ± 1.02	0.10 ± 0.01	64 ± 6	7.44 ± 0.21	6.48 ± 0.14	-4.30 ± 0.08	0.65 ± 0.07	8.21 ± 0.09	9.03 ± 0.14	-1.04 ± 0.08	0.45 ± 0.09
3578	13.21 ± 0.11	0.03 ± 0.01	198 ± 2	10.40 ± 0.03	8.86 ± 0.03	-0.60 ± 0.10	6.63 ± 0.56	10.41 ± 0.03	9.85 ± 0.23	0.29 ± 0.11	3.46 ± 0.73
3589	13.60 ± 0.01	0.28 ± 0.01	72 ± 2	7.46 ± 0.01	5.83 ± 0.37	-5.06 ± 0.44	0.20 ± 0.01	7.48 ± 0.02	9.24 ± 0.04	-1.71 ± 0.01	0.06 ± 0.00
3590	11.38 ± 0.82	0.10 ± 0.01	53 ± 5	7.38 ± 0.18	6.18 ± 0.07	-4.86 ± 0.14	0.58 ± 0.06	7.73 ± 0.09	8.80 ± 0.13	-1.46 ± 0.08	0.33 ± 0.06
3599	11.94 ± 1.29	0.16 ± 0.03	58 ± 9	7.29 ± 0.33	5.78 ± 0.22	-5.89 ± 0.47	0.35 ± 0.05	7.62 ± 0.10	8.94 ± 0.20	-1.57 ± 0.09	0.17 ± 0.04
3633	10.55 ± 2.55	0.18 ± 0.05	73 ± 28	7.23 ± 0.95	5.85 ± 0.43	-5.86 ± 0.23	0.30 ± 0.01	7.79 ± 0.47	9.17 ± 0.53	-1.42 ± 0.40	0.15 ± 0.04
3659	10.80 ± 2.80	0.47 ± 0.33	284 ± 254	7.75 ± 2.39	5.66 ± 1.15	-6.28 ± 1.13	0.22 ± 0.03	8.36 ± 1.79	9.87 ± 1.79	-1.07 ± 1.47	0.11 ± 0.02

7. A Detailed case: Transition of a gas-rich UDG into a gas-poor UDG

Summary

7.1 Introduction . . . 135
7.2 Data . . . 137
7.3 Galaxy evolution models with ram-pressure stripping applied to NGVS 3543 . . . 137
7.4 Identification and selection of young regions around the UDG . . . 141
7.4.1 u-band selection of regions . . . 142
7.4.2 NUV selection of regions . . . 142
7.5 Photometry of the selected regions . . . 145
7.6 Age and stellar mass estimation . . . 145
7.6.1 Fitting Starburst99 models with the photometry . . . 145
7.6.2 Confirmation with CIGALE . . . 150
7.6.3 Gradients among the regions . . . 152
7.7 A global scenario for the blue to red transition of a UDG . . . 152

7.1. Introduction

During the analysis of the sample of LSB galaxies discussed in Chapter 5 and 6, we noticed blue knots, diffuse UV emission and Hα detections within a few kiloparsecs of one of our target UDGs (source ID 3543 from Table. 5.2), which hereafter I refer to as NGVS 3543 (see Fig. 7.1).

Most of this emission is concentrated in blue knots close to the position of AGC 226178, an H I cloud detected during the ALFALFA H I blind survey (Haynes et al. 2011). The H I cloud of AGC 226178 was previously identified as an "almost dark galaxy" by Cannon et al. (2015), due to the absence of an evident optical counterpart to the elongated UV emission and H I detection observed for the source at the time. Cannon et al. (2015) also made deep higher resolution follow-up H I observations of AGC 226178 with VLA (a better spatial resolution in VLA with a beam size of 49″ compared to the ~3.5′ beam of ALFALFA), and confirmed that AGC 226178 is indeed at the distance of the Virgo cluster.

"Dark galaxies" (galaxies with gas but no stars) were considered as a possible solution to the large number of small galaxies predicted by the ΛCDM cosmology (Verde et al. 2002). However, stars were eventually found in most of the candidates, and the interest turned to "almost dark galaxies" (gas-rich objects with very little stellar light; Cannon et al. 2015; Janowiecki et al. 2015). The origin of AGC 226178 and other almost dark galaxies have been studied in the literature without obtaining a definitive answer (Cannon et al. 2015; Janowiecki et al. 2015; Leisman et al. 2017; Brunker et al. 2019). Cannon et al. (2015) classify their sample of almost dark candidates as either tidal debris or dwarf galaxies (AGC 226178 as the latter one). Among other propositions for the origin of dark galaxies are: disks of high angular momentum (spin) that are stable against star formation (Leisman et al. 2017; Jimenez & Heavens 2020); galaxies with low star formation efficiency (Janowiecki et al. 2015); galaxies that are gas stripped by or falling onto a companion galaxy (Sorgho et al. 2020); or tidal debris (Beccari et al. 2017).

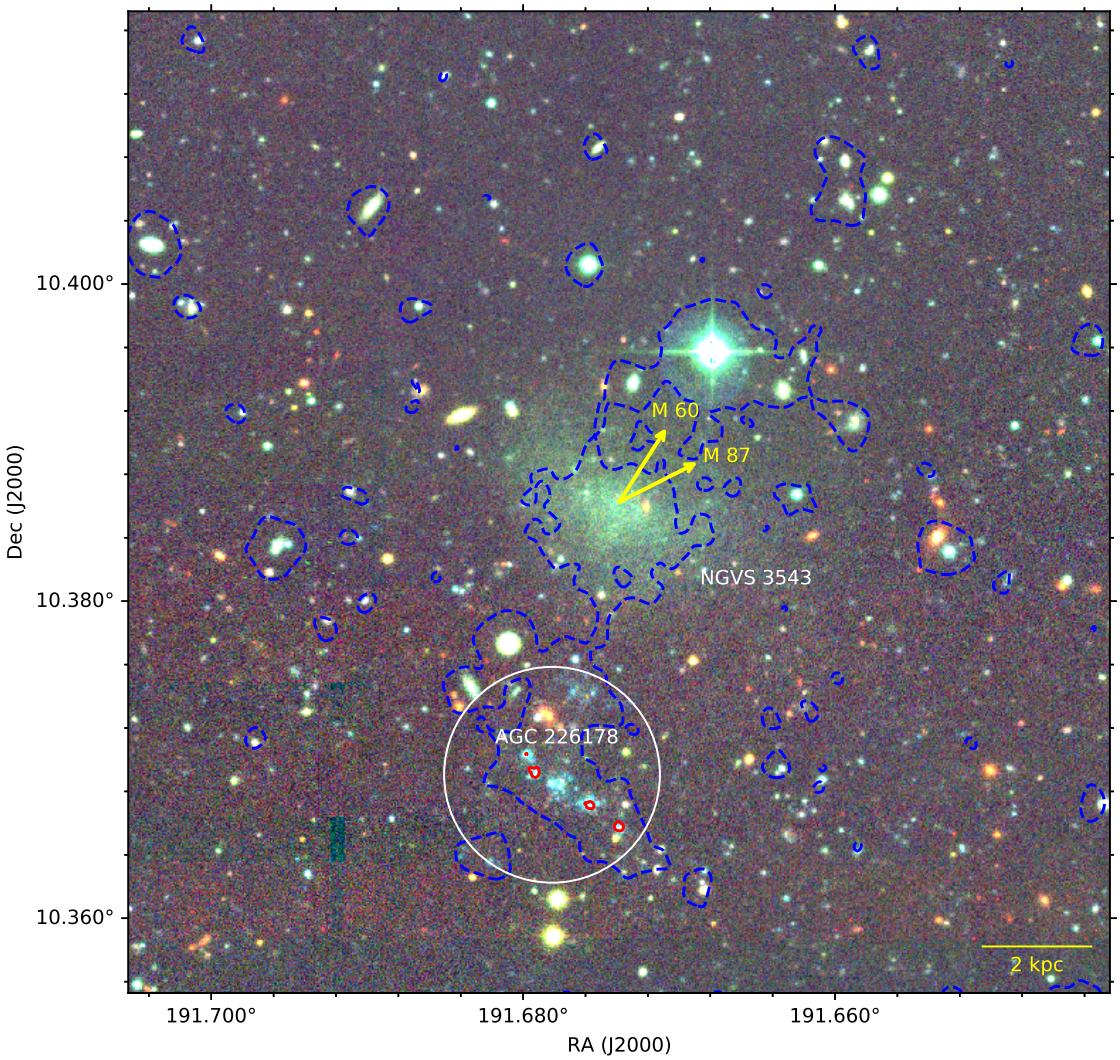

Figure 7.1.: NGVS *u, g, i*-colour composite image of the UDG galaxy NGVS 3543. The yellow arrows indicate the direction towards the Virgo cluster elliptical galaxies M87 and M60 at a distance of 1.26 Mpc and 0.39 Mpc, respectively. Blue dashed contours indicate the GALEX NUV detection at a surface brightness level of 27 mag arcsec^{-2} and red contours indicate the Hα detection in VESTIGE at the level of 1.6×10^{-17} erg s^{-1} cm^{-2} arcsec^{-2} (3σ). The white circle marks the position of the VLA HI detection of the source AGC 226178 from Cannon et al. (2015) with a beam size of $49''$.

In our new NGVS data (shown in Fig. 7.1), the optical counterpart to the elongated UV emission is resolved into very bright blue knots, several of them with detection of Hα emission. More knots and diffuse emission with star formation are seen to the south of the galaxy, with a morphology similar to tails within ram-pressure stripped galaxies, which are now quite commonly observed in nearby clusters including Virgo (Fumagalli et al. 2011; Kenney et al. 2014; Fossati et al. 2016; Boselli et al. 2020; Gullieuszik et al. 2020). However, so far they have not been found to be associated with dwarf quiescent galaxies. It is for the first time that such a tail of star forming regions is found in connection with a UDG. This makes NGVS 3543 an important object that could potentially help in understanding the debated formation and evolution of UDGs.

In this chapter, I present a summary of the work I recently published in Junais et al. (2021), where I analyse the full system of the UDG galaxy NGVS 3543 and the associated blue knots in its vicinity.

7.2. Data

For the study of NGVS 3543 and the star-forming regions in its vicinity, I used the photometric data from NGVS, VESTIGE and GUViCS in optical, Hα narrow-band and UV, respectively (see Sect. 5.2 for more details on the data). NGVS 3543 is one among the sample of 135 LSB galaxies discussed in Chapter 5 and 6, where I already presented the measurements and extracted surface brightness profiles for the entire sample. Chronologically speaking, I performed and finished the work on NGVS 3543 (presented in this chapter and published in Junais et al. 2021) before the complete analysis on the larger sample of LSBs discussed in Chapter 5 and 6. This also allowed me to test and verify all the measurement procedures beforehand for a single source and extending them to the larger sample later.

Fig. 7.2 shows measured radial surface profiles of NGVS 3543. The profiles are very close to exponential in the *u*, *g*, *r*, *i*, *z* and NUV bands. There is only an upper limit in the Hα narrow band, and a central detection in FUV, suggesting that star formation has been low throughout the last 100 Myr. The exponential decomposition of the profile from Sect. 5.4.5 gives a disk central surface brightness $\mu_{0,g} = 25.06$ mag arcsec^{-2} and disk effective radius $R_{e,g} = 23\farcs72$ (1.89 kpc). These values are close to the NGVS ones given in Table 5.2, which confirms that NGVS 3543 falls under the classical definition of the UDG regime (van Dokkum et al. 2015), discussed in Sect. 2.3. NGVS 3543 is not included in the outlier definition by Lim et al. (2020), where UDGs are defined as 2.5σ outliers in scaling relationships (see Sect. 2.3). However, I verified that NGVS 3543 lies very close (at 2.2σ) to the separation curve in these relations.

7.3. Galaxy evolution models with ram-pressure stripping applied to NGVS 3543

As discussed in detail in Chapter 6, I applied the galaxy evolution models with ram-pressure stripping for the UDG galaxy NGVS 3543, with the grid of model parameters from Table 6.1. Figure 7.3 shows the χ^2 distribution around the best solution.

The best model indicates that NGVS 3543 is an extended low-mass galaxy ($V_C = 42^{+4}_{-2}$ km s^{-1}; $\lambda = 0.15 \pm 0.01$) with an ongoing ram-pressure stripping event that will peak at ~30 Myr in the future ($t_{rps} = 13.53^{+0.01}_{-0.09}$ Gyr). The best model values obtained here are slightly different from the values published in Junais et al. 2021 ($V_C = 42^{+8}_{-4}$ km s^{-1}, $\lambda = 0.14^{+0.02}_{-0.01}$ and $t_{rps} = 13.4 \pm 0.1$ Gyr), since at the time we did not used the hyper-fine grid, discussed in Sect. 6.2, for modelling very recent RPS. However, both the models agree with each other within their error bars. This indicate that the galaxy originates in a dwarf ($V_C = 42$ km s^{-1}), extended disk ($\lambda = 0.14$ to 0.15 are typically associated to LSB regime, and not regular galaxies; Boissier et al. 2003), and with a very recent RPS event (since the peak of RPS is between 100 Myr in the past and 30 Myr in the future with a 150 Myr FWHM Gaussian distribution).

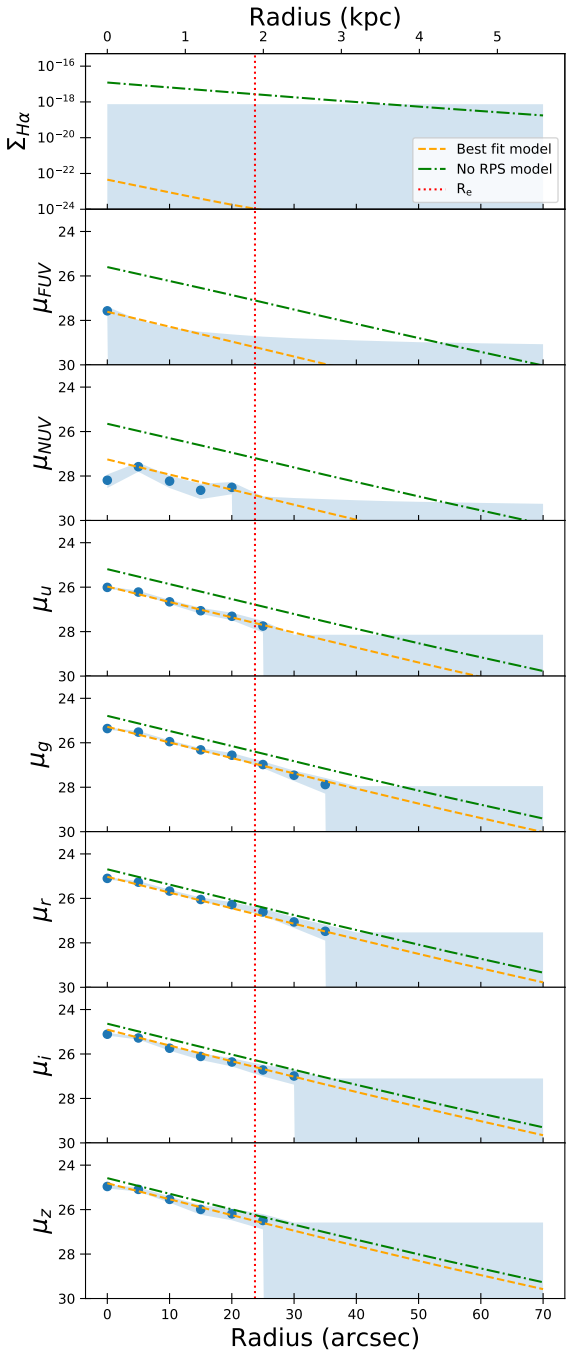

Figure 7.2.: Radial surface-brightness profiles of NGVS 3543 measured in eight bands, shown as blue filled dots (similar to the profiles from Fig. 5.7). The surface brightness units are in mag arcsec^{-2} for all the bands except for Hα which is in erg s^{-1} cm^{-2} arcsec^{-2}. The blue shaded area marks the 1σ error (for data points) and upper limits (3σ). The orange dashed line indicates the best-fit model described in Sect. 7.3 for a ram-pressure stripped galaxy (V_C = 42 km s^{-1}, λ = 0.15 and t_{rps} = 13.53 Gyr). The green dot-dashed line shows the same model for an unperturbed system (without RPS). The vertical red dotted line gives the g-band effective radius I measured for the galaxy.

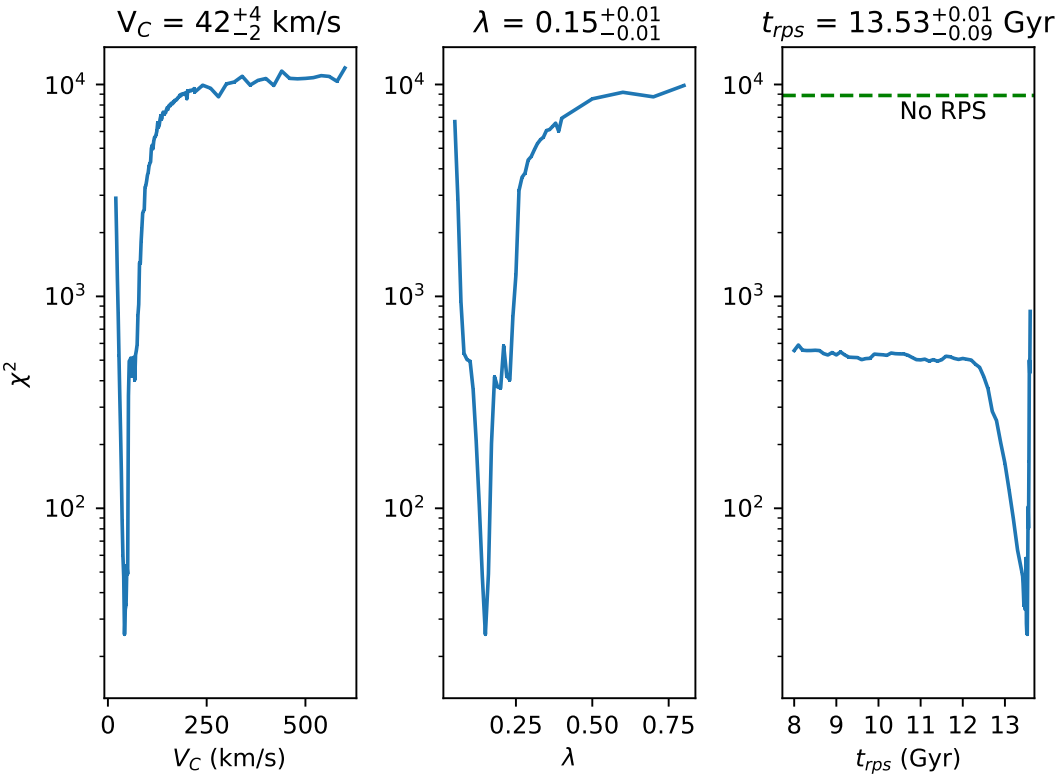

Figure 7.3.: χ^2 distribution for the determination of the best model parameters (V_C, λ, t_{rps}) for NGVS 3543, as discussed in Sect. 6.3. The best-fit parameters are given in the upper part of each panel. The given confidence limits (3σ) in each parameter are obtained following Avni (1976). The green horizontal dashed line in the right panel marks the χ^2 value corresponding to a model without RPS, keeping the same values of V_C and λ as in the best-fit model.

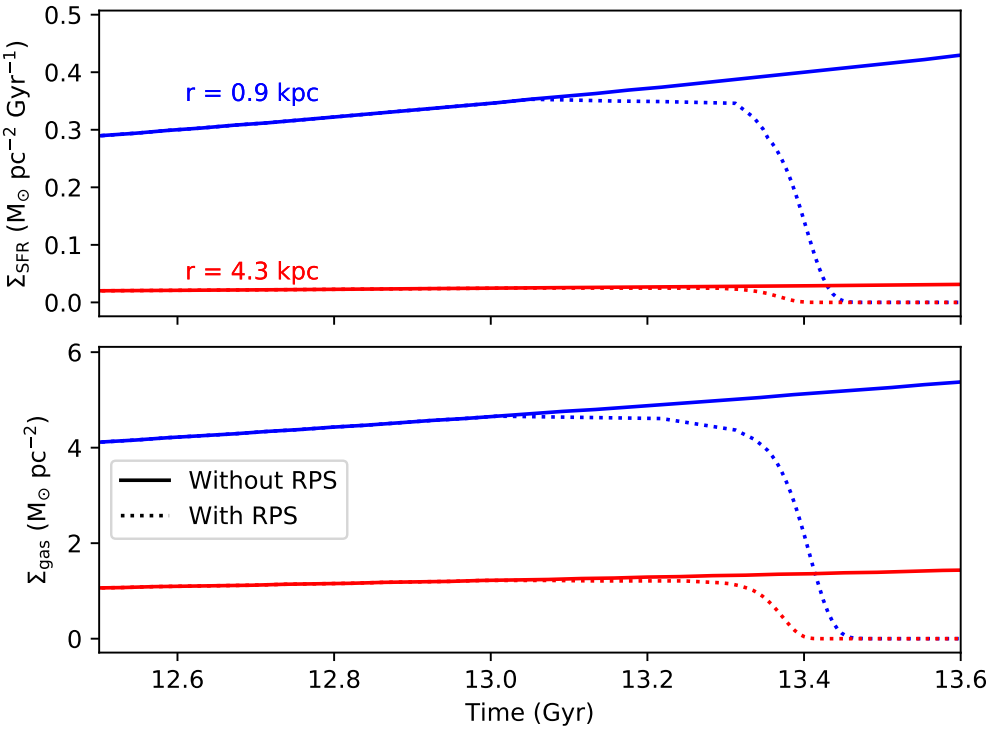

Figure 7.4.: Evolution of the surface densities of SFR and gas for the disk of NGVS 3543 obtained from the models. The dotted and solid lines show the best model with RPS and without RPS, respectively. The blue and red curves show the evolution at 0.9 kpc and 4.3 kpc from the galaxy centre.

The multi-wavelength profiles (including upper limits) of the UDG galaxy are very well fitted by these RPS models. Moreover, it is evidently clear from Figures 7.2 and 7.3 that a model without RPS is inconsistent with the observations. Hα upper limits and UV data proves to be of paramount importance to show that a recent RPS is present. Indeed, on short timescales, only these bands are very sensitive to the gas removal and quenching of star formation.

Figure 7.4 illustrates the effect of RPS on the UDG at two different radii (r = 0.9 and 4.3 kpc). The evolution of the gas and star formation rate surface density with and without the RPS shows that, although the peak of RPS is not yet reached based on the best model (t_{rps} = 13.53 Gyr), the RPS event had already started ~200 Myr ago. Due to the weak gravitational potential of the UDG, the RPS event very efficiently removed almost all of the gas in the galaxy well before reaching its peak. Therefore, although the RPS efficiency evolves as a Gaussian, we can see that the gas-loss rate is not symmetric around the peak because most of the gas has already been removed at that time. This is similar to what was found with much more sophisticated models of RPS by Roediger & Hensler (2005), suggesting RPS models specifically for UDGs may be needed in the future.

To check the robustness of my results, I also estimated the effect of varying the RPS peak efficiency and duration parameters (ϵ_0 and FWHM), on the best fit models. As discussed in Sect. 6.1.3, the choice of a constant RPS efficiency (ϵ_0 = 1.2 $M_\odot$ kpc^{-2} yr^{-1}) and a unique FWHM of 150 Myr was done to simplify the modelling and to reduce long computation time for the large grid of models used in this

Table 7.1.: Properties of the best RPS models, and the model with the same spin and velocity but without the RPS. The uncertainties given in the RPS models are from the confidence limits in t_{rps}, λ and V_C parameters. For the non-RPS models, the uncertainties are from the error in λ and V_C alone.

Property	RPS models	Model without RPS
$R_{e,g}$ (kpc)	2.13 ± 0.28	2.21 ± 0.36
$\mu_{0,g}$ (mag arcsec^{-2})	25.30 ± 0.06	24.82 ± 0.41
log $M_\star$ ($M_\odot$)	7.11 ± 0.07	7.15 ± 0.09
log $M_{\rm gas}$ ($M_\odot$)	3.84 ± 0.06	8.59 ± 0.43
log SFR ($M_\odot$ yr^{-1})	-8.61 ± 0.06	-1.99 ± 0.43
$Z_{\rm gas}$ ($Z_\odot$)	0.28 ± 0.04	0.14 ± 0.10

work. However, for the single case of NGVS 3543, I made several tests to estimate the uncertainties that this assumption brings to the final results of my RPS modelling. For this purpose, I fixed the λ and V_C obtained from the best fit model, because these two parameters affect mostly the long-wavelength range and are weakly affected by a recent RPS event (Boselli et al. 2006). Then, we computed new models with ϵ_0 in the range of 0.2 to 1.6 $M_\odot$ kpc^{-2} yr^{-1} and the Gaussian shape of the RPS with FWHM in the range 100 to 200 Myr following Boselli et al. (2006) and Vollmer et al. (2001), respectively. This was done for the t_{rps} values in the range of 13.0 to 13.6 Gyr (because my best fit clearly indicates a recent RPS event). However, fitting the observed profiles with all these new models still do not change our previously obtained best model (the new best model is within the uncertainty of the previous one), proving the robustness of the results.

The results from the modelling suggest that only the combination of a dwarf galaxy velocity with a large spin and recent RPS could reproduce the observed properties of NGVS 3543. Table 7.1 gives several parameters of NGVS 3543 obtained from the models. The comparison of the RPS models with the unperturbed one also tells us how much the galaxy is affected by the ongoing RPS event. The galaxy before undergoing RPS was dominated by gas and because of the weak potential of the galaxy, most of the gas has been removed in the RPS model, without much variation in the stellar mass. As a result, star formation has been almost totally quenched with respect to the non-RPS model, consistent with the faintness of the galaxy in UV and blue optical wavelengths.

In the case of metallicity, the gas-phase metallicity is slightly larger in the RPS model, which is to be expected because now the metals expelled by the previous generation of stars are diluted in a much smaller amount of remaining gas after the RPS event started (although its peak is not attained). Finally, we can note that the effective radius and the central surface brightness before and after the RPS event have not changed much. Therefore, with these values, the unperturbed galaxy before entering the cluster would still be a UDG, but a star-forming one with bluer colours. This could correspond to the population of blue UDGs whose existence is mainly found in the field rather than cluster environments (Prole et al. 2019).

7.4. Identification and selection of young regions around the UDG

The recent RPS event in NGVS 3543 obtained from the models discussed in Sect. 7.3, along with the blue knots of star-forming regions in its vicinity points to the direction of a correlation between the RPS scenario and the formation of AGC 226178. To investigate this, I decided to study the properties of the newly formed young stellar regions in the vicinity of NGVS 3543.

The initial step in this process was to identify the potential young regions within the system. For this purpose, I followed two different selection criteria. The first one was an automated selection of young regions based on the u-band image with a high angular resolution. The second one was a manual selection based on the NUV image, which despite its poor angular resolution, is very sensitive to the young stellar population and thus perfectly suitable to identify newly formed objects.

7.4.1. u-band selection of regions

The u-band selection of young regions was done using the `Photutils find_peaks` Python package. This procedure automatically identifies all the local peaks in the u-band image of NGVS 3543, above a certain given threshold (5σ) of the background sky level. A total of 330 regions were selected at this stage, which was then used as an initial set of regions for which I performed aperture photometry within circular regions of $3''$ diameter. The size of the aperture was optimally chosen such that they are big enough to include the entire flux of a region and at the same time resolve them from nearby companions. The photometry was performed with the `Photutils aperture_photometry` package in the optical bands and corrected for Milky Way foreground Galactic extinction (similar correction as done for the surface brightness profiles of NGVS 3543, described in Sect. 5.4.4).

To identify newly formed regions among the initial set of regions, I compared their measured $u-g$ colors to that of the colors for a single burst population from Boselli et al. (2009), created using `Starburst99` (Leitherer et al. 1999), as shown in Fig. 7.5. The `Starburst99` models were created using a Kroupa (2001) initial mass function (IMF) between 0.1 and 100 $M_{\odot}$, and four different metallicities (0.05, 0.4, 1, 2 $Z_{\odot}$) based on Geneva stellar evolution tracks. From Fig. 7.5, we can see that the $u-g$ colour evolution of a single burst population, irrespective of the metallicity, has a similar colour of $u-g \sim 0.4$ mag when close to the age of 100 Myr. Colours bluer than this always correspond to a young population. Therefore, here I chose to adopt this $u-g$ colour-cut to select the young stellar regions from my initial set of identified regions. Applying the colour selection, followed by the removal of regions corresponding to known background NED sources, resulted in a total of 73 regions along the vicinity of NGVS 3543.

Figure 7.6 shows the number density of the 73 u-band selected regions around NGVS 3543, measured within a grid of $25'' \times 25''$ [1]. There is a clear over-density of blue regions towards the south of NGVS 3543, coinciding with the H I detection of AGC 226178. This confirms the visual impression that the blue knots are associated with AGC 226178. Therefore, in the following analysis, I focus on the southern quadrant of the NGVS 3543 stamp (shown as a red dashed box in Fig. 7.6), where a total of 38 regions are selected.

It is likely that the 38 u-band selected regions, even after the colour-selection and removal of known NED catalogued sources, can have some contaminant background regions not associated to NGVS 3543 or AGC 226178. To estimate this, I used the dispersion from the density map shown in Fig. 7.6 and found that 29 out of the 38 regions lie outside the 3σ level of the mean background density (white dashed box in Fig. 7.6), indicating that we cannot rule out the possibility that they are background contaminants. However, for the remaining 9 sources coinciding with AGC 226178 H I detection, with a 3σ confidence, we can assume that they are associated with AGC 226178.

7.4.2. NUV selection of regions

For the sake of completeness, I also made a selection of young regions based on the GALEX NUV image of NGVS 3543, which is more sensitive to the young stellar population than the u-band. First, I created contours of the NUV image at an arbitrarily low surface brightness level of 27 mag arcsec^{-2} and smoothing of 2 GALEX pixels (blue dashed contours in Fig. 7.1). Inspecting these contours helped me to visually identify diffuse emission coinciding with AGC 226178, along with few other UV regions

[1] The grid size of $25''$ was chosen to sample the AGC 226178 H I beam size of $49''$.

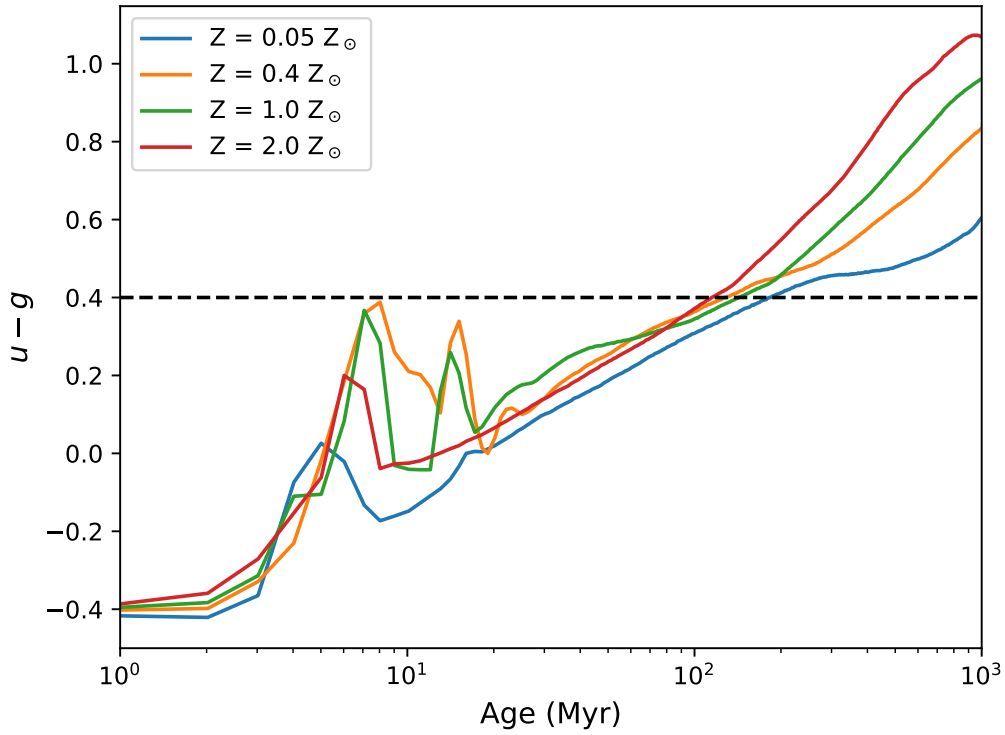

Figure 7.5.: $u-g$ color evolution of a single-burst population derived using `Starburst99` models for different metallicities. The black dashed line marks the $u-g$ colour limit (corresponding to an approximate age of less than 100 Myr) I adopted for the selection of young regions discussed in Sect. 7.4.1.

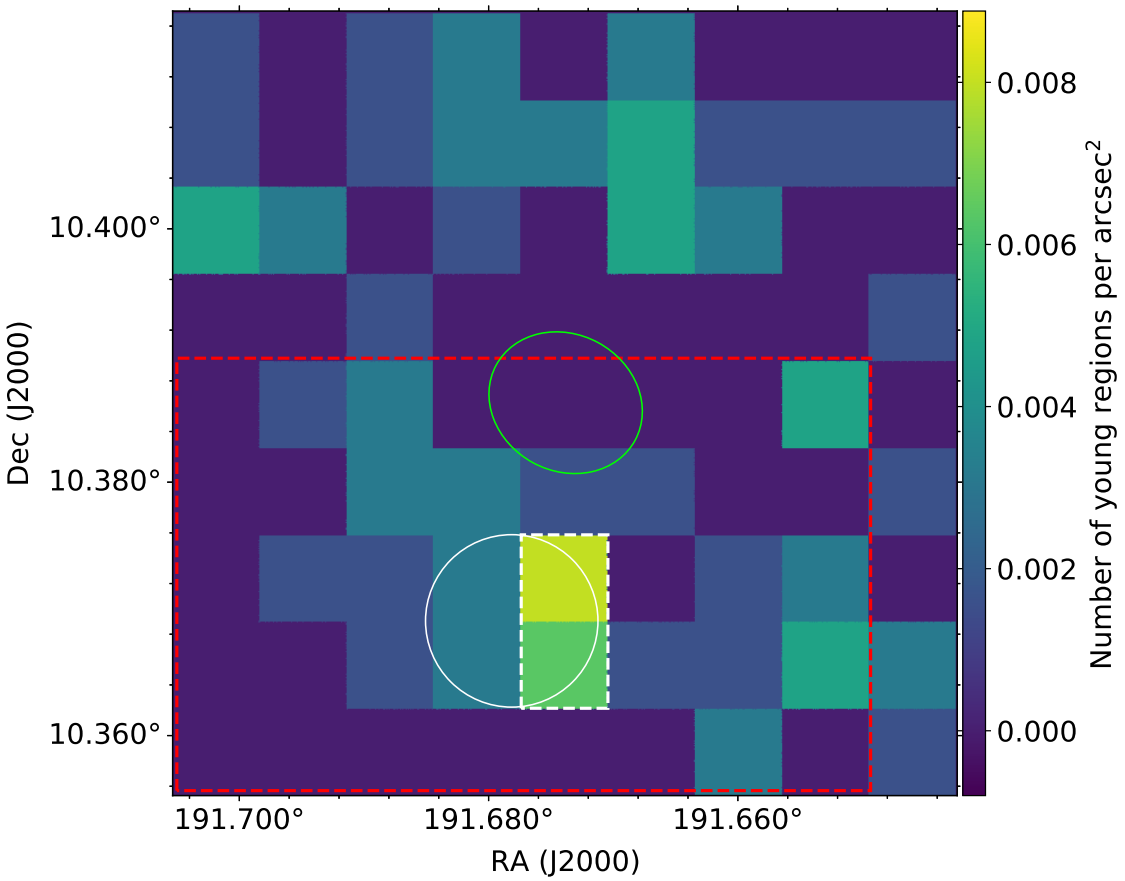

Figure 7.6.: Number density of the u-selected blue ($u - g < 0.4$ mag) regions around the galaxy NGVS 3543 (marked as the green ellipse). The white circle marks the position of the VLA HI detection of AGC 226178 from Cannon et al. (2015), with a beam size of $49''$. The white dashed box indicates the region above 3σ level of the mean background number density. The red dashed box ($190'' \times 120''$) shows the area where the properties of the blue regions are analysed in this work.

along its vicinity. In this way, I selected a total of 14 UV regions, after visual identification and removal of any known NED catalogued sources. For the UV selected regions too, I needed to quantify the possible number of background contaminants. Following Boselli et al. (2018b), I estimated the possible contamination of background UV sources using the number counts given in Xu et al. (2005). At the limiting magnitude of our detections ($NUV \leq 22.7$ mag, for a GALEX MIS imaging; Morrissey et al. 2005), the expected number of background contaminants is ~1700 sources per deg^2, or equivalently 3 contaminant UV sources in the area of $190'' \times 120''$ NUV data I inspected. Therefore, the rest of the UV regions (11 out of 14) are likely related to the system under study.

Figure. 7.7 shows the 38 u-band and 14 UV selected regions discussed above. These regions will be subjected to further measurements analysis in the following sections.

7.5. Photometry of the selected regions

The photometric measurements of the u-band and UV selected regions were done using the `Photutils` `aperture_photometry` Python package. For the u-band selected regions, the flux in each region was measured on the optical images, retaining the original resolution of the images. However, for the UV selected regions, the photometry was done on the optical as well as the UV images. In this case, the optical images were convolved with a Gaussian kernel (corresponding to their original resolution given in Table 5.1) to match the GALEX resolution. All the photometric measurements were also corrected for the Milky Way foreground Galactic extinction. Table 7.2 gives the photometric measurements of all the selected regions.

7.6. Age and stellar mass estimation

7.6.1. Fitting Starburst99 models with the photometry

For characterising the nature of the selected regions, one needs to quantify their physical properties. For this purpose, I used the `Starburst99` models discussed in Sect. 7.4.1 along with the photometry from Table. 7.2, to estimate the stellar mass and age of the regions.

Figure. 7.8 shows the evolution of a single-burst population of stellar-mass 1 $M_\odot$ obtained from the `Starburst99` models (see Sect. 7.4.1). Fitting these models to match the observed photometry in all the bands give the stellar mass and age of each region. For this purpose, I performed a χ^2 minimisation procedure to fit the observation with the models of different metallicities. Any model violating the observed upper limits (shown in Table 7.2) was also rejected. The Hα measurements play a major role in constraining the age of the regions, with an upper limit indicating an age greater than 10 Myr in massive regions. In this way, I estimated the stellar mass, age and metallicity for each of my selected regions (both u-band and UV selected regions).

Figure 7.9 shows an example of the χ^2 minimisation result obtained for region 25. The best fit model with the least χ^2 value indicate that region 25 has a stellar mass of ~500 $M_\odot$, age 8.2 ± 0.2 Myr and a metallicity 0.4 times the solar value. Similar results for all the regions are shown in Fig. 7.10. We can see that both the u-selected and UV-selected regions with Hα detection have younger ages. For regions without an Hα detection, the ages of the UV-selected regions tend to be larger than those of the u-selected regions, although UV emission is usually related to a younger population than u-band emission. However, the larger apertures of the UV regions make them more likely to be affected by any older underlying stellar population or background sources, as discussed in Sect. 7.4. For a few of the fainter regions with low stellar mass and larger error bars, we are close to the u-band detection limit on age measured for a $3''$ aperture at the depth of the u-band data and the predictions from the `Starburst99` models.

For regions younger than 100 Myr (blue regions) in Fig. 7.10, I obtained a mean age of 14 ± 1 Myr and 21 ± 4 Myr, and a corresponding mean stellar mass of 2.4×10^3 $M_\odot$ and 2.3×10^4 $M_\odot$, for the u-band

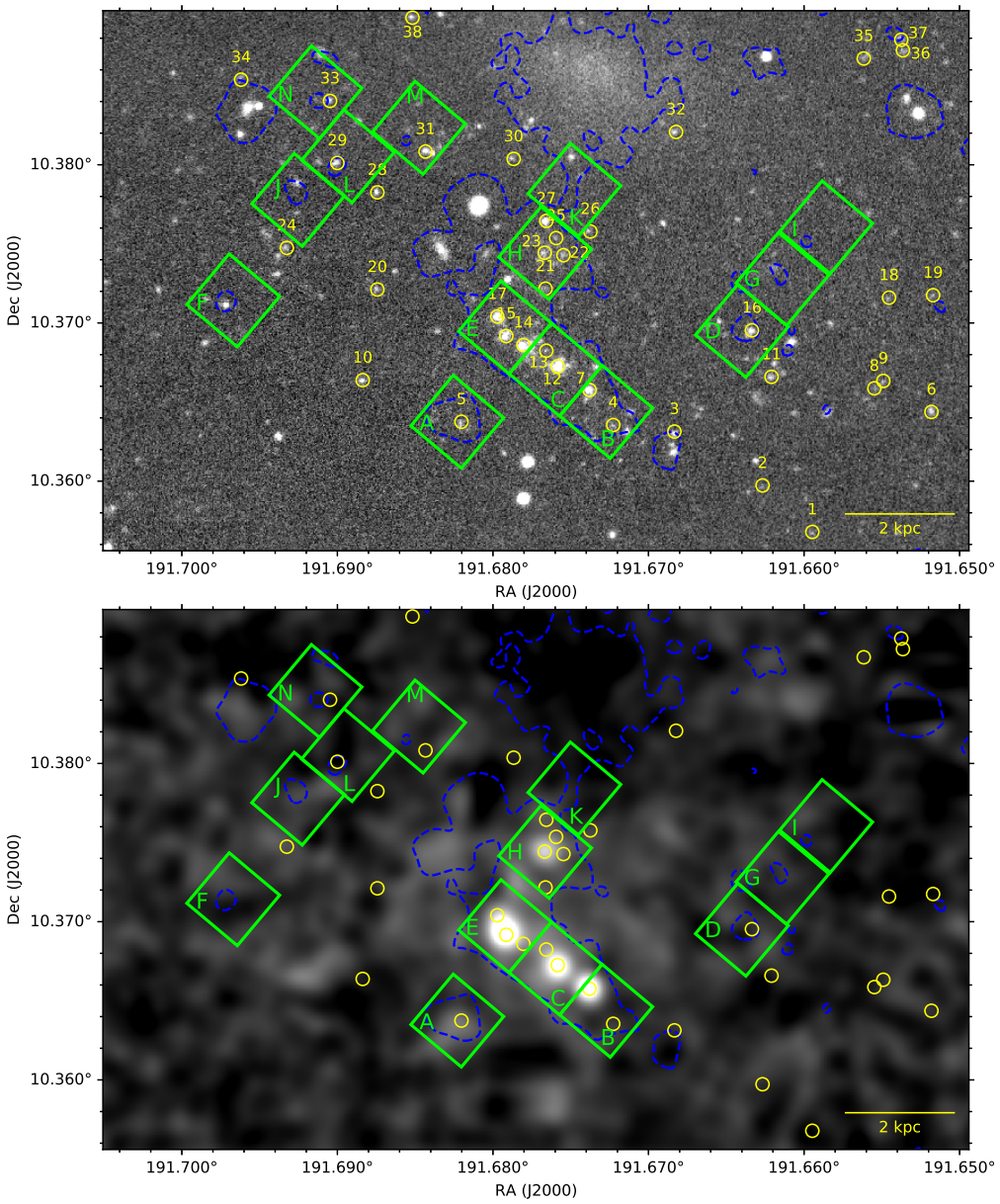

Figure 7.7.: *Top:u*-band grayscale image along the area selected for my analysis. *Bottom:* VESTIGE continuum-subtracted Hα image smoothed at the resolution of GALEX. The yellow circles and the green boxes, marked with their names, are respectively the *u*-band-selected and UV-selected regions, discussed in Sect. 7.4. The region names are attributed based on increasing declination. The blue dashed lines are the same NUV contours from GALEX as shown in Fig. 7.1.

Table 7.2.: Photometry for the *u*-band selected (top panel) and UV selected regions (bottom panel). Column details: (1) Name of the region. (2) Projected distance of the region from the centre of NGVS 3543. (3-7) *u*, *g*, *r*, *i* and *z*-band magnitudes. (8) VESTIGE Hα flux. (9-10) GALEX *NUV* and *FUV* magnitudes. The upper limits (3σ) in the broad-band magnitudes and in the Hα fluxes are denoted with > and < symbols, respectively.

Region	Distance	*u*	*g*	*r*	*i*	*z*	Hα Flux	*NUV*	*FUV*
	(kpc)	(mag)	(mag)	(mag)	(mag)	(mag)	(10^{-16} erg s^{-1} cm^{-2})	(mag)	(mag)
(1)	(2)	(3)	(4)	(5)	(6)	(7)	(8)	(9)	(10)
1	9.4	24.97 ± 0.21	24.96 ± 0.22	> 24.45	24.31 ± 0.34	> 23.95	< 0.14	–	–
2	8.3	25.26 ± 0.29	25.3 ± 0.32	> 24.45	> 24.47	> 23.95	< 0.14	–	–
3	6.8	24.1 ± 0.1	23.84 ± 0.08	23.85 ± 0.22	23.47 ± 0.15	23.42 ± 0.23	< 0.14	–	–
4	6.6	24.52 ± 0.14	24.34 ± 0.12	24.06 ± 0.26	23.78 ± 0.2	> 23.95	< 0.14	–	–
5	6.9	24.26 ± 0.11	24.26 ± 0.12	> 24.45	> 24.47	> 23.95	0.24 ± 0.02	–	–
6	8.9	24.04 ± 0.08	23.82 ± 0.08	23.92 ± 0.23	23.22 ± 0.12	23.22 ± 0.18	< 0.14	–	–
7	5.9	23.01 ± 0.05	22.94 ± 0.05	22.44 ± 0.06	22.46 ± 0.06	22.38 ± 0.08	1.54 ± 0.03	–	–
8	7.8	25.08 ± 0.24	25.08 ± 0.25	> 24.45	24.3 ± 0.34	> 23.95	< 0.14	–	–
9	7.8	24.88 ± 0.2	24.93 ± 0.22	> 24.45	24.03 ± 0.25	> 23.95	< 0.14	–	–
10	7.0	24.1 ± 0.1	24.02 ± 0.1	23.48 ± 0.15	23.41 ± 0.14	> 23.95	< 0.14	–	–
11	6.6	24.12 ± 0.1	23.99 ± 0.09	23.56 ± 0.16	23.04 ± 0.1	23.03 ± 0.16	< 0.14	–	–
12	5.5	22.48 ± 0.05	22.4 ± 0.05	22.42 ± 0.06	22.68 ± 0.07	23.12 ± 0.18	1.17 ± 0.02	–	–
13	5.2	24.58 ± 0.15	24.54 ± 0.15	> 24.45	> 24.47	> 23.95	0.27 ± 0.02	–	–
14	5.2	22.63 ± 0.05	22.57 ± 0.05	22.74 ± 0.08	22.9 ± 0.08	23.27 ± 0.2	0.2 ± 0.02	–	–
15	5.1	22.9 ± 0.05	22.95 ± 0.05	22.9 ± 0.08	23.06 ± 0.1	23.84 ± 0.36	1.59 ± 0.03	–	–
16	5.7	23.51 ± 0.05	23.27 ± 0.05	23.02 ± 0.1	22.49 ± 0.06	22.32 ± 0.08	< 0.14	–	–
17	4.9	22.85 ± 0.05	22.55 ± 0.05	22.32 ± 0.05	22.4 ± 0.06	22.64 ± 0.11	0.55 ± 0.02	–	–
18	6.9	24.92 ± 0.2	24.85 ± 0.2	> 24.45	24.18 ± 0.3	> 23.95	< 0.14	–	–
19	7.5	24.98 ± 0.21	25.06 ± 0.25	> 24.45	> 24.47	> 23.95	< 0.14	–	–
20	5.6	24.47 ± 0.13	24.24 ± 0.12	23.88 ± 0.22	23.52 ± 0.16	23.69 ± 0.3	< 0.14	–	–
21	4.1	24.32 ± 0.12	24.08 ± 0.1	23.87 ± 0.22	23.06 ± 0.1	22.86 ± 0.14	< 0.14	–	–
22	3.5	24.09 ± 0.09	23.96 ± 0.08	23.77 ± 0.2	23.57 ± 0.16	23.44 ± 0.24	< 0.14	–	–
23	3.5	23.74 ± 0.06	23.71 ± 0.07	23.53 ± 0.16	23.74 ± 0.19	23.84 ± 0.36	0.64 ± 0.02	–	–
24	6.4	24.4 ± 0.12	24.28 ± 0.12	23.7 ± 0.18	23.26 ± 0.12	> 23.95	< 0.14	–	–
25	3.2	24.76 ± 0.17	24.87 ± 0.21	> 24.45	24.16 ± 0.29	> 23.95	0.2 ± 0.02	–	–
26	3.0	24.53 ± 0.14	24.37 ± 0.13	24.1 ± 0.28	24.08 ± 0.26	23.62 ± 0.29	< 0.14	–	–
27	2.9	23.14 ± 0.05	23.14 ± 0.05	22.96 ± 0.1	22.55 ± 0.06	22.6 ± 0.11	< 0.14	–	–
28	4.5	24.24 ± 0.11	24.17 ± 0.11	24.27 ± 0.33	23.98 ± 0.24	> 23.95	< 0.14	–	–
29	4.9	23.9 ± 0.08	23.7 ± 0.07	23.34 ± 0.13	22.74 ± 0.08	22.73 ± 0.12	< 0.14	–	–
30	2.2	24.52 ± 0.14	24.32 ± 0.12	24.06 ± 0.26	23.52 ± 0.16	23.46 ± 0.24	< 0.14	–	–
31	3.4	23.52 ± 0.06	23.41 ± 0.05	23.08 ± 0.11	23.32 ± 0.12	23.14 ± 0.18	< 0.14	–	–
32	2.0	24.08 ± 0.09	23.9 ± 0.08	23.46 ± 0.15	23.38 ± 0.14	23.0 ± 0.15	< 0.14	–	–
33	4.8	24.1 ± 0.1	24.21 ± 0.11	23.92 ± 0.23	23.58 ± 0.16	23.64 ± 0.29	< 0.14	–	–
34	6.3	24.72 ± 0.16	25.03 ± 0.24	24.15 ± 0.29	24.12 ± 0.28	> 23.95	< 0.14	–	–
35	5.0	24.46 ± 0.13	24.31 ± 0.12	> 24.45	24.16 ± 0.29	23.87 ± 0.37	< 0.14	–	–
36	5.7	24.42 ± 0.12	24.34 ± 0.12	23.37 ± 0.14	22.95 ± 0.09	22.55 ± 0.1	< 0.14	–	–
37	5.7	24.38 ± 0.12	24.2 ± 0.11	24.22 ± 0.32	23.64 ± 0.17	23.22 ± 0.19	< 0.14	–	–
38	3.3	24.16 ± 0.1	23.96 ± 0.08	23.28 ± 0.12	22.78 ± 0.08	22.56 ± 0.11	< 0.14	–	–
A	6.9	> 22.29	> 22.21	> 21.64	> 21.26	> 20.8	< 1.79	22.56 ± 0.12	22.48 ± 0.11
B	6.3	21.82 ± 0.24	21.2 ± 0.15	20.7 ± 0.16	20.0 ± 0.12	20.26 ± 0.24	2.82 ± 0.27	21.81 ± 0.06	21.81 ± 0.06
C	5.6	20.94 ± 0.11	20.74 ± 0.1	20.86 ± 0.18	20.48 ± 0.18	> 20.8	5.45 ± 0.26	20.89 ± 0.05	20.87 ± 0.05
D	5.6	> 22.29	22.0 ± 0.32	> 21.64	21.16 ± 0.36	> 20.8	< 1.79	23.26 ± 0.22	> 23.82
E	5.0	20.94 ± 0.11	20.68 ± 0.08	20.69 ± 0.15	20.22 ± 0.14	20.61 ± 0.33	5.63 ± 0.26	20.79 ± 0.05	20.83 ± 0.05
F	7.8	> 22.29	> 22.21	> 21.64	> 21.26	> 20.8	< 1.79	23.7 ± 0.36	> 23.82
G	5.2	> 22.29	> 22.21	> 21.64	20.59 ± 0.2	20.42 ± 0.26	< 1.79	23.52 ± 0.29	> 23.82
H	3.5	21.42 ± 0.16	21.2 ± 0.14	20.63 ± 0.15	19.78 ± 0.1	19.62 ± 0.12	3.16 ± 0.27	21.48 ± 0.05	21.64 ± 0.05
I	5.2	> 22.29	> 22.21	> 21.64	20.97 ± 0.3	20.66 ± 0.34	< 1.79	> 23.82	> 23.82
J	5.8	> 22.29	> 22.21	> 21.64	20.86 ± 0.26	> 20.8	< 1.79	> 23.82	> 23.82
K	2.3	22.06 ± 0.32	21.4 ± 0.18	20.78 ± 0.16	20.12 ± 0.13	20.2 ± 0.22	< 1.79	22.92 ± 0.16	23.26 ± 0.22
L	4.7	> 22.29	> 22.21	> 21.64	21.17 ± 0.37	> 20.8	< 1.79	> 23.82	> 23.82
M	3.3	> 22.29	> 22.21	> 21.64	> 21.26	> 20.8	< 1.79	> 23.82	> 23.82
N	5.0	> 22.29	> 22.21	> 21.64	> 21.26	> 20.8	< 1.79	23.66 ± 0.34	> 23.82

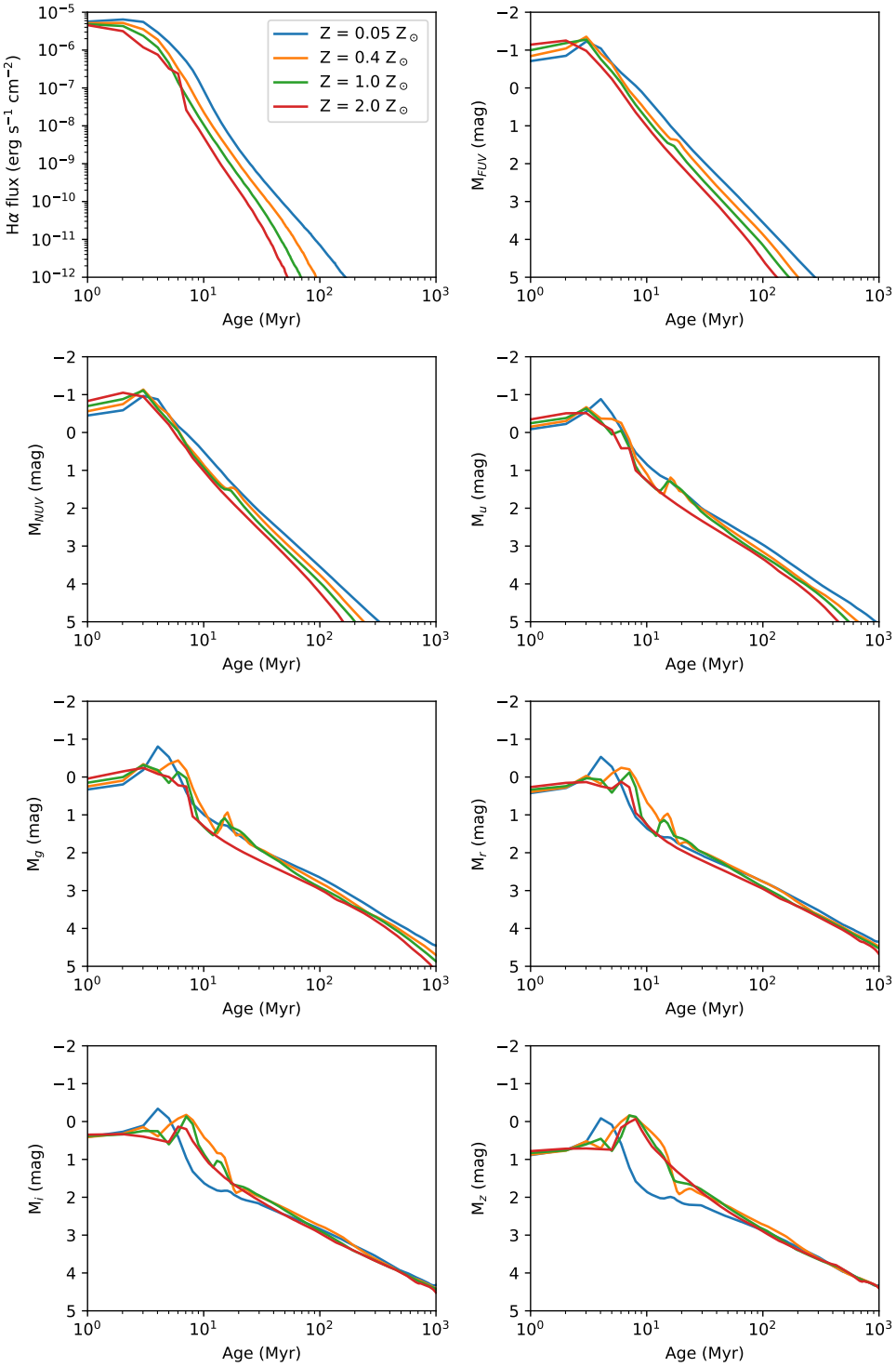

Figure 7.8.: Evolution of the `Starburst99` models for a single-burst population of stellar-mass 1 $M_\odot$, for all the photometric bands, studied in this work. The magnitudes are absolute magnitudes in AB units (except for the Hα flux in erg s^{-1} cm^{-2}). The different coloured lines indicate the models in four different metallicities.

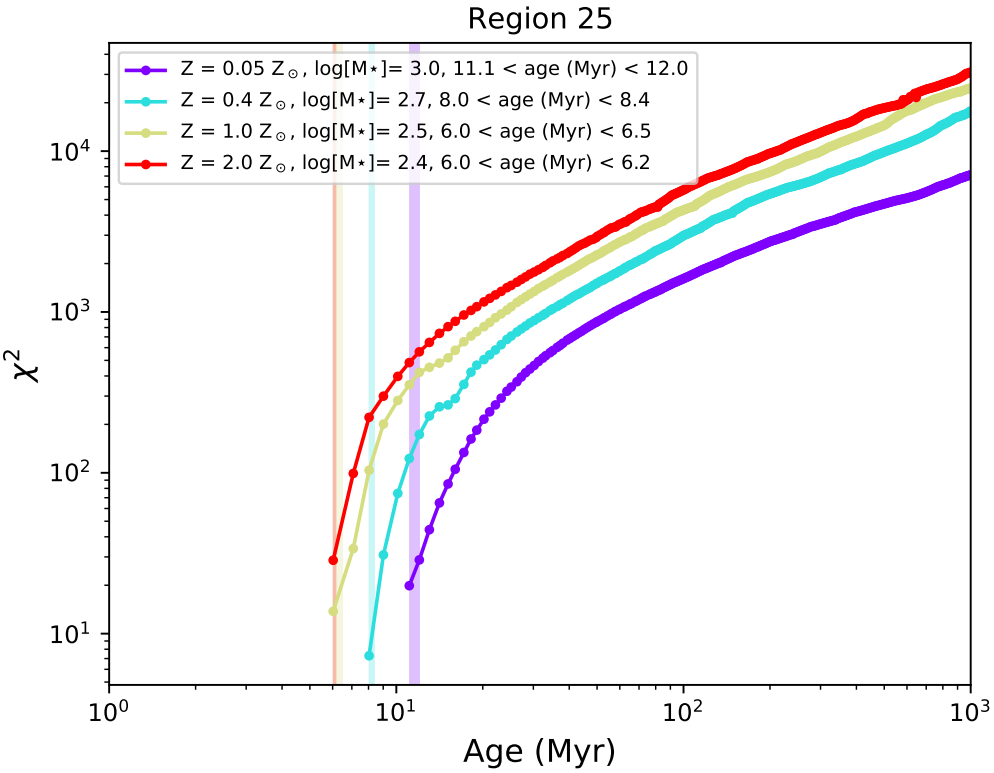

Figure 7.9.: Example of the χ^2 distribution for determination of the stellar mass, age and metallicity of region 25 (shown in Table 7.2). The vertical shaded bands are the 3σ confidence limits around the best-fit ages. Note that all the models with an age of less than 6 Myr for this region are rejected due to upper limit violations, resulting in the unusual single-sided χ^2 distribution above.

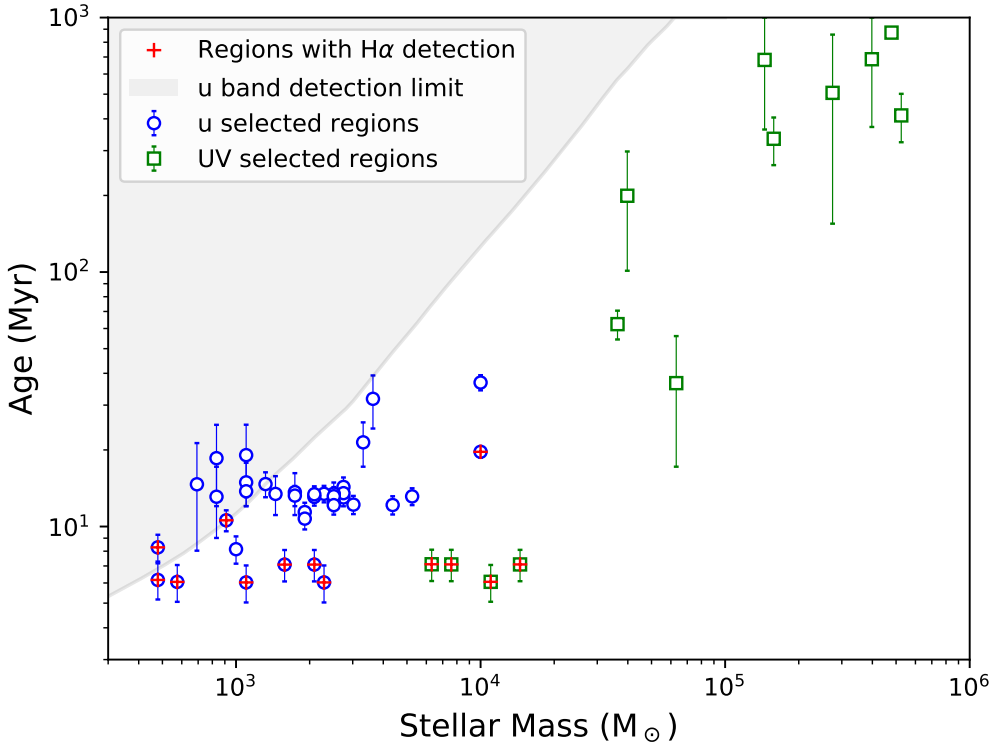

Figure 7.10.: Age and stellar mass determined for all the selected regions. The blue circles and green squares represent u-band- and UV-selected regions, respectively. The grey shaded area is the u-band detection limit (lower mass or older clusters in this area would not be detected based on the luminosity predicted by the `Starburst99` models). The red crosses identify the Hα detected regions.

and UV-selected regions, respectively. This is within the mass range of $10^3 - 10^5$ $M_\odot$ found in giant molecular clouds and HII regions (Kennicutt 1989). For most cases, the metallicity is not very well constrained due to the lack of enough data to discriminate between different metallicities. However, the age and stellar mass usually change by less than a few million years and a few tenths of dex, respectively, over various metallicities. Therefore, further in this work, I focus only on the stellar mass and age of these regions, which are relatively well constrained.

7.6.2. Confirmation with CIGALE

Numerous assumptions in the stellar population models and fitting methodology could affect the results discussed in Sect. 7.6.1. To investigate this, I carried out a completely independent estimation of the properties of the regions using the SED modelling code CIGALE (Burgarella et al. 2005; Noll et al. 2009; Boquien et al. 2019). This was done with the help of my collaborator Médéric Boquien (University of Antofagasta), who ran the CIGALE models on the measured photometry of the regions. Unlike the χ^2 minimisation procedure I followed for the `Starburst99` models, CIGALE uses a Bayesian approach where physical parameters are estimated by a maximum likelihood method, also taking in to account

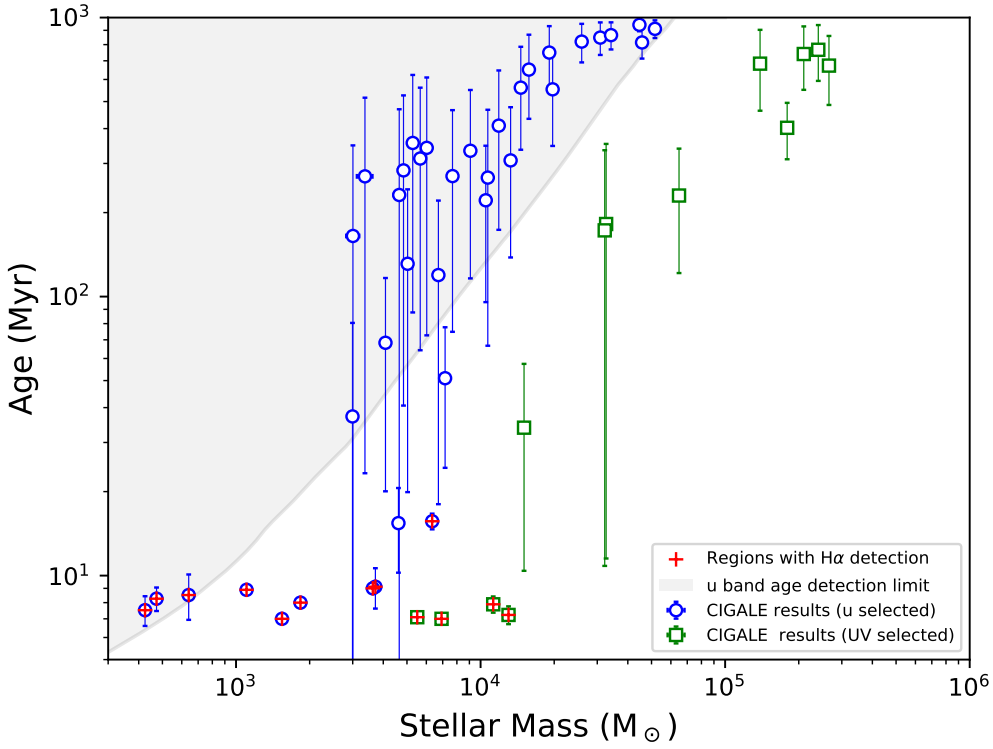

Figure 7.11.: Age and stellar mass determined for all the regions using CIGALE. This figure can be directly compared to the Fig. 7.10 obtained with `Starburst99` models.

the upper-limits in observations. Other key differences in CIGALE with respect to the `Starburst99` models are the assumed Chabrier (2003) IMF instead of the Kroupa (2001) IMF, and the Bruzual & Charlot (2003) population synthesis models.

The stellar masses and ages obtained with CIGALE are shown in Fig. 7.11. This can be directly compared to those derived using `Starburst99` (see Fig. 7.10). CIGALE gives older ages and larger scatters than `Starburst99` for many of the u-band and UV-selected regions. This can be due to the different spectrum of very young stellar populations between `Starburst99` and Bruzual & Charlot (2003). In the age range 5-20 Myr for single star populations, `Starburst99` models have red supergiants as an important contributor, resulting in variations in the model predictions. This is also the reason for the presence of peaks seen in Fig. 7.8 at this age range (these peaks are less large when Bruzual & Charlot (2003) populations are considered). On the other hand, for regions with Hα detection, both CIGALE and `Starburst99` consistently gives young ages. The Hα measurements prove to be a very strong constraint in the modelling of very young star-forming regions.

Therefore, regardless of the code used for the stellar population or the fitting procedure, we always find that a significant number of regions are indeed young (< 20 Myr), with similar stellar masses. For further analysis in this work, I use the stellar mass and ages obtained from the `Starburst99` models.

7.6.3. Gradients among the regions

The results obtained from the previous sections shows that the majority of the star complexes studied in association with the UDG galaxy NGVS 3543 have ages of a few tens of millions of years (see Fig. 7.10). These regions might therefore have formed within the gas removed from the NGVS 3543 after an RPS event that started ~200 Myr ago. To test this, I looked at the measured properties of the regions to see if there is any visible gradient among them in connection to NGVS 3543.

Figure 7.12 shows the $u-g$ colour and age of the young regions as a function of their projected distance from the centre of the UDG. The top panel of Fig. 7.12 shows a comparison of the measured $u-g$ colour of our regions with that of a similar estimate on the blue tail of another Virgo cluster galaxy VCC 1217/IC 3418 from Fumagalli et al. (2011). Although the $u-g$ colours I measured are consistent with theirs, there is no indication of a clear gradient, contrary to what they observed in the outermost part of the extended tail. In our case, with a large dispersion in the colour and proximity to NGVS 3543, it is hard to draw strong conclusions as to the presence of a colour gradient among the regions.

The bottom panel of Fig. 7.12 shows the measured age of the regions as a function of their distance from the centre of the UDG. I compared this with the empirical relation for the age gradient from the head to the tail of a linear stellar stream formed by the RPS of a gas cloud, provided by Kenney et al. (2014) as

$$t_{\rm stream} = \sqrt{\frac{2\,L\,\Sigma_{\rm gas}}{\rho_{\rm ICM}\,v^2}} \tag{7.1}$$

where $t_{\rm stream}$ is the timescale for creating a linear stellar stream of length L (the length L is defined with respect to the head of the stellar stream moving away from the source galaxy where the RPS has occurred. So this is inversely proportional to the distance from the source galaxy). $\Sigma_{\rm gas}$ and $\rho_{\rm ICM}$ are the galaxy gas surface density and the intra-cluster medium density, respectively. v is the relative velocity of the gas cloud with respect to the ICM. In my case, I assumed a stellar stream of length 9.4 kpc (the farthest region I observe), $\Sigma_{\rm gas} = 1\,M_{\odot}\,{\rm pc}^{-2}$ (the gas density of NGVS 3543 before RPS, obtained from the models discussed in Sect. 7.3), and a relative velocity of $v = 1084$ km s^{-1} for the H I gas cloud of AGC 226178 with respect to the Virgo cluster center (Boselli et al. 2014; Cannon et al. 2015). I adopted two different values for the ICM density, with $\rho_{\rm ICM} = 10^{-4}$ and 10^{-3} cm^{-3}, corresponding to the ICM density at the distance of NGVS 3543 from the cluster center (Simionescu et al. 2017) and a typical ICM density of the Virgo cluster from Vollmer et al. (2001), respectively. Using these values in Eqn. 7.1, I obtain a gradient of a few tens of millions of years from the head to the tail of my stream, as shown in Fig. 7.12. The ages that I measure are also consistent in order of magnitude with the expected age gradient for a stream of this length. However, considering the uncertainties and the scatter of the data, it is difficult to determine an age gradient is present from the observations. Moreover, it is not surprising to see a lack of a strong age gradient because these regions are very young. Clear gradients are usually seen in galaxies that interacted slightly longer ago (Fumagalli et al. 2011).

Once all the measurements on age, stellar mass and gradients of the regions are done, now it is time for us to combine them with the initial results obtained from the modelling of the UDG NGVS 3543, to have a global picture of the formation of the system. This is discussed in Sect. 7.7.

7.7. A global scenario for the blue to red transition of a UDG

The analysis of the RPS models of NGVS 3543 and the identification of some very young star-forming regions near it leads us to an interesting question on how this system was formed. An answer to this question can be obtained from the Figure 7.13, which shows a comparison of the stellar mass vs. H I mass of our UDG and AGC 226178 with that of an H I-selected sample of regular spirals, UDGs and dark galaxies from the literature. Leisman et al. (2017) provide a sample of HI-bearing UDGs from the

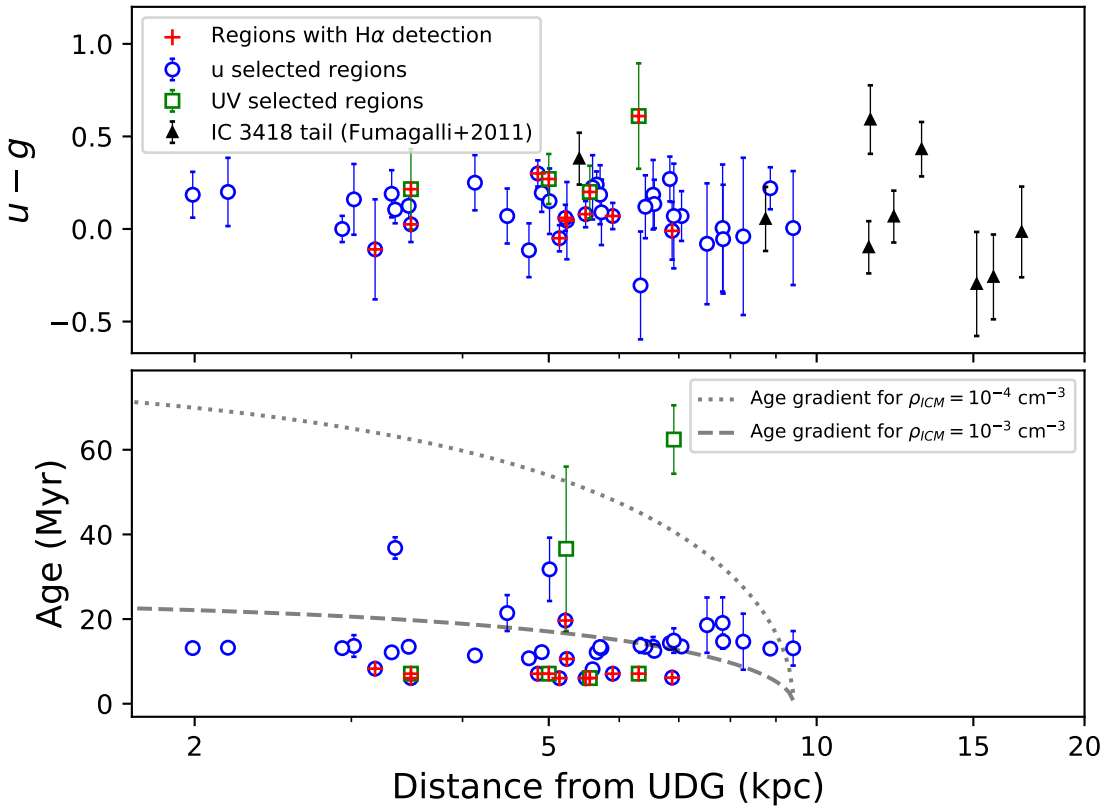

Figure 7.12.: $u-g$ color and age of the young regions as a function of their distance from the center of NGVS 3543. Black triangles represent the knots and filaments from Fumagalli et al. (2011). The black dotted and dashed lines indicate the age gradients we measured for a 9.4 kpc stream following Eqn. 2 of Kenney et al. (2014), for two different ICM densities with $\rho_{\rm ICM} = 10^{-4}$ and 10^{-3} cm^{-3}, respectively, as discussed in Sect. 7.6.3. The blue open circles and green open squares mark our u-band and UV-selected regions, respectively. The red crosses identify the Hα detected regions.

ALFALFA survey. I estimated the stellar mass of these UDGs from their g-band absolute magnitudes and $g-r$ colour, following a stellar mass-to-light-ratio-colour relation for LSB galaxies given in Du et al. (2020). The distribution of gas-rich UDGs from Leisman et al. (2017) falls along the low-stellar-mass tail of the $M_\star$-$M_{\rm HI}$ relation for regular galaxies from Parkash et al. (2018). These gas-rich, low-stellar-mass UDGs can be considered as the population of field blue UDGs discussed by Prole et al. (2019). The stellar mass and HI mass of our model for NGVS 3543 before the RPS event ($\sim 10^7\,M_\odot$ and $\sim 10^8\,M_\odot$, respectively from Table 7.1) suggest that its progenitor was similar to the population of blue UDGs.

The RPS event quickly transformed this galaxy into a gas-poor ($M_{HI} \sim 10^5\,M_\odot$), red UDG and totally quenched its star formation activity. Therefore, the non-detection in H I for NGVS 3543 (Cannon et al. 2015) is in complete agreement with our RPS scenario. Later, the stripped gas from the UDG resulted in the formation of AGC 226178 with an H I mass of $\sim 4\times 10^7\,M_\odot$ (Cannon et al. 2015) and stellar mass of $\sim 10^5\,M_\odot$ [2]. This stellar mass and H I mass of AGC 226178 is also consistent with the sample of other almost dark galaxy candidates from the literature (Cannon et al. 2015; Janowiecki et al. 2015).

In summary, my analysis strongly suggests that NGVS 3543 is in the process of transformation from a blue UDG into a red UDG by an RPS event. The fact that red UDGs are very frequent in nearby rich clusters (Koda et al. 2015; van der Burg et al. 2016), suggests that RPS could be one of the major processes in the formation of gas-poor red UDGs. As in the case of AGC 226178, my observations also suggest that RPS could be the mechanism responsible for the formation of the almost dark objects discussed in the literature (Cannon et al. 2015; Janowiecki et al. 2015; Leisman et al. 2017; Brunker et al. 2019). It is interesting to think that there could many many gas-poor parent galaxies similar to NGVS 3543, still undetected in the vicinity of these almost dark objects.

[2] The total stellar mass of AGC 226178 was obtained by combining my stellar mass estimates of u-band and UV selected regions within the H I contour of AGC 226178 (as shown in Fig. 7.1).

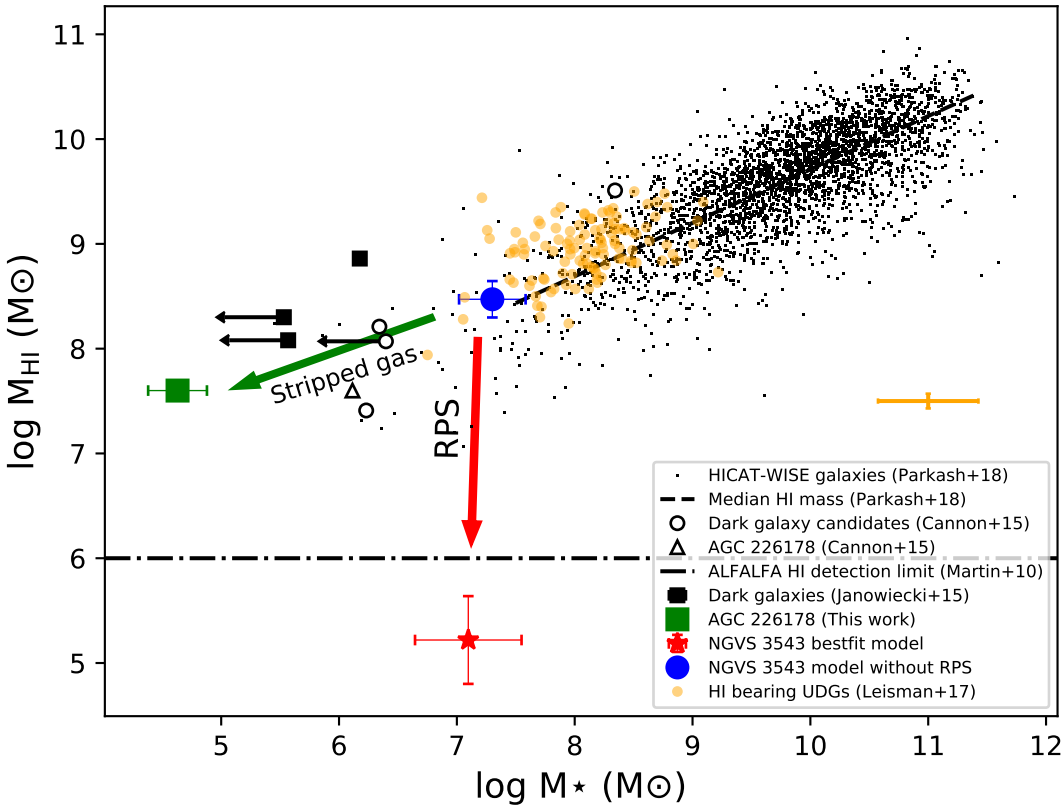

Figure 7.13.: Stellar mass vs. H I mass of the H I-selected sample of spirals, UDGs and "dark" galaxies. The blue circle and the red star respectively mark the position of NGVS 3543 before and after the RPS event, as given in Table 7.1. The total gas masses from the models were converted into H I by multiplying by a factor of 0.74 to take into account Helium and metals. Part of the stripped gas from the UDG can form AGC 226178, shown as the green square. The small black squares show the dark galaxies from Janowiecki et al. (2015), the black open circles and triangle are those from Cannon et al. (2015). The black points and the black dashed line are the H I-selected spirals and their median HI mass, respectively, from Parkash et al. (2018). The small yellow circles and error bars are the H I bearing UDGs and the mean dispersion from Leisman et al. (2017), respectively. The black dot-dashed line marks the H I mass detection limit of the ALFALFA survey (Martin et al. 2010).

Conclusions and perspectives

In this thesis, I presented the importance of the population of low surface brightness galaxies and studied several of their properties to better understand their nature. LSBs consists of a large population of galaxies in the universe. However, all throughout the history of extra-galactic studies, until now, we were limited by their extreme faintness to perform deep observational analysis. This situation has changed in recent years with powerful instruments [Dragonfly Telescope (Abraham & van Dokkum 2014); CFHT Megacam with Elixir LSB pipeline (Ferrarese et al. 2012); Subaru Hyper Suprime-Cam (Miyazaki et al. 2018)], that paved way for more detailed LSB studies, like the ones I performed in this work.

Giant LSBs and UDGs form two prominent sub-populations of LSBs, on which I focused in this thesis. Among GLSBs, the Malin 1 galaxy is considered an archetype which has attracted a lot of attention in the past decades due to its extreme physical properties. However, Malin 1 still remains a puzzle for astronomers. This motivated me to investigate more on this galaxy. I performed an analysis of Malin 1 spectra obtained from the Magellan Telescope and got some very interesting results. For the first time, I observe a steep rise in the inner rotation curve of this galaxy up to ~ 350 km s^{-1} (with a large dispersion). A mass modelling based on this data illustrated that the central region of Malin 1 could be dominated by baryons, but a large dark matter halo remains necessary for its huge extended disk. However, our modelling could not explain well enough the largest observed velocities in Malin 1. Moreover, the SFR surface density estimated from the Hα emission also indicates an early type central region for Malin 1 with an extended disc typical of late-type spirals. Observations with higher quality IFU-like data is necessary to confirm this and understand Malin 1 more in detail.

This increased the relevance of the MUSE proposal we submitted for the observation of Malin 1, for which I am a Co-I. The observations are partially completed as of June 2021 (1 out of the 4 proposed fields is observed). Once the observations are completed, they will provide us with vital information to answer several key questions. For instance, I will contribute to obtain an Hα emission line map for Malin 1 (together with other lines), which is crucial for understanding the star formation spread in this galaxy, along with the kinematics in the central region where we observed a very steep rise. The high resolution of the MUSE data will help us to untangle this unusual kinematic behaviour. We can also directly compare the results I obtained in Junais et al. (2020), and test the various uncertainties associated with those results (e.g. presence of non-circular velocities, geometrical assumptions, beam smearing effect). Moreover, various other interesting analyses can also be performed using the MUSE data. The Hα to UV ratio (combining the MUSE data with the UVIT data of Malin 1) provides a clue on the universality of IMF, whereas the Balmer ratio gives an indication of the dust content, which is generally considered to be very low in LSBs (but was not tested from Balmer lines directly).

The work on Malin 1 should be followed by a new focus on the population of GLSBs as a whole. A sample of H I and UV selected GLSBs I assembled during this thesis aims towards this purpose. A similar analysis to the one performed in Junais et al. (2020) for Malin 1 will be extended for this sample of GLSBs in my future works. This need to be accompanied by the acquisition of spectro-photometric data for the sample. I already initiated this process with several observing proposals submitted (e.g. UVIT, IMACS-Magellan proposals). However, similar to the upcoming Malin 1 MUSE data, in the future, it will also be ideal to have IFU observations for the entire GLSB sample. The proposed BlueMUSE instrument at VLT, with its high-resolution imaging power and large field of view, will be a perfect instrument for such an observational campaign. This will completely change our understanding of GLSBs, or LSBs in general by testing the several proposed scenarios for the formation of GLSBs (e.g. rotating discs in large haloes, late gas accretion, results of past interactions; Saburova et al. 2021).

UDGs are another interesting class of objects. They are a population that attracted a lot of attention in the past few years, where they were found in large numbers in galaxy clusters. Following this new interest, along with a collection of good quality multi-wavelength data, I studied a sample of UDGs and other LSBs in the Virgo cluster. This was done in order to study the role of cluster environment on the formation and evolution of these sources. Moreover, the Virgo cluster being one of the nearest and richest clusters of galaxies is perfectly suited for such a study.

I made a detailed analysis of the photometric properties of the LSBs in my sample. This resulted in several interesting results. A comparison of the effective radii of the galaxies I measured for the

sample revealed that for very faint UDGs, the measured effective radii differ from the values catalogued in the NGVS survey of Virgo. This shows that the procedures followed for such measurements (e.g. background sky estimation and subtraction, measurement apertures) play a big role in the data analysis of UDGs. Thus, an arbitrary UDG selection criteria based on the effective radius and surface brightness, as commonly found in the literature, will have high possibilities to contain a bias where they over/under predicts the "true" UDG population. One needs to be cautious about such effects. Incorporating different LSB selection criteria, as did in this work, will be helpful to some extent. However, I believe that we are still far from a more ideal situation where we have a well-defined classification for UDGs or LSBs in general, which is not the case now. But the quick advances we are making now in this field is very promising.

On continuing the analysis of my sample, the distribution of the optical colours revealed another result. The LSB population in my sample was found to be predominantly red, consistent with what generally found in cluster environments. However, there are also few bluer galaxies present among them, that are located far from the cluster centre in a relatively low-density environment. Upon cross-matching them with the ALFALFA H I survey, we found that the sources that are bluer also have associated H I counterparts. This is similar to the presence of H I bearing blue UDGs found in groups, discussed in literature (Leisman et al. 2017; Prole et al. 2019). The presence of a distance gradient in the colours of the LSB sample indicates that the environment in which they reside play a crucial role in shaping their evolution. This was further investigated using a set of galaxy evolution models that include the environmental effect of ram-pressure stripping, commonly found in clusters. By comparing the observed data with the models, we found that almost all of the galaxies in my sample had experienced the effect of ram-pressure stripping in their lifetime. This had a major impact in their evolution. Based on the prediction from the models, the Virgo cluster LSBs studied here were once rich in gas and star forming before they entered the cluster. However, on entering the cluster, the ram-pressure stripping completely transformed them into gas poor red LSBs that we observe now. This scenario was further verified by a detailed study of one of the UDGs in the sample that was caught in the act of an ongoing ram-pressure stripping process. Analysing this system revealed that this UDG was transformed from a blue UDG to a red UDG within the last 200 million years. This stripping process also resulted in the formation of a tail of star forming regions and an H I gas cloud (previously identified as a "dark galaxy") in the vicinity of the UDG. Our results indicate that such a scenario is well feasible in a cluster environment and will explain the large number of red UDGs generally found in clusters. Ram-pressure stripping could be one of the major mechanisms driving the formation of UDGs in clusters, which is still debated.

This work explored the power of observational data combined with simple numerical models to understand the nature of LSBs. We are at the right moment when LSB studies are taking a good pace. The results I obtained in this work can be easily tested (and should be tested) using follow-up observations. For instance, an interesting follow-up can be done on the blue LSBs I found along the cluster edges with possible H I counterparts. The presence of the H I gas can be detected and quantified with great precision using VLA observations (VLA will obtain ~5 times higher resolution than ALFALFA). This will be a perfect test-bed for the gas mass predictions obtained from our models and also verify that indeed the H I gas detected is associated with the LSBs I studied, where they experienced the impact of the RPS. The H I observations can also be complemented using spectroscopic follow-up of the sub-sample. This will be useful for constraining various properties of these sources (e.g., stellar population, metallicity, redshift).

Apart from the follow-up works on the same sample, a similar study can be extended to a large number of LSBs in different environments. For instance, my collaborator Jin Koda in New York have HSC-Subaru data of various other clusters including the Coma cluster. Using these data, I can perform a similar analysis and directly compare them with my results from this work. This will illustrate the variety of LSB properties within different clusters. At a later stage, it will be ideal to enlarge this study on LSBs in all kinds of environments (e.g., clusters, groups, isolated) and more wavelengths (e.g., IR: to study dust in LSBs, sub-mm: to probe molecular gas content in LSBs, X-ray: investigate AGN presence in LSBs). This will be possible with the data from many current and future surveys (e.g., DES, CFIS-UNIONS,

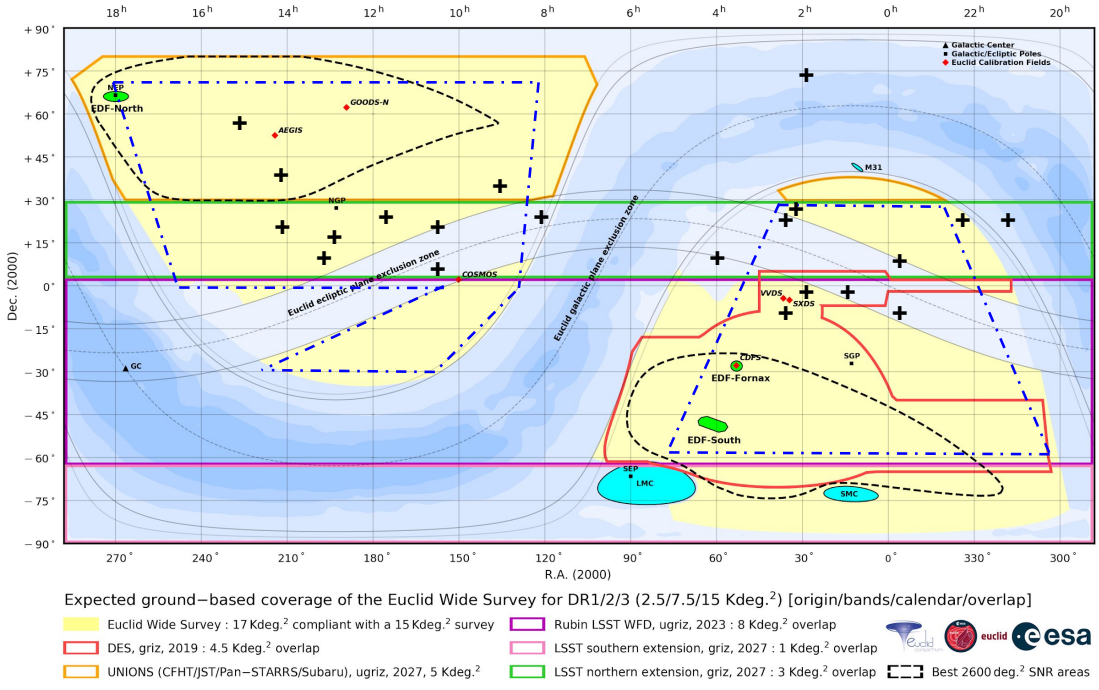

Figure 7.14.: The overlapping coverage of various current and future surveys (DES, CFIS-UNIONS, Euclid, LSST). The blue dot-dashed lines show the coverage of several existing UDG and XUV samples (Thilker et al. 2007; Koda et al. 2015; Leisman et al. 2017; Prole et al. 2019; Junais et al. in preparation; Bouquin et al. in preparation). The black crosses mark a sample of H I and UV selected GLSBs from Chapter 4.

LSST, Euclid, SKA) where LSBs will be detected in large numbers. For instance, LSST will reach a surface brightness level of ~30 mag arcsec^{-2} over an area of 20000 deg^2, in comparison to the 29 mag arcsec^{-2} depth and ~100 deg^2 coverage of the NGVS data I studied. Similarly, SKA should be able to detect Malin 1 like giant H I disk up to redshift 1 (Acero et al. 2017), independently of the surface brightness of their stellar disk. Moreover, many known LSB samples (and many more to discover) are already within the coverage of these surveys (see Fig. 7.14). Therefore, I strongly believe that the results I obtained in this work will be useful and motivate many future works on LSBs. There is no doubt that the low surface brightness universe has a "bright" future.

Finally, separating galaxies on any criterion always creates some bias. In the future, I hope to study all types of galaxies in a global context to answer several existing questions on their nature. For instance, are XUV galaxies (discovered by GALEX; Thilker et al. 2007) fundamentally different from GLSBs? Is there a continuity of properties among galaxies (e.g. metallicity, dust, SFR) when studying them as a function of their surface brightness (when, for example, the stellar mass is kept constant)? There are many more questions like this that we still need to find answers to. It is always exciting to be a part of that process.

Bibliography

Freeman, K. C. (June 1970). In: 160, p. 811. DOI: 10.1086/150474 (cit. on pp. 3, 37, 39–41, 86).

Osterbrock, Donald E. (1974) (cit. on p. 61).

Avni, Y. (1976). In: 210, pp. 642–646. DOI: 10.1086/154870 (cit. on pp. 123, 125, 139).

Disney, M. J. (Oct. 1976). In: 263.5578, pp. 573–575. DOI: 10.1038/263573a0 (cit. on p. 37).

Baldwin, J. A. et al. (Feb. 1981). In: 93, pp. 5–19. DOI: 10.1086/130766 (cit. on p. 62).

van Moorsel, G. A. (Mar. 1982). In: 107, pp. 66–74 (cit. on p. 72).

Sandage, A. & B. Binggeli (July 1984). In: 89, pp. 919–931. DOI: 10.1086/113588 (cit. on p. 43).

Binggeli, B. et al. (Sept. 1985). In: 90, pp. 1681–1758. DOI: 10.1086/113874 (cit. on p. 84).

Kent, S. M. (1986). In: 91, pp. 1301–1327. DOI: 10.1086/114106 (cit. on p. 68).

Bothun, G. D. et al. (July 1987). In: 94, pp. 23–29. DOI: 10.1086/114443 (cit. on pp. 4, 40, 43, 45, 46).

Cardelli, Jason A. et al. (Oct. 1989). In: 345, p. 245. DOI: 10.1086/167900 (cit. on p. 98).

Kennicutt Robert C., Jr. (Sept. 1989). In: 344, p. 685. DOI: 10.1086/167834 (cit. on pp. 40, 150).

Wyse, Rosemary F. G. & Joseph Silk (Apr. 1989). In: 339, p. 700. DOI: 10.1086/167329 (cit. on p. 120).

Bothun, Gregory D. et al. (Sept. 1990). In: 360, p. 427. DOI: 10.1086/169133 (cit. on p. 70).

Hoffman, Yehuda et al. (Mar. 1992). In: 388, p. L13. DOI: 10.1086/186319 (cit. on p. 70).

Massey, P. et al. (Apr. 1992). In: (cit. on p. 48).

Kroupa, Pavel et al. (June 1993). In: 262, pp. 545–587. DOI: 10.1093/mnras/262.3.545 (cit. on p. 119).

McGaugh, Stacy S. et al. (May 1995). In: 109, p. 2019. DOI: 10.1086/117427. arXiv: astro-ph/9501085 [astro-ph] (cit. on p. 40).

Sprayberry, D. et al. (Feb. 1995). In: 109, p. 558. DOI: 10.1086/117300 (cit. on pp. 4, 6, 40, 41, 62, 70–72, 85, 86).

Bertin, E. & S. Arnouts (June 1996). In: 117, pp. 393–404. DOI: 10.1051/aas:1996164 (cit. on p. 83).

McGaugh, Stacy S. (May 1996). In: 280.2, pp. 337–354. DOI: 10.1093/mnras/280.2.337. arXiv: astro-ph/9511010 [astro-ph] (cit. on p. 39).

de Blok, W. J. G. et al. (Nov. 1996). In: 283.1, pp. 18–54. DOI: 10.1093/mnras/283.1.18. arXiv: astro-ph/9605069 [astro-ph] (cit. on p. 38).

Impey, C. & G. Bothun (1997). In: 35, pp. 267–307. DOI: 10.1146/annurev.astro.35.1.267 (cit. on pp. 3, 4, 40, 45, 48).
Massey, P. (Feb. 1997). In: (cit. on p. 48).
Pickering, T. E. et al. (Nov. 1997). In: 114, p. 1858. DOI: 10.1086/118611 (cit. on pp. 3, 4, 43, 46, 48, 58, 70, 71).
de Blok, W. J. G. & S. S. McGaugh (Sept. 1997). In: 290, pp. 533–552. DOI: 10.1093/mnras/290.3.533. eprint: astro-ph/9704274 (cit. on pp. 40, 58).
Mo, H. J. et al. (Apr. 1998). In: 295.2, pp. 319–336. DOI: 10.1046/j.1365-8711.1998.01227.x. arXiv: astro-ph/9707093 [astro-ph] (cit. on p. 120).
Schlegel, David J. et al. (June 1998). In: 500.2, pp. 525–553. DOI: 10.1086/305772. arXiv: astro-ph/9710327 [astro-ph] (cit. on p. 88).
Boissier, S. & N. Prantzos (Aug. 1999). In: 307.4, pp. 857–876. DOI: 10.1046/j.1365-8711.1999.02699.x. arXiv: astro-ph/9902148 [astro-ph] (cit. on pp. 7, 119, 120, 123).
Klypin, Anatoly et al. (Sept. 1999). In: 522.1, pp. 82–92. DOI: 10.1086/307643. arXiv: astro-ph/9901240 [astro-ph] (cit. on p. 38).
Leitherer, Claus et al. (July 1999). In: 123.1, pp. 3–40. DOI: 10.1086/313233. arXiv: astro-ph/9902334 [astro-ph] (cit. on p. 142).
Verheijen, M. & B. Tully (Jan. 1999). In: *The Low Surface Brightness Universe*. Ed. by J. I. Davies et al. Vol. 170. Astronomical Society of the Pacific Conference Series, p. 92. arXiv: astro-ph/9810297 [astro-ph] (cit. on p. 46).
Boissier, S. & N. Prantzos (Feb. 2000). In: 312.2, pp. 398–416. DOI: 10.1046/j.1365-8711.2000.03133.x (cit. on pp. 7, 119–123).
O'Neil, K. & G. Bothun (Feb. 2000). In: 529.2, pp. 811–815. DOI: 10.1086/308322 (cit. on pp. 3, 38, 39).
Kewley, L. J. et al. (July 2001). In: 556.1, pp. 121–140. DOI: 10.1086/321545. arXiv: astro-ph/0106324 [astro-ph] (cit. on pp. 62, 64).
Kroupa, Pavel (Apr. 2001). In: 322.2, pp. 231–246. DOI: 10.1046/j.1365-8711.2001.04022.x. arXiv: astro-ph/0009005 [astro-ph] (cit. on pp. 119, 142, 151).
Matthews, L. D. et al. (Jan. 2001). In: 365, pp. 1–10. DOI: 10.1051/0004-6361:20000002. eprint: astro-ph/0010075 (cit. on pp. 4, 40, 46, 48, 70–72).
Noguchi, Masafumi (Dec. 2001). In: 328.2, pp. 353–358. DOI: 10.1046/j.1365-8711.2001.04910.x (cit. on p. 70).
Vollmer, B. et al. (Nov. 2001). In: 561.2, pp. 708–726. DOI: 10.1086/323368. arXiv: astro-ph/0107237 [astro-ph] (cit. on pp. 121, 122, 141, 152).
Denicoló, Glenda et al. (Feb. 2002). In: 330.1, pp. 69–74. DOI: 10.1046/j.1365-8711.2002.05041.x. arXiv: astro-ph/0110356 [astro-ph] (cit. on p. 62).
Peng, Chien Y. et al. (July 2002). In: 124.1, pp. 266–293. DOI: 10.1086/340952. arXiv: astro-ph/0204182 [astro-ph] (cit. on pp. 83, 86, 98).
Teuben, P. J. (Dec. 2002). In: *Disks of Galaxies: Kinematics, Dynamics and Peturbations*. Ed. by E. Athanassoula et al. Vol. 275. Astronomical Society of the Pacific Conference Series, pp. 217–228. arXiv: astro-ph/0204471 [astro-ph] (cit. on p. 55).

Verde, Licia et al. (Oct. 2002). In: 336.2, pp. 541–549. DOI: 10.1046/j.1365-8711.2002.05771.x. arXiv: astro-ph/0202283 [astro-ph] (cit. on pp. 7, 135).
Boissier, S. et al. (Aug. 2003). In: 343.2, pp. 653–664. DOI: 10.1046/j.1365-8711.2003.06703.x. arXiv: astro-ph/0304313 [astro-ph] (cit. on pp. 120–122, 124, 137).
Bruzual, G. & S. Charlot (Oct. 2003). In: 344.4, pp. 1000–1028. DOI: 10.1046/j.1365-8711.2003.06897.x. arXiv: astro-ph/0309134 [astro-ph] (cit. on p. 151).
Chabrier, Gilles (July 2003). In: 115.809, pp. 763–795. DOI: 10.1086/376392. arXiv: astro-ph/0304382 [astro-ph] (cit. on p. 151).
Sabatini, S. et al. (May 2003). In: 341.3, pp. 981–992. DOI: 10.1046/j.1365-8711.2003.06484.x. arXiv: astro-ph/0301585 [astro-ph] (cit. on p. 38).
Pettini, Max & Bernard E. J. Pagel (Mar. 2004). In: 348.3, pp. L59–L63. DOI: 10.1111/j.1365-2966.2004.07591.x. arXiv: astro-ph/0401128 [astro-ph] (cit. on pp. 62, 63).
Blanton, Michael R. et al. (2005). In: 631.1, pp. 208–230. DOI: 10.1086/431416. arXiv: astro-ph/0410164 [astro-ph] (cit. on p. 3).
Burgarella, D. et al. (July 2005). In: 360.4, pp. 1413–1425. DOI: 10.1111/j.1365-2966.2005.09131.x. arXiv: astro-ph/0504434 [astro-ph] (cit. on p. 150).
Erben, T. et al. (July 2005). In: *Astronomische Nachrichten* 326.6, pp. 432–464. DOI: 10.1002/asna.200510396. arXiv: astro-ph/0501144 [astro-ph] (cit. on p. 83).
Gil de Paz, A. et al. (July 2005). In: 627.1, pp. L29–L32. DOI: 10.1086/432054. arXiv: astro-ph/0506357 [astro-ph] (cit. on p. 96).
Morrissey, Patrick et al. (Jan. 2005). In: 619.1, pp. L7–L10. DOI: 10.1086/424734. arXiv: astro-ph/0411310 [astro-ph] (cit. on pp. 84, 98, 145).
Noordermeer, E. et al. (Oct. 2005). In: 442.1, pp. 137–157. DOI: 10.1051/0004-6361:20053172. arXiv: astro-ph/0508319 [astro-ph] (cit. on p. 72).
Roediger, E. & G. Hensler (Apr. 2005). In: 433.3, pp. 875–895. DOI: 10.1051/0004-6361:20042131 (cit. on p. 140).
Xu, C. Kevin et al. (Jan. 2005). In: 619.1, pp. L11–L14. DOI: 10.1086/425252. arXiv: astro-ph/0411317 [astro-ph] (cit. on p. 145).
Boselli, A. et al. (Nov. 2006). In: 651.2, pp. 811–821. DOI: 10.1086/507766. arXiv: astro-ph/0609020 [astro-ph] (cit. on pp. 7, 119, 121, 122, 141).
Kewley, Lisa J. et al. (Nov. 2006). In: 372.3, pp. 961–976. DOI: 10.1111/j.1365-2966.2006.10859.x. arXiv: astro-ph/0605681 [astro-ph] (cit. on p. 62).
Moore, L. & Q. A. Parker (Mar. 2006). In: 23, pp. 165–169. DOI: 10.1071/AS06022. eprint: astro-ph/0702551 (cit. on pp. 4, 45).
Barth, A. J. (Mar. 2007). In: 133, pp. 1085–1091. DOI: 10.1086/511180. eprint: astro-ph/0701018 (cit. on pp. 46, 48, 58, 61, 62, 65).
Boissier, Samuel et al. (Dec. 2007). In: 173.2, pp. 524–537. DOI: 10.1086/516642. arXiv: astro-ph/0609071 [astro-ph] (cit. on p. 74).
Hinz, J. L. et al. (July 2007). In: 663, pp. 895–907. DOI: 10.1086/518817. arXiv: 0704.2059 (cit. on pp. 61, 79, 98).

Mei, Simona et al. (Jan. 2007). In: 655.1, pp. 144–162. DOI: 10.1086/509598. arXiv: astro-ph/0702510 [astro-ph] (cit. on pp. 35, 81).
Rahman, N. et al. (July 2007). In: 663, pp. 908–923. DOI: 10.1086/518554. arXiv: 0704.1483 (cit. on pp. 61, 70, 98).
Schawinski, Kevin et al. (Dec. 2007). In: 382.4, pp. 1415–1431. DOI: 10.1111/j.1365-2966.2007.12487.x. arXiv: 0709.3015 [astro-ph] (cit. on p. 64).
Thilker, David A. et al. (Dec. 2007). In: 173.2, pp. 538–571. DOI: 10.1086/523853. arXiv: 0712.3555 [astro-ph] (cit. on pp. 5, 46, 79, 159).
Wyder, Ted K. et al. (Dec. 2007). In: 173.2, pp. 293–314. DOI: 10.1086/521402. arXiv: 0706.3938 [astro-ph] (cit. on p. 114).
Bigiel, F. et al. (Dec. 2008). In: 136.6, pp. 2846–2871. DOI: 10.1088/0004-6256/136/6/2846. arXiv: 0810.2541 [astro-ph] (cit. on p. 74).
Boissier, S. et al. (July 2008). In: 681.1, pp. 244–257. DOI: 10.1086/588580. arXiv: 0803.3877 [astro-ph] (cit. on pp. 3, 40, 48, 71, 72).
Boselli, A. et al. (Feb. 2008a). In: 674.2, pp. 742–767. DOI: 10.1086/525513. arXiv: 0801.2113 [astro-ph] (cit. on pp. 119, 122).
Boselli, A. et al. (Oct. 2008b). In: 489.3, pp. 1015–1022. DOI: 10.1051/0004-6361:200809546. arXiv: 0807.3282 [astro-ph] (cit. on p. 119).
Mapelli, M. et al. (Jan. 2008). In: 383.3, pp. 1223–1231. DOI: 10.1111/j.1365-2966.2007.12650.x. arXiv: 0710.5354 [astro-ph] (cit. on p. 71).
Blakeslee, John P. et al. (Mar. 2009). In: 694.1, pp. 556–572. DOI: 10.1088/0004-637X/694/1/556. arXiv: 0901.1138 [astro-ph.CO] (cit. on p. 81).
Boselli, A. et al. (Dec. 2009). In: 706.2, pp. 1527–1544. DOI: 10.1088/0004-637X/706/2/1527. arXiv: 0910.3521 [astro-ph.CO] (cit. on pp. 74, 142).
Erben, T. et al. (Jan. 2009). In: 493.3, pp. 1197–1222. DOI: 10.1051/0004-6361:200810426. arXiv: 0811.2239 [astro-ph] (cit. on p. 83).
Noll, S. et al. (Dec. 2009). In: 507.3, pp. 1793–1813. DOI: 10.1051/0004-6361/200912497. arXiv: 0909.5439 [astro-ph.CO] (cit. on p. 150).
Wyder, Ted K. et al. (May 2009). In: 696.2, pp. 1834–1853. DOI: 10.1088/0004-637X/696/2/1834. arXiv: 0903.3015 [astro-ph.CO] (cit. on pp. 3, 40).
Bigiel, F. et al. (Nov. 2010). In: 140, pp. 1194–1213. DOI: 10.1088/0004-6256/140/5/1194. arXiv: 1007.3498 (cit. on pp. 3, 5, 40, 58, 60, 61).
Epinat, B. et al. (Feb. 2010). In: 401.4, pp. 2113–2147. DOI: 10.1111/j.1365-2966.2009.15688.x. arXiv: 0904.3891 [astro-ph.CO] (cit. on p. 65).
Jacob, Joseph C. et al. (May 2010). In: *arXiv e-prints*, arXiv:1005.4454, arXiv:1005.4454. arXiv: 1005.4454 [astro-ph.IM] (cit. on p. 94).
Lelli, F. et al. (June 2010). In: 516, A11, A11. DOI: 10.1051/0004-6361/200913808. arXiv: 1003.1312 (cit. on pp. 5, 46, 48, 55, 58, 59, 65, 71).
Martin, Ann M. et al. (Nov. 2010). In: 723.2, pp. 1359–1374. DOI: 10.1088/0004-637X/723/2/1359. arXiv: 1008.5107 [astro-ph.CO] (cit. on p. 155).
Moustakas, John et al. (Oct. 2010). In: 190.2, pp. 233–266. DOI: 10.1088/0067-0049/190/2/233. arXiv: 1007.4547 [astro-ph.CO] (cit. on p. 62).

Reshetnikov, V. P. et al. (July 2010). In: 406.1, pp. L90–L94. DOI: 10.1111/j.1745-3933.2010.00888.x. arXiv: 1005.5294 [astro-ph.CO] (cit. on pp. 46, 47, 65).
de Blok, W. J. G. (Jan. 2010). In: *Advances in Astronomy* 2010, 789293, p. 789293. DOI: 10.1155/2010/789293. arXiv: 0910.3538 [astro-ph.CO] (cit. on p. 40).
Boselli, A. et al. (Apr. 2011). In: 528, A107, A107. DOI: 10.1051/0004-6361/201016389. arXiv: 1102.1316 [astro-ph.CO] (cit. on pp. 6, 47, 81, 83, 84).
Fumagalli, Mattia et al. (Apr. 2011). In: 528, A46, A46. DOI: 10.1051/0004-6361/201015463. arXiv: 1011.1665 [astro-ph.CO] (cit. on pp. 137, 152, 153).
Galaz, Gaspar et al. (Feb. 2011). In: 728.2, 74, p. 74. DOI: 10.1088/0004-637X/728/2/74. arXiv: 1007.4014 [astro-ph.CO] (cit. on p. 62).
Gavazzi, G. et al. (Oct. 2011). In: 534, A31, A31. DOI: 10.1051/0004-6361/201117461. arXiv: 1107.3702 [astro-ph.CO] (cit. on p. 62).
Haynes, Martha P. et al. (Nov. 2011). In: 142.5, 170, p. 170. DOI: 10.1088/0004-6256/142/5/170. arXiv: 1109.0027 [astro-ph.CO] (cit. on p. 135).
Muñoz-Mateos, J. C. et al. (Apr. 2011). In: 731.1, 10, p. 10. DOI: 10.1088/0004-637X/731/1/10. arXiv: 1102.1724 [astro-ph.CO] (cit. on pp. 96, 121, 122).
Sousbie, T. (June 2011). In: 414.1, pp. 350–383. DOI: 10.1111/j.1365-2966.2011.18394.x. arXiv: 1009.4015 [astro-ph.CO] (cit. on pp. 65, 66).
Taylor, Edward N. et al. (Dec. 2011). In: 418.3, pp. 1587–1620. DOI: 10.1111/j.1365-2966.2011.19536.x. arXiv: 1108.0635 [astro-ph.CO] (cit. on p. 65).
Ferrarese, L. et al. (May 2012). In: 200, 4, p. 4. DOI: 10.1088/0067-0049/200/1/4 (cit. on pp. 5, 6, 45–47, 81–83, 98, 157).
Koda, Jin et al. (Apr. 2012). In: *The Astrophysical Journal* 749.1, p. 20. ISSN: 0004-637X. DOI: 10.1088/0004-637X/749/1/20. URL: http://stacks.iop.org/0004-637X/749/i=1/a=20?key=crossref.58e4b0298a5a4cbd3c47751e262eca8a (cit. on p. 74).
Kumar, Amit et al. (2012). In: vol. 8443. Society of Photo-Optical Instrumentation Engineers (SPIE) Conference Series, 84431N. DOI: 10.1117/12.924507 (cit. on p. 73).
Ludwig, Randi R. et al. (2012). In: 756.1, 51, p. 51. DOI: 10.1088/0004-637X/756/1/51. arXiv: 1208.1303 [astro-ph.CO] (cit. on p. 55).
Boissier, Samuel (2013a). In: *Planets, Stars and Stellar Systems. Volume 6: Extragalactic Astronomy and Cosmology*. Ed. by Terry D. Oswalt & William C. Keel. Vol. 6, p. 141. DOI: 10.1007/978-94-007-5609-0_3 (cit. on p. 33).
– (2013b). In: *Planets, Stars and Stellar Systems. Volume 6: Extragalactic Astronomy and Cosmology*. Ed. by Terry D. Oswalt & William C. Keel. Vol. 6, p. 141. DOI: 10.1007/978-94-007-5609-0_3 (cit. on pp. 58, 120).
Marino, R. A. et al. (Nov. 2013). In: 559, A114, A114. DOI: 10.1051/0004-6361/201321956. arXiv: 1307.5316 [astro-ph.CO] (cit. on pp. 62, 63).
Oswalt, Terry D. & William C. Keel (2013). DOI: 10.1007/978-94-007-5609-0 (cit. on p. 36).
Vollmer, Bernd (2013). In: *Planets, Stars and Stellar Systems: Volume 6: Extragalactic Astronomy and Cosmology*. Ed. by Terry D. Oswalt & William C. Keel. Springer Nether-

lands, 207–263. ISBN: 978-94-007-5609-0. DOI: 10.1007/978-94-007-5609-0_5. URL: https://doi.org/10.1007/978-94-007-5609-0_5 (cit. on p. 35).
Abraham, Roberto G. & Pieter G. van Dokkum (Jan. 2014). In: 126.935, p. 55. DOI: 10.1086/674875. arXiv: 1401.5473 [astro-ph.IM] (cit. on p. 157).
Boselli, A. et al. (Oct. 2014). In: 570, A69, A69. DOI: 10.1051/0004-6361/201424419. arXiv: 1407.4986 [astro-ph.GA] (cit. on pp. 119, 152).
Kenney, Jeffrey D. P. et al. (Jan. 2014). In: 780.2, 119, p. 119. DOI: 10.1088/0004-637X/780/2/119. arXiv: 1311.5501 [astro-ph.CO] (cit. on pp. 137, 152, 153).
Barbosa, C. E. et al. (Nov. 2015). In: 453.3, pp. 2965–2981. DOI: 10.1093/mnras/stv1685. arXiv: 1508.03004 [astro-ph.GA] (cit. on pp. 65, 98).
Cannon, John M. et al. (Feb. 2015). In: 149.2, 72, p. 72. DOI: 10.1088/0004-6256/149/2/72. arXiv: 1412.3018 [astro-ph.GA] (cit. on pp. 7, 8, 36, 135, 136, 144, 152, 154, 155).
Galaz, Gaspar et al. (Dec. 2015). In: 815.2, L29, p. L29. DOI: 10.1088/2041-8205/815/2/L29. arXiv: 1512.01095 [astro-ph.GA] (cit. on pp. 43, 45, 47).
Janowiecki, Steven et al. (Mar. 2015). In: 801.2, 96, p. 96. DOI: 10.1088/0004-637X/801/2/96. arXiv: 1502.01296 [astro-ph.GA] (cit. on pp. 8, 135, 154, 155).
Koda, Jin et al. (July 2015). In: 807.1, L2, p. L2. DOI: 10.1088/2041-8205/807/1/L2. arXiv: 1506.01712 [astro-ph.GA] (cit. on pp. 6, 43, 154, 159).
Kubryk, M. et al. (Aug. 2015). In: 580, A126, A126. DOI: 10.1051/0004-6361/201424171. arXiv: 1412.0585 [astro-ph.GA] (cit. on p. 119).
Meert, Alan et al. (Feb. 2015). In: 446.4, pp. 3943–3974. DOI: 10.1093/mnras/stu2333. arXiv: 1406.4179 [astro-ph.GA] (cit. on p. 71).
van Dokkum, Pieter G. et al. (May 2015). In: 804.1, L26, p. L26. DOI: 10.1088/2041-8205/804/1/L26. arXiv: 1504.03320 [astro-ph.GA] (cit. on pp. 4, 6, 40–43, 85, 86, 102, 103, 137).
Amorisco, N. C. & A. Loeb (June 2016). In: 459.1, pp. L51–L55. DOI: 10.1093/mnrasl/slw055. arXiv: 1603.00463 [astro-ph.GA] (cit. on p. 43).
Boissier, S. et al. (Oct. 2016). In: 593, A126, A126. DOI: 10.1051/0004-6361/201629226. arXiv: 1610.00918 [astro-ph.GA] (cit. on pp. 43, 46–48, 51, 62, 77, 96, 122).
Comparat, Johan et al. (Sept. 2016). In: 461.1, pp. 1076–1087. DOI: 10.1093/mnras/stw1393. arXiv: 1605.02875 [astro-ph.GA] (cit. on p. 55).
Fossati, Matteo et al. (Jan. 2016). In: 455.2, pp. 2028–2041. DOI: 10.1093/mnras/stv2400. arXiv: 1510.04283 [astro-ph.GA] (cit. on p. 137).
González Delgado, R. M. et al. (May 2016). In: 590, A44, A44. DOI: 10.1051/0004-6361/201628174. arXiv: 1603.00874 [astro-ph.GA] (cit. on pp. 58, 60).
Hagen, Lea M. Z. et al. (Aug. 2016). In: 826.2, 210, p. 210. DOI: 10.3847/0004-637X/826/2/210. arXiv: 1607.02147 [astro-ph.GA] (cit. on pp. 41, 43, 71, 72).
Meert, Alan et al. (Jan. 2016). In: 455.3, pp. 2440–2452. DOI: 10.1093/mnras/stv2475. arXiv: 1510.07631 [astro-ph.GA] (cit. on p. 71).
Subramanian, S. et al. (Jan. 2016). In: 455, pp. 3148–3168. DOI: 10.1093/mnras/stv2500. arXiv: 1510.07743 [astro-ph.GA] (cit. on pp. 62, 64).

Wetzel, Andrew R. et al. (Aug. 2016). In: 827.2, L23, p. L23. DOI: 10.3847/2041-8205/827/2/L23. arXiv: 1602.05957 [astro-ph.GA] (cit. on p. 38).
van der Burg, Remco F. J. et al. (May 2016). In: 590, A20, A20. DOI: 10.1051/0004-6361/201628222. arXiv: 1602.00002 [astro-ph.GA] (cit. on pp. 6, 111, 154).
Acero, F. et al. (Dec. 2017). In: *arXiv e-prints*, arXiv:1712.06950, arXiv:1712.06950. arXiv: 1712.06950 [astro-ph.IM] (cit. on p. 159).
Beccari, G. et al. (Feb. 2017). In: 465.2, pp. 2189–2197. DOI: 10.1093/mnras/stw2874. arXiv: 1611.02876 [astro-ph.GA] (cit. on p. 135).
Disseau, K. et al. (Apr. 2017). In: 466.2, pp. 2337–2351. DOI: 10.1093/mnras/stw3157. arXiv: 1612.02822 [astro-ph.GA] (cit. on p. 40).
Leisman, Lukas et al. (June 2017). In: 842.2, 133, p. 133. DOI: 10.3847/1538-4357/aa7575. arXiv: 1703.05293 [astro-ph.GA] (cit. on pp. 7, 43, 115, 135, 152, 154, 155, 158, 159).
Mishra, A. et al. (Jan. 2017). In: 464.3, pp. 2741–2751. DOI: 10.1093/mnras/stw2506. arXiv: 1609.07544 [astro-ph.GA] (cit. on pp. 71, 72).
Román, Javier & Ignacio Trujillo (June 2017). In: 468.1, pp. 703–716. DOI: 10.1093/mnras/stx438. arXiv: 1603.03494 [astro-ph.GA] (cit. on pp. 43, 111).
Simionescu, A. et al. (Aug. 2017). In: 469.2, pp. 1476–1495. DOI: 10.1093/mnras/stx919. arXiv: 1704.01236 [astro-ph.CO] (cit. on p. 152).
Baushev, A. N. (Apr. 2018). In: 60, pp. 69–73. DOI: 10.1016/j.newast.2017.10.008. arXiv: 1608.04356 [astro-ph.GA] (cit. on p. 43).
Boselli, A. et al. (June 2018a). In: 614, A56, A56. DOI: 10.1051/0004-6361/201732407. arXiv: 1802.02829 [astro-ph.GA] (cit. on pp. 6, 81, 83, 84, 98).
Boselli, A. et al. (July 2018b). In: 615, A114, A114. DOI: 10.1051/0004-6361/201732410. arXiv: 1803.04177 [astro-ph.GA] (cit. on p. 145).
Boselli, A. et al. (Dec. 2018c). In: 620, A164, A164. DOI: 10.1051/0004-6361/201833914. arXiv: 1810.09234 [astro-ph.GA] (cit. on p. 64).
Greco, Johnny P. et al. (Apr. 2018). In: 857.2, 104, p. 104. DOI: 10.3847/1538-4357/aab842. arXiv: 1709.04474 [astro-ph.GA] (cit. on pp. 111, 113).
Haynes, Martha P. et al. (July 2018). In: 861.1, 49, p. 49. DOI: 10.3847/1538-4357/aac956. arXiv: 1805.11499 [astro-ph.GA] (cit. on pp. 7, 115, 117).
Miyazaki, Satoshi et al. (Jan. 2018). In: 70, S1, S1. DOI: 10.1093/pasj/psx063 (cit. on p. 157).
Parkash, Vaishali et al. (Sept. 2018). In: 864.1, 40, p. 40. DOI: 10.3847/1538-4357/aad3b9. arXiv: 1807.06246 [astro-ph.GA] (cit. on pp. 154, 155).
Shi, Yong et al. (2018). In: 853.2, 149, p. 149. DOI: 10.3847/1538-4357/aaa3e6. arXiv: 1801.00888 [astro-ph.GA] (cit. on p. 74).
Zhu, Qirong et al. (Oct. 2018). In: 480.1, pp. L18–L22. DOI: 10.1093/mnrasl/sly111. arXiv: 1805.09341 [astro-ph.GA] (cit. on pp. 43, 47).
Boquien, M. et al. (Feb. 2019). In: 622, A103, A103. DOI: 10.1051/0004-6361/201834156. arXiv: 1811.03094 [astro-ph.GA] (cit. on p. 150).
Boselli, A. et al. (Mar. 2019). In: 623, A52, A52. DOI: 10.1051/0004-6361/201834492. arXiv: 1810.09804 [astro-ph.GA] (cit. on p. 84).

Bradley, Larry et al. (Oct. 2019). Version v0.7.1. DOI: 10.5281/zenodo.3478575 (cit. on p. 96).
Brunker, Samantha W. et al. (Feb. 2019). In: 157.2, 76, p. 76. DOI: 10.3847/1538-3881/aafb39 (cit. on pp. 135, 154).
Dey, Biprateep et al. (Sept. 2019). In: 488.2, pp. 1926–1940. DOI: 10.1093/mnras/stz1777. arXiv: 1906.02273 [astro-ph.GA] (cit. on p. 74).
Di Cintio, Arianna et al. (June 2019). In: 486.2, pp. 2535–2548. DOI: 10.1093/mnras/stz985. arXiv: 1901.08559 [astro-ph.GA] (cit. on p. 43).
Ferreras, Ignacio (2019). UCL Press. ISBN: 9781911307624. URL: http://www.jstor.org/stable/j.ctv8jnzhq (cit. on pp. 32, 36).
Janowiecki, Steven et al. (Nov. 2019). In: 490.1, pp. 566–577. DOI: 10.1093/mnras/stz1868. arXiv: 1906.11543 [astro-ph.GA] (cit. on pp. 7, 115).
Martin, G. et al. (May 2019). In: 485.1, pp. 796–818. DOI: 10.1093/mnras/stz356. arXiv: 1902.04580 [astro-ph.GA] (cit. on pp. 3, 38–40, 43).
Prole, D. J. et al. (Sept. 2019). In: 488.2, pp. 2143–2157. DOI: 10.1093/mnras/stz1843. arXiv: 1907.01559 [astro-ph.GA] (cit. on pp. 6, 43, 111, 115, 141, 154, 158, 159).
Prole, Daniel J. (Oct. 2019). PhD thesis. Cardiff University. URL: http://orca.cardiff.ac.uk/id/eprint/125767 (cit. on p. 30).
Richard, Johan et al. (June 2019). In: *arXiv e-prints*, arXiv:1906.01657, arXiv:1906.01657. arXiv: 1906.01657 [astro-ph.IM] (cit. on p. 79).
Singh, Pranjal Rajendra et al. (May 2019). In: 157.5, 212, p. 212. DOI: 10.3847/1538-3881/ab16f2 (cit. on pp. 111, 114).
Boselli, A. et al. (Dec. 2020). In: *arXiv e-prints*, arXiv:2012.07377, arXiv:2012.07377. arXiv: 2012.07377 [astro-ph.GA] (cit. on p. 137).
Chamba, Nushkia et al. (Jan. 2020). In: 633, L3, p. L3. DOI: 10.1051/0004-6361/201936821. arXiv: 2001.02691 [astro-ph.GA] (cit. on p. 102).
Du, Wei et al. (Apr. 2020). In: 159.4, 138, p. 138. DOI: 10.3847/1538-3881/ab6efb. arXiv: 2007.08610 [astro-ph.GA] (cit. on p. 154).
Ferrarese, Laura et al. (Feb. 2020). In: 890.2, 128, p. 128. DOI: 10.3847/1538-4357/ab339f (cit. on pp. 83–85, 95).
Gullieuszik, Marco et al. (Aug. 2020). In: 899.1, 13, p. 13. DOI: 10.3847/1538-4357/aba3cb. arXiv: 2006.16032 [astro-ph.GA] (cit. on p. 137).
Jimenez, Raul & Alan F. Heavens (Aug. 2020). In: DOI: 10.1093/mnrasl/slaa135. arXiv: 2005.11798 [astro-ph.GA] (cit. on p. 135).
Junais et al. (May 2020). In: 637, A21, A21. DOI: 10.1051/0004-6361/201937330. arXiv: 2003.09492 [astro-ph.GA] (cit. on pp. 5, 48, 76, 78, 79, 157).
Koribalski, Bärbel S. et al. (July 2020). In: 365.7, 118, p. 118. DOI: 10.1007/s10509-020-03831-4. arXiv: 2002.07311 [astro-ph.GA] (cit. on p. 129).
Lim, Sungsoon et al. (Aug. 2020). In: 899.1, 69, p. 69. DOI: 10.3847/1538-4357/aba433. arXiv: 2007.10565 [astro-ph.GA] (cit. on pp. 6, 40, 42, 43, 84, 85, 137).
Lombardo, S. et al. (June 2020). In: *arXiv e-prints*, arXiv:2006.13956, arXiv:2006.13956. arXiv: 2006.13956 [astro-ph.IM] (cit. on p. 79).

Sorgho, A. et al. (Apr. 2020). In: 493.2, pp. 2618–2631. DOI: 10.1093/mnras/staa415. arXiv: 2002.03813 [astro-ph.GA] (cit. on p. 135).

Trujillo, Ignacio et al. (Mar. 2020). In: 493.1, pp. 87–105. DOI: 10.1093/mnras/staa236. arXiv: 2001.02689 [astro-ph.GA] (cit. on p. 102).

Junais et al. (June 2021). In: 650, A99, A99. DOI: 10.1051/0004-6361/202040185. arXiv: 2104.02492 [astro-ph.GA] (cit. on pp. 8, 122, 137).

McGaugh, Stacy (Mar. 2021). In: *arXiv e-prints*, arXiv:2103.05003, arXiv:2103.05003. arXiv: 2103.05003 [astro-ph.GA] (cit. on p. 38).

Saburova, Anna S. et al. (May 2021). In: 503.1, pp. 830–849. DOI: 10.1093/mnras/stab374. arXiv: 2011.01238 [astro-ph.GA] (cit. on pp. 43, 47, 71, 157).

Saha, Kanak et al. (Jan. 2021). In: *arXiv e-prints*, arXiv:2101.07002, arXiv:2101.07002. arXiv: 2101.07002 [astro-ph.GA] (cit. on pp. 43, 47, 74).

Tanoglidis, D. et al. (Feb. 2021). In: 252.2, 18, p. 18. DOI: 10.3847/1538-4365/abca89. arXiv: 2006.04294 [astro-ph.GA] (cit. on pp. 111–113).

ANNEXES

A. Published papers

A.1. First spectroscopic study of ionised gas emission lines in the extreme low surface brightness galaxy Malin 1

A&A 637, A21 (2020)
https://doi.org/10.1051/0004-6361/201937330

Astronomy & Astrophysics

First spectroscopic study of ionised gas emission lines in the extreme low surface brightness galaxy Malin 1

Junais[1], S. Boissier[1], B. Epinat[1], P. Amram[1], B. F. Madore[2], A. Boselli[1], J. Koda[3], A. Gil de Paz[4], J. C. Muños Mateos[5], and L. Chemin[6]

[1] Aix Marseille Univ, CNRS, CNES, LAM, Marseille, France
e-mail: junais.madathodika@lam.fr
[2] Observatories of the Carnegie Institution for Science, 813 Santa Barbara Street, Pasadena, CA 91101, USA
[3] Department of Physics and Astronomy, Stony Brook University, Stony Brook, NY 11794-3800, USA
[4] Departamento de Astrofísica, Universidad Complutense de Madrid, 28040 Madrid, Spain
[5] European Southern Observatory, Alonso de Cordova 3107, Vitacura, Casilla 19001, Santiago, Chile
[6] Centro de Astronomía (CITEVA), Universidad de Antofagasta, Avenida Angamos 601, Antofagasta, Chile

Received 16 December 2019 / Accepted 20 March 2020

ABSTRACT

Context. Malin 1 is the largest known low surface brightness (LSB) galaxy, the archetype of so-called giant LSB galaxies. The structure and origin of such galaxies are still poorly understood, especially because of the lack of high-resolution kinematics and spectroscopic data.
Aims. We use emission lines from spectroscopic observations of Malin 1 aiming to bring new constraints on the internal dynamics and star formation history of Malin 1.
Methods. We extracted a total of 16 spectra from different regions of Malin 1 and calculated the rotational velocities of these regions from the wavelength shifts and star formation rates from the observed Hα emission line fluxes. We compared our data with existing data and models for Malin 1.
Results. For the first time we present the inner rotation curve of Malin 1, characterised in the radial range $r < 10$ kpc by a steep rise in the rotational velocity up to at least $\sim$350 km s^{-1} (with a large dispersion), which had not been observed previously. We used these data to study a suite of new mass models for Malin 1. We show that in the inner regions dynamics may be dominated by the stars (although none of our models can explain the highest velocities measured) but that at large radii a massive dark matter halo remains necessary. The Hα fluxes derived star formation rates are consistent with an early-type disc for the inner region and with the level found in extended UV galaxies for the outer parts of the giant disc of Malin 1. We also find signs of high metallicity but low dust content for the inner regions.

Key words. galaxies: individual: Malin 1 – galaxies: kinematics and dynamics – galaxies: star formation

1. Introduction

The faint and diffuse galaxies that emit much less light per unit area than normal galaxies are known as low surface brightness (LSB) galaxies. Although there is no clear-cut convention for defining LSB galaxies, they are usually broadly defined as galaxies with a disc central surface brightness (μ_0) much fainter than the typical Freeman (1970) value for disc galaxies ($\mu_{0,B} = 21.65 \pm 0.30$ mag arcsec^{-2}). Low surface brightness galaxies may account for a very large galaxy population and dark matter (DM) content (Impey & Bothun 1997; Blanton et al. 2005; de Blok & McGaugh 1997). Therefore, understanding this type of galaxies and their rotation curves (RCs), provided we have good kinematics data, could offer some new insights into our current galaxy formation and evolution scenarios.

The LSB galaxies span a wide range of sizes, masses, and morphology from the largest existing galaxies down to the more common dwarfs. Giant low surface brightness galaxies (GLSBs) are a sub-population of LSB galaxies, which have an extremely extended LSB disc with scale lengths ranging from ~10 kpc to ~50 kpc (Bothun et al. 1987); GLSBs are also rich in gas content ($M_{\rm HI} \sim 10^{10}\,M_\odot$; Matthews et al. 2001). Despite their low central surface brightness they are sometimes as massive as many "regular" galaxies (see Fig. 3 of Sprayberry et al. 1995). The origin of giant LSBs has been much debated with many propositions, for example face-on collisions (Mapelli & Moore 2008), cooling gas during a merger (Zhu et al. 2018; Saburova et al. 2018), large initial angular momentum (Boissier et al. 2003; Amorisco & Loeb 2016), and accretion from cosmic filaments (Saburova et al. 2019). Few spectroscopic studies were possible in GLSBs (e.g. Saburova et al. 2019), even though this sub-population could offer important information to distinguish between these possibilities.

Malin 1 was discovered in 1986 (Bothun et al. 1987) and is the archetype of GLSB galaxies with a radial extent of ~120 kpc (Moore & Parker 2006). The galaxy was accidentally discovered in the course of a systematic survey of the Virgo cluster region designed to detect extremely LSB objects (Bothun et al. 1987). Malin 1 has an extrapolated disc central surface brightness of $\mu_{0,V} \approx 25.5$ mag arcsec^{-2} (Impey & Bothun 1997). However, despite its faint surface brightness disc, Malin 1 is a massive galaxy with a total absolute magnitude of $M_V \approx -22.9$ mag (Pickering et al. 1997). It is among the most gas-rich galaxies

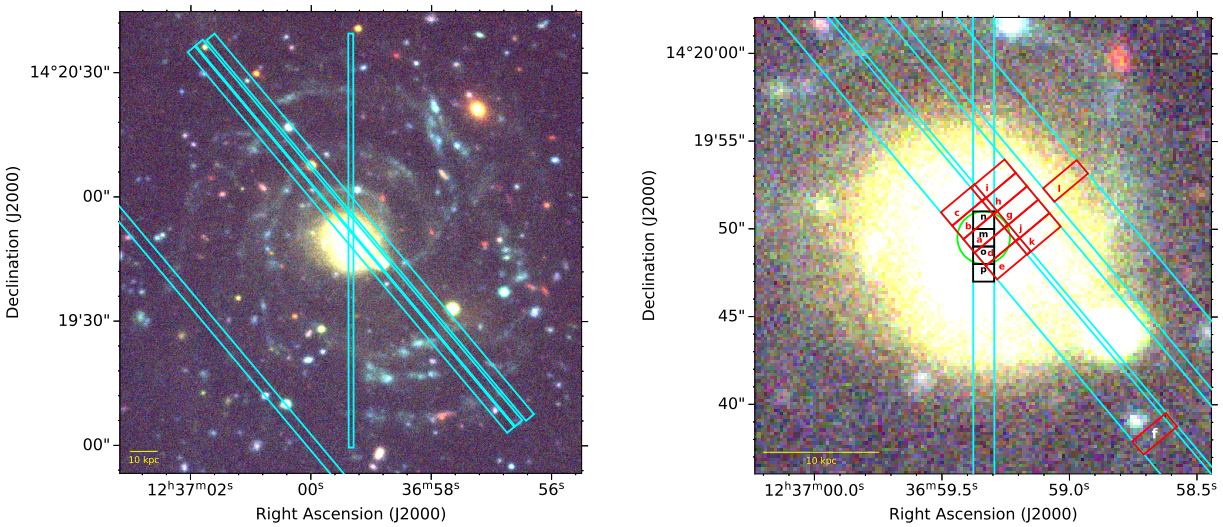

Fig. 1. *Left*: colour composite image of Malin 1 from the CFHT-Megacam NGVS (Ferrarese et al. 2012) *u*, *g*, and *i* band images. The slit positions of our observations are shown as blue rectangles. *Right*: positions of the 16 apertures in which we could extract a spectrum. The 2016 and 2019 observations are denoted as red and black regions, respectively, along with their designated region names (see Tables 2 and 3). The green circular region indicated in the centre is the location of a SDSS spectrum of Malin 1 with an aperture of 3″ diameter.

known with an H I mass of $\sim 5 \times 10^{10}\, M_\odot$ (Pickering et al. 1997; Matthews et al. 2001). Malin 1 lies in a relatively low-density environment in the large-scale structure, typical for LSB galaxies (Reshetnikov et al. 2010). Using the DisPerSE code (Sousbie 2011) with SDSS/BOSS data, we found Malin 1 lies at a distance of about 10 Mpc from the edge of its closest filament. This relatively low density but proximity to a filament could account for the stability and richness of its extremely huge gaseous disc. The analysis of a Hubble Space Telescope (HST) *I*-band image by Barth (2007) suggests that Malin 1 has a normal barred inner spiral disc embedded in a huge diffuse LSB envelope, making it similar to galaxies with an extended ultraviolet (XUV) disc found in 30% of nearby galaxies (Thilker et al. 2007). Therefore Malin 1 can also be seen as the most extreme case of this class of galaxies. It is especially interesting to understand the nature of such discs given that more extended galaxies have recently been found (Hagen et al. 2016; Zhang et al. 2018). So far, limited spectroscopic data have been available for Malin 1. A full velocity map is provided by Lelli et al. (2010), but it is obtained from HI data, with a low spatial resolution. In the optical, a spectrum of the central 3 arcsec was obtained by SDSS (region shown in Fig. 1) and is used by Subramanian et al. (2016) to analyze the active galactic nuclei (AGN) properties of a sample of LSBs including Malin 1. Finally, Reshetnikov et al. (2010) obtained spectra along one long-slit passing by the centre of Malin 1 and a companion, but they did not extract from their data an in-plane RC of the galaxy, and rather concentrated on the possible interaction of Malin 1 and its companion. In this work we analyze new spectroscopic data concerning Malin 1. We derive new constraints on the inner kinematics and star formation rate (SFR) surface densities within about 26 kpc. For the sake of comparison, we adopt the same cosmology as Lelli et al. (2010) with $H_0 = 70\,\mathrm{km\,s^{-1}\,Mpc^{-1}}$, $\Omega_\mathrm{M} = 0.27$ and $\Omega_\Lambda = 0.73$, which corresponds to a projected angular scale of $1.56\,\mathrm{kpc\,arcsec^{-1}}$ and a distance of 377 Mpc. This cosmology is consistent with those found in modern cosmological experiments and close to the WMAP9 results (Hinshaw et al. 2013). The basic properties of the galaxy adopted in this work are summarised in Table 1. In Sect. 2 we discuss the data used in this work along with the steps followed for the data reduction. Section 3 gives the major results we obtained in this work. A detailed discussion on the consequences of our results along with a comparison of existing data and models is given in Sect. 4. Section 5 is dedicated to an extensive study of a suite of new Malin 1 mass models. Conclusions are given in Sect. 6.

Table 1. Selected properties of Malin 1.

Property	Value	References
RA (J2000)	$12^\mathrm{h}\ 36^\mathrm{m}\ 59.350^\mathrm{s}$	1
Dec (J2000)	$+14°\ 19'\ 49.32''$	1
Redshift	0.0826 ± 0.0017	2
V_sys ($\mathrm{km\,s^{-1}}$)	24766.7 ± 4.0	2
D_L (Mpc)	377 ± 8	2
Inclination angle	$38° \pm 3°$	2
Position angle (PA) [(†)]	0°	2

Notes. [(†)]PA is adopted to be 0° for the regions of Malin 1 within $r < 26$ kpc, where we have data in this work (see Fig. 2 of Lelli et al. 2010).
References. (1) NED database; (2) Lelli et al. (2010).

2. Data and reduction

The spectroscopic data of Malin 1 used in this work were obtained with the IMACS spectrograph at the 6.5 m Magellan Baade telescope in the Las Campanas Observatory, Chile. Two runs of observation took place in 2016 and 2019 with long slits of width 2.5″ and 1.2″, respectively.

In 2016, four slit positions were observed. We extracted a total of 12 spectra from different regions of size $1'' \times 2.5''$ each, for the three slit positions for which it was possible to obtain a clear signal. This includes a region at ∼26 kpc, which is relatively far from the centre of Malin 1 (see Fig. 1, region *f*).

These observations cover a wavelength range of 4250−7380 Å with a dispersion of 0.378 Å pix^{-1} and a spectral resolution $R \sim 850$. The large width of the slit was chosen to optimise the chance of detecting H II regions within the slit. The orientation of the slits was chosen on the basis of UV images from Boissier et al. (2008). Each of the slit positions had an exposure time of 3×1200 s, oriented at a position angle (PA) of 39.95° with respect to the major axis of the galaxy (see Fig. 1). The initial position passes through the galaxy centre. For subsequent positions, the slit positions were shifted from each other by a distance of 2.5″ towards the west (except for the fourth slit position, which was moved about 50″ towards east to pass through distant UV blobs, but we could not detect anything at this position. In order to obtain a precise position for each observations, we simulated the expected continuum flux along the slit, based on an image of Malin 1 acquired during the night of the observations (see Appendix A). A χ^2 comparison with our spectral data allowed us to deduce the position of the slit. We estimated the position uncertainty following Avni (1976) and found it to be of the order of 0.1″ (99% confidence level). This process resulted in a small overlap for the slit positions 1 and 2, that is, however, negligible considering the size of the apertures in which we extracted our spectra and thereby each of our apertures are considered as independent regions.

The 2019 observation of Malin 1 was performed using a narrower slit width of 1.2″ oriented at a PA of 0°, along the major axis of the galaxy. The observations were done for a single position with an exposure time of 2×1200 s and a wavelength coverage of 3650−6770 Å to obtain a spectral resolution $R \sim 1000$. We extracted four spectra from this run for which the [O II] doublet (λ3727,3729) is clearly detected (although the two lines overlap at our resolution), each with an aperture size of $1'' \times 1.2''$. The average atmospheric seeing measured at the location was ∼1″, with an airmass of 1.4 and a spatial sampling of 0.111″ pix^{-1} for all the Malin 1 observations.

For both runs, the data reduction and spectral extraction were carried out using standard IRAF[1] tasks within the *ccdred* and *onedspec* packages. The wavelength calibration was done using a standard HeNeAr arc lamp for each aperture independently. Flux calibration of the extracted spectra from the 2016 observation was done using the reference star LTT 3218 (observed at an airmass of 1.011). We did not perform a flux calibration for the 2019 data, since we do not have a proper reference star for this observation. For illustration purposes, as shown in the fourth row of Fig. 2, we normalised the flux with the Next Generation Virgo cluster Survey (NGVS) *u*-band photometry in the same aperture as our slit. Since this is not a proper calibration, we do not provide line fluxes in this case. However, we checked that if we adjust the continuum level with this *u*-band photometry (or with the overlapping spectra from 2016 observations), the [O II]$_{3727}$/Hα flux ratio obtained is within the values found by Mouhcine et al. (2005).

We were able to extract a total of 16 spectra from different regions of Malin 1 (indicated in Fig. 1), where it was possible to obtain a clear signal for our target emission lines (Hα and [O II]). For each slit position, we started from the peak of emission and moved outwards until no signal was measured around the expected line position (the naming of each region shown in Fig. 1 is based on this). This allowed us to obtain 15 measurements in the central region. We kept any regions for which the peak of the emission line is visible above the noise level (above about 2σ). With this approach, we found we could fit a line (sometimes after spectral re-binning for few regions, as explained further). The inner part of the galaxy, as visible in the broad-band image (Fig. 1), is more extended than the regions for which we could secure a detection. This is because the central region is basically similar to an early-type disc (Barth 2007) with old stars but little gas, thus the emission signal drops quickly to very low level.

After extracting 15 spectra in the inner part of the galaxy, we inspected the rest of the galaxy where we had data and searched for emission, especially those regions close to spiral arms observed in optical wavelength or blobs in the GALEX UV images of Malin 1 (Boissier et al. 2016). For this, we used apertures of the same size as that applied in the inner galaxy, but also larger apertures to increase the signal-to-noise ratio in case of extended emission. However, we were able to recover only one additional spectrum ∼26 kpc away from the centre, close to a compact source visible in the broad-band images from NGVS (Ferrarese et al. 2012), as shown in Fig. 1. This also coincides with a UV blob from the GALEX images of Malin 1. We checked that some of the UV emission overlaps with our aperture, however, the GALEX resolution of about 5″ make this association uncertain. We thus turned to UVIT (Kumar et al. 2012) images of Malin 1, which recently became publicly available and we still found some UV emission at this position (at the UVIT resolution of 1.8″, close to the size of our aperture).

We focussed on the Hα and [O II] emission lines, which were the strongest among those in the observed wavelength range (Hα for the 2016 observation and [O II] for the 2019 observations). For simplicity, we refer to the 2016 and 2019 observations as to the Hα and [O II] observations respectively.

We performed a fit of the emission lines using Python routines implementing a Markov chain Monte Carlo (MCMC) method on a Gaussian line profile to obtain the peak wavelength, flux, and the associated error bars of each emission line (see Appendix A). We fitted the overlapping lines (Hα and [N II]; and the [O II] doublet) simultaneously. Various constraints were applied on the emission lines during the fitting procedure, including a fixed line ratio for the [N II] and [O II] doublets ([N II]$_{6583}$/[N II]$_{6548}$ = 2.96 adopted from Ludwig et al. 2012; [O II]$_{3729}$/[O II]$_{3727}$ = 0.58 from Pradhan et al. 2006; Comparat et al. 2016). The line ratio of the [O II] doublet depends on the electron density. We performed tests with values covering the range 0.35−1.5 and finally adopted the typical ratio of 0.58, since we do not know for sure the physical conditions in galaxies of very LSB and the choice was not affecting our conclusions. We also fixed the line separations using the laboratory air wavelengths of the emission lines and taking into account the redshift (given in Table 1), where $\Delta\lambda_{obs} = \Delta\lambda_{lab}(1 + z)$. The uncertainty in the redshift is negligible (within 1σ error of the wavelength and flux values) and does not affect our results. We also performed a spectral re-binning by a factor 3 for a few of our observations affected by a considerably weaker signal that are at the limit of our detection (regions *f*, *l* and *p* from Fig. 2) to increase the signal-to-noise ratio; this allows us to secure a measurement in these apertures at the price of a lower spectral resolution. The detailed results of our fitting procedure are shown in Fig. 2, Tables 2 and 3.

The robustness of the spectral extraction was checked by the comparison of our central region spectrum (region *a*) with that of an SDSS spectrum (DR12) of Malin 1 (see Fig. 4). The entire range of both spectra are consistent in terms of the line

[1] IRAF is distributed by the National Optical Astronomy Observatory, which is operated by the Association of Universities for Research in Astronomy (AURA) under a cooperative agreement with the National Science Foundation.

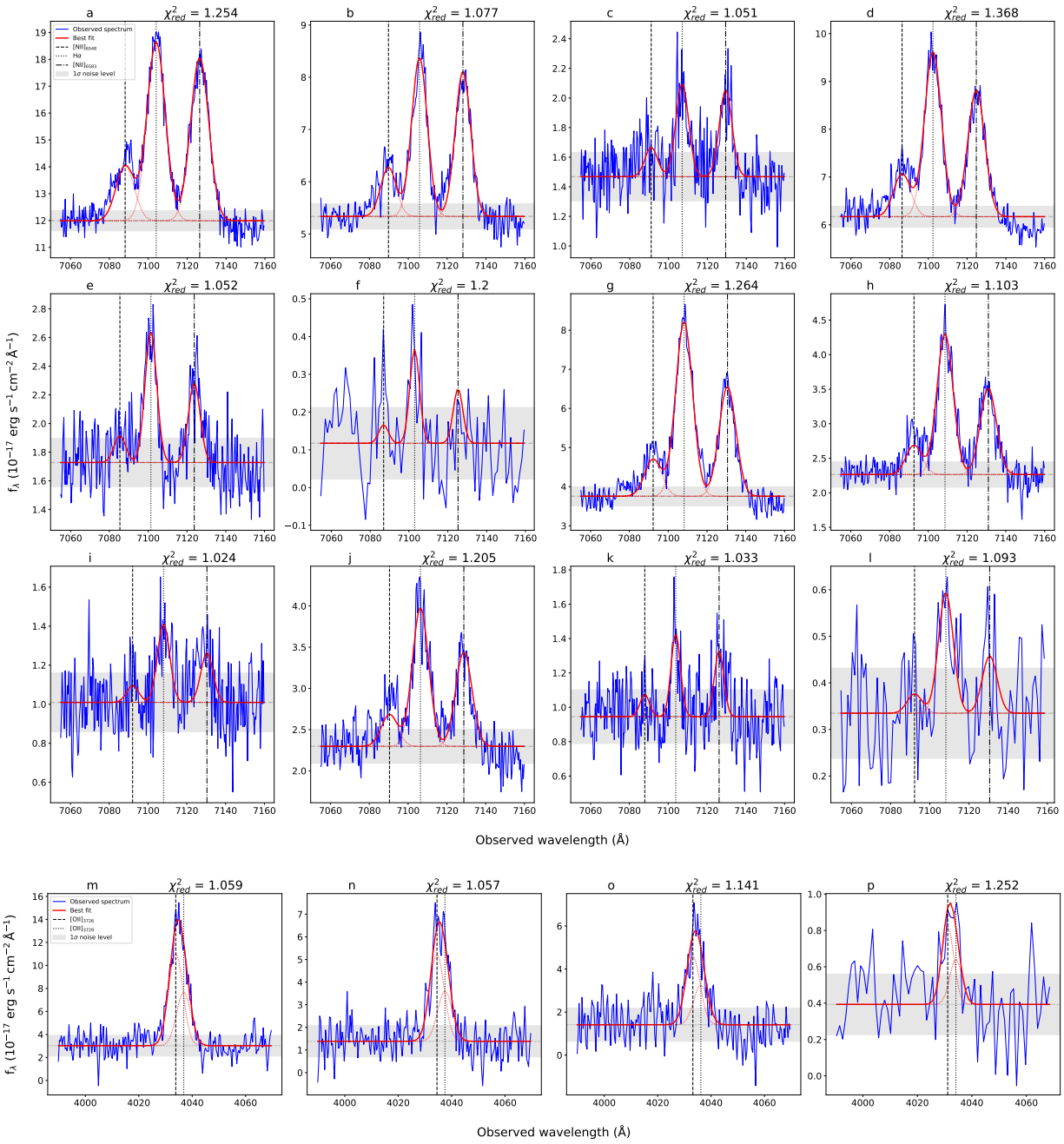

Fig. 2. Zoom on the wavelength range of interest for the 16 spectra extracted in this work (12 Hα spectra in the top three rows and 4 [O II] spectra in the fourth row). The solid red curve is the best fit along with its decomposition in single lines shown as thin red dotted lines. The gray dashed line and shaded region indicates the continuum level obtained from the fitting with the 1σ noise level. The black dashed, dotted, and dot-dashed vertical lines indicate the positions of the [N II]$_{6548}$, Hα and [N II]$_{6583}$ emission lines, respectively, for the *three top rows*. The dashed and dotted lines in the *bottom row* show the position of the two components of the [OII] doublet. The region name and the reduced χ^2 are indicated on top of the each panel.

positions and features. The continuum flux levels in both spectra are also consistent with the expected photometric flux levels measured within their corresponding apertures (shown in Fig. 1) using NGVS *g*- and *i*- band images of Malin 1. For this central region, we also performed an underlying stellar continuum fit using the pPXF (penalized pixel-fitting) method by Cappellari (2017), and we also tried to include a broad component to take into account the nucleus activity. However, the stellar continuum subtraction together with the additional active nucleus Hα broad-line component modified our emission line measurement results

Table 2. Extracted data for Malin 1 from the 2016 observation.

Region name	Radius	Wavelength	Velocity	Flux			
		$\lambda_{H\alpha}$	V_{rot}	Hα	[N II]$_{6583}$	Hβ	[O III]$_{5007}$
	(kpc)	(Å)	(km s^{-1})				
(1)	(2)	(3)	(4)	(5)	(6)	(7)	(8)
a	0.58 ± 0.38	7104.07 ± 0.08	−53 ± 54	78.3 ± 1.5	71.4 ± 1.6	10.8 ± 1.2	25.7 ± 1.7
b	2.00 ± 0.37	7105.77 ± 0.09	80 ± 23	30.5 ± 0.9	27.9 ± 0.9	4.7 ± 0.7	...
c	3.70 ± 0.40	7107.04 ± 0.27	197 ± 39	5.2 ± 0.6	4.8 ± 0.6	...	1.7 ± 0.5
d	1.64 ± 0.48	7102.38 ± 0.09	408 ± 173	37.8 ± 0.9	29.1 ± 0.9	7.0 ± 0.9	12.4 ± 0.9
e	3.33 ± 0.46	7101.37 ± 0.22	420 ± 87	7.0 ± 0.6	4.2 ± 0.5	3.5 ± 1.1	2.7 ± 0.6
f*	25.9 ± 0.43	7102.93 ± 0.88	189 ± 91	1.6 ± 0.5	1.0 ± 0.5	...	...
g	4.53 ± 0.20	7108.22 ± 0.08	393 ± 24	48.9 ± 1.0	30.7 ± 0.9	11.2 ± 0.6	9.1 ± 0.7
h	4.56 ± 0.18	7108.62 ± 0.13	308 ± 13	21.2 ± 0.7	13.0 ± 0.7	3.1 ± 0.6	3.5 ± 0.6
i	5.21 ± 0.14	7108.02 ± 0.47	228 ± 33	3.2 ± 0.5	2.0 ± 0.5	...	1.9 ± 0.5
j	5.12 ± 0.19	7106.38 ± 0.17	367 ± 54	17.7 ± 0.8	12.1 ± 0.8	3.5 ± 0.8	5.6 ± 0.7
k	6.16 ± 0.17	7103.89 ± 0.33	−1092 ± 692	3.0 ± 0.5	2.4 ± 0.4	...	...
l*	10.51 ± 0.27	7108.20 ± 1.08	489 ± 155	2.5 ± 0.7	1.2 ± 0.8	...	1.7 ± 0.4

Notes. (1) Name of the spectral extraction region. The * symbol indicates spectra that were re-binned for the analysis (see Sect. 2). (2) Radius in the galaxy plane. (3) Hα observed wavelength. (4) Rotational velocity in the plane of the galaxy. (5–8) Observed flux of Hα, [N II]$_{6583}$, Hβ, and [O III]$_{5007}$ emission lines, respectively, within the 1″ × 2.5″ regions. The flux units are in 10^{-17} erg s^{-1} cm^{-2}. The error bars shown in the table include the positioning error (Col. 2), fitting errors (Cols. 3 and 5 to 8), or both (Col. 4) (see Appendix A).

Table 3. Extracted data for Malin 1 from the 2019 observation (2019 data are not flux calibrated).

Region name	Radius	Wavelength	Velocity
		$\lambda_{[O II]3727}$	V_{rot}
	(kpc)	(Å)	(km s^{-1})
(1)	(2)	(3)	(4)
m	0.00 ± 0.64	4033.85 ± 0.11	23 ± 13
n	1.56 ± 0.13	4034.52 ± 0.18	104 ± 23
o	1.56 ± 0.13	4033.20 ± 0.24	55 ± 29
p*	3.11 ± 0.07	4031.14 ± 0.67	304 ± 81

Notes. (1) Name of the spectral extraction region. The * symbol indicates spectra that were re-binned for the analysis (see Sect. 2). (2) Radius in the galaxy plane. (3) [O II]$_{3727}$ observed wavelength. (4) Rotational velocity in the plane of the galaxy. The error bars shown in the table include the positioning error (Col. 2), fitting error (Col. 3), or both (Col. 4).

by less than 1.5σ. Since the continuum is too noisy in many of the apertures, it would not be possible to fit it with pPXF in each apertures. Since the effects in the centre, which should be the largest, do not affect our conclusion, we chose to adopt the same procedure in each aperture (i.e. not fitting the underlying stellar continuum subtraction and broad-line component in the results presented in the paper (Table 2)).

3. Results

3.1. Rotation curve

Rotation curves in LSB galaxies have long been debated (see e.g. de Blok & McGaugh 1997; Pickering et al. 1997; Lelli et al. 2010). The analysis of RCs is of utmost importance in understanding the dynamics and underlying mass distribution and may help to understand the origin of giant LSBs (Saburova et al. 2019). One of the main results of this work is the extraction of a RC for Malin 1 using the observed wavelength of Hα and [O II]$_{3727}$ emission lines at different positions within the galaxy.

The global systemic velocity (V_{sys}) of Malin 1 was adopted from Lelli et al. (2010) using H I measurements (see Table 1), which is consistent with the velocity we measure in our Malin 1 centre observation. The observed velocity shift at different regions of the galaxy from V_{sys} is used for the calculation of the rotational velocities on the galaxy plane as a function of radius. We apply a correction for the galaxy inclination angle and PA (see Table 1), assuming an axi-symmetric geometry and a thin disc. However, a region that is too close to the minor axis of the galaxy (region k) is eliminated from the RC since it has a huge azimuthal correction ($\cos\theta = 0.05 \pm 0.02$) when re-projecting the observed velocity to the plane of the galaxy (see Table 2). An additional correction for the heliocentric velocity due to the Earth's motion at the time and location of the observations is also added to the observed velocities ($V_{helio} = -9.1$ km s^{-1} and -16.3 km s^{-1} for the 2016 and 2019 data, respectively).

The uncertainties on the velocities are computed by propagating the line-of-sight velocity measurements using the projection parameters of Malin 1 (line of sight and azimuthal deprojections). We quadratically add to this uncertainty that related to the slit positioning described in Sect. 2. The impact of these uncertainties on the de-projected rotation velocities is computed using 10 000 Monte Carlo realisations. The inclination and PA that we adopted are also uncertain. However, we do not take into account these uncertainties, since changing the inclination does not affect the relative position of the points in the RC much. For example, a change of i equal to 3° varies the rotation velocity by ∼15 km s^{-1}. A possible effect of uncertainty in inclination is discussed in Lelli et al. (2010) as well. In addition, in this work we combine the optical RC with the H I RC from Lelli et al. (2010), so it is reasonable to use the same inclination and PA as in that work.

Figure 3 shows the extracted RC of Malin 1. We observe a steep rise in the rotational velocity for the inner regions (inside ∼10 kpc) up to ∼350 km s^{-1} (with, however, some spread between 200 and 400 km s^{-1} around a radius of 5 kpc), and a subsequent decline to reach the plateau observed on large scales with H I. Such very high velocities (up to 570 km s^{-1}) are observed in massive spirals (Ogle et al. 2019). Both the Hα and

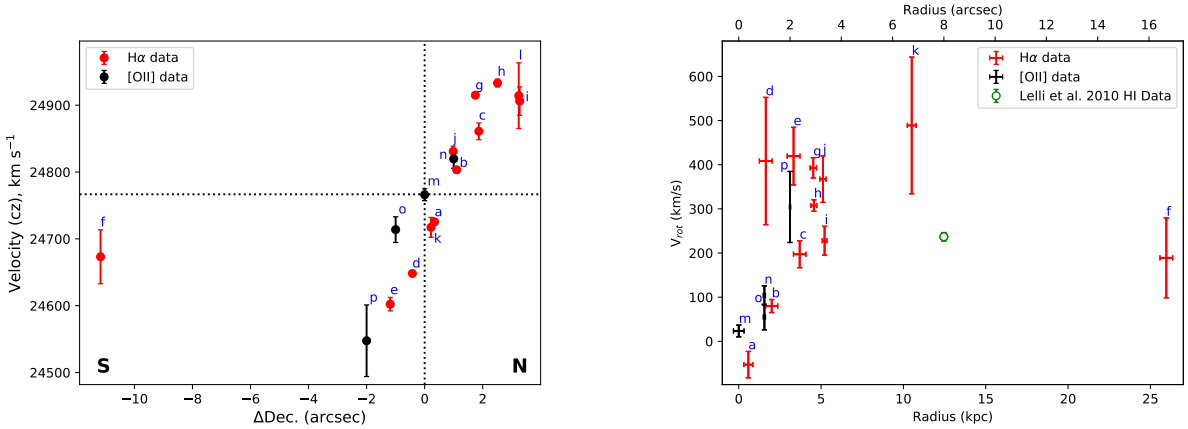

Fig. 3. *Left*: line-of-sight velocity measured from the observed shift in wavelengths for the Hα and [O II] lines (see Tables 2 and 3). The x-axis corresponds to the projected radius on the major axis of the galaxy in the plane of sky. The thick horizontal and vertical dashed lines denote the V_{sys} and major axis of the galaxy, respectively. *Right*: rotation curve of Malin 1, projected on the plane of the galaxy. The red and black points indicate the Hα data and [O II] data, respectively. The green open circle shows the Lelli et al. (2010) H I data point in the same radial range. The region name of each point is inidcated with blue letters.

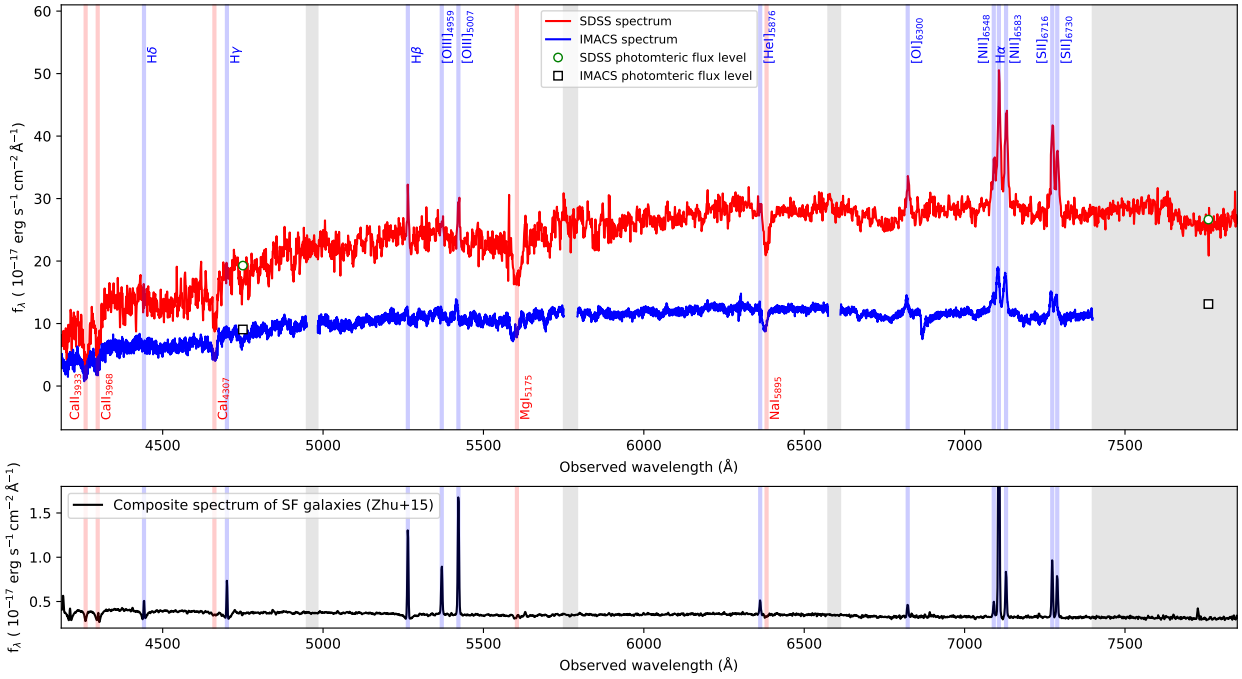

Fig. 4. *Top*: central region spectra of Malin 1. The blue curve is the spectrum extracted in our central 1″ × 2.5″ aperture (region *a* in Fig. 1). The red curve is the SDSS spectrum of the centre of the galaxy, extracted within its circular optical fibre of diameter 3″ (shown in Fig. 1). The green open circles and black open squares indicate the photometric flux levels obtained within the SDSS and our aperture, respectively, using the NGVS *g* and *i* band photometric images of Malin 1. The gray shaded area represent the regions in which we do not have data. *Bottom*: for comparison, we show the median composite spectrum of all star-forming galaxies (at $0 < z \lesssim 1.5$) from the SDSS eBOSS observations (Zhu et al. 2015), shifted to the redshift of Malin 1. The blue and red vertical shaded regions indicate the main identified emission and absorption lines.

[O II] velocities in our data appear to follow a similar trend and are consistent with each other. A steep inner rise of RC is typical for a high surface brightness (HSB) system. For Malin 1, it is the first time that we observe this behaviour, unlike the slowly rising RC predicted by Pickering et al. (1997) or the poorly resolved inner RC from Lelli et al. (2010) using H I data. The implications of this result and a comparison to existing models and data are discussed in Sect. 4 and motivate the computation of new mass models (Sect. 5).

3.2. Hα surface brightness and star formation rate

We extract the Hα flux for the 12 regions of Malin 1 discussed in Sect. 2. The observed flux is corrected for inclination

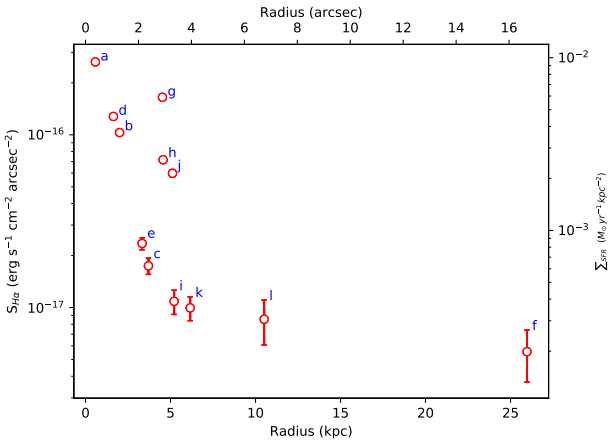

Fig. 5. Hα surface brightness measured for different regions of Malin 1. The axis in the right shows the star formation surface density (Σ_{SFR}), corresponding to the observed Hα flux, using the calibration from Boissier (2013). The region name of each point is indicated with blue letters.

and also for the Milky Way foreground Galactic extinction (Schlegel et al. 1998) using the standard Cardelli et al. (1989) dust extinction law. We expect a low dust attenuation within Malin 1 itself, since LSB galaxies in general host very small amounts of dust (Hinz et al. 2007; Rahman et al. 2007). With our data, we can probe the effect of dust attenuation on the Balmer ratio, compared to its theoretical value in the absence of dust. Indeed, we measure both the Hα and Hβ fluxes in eight apertures. The Balmer ratio is however also affected by the underlying stellar absorption. Since our data lack spectral resolution to measure this ratio or signal in the continuum to fit the stellar populations in all of our regions, we applied standard equivalent width (EW) corrections. A large diversity of stellar underlying absorption EW for Hα and Hβ is found in the literature (Moustakas & Kennicutt 2006; Moustakas et al. 2010; Boselli et al. 2013). We first chose to apply the EW corrections that were measured by Gavazzi et al. (2011) for 5000 galaxies (EW Hα_{abs} = 1.3 Å) and by Moustakas et al. (2010) for the representative SINGS sample (EW Hβ_{abs} = 2.5 Å). The Balmer ratio of our eight regions was then found within 3σ of the theoretical value of 2.86 for Case B recombination (Osterbrock 1974). The ratio is especially sensitive to the correction to the weaker Hβ line. In order to check the effect of our choice, if we adopt instead another value among the literature, that is EW Hβ_{abs} = 5.21 Å (Boselli et al. 2013), the Balmer ratio in the eight regions is now systematically below the theoretical value of 2.86. The Hα_{abs} and Hβ_{abs} EW values adopted above from the literature are also consistent with the EW values we obtained from our stellar continuum pPXF fitting of the region *a* discussed in Sect. 2. Although our EW correction procedure is uncertain, both choices of correction for the underlying stellar absorption lead to a Balmer ratio that is consistent with the absence of dust attenuation. Moreover, Malin 1 is also undetected in the far-infrared with *Spitzer* and *Herschel*, which also indicates low attenuation (Boissier et al. 2016). Therefore we can reasonably assume that the Hα flux we measured in this work is only weakly affected from dust attenuation within Malin 1.

Figure 5 shows the extracted Hα surface brightness for the 12 detected regions of Malin 1 plotted as a function of the radius. There is a steep decrease in the surface brightness for the inner regions of Malin 1, similar to a trend that was observed in the Malin 1 *I*-band surface brightness profile by Barth (2007). This could imply that in the inner regions of Malin 1, the gas profile follows the stellar profile as in normal galaxies (Combes 1999).

The presence of Hα emission in a galaxy is also a direct indicator of star formation activity at recent times (within ~10 Myr; e.g. Boissier 2013) provided there is no other source of ionisation like an AGN. However, the effect of a nucleus as a source of ionisation is confined to the single central point of our measurements and cannot have much effect on our kpc scales (see Appendix B on the nuclear activity of Malin 1). Therefore, except for the central region, we can convert with confidence the measured Hα flux to the SFR using standard approximations. We estimate the surface density of SFR (Σ_{SFR}) for the 12 regions of Malin 1 following Boissier (2013) who gives for a Kroupa (2001) initial mass function,

$$\mathrm{SFR}\,(M_\odot\,\mathrm{yr}^{-1}) = 5.1 \times 10^{-42}\, L_{H\alpha}\,(\mathrm{erg\,s}^{-1}). \quad (1)$$

Our apertures cover several kpc. In the central regions of the galaxy with relatively elevated SFR, we expect to find several H II regions per aperture, so that the assumption of quasi-constant star formation history on 10 Myr timescale for Eq. (1) is valid. In the outer aperture, however, star formation is less elevated and may be stochastic so the derived SFR is less robust.

4. Discussions

4.1. Surface density of the SFR

Figure 6 shows a comparison of our Malin 1 estimates of the density of SFR at various radii from Sect. 3.2 compared to the SFR radial profile for samples of disc galaxies from the CALIFA survey that have different morphologies (González Delgado et al. 2016). These profiles are normalised to the half light radius (HLR). We estimate the HLR of Malin 1 to be equal to 2.6″, calculated within 20″ of the centre of the galaxy using the *I*-band surface brightness profile discussed later and shown in Fig. 7. We adopt this limit such that the comparison is based on the inner galaxy at the centre of Malin 1 as described by Barth (2007) rather than the extended disc because we believe the CALIFA survey (with data from SDSS) corresponds to this inner galaxy better. If we were computing the HLR over the full observed profiles, its value would increase to 18.28″ and the Malin 1 points in Fig. 6 would be much more concentrated.

Our measurements within ~1.5 HLR behave like an intermediate S0/Sa early-type spiral galaxy (Fig. 6), consistent with the observation from Barth (2007). We also verified that a comparison with the specific SFR radial profile (using the stellar profile in Boissier et al. 2016) leads to the same conclusion. A similar work on two GLSB galaxies Malin 2 and UGC 6614 from Yoachim et al. (in prep.) also shows that GLSB galaxies in general behave like large early-type galaxies at their centre. Our region at 26 kpc from the centre is likely to be part of the extended disc (Barth 2007). Since we detect Hα at only one region really in the extended disc, it is impossible to draw conclusions using this value concerning the overall surface brightness and SFR at that radius. However this surface density of SFR is consistent with the expectations based on the UV blobs luminosity measured in the UV images. It also falls within the 1σ dispersion around the average SFR surface density seen in extended discs of spiral galaxies by Bigiel et al. (2010), as shown in Fig. 6. Finally, a model from Boissier et al. (2016) for Malin 1 also predicts the SFR surface density around this radius to be 0.08 $M_\odot$ Gyr^{-1} pc^{-2}, which is consistent with our measurement.

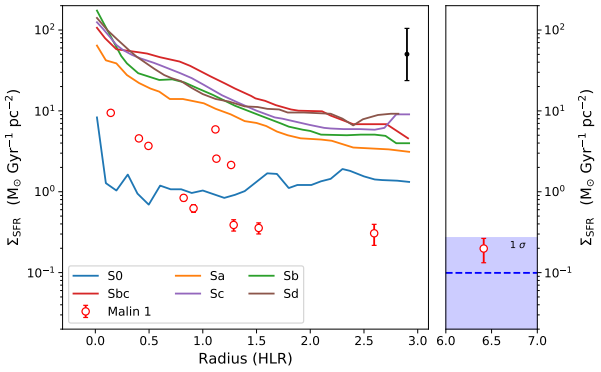

Fig. 6. Radial profiles, in units of HLR, of the surface density of the SFR (Σ_{SFR}). The curves correspond to the averages obtained for six morphologies of spiral galaxies from González Delgado et al. (2016). The red points shows our extracted Hα data for Malin 1. The blue dashed line indicates the mean level of Σ_{SFR} in the extended disc of spiral galaxies from Bigiel et al. (2010) with a 1σ level of dispersion (blue shaded region). The error bar in black indicates the typical dispersion among galaxies provided by González Delgado et al. (2016) around each solid curve.

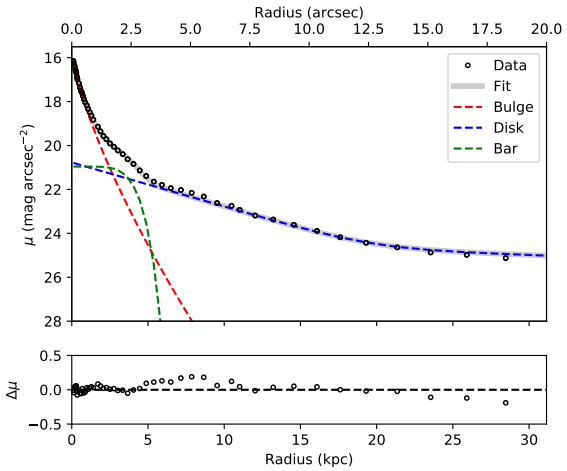

Fig. 7. Malin 1 *I*-band surface brightness decomposition. *Bottom panel*: difference between the observed surface brightness distribution and the model fit shown in the *top panel*.

However it should be kept in mind that the model predicts the azimuthal average SFR, while our measured value value corresponds to a single detected region. Moreover, the detection at 26 kpc is very uncertain owing to the sky level. Deeper observations would help to confirm this and possibly detect other faint H II regions in the extended disc.

4.2. Comparison of our rotation curve with other data

Lelli et al. (2010) provided a RC for Malin 1 using H I data (Fig. 8). However the poor spatial resolution of their data makes it hard to study the dynamics in the inner regions of the galaxy ($r < 10$ kpc) and especially to measure the mass content of the DM in LSB galaxies.

Yet another work on spectral analysis of the inner regions of Malin 1 was performed by Reshetnikov et al. (2010) using stellar absorption lines (shown in Fig. 8). However, these authors only provide the radial velocity data corresponding to a single slit position (PA = 55°), which we converted to the rotational velocities in the plane of the galaxy taking into account the same geometrical assumptions we adopt in this work (Sect. 3.1). The rotational velocities from Reshetnikov et al. (2010) within ∼10 kpc are in broad agreement with our data considering their large error bars. This suggests that the gas and stars rotate together in a coherent way in the central regions of Malin 1. Some stellar absorption lines were also detected in very few regions of our data, and these were consistent with our observed RC. However, we prefer not to use these stellar absorption lines considering the poor signal-to-noise ratio and the small number of detected regions. An accurate comparison of the stellar and gaseous dynamics would require, for exmaple IFU data.

In other GLSBs, other behaviours have sometimes been observed, such as counter-rotation in UGC 1922 (Saburova et al. 2018). Yoachim et al. (in prep.) observes a slowly rising RC for the GLSB galaxies Malin 2 and UGC 6614 using stellar absorption lines, unlike the trend we observe for Malin 1 in this work.

4.3. Comparison of our rotation curve with existing models

A mass model for Malin 1 from Lelli et al. (2010) using H I data (shown in Fig. 8), does not capture the highest rotational velocities we observe for the inner regions and do not show the rise of the RC. This could be due to the low resolution of the H I data used as the basis of their modelling. Our new observations with high spatial resolution in the centre of Malin 1 call for a new mass modelling attempt that is consistent with our observed rotational curve, taking into account all the stellar, DM, and gas contributions for the rotational velocity within the galaxy, which is discussed in the Sect. 5.

A recent publication by Zhu et al. (2018) based on the IllustrisTNG simulations also puts forward some interesting results. These authors were able to find a Malin 1 analog with similar features to Malin 1 observations and its vast extended LSB disc in the volume of a 100 Mpc box size simulation. They discuss the formation of a "Malin 1 analog" from the cooling of hot halo gas, triggered by the merger of a pair of intruding galaxies. Their results also include a prediction for the RC of the simulated galaxy with a maximum rotational velocity of 430 km s^{-1} (shown in Fig. 8), close to the maximal value observed for Malin 1 in our analysis. However, the sudden rise of the inner RC for Malin 1 followed by a decline to ∼200 km s^{-1} seen in our analysis is not observed in their RC. This comparison demonstrates that our observational results offer a new constraint for this type of simulations in the future or any other model of Malin 1 or Malin 1 analogs. Indeed, LSBs and GLSBs can now be studied in the context of cosmological simulations (Kulier et al. 2019; Martin et al. 2019).

5. New mass modelling

We use our Hα and [O II] RCs in combination with H I measurements from Lelli et al. (2010) and the HST *I*-band photometry (Barth 2007) to construct a new mass model for Malin 1.

We have the total circular velocity components within a disc galaxy given by

$$V_{cir}(r) = \sqrt{V^2_{disc} + V^2_{bulge} + V^2_{gas} + V^2_{halo}}, \quad (2)$$

where V_{cir} is the circular velocity of the galaxy as a function of radius. V_{disc}, V_{bulge}, V_{gas}, and V_{halo} are the stellar disc, stellar bulge, gas, and DM halo velocity components, respectively.

Table 4. Decomposition parameters obtained for Malin 1 from the fitting results.

	Sérsic				
	μ_e (mag arcsec^{-2})		r_e (arcsec)		n
Bulge	18.26 ± 0.05		0.59 ± 0.05		1.39 ± 0.02
Bar	21.07 ± 0.18		1.82 ± 0.28		0.17 ± 0.36
	Broken exponential				
	μ_0 (mag arcsec^{-2})	h_i (arcsec)	h_o (arcsec)	r_b (arcsec)	α
Disc	20.77 ± 0.21	3.4 ± 0.5	26.9 ± 4.9	12.6 ± 1.38	0.7 ± 0.2

Notes. The top two rows show the parameters for the Sérsic function of the bulge and the bar. The bottom row indicates the parameters for the disc according to the broken exponential function from Erwin et al. (2008).

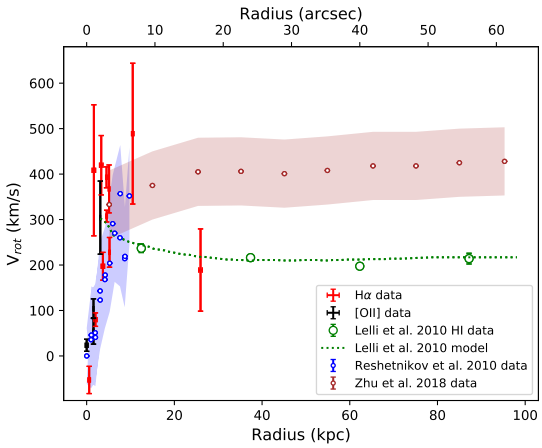

Fig. 8. Existing models and data for Malin 1. In addition to the data presented in Fig. 3, the green dotted curve is a model from Lelli et al. (2010), assuming a constant stellar mass-to-light ratio ($M_\star/L = 3.4$). The brown open circles with the shaded region correspond to an IllustrisTNG100 simulated data from Zhu et al. (2018) for a galaxy similar to Malin 1. The blue open circles indicate the data from Reshetnikov et al. (2010) using stellar absorption lines with the error bars denoted as the blue shaded region.

We use the H I gas distribution from Lelli et al. (2010), corrected for the distance adopted, to derive the gas velocity component. However, to constrain the stellar bulge and disc velocity components, we need to make a light profile decomposition of Malin 1, discussed in Sect. 5.1.

5.1. Light profile decomposition

We adopt the I-band light profile provided by Lelli et al. (2010) who combined the HST I-band surface brightness profile of Malin 1 from Barth (2007) for $r \lesssim 10$ kpc (high spatial resolution) and the R-band profile from Moore & Parker (2006) for $r \gtrsim 10$ kpc (large spatial extent). This high spatial resolution in the centre is of primordial importance for the RC study, making the use of HST data necessary for the inner part. At larger radii, we check that this profile is consistent with the recent NGVS (Ferrarese et al. 2012) data of Malin 1 (Boissier et al. 2016).

We perform a decomposition of the I-band surface brightness profile following procedures from Barbosa et al. (2015), into a Sérsic bulge, bar and a broken exponential disc component (Erwin et al. 2008) described as

$$I_d(r) = S\, I_0 e^{-\frac{r}{h_i}} \left[1 + e^{\alpha(r-r_b)}\right]^{\frac{1}{\alpha}\left(\frac{1}{h_i} - \frac{1}{h_o}\right)}. \quad (3)$$

The broken exponential function consists of a disc with an inner and outer scale length, h_i and h_o, respectively. The parameters r_b is the break radius of the disc and α gives the sharpness of the disc transition. Table 4 and Fig. 7 shows the results of our surface brightness decomposition. These values are in good agreement with the decomposition from Barth (2007), although we obtain a relatively stronger bulge and a weaker bar than in their decomposition. This is a minor difference with negligible effects on our further results. It is well known that bars can cause non-circular motions (Athanassoula & Bureau 1999; Koda & Wada 2002; Chemin et al. 2015). However, the orientation of the bar in Malin 1 (approximately 45° with respect to the PA) could not create major non-circular velocity contributions. As a consequence of the scarcity of measurements, we do not include a bar contribution in our mass modelling. Therefore, to make the mass models, we finally consider two components: the Sérsic bulge obtained as the fit described previously and the "disc", which is the observed profile minus the bulge (in order to account for all the light, but distinguish the spherical geometry of the bulge). These profiles are further corrected for the inclination to be used in the mass models.

5.2. Mass-to-light ratio

During the construction of mass models (Sect. 5.4), the surface brightness values are converted into stellar mass profiles, in some cases by fitting the RC, keeping the stellar mass-to-light ratio as a free parameter. However, it is also possible to fix this ratio on the basis of the colour index profile. Taylor et al. (2011) gives the following empirical relation for the conversion g-i colour to stellar mass-to-light ratio:

$$\log(M_\star/L_i)_\odot = -0.68 + 0.70(g - i), \quad (4)$$

where $M_\star/L_i$ is the i-band stellar mass-to-light ratio in solar units. The values g and i are the g-band and i-band magnitudes, respectively. We use the above relation to obtain $M_\star/L_i$ to a 1σ accuracy of ≈0.1 dex.

We measure a radial profile of the g-i colour from the NGVS images of Malin 1 using the *ellipse* task in IRAF. Our measured values, computed at the NGVS resolution of ∼1″, are in good agreement with the g-i colour of Malin 1 from Boissier et al. (2016) computed at the GALEX resolution of 5″. Therefore, we use our measured g-i colour profile to obtain a $M_\star/L_i$ profile of Malin 1 using the empirical relation given in Eq. (4). Figure 9 shows our extracted colour and $M_\star/L_i$ as a function of radius. We carry out a polynomial fit of the order of 3 on the extracted $M_\star/L_i$ profile as follows:

$$\frac{M_\star}{L_i}(r) = 1.69 - 0.0986r + 0.0025r^2 - 0.0000208r^3. \quad (5)$$

This Eq. (5) is only valid for a radius $1'' < r < 40''$. For radius $r < 1''$, we adopt a peak value of $M_\star/L_i = 3.765$ from the colour profile. For $r > 40''$, we adopt a value of $M_\star/L_i = 0.379$ in order to make a flat profile for the extended disc.

In Sect. 5.4, three assumptions are adopted concerning the $M_\star/L_i$: keeping this ratio as a free parameter, fixing it on the basis of Eq. (5) for the disc, or maintaining the constant $M_\star/L_i$ value of 3.765 for the bulge.

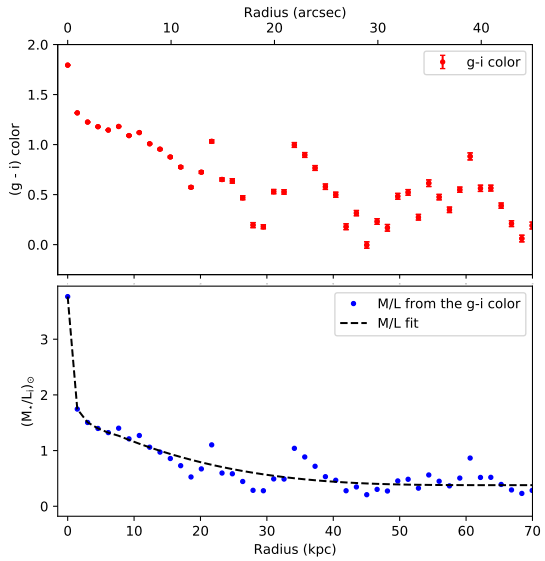

Fig. 9. *Top*: *g-i* colour profile of Malin 1 measured from the NGVS *g*-band and *i*-band images. *Bottom*: stellar mass-to-light ratio of Malin 1 in *i*-band measured using the empirical relation from Taylor et al. (2011). The black dashed line indicates the best fit for the measured $M_\star/L_i$.

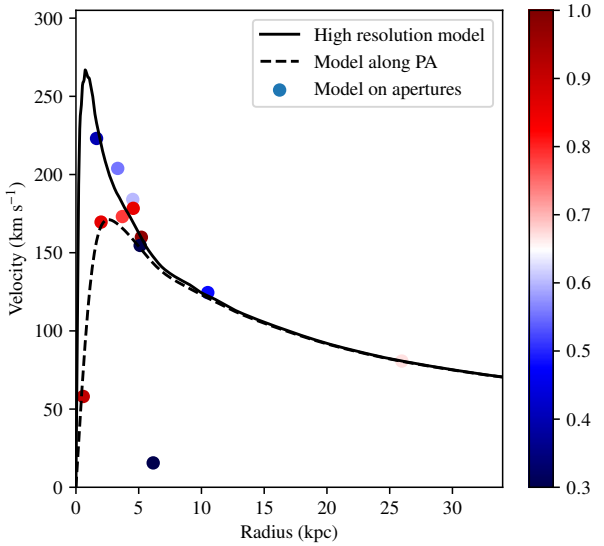

Fig. 10. Effect of beam smearing on the RC. The dashed line indicates the high-resolution model, where all the light is supposed to come from the disc, with the M/L that varies as described in Sect. 5.2. The solid line indicates the model after accounting for the effect of the beam smearing: the velocity is computed for apertures of 2.5″, with a slit aligned with the major axis. The dots correspond to the model on the actual apertures of the Hα dataset and their colour indicates their cosine of the azimuth in the galaxy plane.

5.3. Beam smearing correction

The decomposition of the light profile (Fig. 7) is used to compute the circular velocities of the bulge and disc stellar components. We assume a thin disc and spherical bulge to compute those velocities. These velocities indicate that the rotation is expected to rise more steeply than what is actually observed. One possible reason for this is that the long-slit data is severely affected by resolution owing to the seeing, the size of the slit, and the apertures used to generate the RC in conjunction with the large distance of Malin 1 and the shape of its inner stellar distribution. The impact of this effect can be computed on models, using an observed or modelled light distribution. Epinat et al. (2010) detailed how to perform such computations on velocity fields. In our case, we use the expected geometry of Malin 1 (inclination and position of the major axis) together with the light distribution measured in Hα fit by a third order polynomial supposed to be axisymmetric. High-resolution velocity fields (oversampling by a factor 8 with respect to the actual pixel size) are drawn from idealised RCs derived from stellar mass profiles and we then model the impact of seeing using the recipes presented in Epinat et al. (2010): a convolution of the velocity field weighted by the line flux map normalised by the convolved line flux map. An observational velocity is then derived as the weighted mean of the velocity field on each aperture and the resulting deprojected velocity is computed using the azimuth of the aperture centre and the galaxy inclination. For each stellar component (bulge and disc), the high-resolution mass profiles, obtained both with and without an optimised and varying with radius M/L ratio (see Sect. 5.2), are used to infer the beam smearing curve. The impact of beam smearing is shown in Fig. 10, which clearly illustrates that beam smearing decreases the amplitude of the velocity and offsets the peak of velocity to larger radii. These modifications depend on both the seeing and the slit width. It also clearly shows that depending on the azimuth, the corrections differ and that it is therefore mandatory to compute the beam smearing for each aperture. In the case of the Hα data, the slit is not aligned with the major axis. Apertures that are centred on the major axis therefore have a different value than the ideal case with the slit aligned with the major axis.

The beam smearing and aperture correction are therefore computed for each individual aperture. These curves are then used in the mass model fitting to describe the stellar components. We did not apply such corrections to other components since they are not expected to strongly dominate in the inner regions where the beam smearing is the most severe.

5.4. Dark matter halo

To quantify the distribution of the DM in Malin 1 we use the observation-motivated ISO sphere with a constant central density cored profile (Kent 1986). The core central density profile of the halo is a single power law and the velocity distribution depends on two free parameters: the halo core radius R_c and velocity dispersion σ, providing the asymptotical circular velocity as $\sqrt{2}\sigma$, that is,

$$V_{\rm halo}(r) = \sqrt{2}\sigma \times \sqrt{\left(1 - \frac{R_c}{r}\arctan\frac{r}{R_c}\right)}. \quad (6)$$

The mass model is adjusted by changing the parameters.

5.5. Weighting of the rotation curve

The analysis of the mass models depends on the weighting of the RCs, especially when we combine different datasets to construct hybrid RCs as is the case in this study (Hα, [O II] and H I). The use of a chi-square test (χ^2) for goodness of fit depends on the variance of the independent variables. The latter variables are

the rotation velocities and the variance is the uncertainty associated with the rotation velocity estimation. The method for calculating uncertainties may differ, depending on the nature of the data and on the authors. In addition, the density of uncorrelated Hα rotation velocities is in general larger than for H I RCs and the uncertainties are intrinsically larger. We normalise the uncertainties in attributing the same total weight to the Hα and to the H I datasets to have a similar contribution to the fit from inner and outer regions. Because the weight of uncertainties in a fit is not an absolute but relative quantity, we do not modify the Hα uncertainties but we redistribute the new weights on the H I data only, using the relation given in Korsaga et al. (2019). The weight given to a velocity point is the inverse of its uncertainty. The impact of using different weighing methods is discussed in Sect. 5.6.

5.6. Results of the mass modelling

We present in Fig. 11 the mass model for two cases. On the top panel (model a) the disc and the bulge stellar mass-to-light ratio (M/L_{Bulge}) are computed using the colour indices, as discussed in Sect. 5.2, and the disc one (M/L_{Disc}) varies with the radius as shown in Fig. 9. The core radius R_c and the velocity dispersion σ of the DM halo are adjusted using a best-fit model (BFM). In the bottom panel (model b), the four parameters of the model are let free to vary; these are minimised by a BFM and M/L_{Bulge} is also forced to be larger than M/L_{Disc}. The parameters of those two models are given in Table 5. Those two models lead to similar halo parameters even though the disc component is about twice as large in model (b) as in model (a) because the larger disc is almost compensated by a weaker bulge in model (b). The DM halo dominates the baryonic components from ∼10 kpc to the end of the RC at ∼100 kpc and the bulge is requested to fit the RC within the first five kpc because the DM halo is not cuspy enough. The main issue of both models is, however, that neither is able to fit the centre of the RC and rotation velocities larger than ∼250 km s^{-1} correctly.

We tested the ability of other models to fit these inner points of the RC and report the results for some of those in Table 5. Model (c) is a MDM in which we force the halo to vanish and the disc to be maximal to better fit the inner velocity points of the RC. The $\chi^2 \sim 8.2$ is smaller than for models (a) and (b) meaning that the fit is better on average. This set of parameters is fully compatible with no bulge and no halo but the price to pay for that is an unrealistically large $M/L_{Disc} \sim 20.2\, M_\odot/L_\odot$, compared to $M/L_{Disc} \sim 1 \pm 0.5\, M_\odot/L_\odot$ provided by colour indexes. Because this model has no halo, it only implies two free parameters (the baryonic components). However, if we divide the non-reduced χ^2 by the number of data points (19) minus four free-parameters instead of two, we get a reduced $\chi^2 \sim 9.3$ as reported in Table 5, Cols. (3) and (5). Model (d), which is a BFM with four free parameters allowing M/L_{Disc} to be larger than M/L_{Bulge}, provides similar results as model (c) with the same absence of bulge, a strong disc, and a weak halo even though it shows that the disc alone cannot adjust the RC. Models (c) and (d) hardly fit some inner velocity points around 300 km s^{-1}, they cannot fit the highest velocity points either; in addition, rotation velocities between 10 kpc and 30 kpc are largely overestimated. We conclude that the "natural" solution when M/L_{Disc} can (non-physically) overpass M/L_{Bulge}, is a model without DM halo and without bulge (or very marginal haloes and/or bulges). It is interesting to compare the mass models when the mass-to-light ratio changes or does not change with the radius. Indeed, in the former case, the ratio varies from $\sim 2\, M_\odot/L_\odot$ in the centre of the galaxy, to

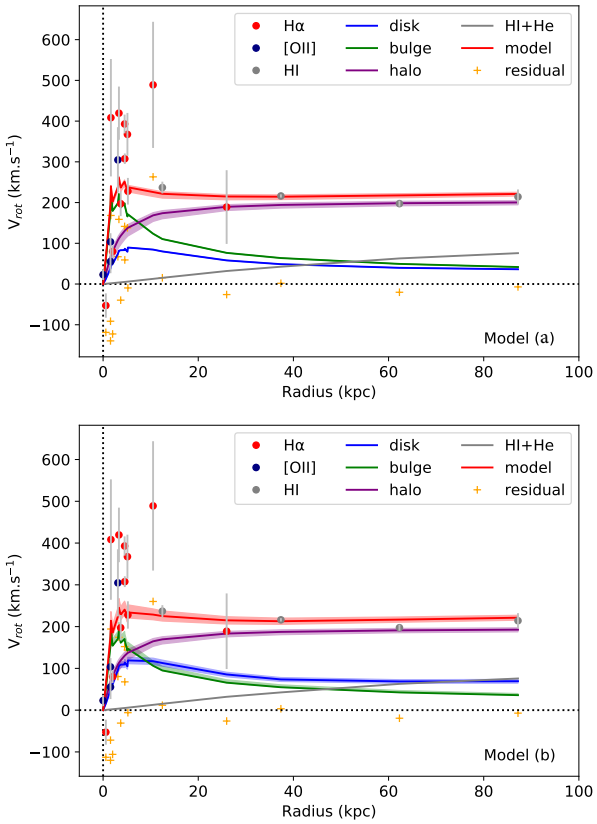

Fig. 11. Hybrid RC is plotted using different symbol to represent Hα, [O II] and H I data. The resulting model, plotted using a red line, is the quadratic sum of the gas, disc, bulge, and dark halo components. The lines correspond to the BFM and the bottom and top of the filled area around these lines represent the first and the third percentile around the median (the second percentile) the χ^2 distribution ranging from χ^2_{min} to $1.10\chi^2$. The orange crosses represent the difference between the observed rotation velocities and the model for each point of the RC. *Top panel* (model a): both disc and bulge mass-to-light ratios are fixed by the colour indexes and M/L_{Disc} varies with the radius as shown in Fig. 9. The halo parameters are computed using a BFM. *Bottom panel* (model b): the disc, bulge, and halo parameters are fitted using a BFM, but M/L_{Disc} is not allowed to be larger than M/L_{Bulge}.

∼0.38 $M_\odot/L_\odot$ at a radius ∼70 kpc, with a median value of ∼1 within the first 25 kpc, where most of the velocity measurements are and where the disc contribution is the highest (see Fig. 9 and Sect. 5.2).

Best-fit models (d) and (f) use a M/L_{Disc} that does not vary with the radius while this parameter does vary in models (a) and (e). By definition, the best χ^2 parameter is obtained when all the parameters are fully free to optimise the fit without any constraints. This is the case for models (d) and (e) for which the physical constraint $M/L_{Bulge} > M/L_{Disc}$ is not imposed to the fit; thus we get the smallest $\chi^2 \sim 7.7$, almost 1.7 smaller than for models (a) and (b), which provide $\chi^2 \sim 13$. Comparing models (d) and (e) shows that the average M/L_{Disc} of model (d) is ∼1.5× larger than that of model (e). The consequence is a stronger halo in model (e) to compensate for its weaker M/L_{Disc} at large radius. Model (f) is a variation of model (a) for which the M/L_{Disc} does not change with the radius. The results for models (a) and (f) are very similar. The impact on the halo seen in model (e) with

Table 5. Results of the mass models.

(1) ID	(2) Colour Symb.	(3) Models	(4) Comments	(5) $\chi^2_{\rm min}$	(6) $M/L_{\rm Disc}$ ($M_\odot/L_\odot$)	(7) $M/L_{\rm Bulge}$ ($M_\odot/L_\odot$)	(8) $R_{\rm c}$ (kpc)	(9) σ (km s^{-1})
(a)	$y\star$	BFM (2)	$M/L_{\rm Disc}(r)$ & $M/L_{\rm Bulge}$ c-fix	12.8	1.5–0.5	3.76	$2.4^{1.1}_{0.3}$	142^{7}_{4}
(b)	$w+$	BFM (4)		13.2	$2.8^{0.4}_{0.4}$	$2.8^{0.6}_{0.1}$	$2.3^{0.7}_{0.3}$	139^{3}_{3}
(c)	OfR	MDM ([a] 2/4)	$M/L_{\rm Disc} \geq M/L_{\rm Bulge}$	[a] 8.2/9.3	$20.2^{0.6}_{0.6}$	$0.0^{0.1}_{0.0}$	∞	0
(d)	OfR	BFM (4)	$M/L_{\rm Disc} \geq M/L_{\rm Bulge}$	7.8	$15.8^{1.0}_{0.4}$	$0.0^{0.2}_{0.0}$	$4.2^{11.9}_{0.5}$	85^{17}_{2}
(e)	$o\square$	BFM (4)	$M/L_{\rm Disc}(r) \geq M/L_{\rm Bulge}$	7.6	[b] $9.7^{1.0}_{0.3}$	$0.0^{0.1}_{0.0}$	$5.9^{8.5}_{0.4}$	115^{17}_{2}
(f)	$b\star$	BFM (2)	$M/L_{\rm Disc}$ & $M/L_{\rm Bulge}$ c-fix	13.0	1.0	3.76	$2.4^{0.8}_{0.3}$	144^{5}_{3}
(g)	$lb\star$	BFM (3)	$M/L_{\rm Bulge}$ c-fix	12.8	$3.7^{0.1}_{0.8}$	3.76	$3.0^{0.8}_{0.6}$	135^{6}_{1}
(h)	$dg\square$	MBM (3)		16.6	$2.6^{2.0}_{0.4}$	6.0	$4.6^{4.9}_{0.1}$	137^{12}_{4}
(i)	$g\circ$	MBM (2)	Bulge only	24.8	–	9.0	$15.2^{0.1}_{8.1}$	119^{2}_{24}
(j)	$l\circ$	MDM (2)	Disc only	32.2	9.0	–	$13.0^{0.3}_{6.0}$	121^{3}_{20}
(k)	$v\circ$	BFM (3)	Bulge only	12.7	–	$3.1^{0.6}_{0.2}$	$2.2^{1.1}_{0.3}$	137^{4}_{4}
(l)	$p\circ$	BFM (3)	Disc only	13.5	$2.3^{0.6}_{0.1}$	–	$1.9^{0.8}_{0.1}$	142^{5}_{3}
(m) [c]	OfR	BFM (2)	(a) & IllustrisTNG100	–	1.5–0.5	3.76	3(hs)–4(ls)	298(hs)–307(ls)
(n) [c]	OfR	BFM (4)	(b) & IllustrisTNG100	–	0(ls)–2(hs)	0(ls)–6(hs)	2(ls)–5(hs)	298(ls)–305(hs)

Notes. Column (1): identification of the model. Column (2): colours (*y*: yellow; *w*: white; OfR: model not plotted because out of the figure range; o: orange; b: blue; lb: light blue; dg: dark green; g: green; l: lime; *v*: violet; and p: pink) and symbols ($\star$ for models using the mass-to-light ratio computed from the colour indexes and $\circ$ for models with only one baryonic component, a disc or a bulge) used in Fig. 12 to locate the results of the mass models. Column (3): BFM, MBM, and MDM means, respectively, best-fit model, maximum bulge model, and maximum disc model. The number after the model indicates the number of free parameters of the fit. Column (4): comments on the models. In all the models, except in (c), (d), (e), (i), and (k), the condition $M/L_{\rm Disc} \leq M/L_{\rm Bulge}$ is imposed; "c-fix" means that mass-to-light ratios have been fixed using the colour indexes (which is not the case when the mass-to-light ratio is fixed in cases of MDM or MBM); $M/L_{\rm Disc}(r)$ means that the mass-to-light ratio is a function of the radius as reported in Fig. 9, while $M/L_{\rm Bulge}$ and $M/L_{\rm Disc}$ mean that the mass-to-light ratio is fixed along the radius. Disc only means that all the stars are distributed in a flat disc component only and bulge only means that all the stars are in a spherical bulge component only. Column (5): best (minimal) reduced chi-square value. Columns (6 and 7): $M/L_{\rm Disc}$ and $M/L_{\rm Bulge}$ are the disc and bulge mass-to-light ratios, respectively. Columns (8 and 9): $R_{\rm c}$ and σ are the core radius and velocity dispersion of the DM halo, respectively. [a]For models (c), two different degrees of freedom provide two different reduced χ^2 values but identical baryonic and halo parameters. [b]For model (e), $M/L_{\rm Disc}$ varies with radius as determined from colour indexes in Sect. 5.2 and that the value is the scaling factor with respect to $M/L_{\rm Disc}$ plotted on Fig. 9, rather than a value in $M_\odot/L_\odot$. [c]Models (m) and (n) correspond to the IllustrisTNG100 RC shown in Fig. 8 instead of the observed RC. We consider the same BFM as for models (a) and (b), respectively; (ls) and (hs) in Cols. (6) to (9) mean "low slope" and "high slope", respectively, they correspond to the inner slope of the RC until the radius where the IllustrisTNG100 RC begins. No value of χ^2 or uncertainties are given because they depend on different Illustris uncertainties from those in the observations.

respect to model (d) is no longer observed because the bulge contribution is similar to that of the disc. In order to check if the inner part could be better fitted, we release the constraint on the $M/L_{\rm Disc}$ fixed by colour indexes in model (g), but we keep that on the bulge. As expected, $M/L_{\rm Disc}$ tends to increase almost to the value of $M/L_{\rm Bulge}$, and as a consequence the growing of the disc marginally weakens the DM halo, but does not provide a better fit to the inner velocity rotations; both models (f) and (g) provide almost the same χ^2 at ∼13.0 and ∼12.8, respectively.

To take this a step further, because the bulge shape is sharper in the inner region than that of the disc, we maximise $M/L_{\rm Bulge}$ to 6 $M_\odot/L_\odot$ in model (h) to try to fit the very inner points. This large, but still reasonable $M/L_{\rm Bulge}$ value (less than twice as high as that determined using colour indexes) allows the model to pass through the large bulk of dispersed rotation velocities within the 5 inner kpc, but therefore does not allow the model to reach the highest rotation velocities around 400 km s^{-1}. In addition to the fact that this model does not reach velocities above 300 km s^{-1}, it poorly fits the velocities within 0 and 5−10 kpc. We note that $M/L_{\rm Disc}$ and DM parameters are highly degenerated in model (h) since a high $M/L_{\rm Disc}$ and a weak DM halo provide almost the same χ^2-value as no disc and a stronger DM halo. However, the principal issue of this model is the slope of the bulge, which is far too sharp to fit the rotation velocities around 200 km s^{-1} but astonishingly has the right shape to fit a velocity of around 400 km s^{-1} even though this slope cannot reach these velocities. We clearly see two regimes of velocities at the same radius within the first 5 kpc. The poor fit within the first 5 kpc of model (h) provides a high $\chi^2 \sim 20$ even though it fits the velocities at larger radius, between 10 and 100 kpc, fairly well. In the last four models, from (i) to (l), we study the impact of the stellar distribution geometry on the fits, since this modifies the shape of the model RC. We observe a bright and peaked surface brightness distribution in the centre which could be either a spherical bulge or eventually a bright nucleus. In models (i) and (k) we therefore distribute all the stars in a spherical bulge component, while in models (j) and (l) we set all the stars in a flat disc component. For models (i) and (j) we maximise the stellar components using for both the same fixed mass-to-light ratio, while in models (k) and (l) we test a BFM to let the halo take place. None of those four models allow us to describe the mass distribution of Malin 1 better than any of the others in the sense that BFM models provide almost the same χ^2-values but do not help to fit the highest rotation velocities, and if the maximum disc or bulge models permit us to better reach them, they increase the velocity

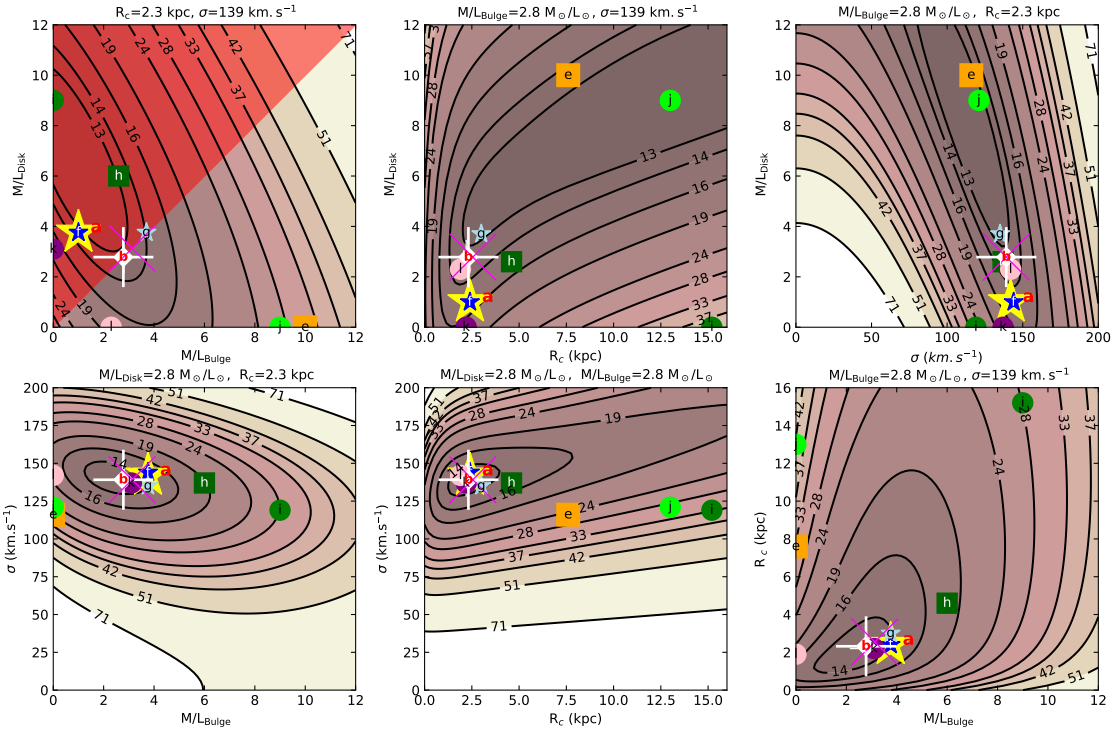

Fig. 12. Reduced χ^2 contours for models using mass-to-light ratios determined from the photometry projected on the six planes corresponding to the four-dimensional space M/L_{Disc}, M/L_{Bulge}, R_c and σ. Each plane is chosen to match the parameters derived for model (b). The forbidden area delimited by the condition $M/L_{Bulge} \leq M/L_{Disc}$ is represented as a red triangle in the *top left panel*. The contours correspond to the following percentile levels [0, 1, 2, 3, 5, 10, 20, 30, 40, 50, 60, 75, 90] of the distribution; these are labelled by reduced χ^2 values. The different symbols, except the large magenta cross, plotted on the six sub-panels, correspond to 10 of the 12 models presented in Table 5 because models (c) and (d) do not fit within the plot limits. Symbols and their colour are described for each model in Table 5. The size of the symbols is random in order to distinguish the different models when they are superimposed. The large white plus symbols used for model (b), do not match with the isocontour centre because of the forbidden volume. The large magenta cross symbols correspond to the median of the 5 percentile of the χ^2 distribution.

dispersion of residuals velocities, which is also indicated by their high χ^2-values.

Models (m) and (n) correspond to the IllustrisTNG100 RC shown in Fig. 8 and discussed in Sect. 4.2. We consider the same BFM as for models (a) and (b), respectively, except that the observed RC is replaced by the IllustrisTNG100 RC, in which we add arbitrary rotation velocities in the first 5 kpc of the galaxy. Indeed, the IllustrisTNG100 RC starts only at a radius of ∼5 kpc while the observed light surface brightness provides constraints within this radius, which are used in the present analysis. We define two different inner slopes for the RC within the first point of the IllustrisTNG100 RC (at a radius of ∼5 kpc). In Table 5, (ls) refers to a "low slope", which more precisely is an almost solid body shape from 0 to 5 kpc with a velocity gradient of ∼65 km s^{-1} kpc^{-1}; the label (hs) indicates a "high slope", which is more precisely a solid body shape RC with two slopes that has a velocity gradient of ∼130 km s^{-1} kpc^{-1} from 0 to 2.5 kpc and a lower slope from 2.5 to 5 kpc to smoothly join the IllustrisTNG100 RC. As a consequence of the fact that the IllustrisTNG100 RC amplitude at large radius is twice as large as the observed RC, for both models (m) and (n), the asymptotical velocity dispersion σ is also about twice as large as for previous models, where the actual RC is used. The σ value is almost the same (∼300 km s^{-1}) for models (m) and (n); this value does not depend on the inner slope of the RC or whether the disc and bulge components are used or not. In contrast, in model (b), where all parameters are free, the inner slope has a direct impact on the bulge and disc mass-to-light ratios: a low inner velocity gradient provides a mass model in which no baryonic component is requested, while a high inner velocity gradient allows significant baryonic components. In model (m), for which bulge and disc components are fixed by colours, the core radius tends to match the inner slope of the RC: it is slightly larger/smaller in the case of a low/high inner slope. For model (n), in the case of a high inner RC slope, a high bulge mass-to-light ratio enables us to fit the inner velocities, thus the core radius is more than twice as large as in the case of a low slope where no bulge can fit. The halo mass estimated at the last H I radius (87.2 kpc), using relation (6), gives almost the same value of $3.46 \pm 0.05 \times 10^{12}\ M_\odot$ for models (m) and (n) and for the two different inner slopes (ls and hs). This is because the total baryonic mass and baryonic matter distribution do not strongly affect the halo shape. In conclusion, the IllustrisTNG100 RC does not reproduce the different datasets, neither at large nor small radii and no constraint is given on the baryonic components when the RC does not provide any constraint in the inner regions.

In order to compare the various models described in this section and tabulated in Table 5, we plot the parameters of the different mass models in Fig. 12. The isocontours of all the panels involving σ show that this is the best-constrained parameter: all the DM haloes a similar asymptotical velocity around $130\sqrt{2}$ km s^{-1}. In addition, most of the DM haloes are relatively

concentrated with a core radius $R_c \sim 2.5$ kpc, this confirms that a massive DM halo is mandatory to adjust the observations. As shown by a different model and the isocontours of panel 5 (R_c versus M/L_{Disc}), the natural trend of the disc is to be massive to extremely massive (for $M/L_{Disc} \sim 6-26\ M_\odot/L_\odot$), but this is an artefact linked to the lack of velocity resolution in the inner part. The M/L_{Bulge} tends to be compatible with that determined by the colour index method if the M/L_{Bulge} value is not allowed to overpass M/L_{Bulge} value.

As introduced in the Sect. 5.5, the weighting of the rotation velocity coming from H I and optical datasets can differ significantly. In the present study, among the 19 independent velocities measurements, only four come from H I data. In addition, the mean uncertainties are ten times larger in the optical dataset than in the H I dataset (∼53 and ∼5 km s^{-1} respectively). Because of the importance of the weighting definition, we test the impact of the uncertainties on the model by testing additional methods to weight the data.

We presented the first method in Sect. 5.5. A second method simply consists of using the original error bars, that is those computed independently for the optical and radio datasets. In that case, the output parameters are only marginally modified; this is mainly because each H I error bar is typically ten times smaller than an optical uncertainty, thus providing on average a weight ten times larger than the optical uncertainty, compensating for the fact that only ∼1/5 velocity measurements come from H I data.

In a third method, we give the same weight to all the velocities, independently of their wavelength or their radial and azimuthal locations in the galaxy. This weight is taken as the median of the uncertainties of all the velocities. In that case, the weight of the outer H I data is on average five times smaller than that of the optical data and the mass models tend to be poorly constrained in the outer region, i.e. for radius larger than 30–40 kpc, which is not really acceptable with respect to the large size of Malin 1. Thus rather than going forward with this third method in which the outer H I velocity points have a weak weight, we prefer to discuss the case study for which no H I velocity point is used, but where the H I surface density contribution is kept.

In this fourth configuration for the uncertainties, we only fit the ∼30 inner percents of the RC. When the H I velocities are not used, the disc mass-to-light ratio decreases on average by ∼38% when it is a free parameter (models b, c, d, e, g, h, l; see Table 5), and the bulge mass-to-light ratio decreases from an average value ∼1.2 to 0 $M_\odot/L_\odot$ when it is a free parameter (models b, c, d, e, k). Except for case (c), the halo parameters are allowed to freely vary. Using the RCs without the H I components, the halo disappears for cases (i) and (j). To compare the behaviour of the core radius R_c, which becomes infinite when no halo component is involved, cases (c), (i), and (j) are discarded. The mean R_c increases by ∼68% from 3.2 kpc to 5.4 kpc, and the mean velocity dispersion σ grows from ∼129 km s^{-1} to ∼260 km s^{-1} (i.e. increases by ∼124%[2]). Those trends mean that baryonic components are largely when no H I velocities are taken into account while the dark haloes are less concentrated but reach larger velocity dispersions. In terms of mass, using relation (6), when the whole RC is used, the mean halo mass measured at the last H I radius (87.2 kpc) is $5.7 \pm 2.3 \times 10^{11}\ M_\odot$ while it inconsiderately jumps to $3.3 \pm 1.9 \times 10^{12}\ M_\odot$ without H I velocities (i.e. an increase by a factor ∼5.7).

On the other hand, the average halo mass computed without the H I velocity for models (a) and (b) is $\sim 4.3 \times 10^{12}\ M_\odot$, which is only ∼1.25 times larger that the halo mass estimated using the IllustrisTNG100 RC for the same models ($\sim 3.5 \times 10^{12}\ M_\odot$). This means that if we only had the Hα RC, we would have thought that the IllustrisTNG100 RC gave a compatible model at large radius.

To conclude this discussion, we carried out a final test. Indeed, looking to the observed RC, we note that the Hα rotation velocities strongly decrease between the two largest radii from V_{Max} ∼489 km s^{-1} (at a galacto-centric radius of ∼10.5 kpc) to ∼189 km s^{-1} (at ∼26.0 kpc), that is to a rotation velocity lower than the average H I velocities of ∼216 km s^{-1}. In order to check that this outermost Hα velocity does not bias the results when we only use the optical data, we rerun the previously labelled "fourth configuration" without considering it. This still increases the disc mass-to-light ratio by ∼31% (instead of ∼38%) and decreases the ratio between the mean halo mass with and without H I from 5.7 to 5.2. Without this outermost Hα velocity, the constraints are still released, however, the disc mass-to-light ratio and the halo parameters do not change much because this outermost Hα data point is weighted by the other 18 optical measurements.

In summary, the new high-resolution and extended RC of Malin 1 does not seem to require a strong DM halo component in the inner part, where the observed stellar mass distribution can explain the dynamics. But a massive DM halo remains necessary to fit the outer regions, whatever the mass model performed. The fit in the inner parts is poor and this may be related to the spatial resolution of the observations, that is at the very limit not to be impacted by beam smearing but also to the assumptions made concerning the geometry of the inner gaseous disc. Ideally, high spectral ($R > 2000$) and spatial (PSF $FWHM < 1''$) resolution integral field spectroscopy data could solve these discrepancies by providing at the same time the actual ionised gas line flux spatial distribution and the geometry of the gas in these inner regions, thanks to their 2D kinematics, with much smaller uncertainties. A discussion on the shape of the DM halo (cusp versus core) is therefore out of the scope of this paper.

6. Conclusions

We present a spectroscopic study of the GLSB galaxy Malin 1 using long-slit data from the IMACS spectrograph. In this work we focussed on the Hα and [O II] emission lines detected in 16 different regions of Malin (12 Hα and 4 [O II] detections). The primary results of this work are as follows:

- We extracted a new RC for Malin 1 using Hα and [O II] emission lines, up to a radial extend of ∼26 kpc.
- For the first time we observe a steep rise in the inner RC of Malin 1 (within $r < 10$ kpc), which is not typical for a GLSB or LSB galaxy in general, with points reaching up to at least 350 km s^{-1} (with a large dispersion) at a few kpc before going back to 200 km s^{-1}, the value found in H I at low resolution.
- We made an estimate of the Hα surface brightness and SFR surface density of Malin 1 as a function of radius, using the observed Hα emission line flux. The Σ_{SFR} within the inner regions of Malin 1 is consistent with an S0/Sa early type spiral. The region detected at ∼26 kpc from the centre of

[2] We do not allow the halo asymptotical velocity $\sqrt{2}\sigma$ to reach a value higher than the maximum observed rotation velocity $V_{Max} = 498$ km s^{-1}. We therefore impose an upper limit $\sigma_{Max} = 346$ km s^{-1} to the velocity dispersion. Except in cases (c), (i) and (j), where $\sigma = 0$ km s^{-1}, $\sigma = \sigma_{Max}$, which leads to the average value $\sigma = 260$ km s^{-1}.

Malin 1 has a Σ_{SFR} close to the level found in the extended disc of spiral galaxies.
- An analysis of the observed Balmer line ratio indicates a very low amount of dust attenuation within Malin 1 (consistent with previous works in the infrared).
- Line ratios, however, point to a relatively high metallicity for the inner regions. The line ratios in the centre are consistent with the previous classification of Malin 1 as a LINER/Seyfert (see Appendix B).
- The new high-resolution and extended RC of Malin 1 does not seem to require a strong DM halo component in the inner part. In these regions, the observed stellar mass distribution can explain the observed dynamics. However, a massive DM halo is required in the outer regions.
- The fit of the RC in the inner parts is poor. This may be due to the coarse spatial resolution of the observations, but also to the assumed geometry of the inner gaseous disc (e.g. non-circular velocity contributions due to the bar).

This work allows us to provide new constraints on Malin 1. It will be important in the future, however, to obtain better quality and complementary data for Malin 1, as well as for other giant LSBs, for example with optical IFU such as MUSE or with ALMA, to provide more constraints on the origin of these galaxies. In the recent years, it has become possible to obtain deeper observations with new telescopes such as Dragonfly (Abraham & van Dokkum 2014) or new instrumentation (e.g. MegaCam at CFHT, Hyper Suprime-Cam at Subaru, Dark Energy Survey Camera at the 4 m Blanco telescope). This allows astronomers to revisit the LSB universe, including GLSB galaxies (e.g. Galaz et al. 2015; Boissier et al. 2016; Hagen et al. 2016), extended UV galaxies discovered with GALEX (Gil de Paz et al. 2005; Thilker et al. 2005), and even to define and study the new class of ultra-diffuse galaxies (UDGs) (e.g. van Dokkum et al. 2015; Koda et al. 2015). Galaxies like Malin 1 will be detectable, if they exist, up to redshift 1 with upcoming projects such as SKA (Acero et al. 2017). The recent studies of Malin 1 and other LSBs or UDGs shows that the LSB universe has a "bright" future.

Acknowledgements. We acknowledge the support by the Programme National Cosmology et Galaxies (PNCG) of CNRS/INSU with INP and IN2P3, co-funded by CEA and CNES. We thank M. Fossati for providing some plotting codes for the line diagnostic diagram and S. Arnouts for his help on the environment of Malin 1. This work also utilised some data from the SDSS DR12 Science Archive Server (SAS) for comparison purposes. Funding for SDSS-III has been provided by the Alfred P. Sloan Foundation, the Participating Institutions, the National Science Foundation, and the US Department of Energy Office of Science. The SDSS-III web site is http://www.sdss3.org/.

References

Abraham, R. G., & van Dokkum, P. G. 2014, PASP, 126, 55
Acero, F., Acquaviva, J. T., Adam, R., et al. 2017, ArXiv e-prints [arXiv:1712.06950]
Amorisco, N. C., & Loeb, A. 2016, MNRAS, 459, L51
Athanassoula, E., & Bureau, M. 1999, ApJ, 522, 699
Avni, Y. 1976, ApJ, 210, 642
Baldwin, J. A., Phillips, M. M., & Terlevich, R. 1981, PASP, 93, 5
Barbosa, C. E., Mendes de Oliveira, C., Amram, P., et al. 2015, MNRAS, 453, 2965
Barth, A. J. 2007, AJ, 133, 1085
Bian, F., Kewley, L. J., Dopita, M. A., & Blanc, G. A. 2017, ApJ, 834, 51
Bigiel, F., Leroy, A., Walter, F., et al. 2010, AJ, 140, 1194
Blanton, M. R., Lupton, R. H., Schlegel, D. J., et al. 2005, ApJ, 631, 208
Boissier, S. 2013, in Star Formation in Galaxies, eds. T. D. Oswalt, & W. C. Keel, 6, 141
Boissier, S., Monnier Ragaigne, D., Prantzos, N., et al. 2003, MNRAS, 343, 653
Boissier, S., Gil de Paz, A., Boselli, A., et al. 2008, ApJ, 681, 244
Boissier, S., Boselli, A., Ferrarese, L., et al. 2016, A&A, 593, A126
Boselli, A., Hughes, T. M., Cortese, L., Gavazzi, G., & Buat, V. 2013, A&A, 550, A114
Boselli, A., Fossati, M., Consolandi, G., et al. 2018, A&A, 620, A164
Bothun, G. D., Impey, C. D., Malin, D. F., & Mould, J. R. 1987, AJ, 94, 23
Braine, J., Herpin, F., & Radford, S. J. E. 2000, A&A, 358, 494
Cappellari, M. 2017, MNRAS, 466, 798
Cardelli, J. A., Clayton, G. C., & Mathis, J. S. 1989, ApJ, 345, 245
Chemin, L., Renaud, F., & Soubiran, C. 2015, A&A, 578, A14
Combes, F. 1999, in H2 in Space, eds. F. Combes, & G. Pineau des Forêts, E.46
Comparat, J., Zhu, G., Gonzalez-Perez, V., et al. 2016, MNRAS, 461, 1076
de Blok, W. J. G., & McGaugh, S. S. 1997, MNRAS, 290, 533
Epinat, B., Amram, P., Balkowski, C., & Marcelin, M. 2010, MNRAS, 401, 2113
Erwin, P., Pohlen, M., & Beckman, J. E. 2008, AJ, 135, 20
Ferrarese, L., Côté, P., Cuillandre, J.-C., et al. 2012, ApJS, 200, 4
Freeman, K. C. 1970, ApJ, 160, 811
Galaz, G., Milovic, C., Suc, V., et al. 2015, ApJ, 815, L29
Gavazzi, G., Savorgnan, G., & Fumagalli, M. 2011, A&A, 534, A31
Gil de Paz, A., Madore, B. F., Boissier, S., et al. 2005, ApJ, 627, L29
González Delgado, R. M., Cid Fernandes, R., Pérez, E., et al. 2016, A&A, 590, A44
Hagen, L. M. Z., Seibert, M., Hagen, A., et al. 2016, ApJ, 826, 210
Hinshaw, G., Larson, D., Komatsu, E., et al. 2013, ApJS, 208, 19
Hinz, J. L., Rieke, M. J., Rieke, G. H., et al. 2007, ApJ, 663, 895
Impey, C., & Bothun, G. 1997, ARA&A, 35, 267
Kent, S. M. 1986, AJ, 91, 1301
Kewley, L. J., Dopita, M. A., Sutherland, R. S., Heisler, C. A., & Trevena, J. 2001, ApJ, 556, 121
Kewley, L. J., Groves, B., Kauffmann, G., & Heckman, T. 2006, MNRAS, 372, 961
Koda, J., & Wada, K. 2002, A&A, 396, 867
Koda, J., Yagi, M., Yamanoi, H., & Komiyama, Y. 2015, ApJ, 807, L2
Korsaga, M., Epinat, B., Amram, P., et al. 2019, MNRAS, 490, 2977
Kroupa, P. 2001, MNRAS, 322, 231
Kulier, A., Galaz, G., Padilla, N. D., & Trayford, J. W. 2019, MNRAS, submitted [arXiv:1910.05345]
Kumar, A., Ghosh, S. K., Hutchings, J., et al. 2012, in Ultra Violet Imaging Telescope (UVIT) on ASTROSAT, SPIE Conf. Ser., 8443, 84431N
Lelli, F., Fraternali, F., & Sancisi, R. 2010, A&A, 516, A11
Ludwig, R. R., Greene, J. E., Barth, A. J., & Ho, L. C. 2012, ApJ, 756, 51
Mapelli, M., & Moore, B. 2008, Astron. Nachr., 329, 948
Marino, R. A., Rosales-Ortega, F. F., Sánchez, S. F., et al. 2013, A&A, 559, A114
Martin, G., Kaviraj, S., Laigle, C., et al. 2019, MNRAS, 485, 796
Matthews, L. D., van Driel, W., & Monnier-Ragaigne, D. 2001, A&A, 365, 1
Moore, L., & Parker, Q. A. 2006, PASA, 23, 165
Mouhcine, M., Lewis, I., Jones, B., et al. 2005, MNRAS, 362, 1143
Moustakas, J., & Kennicutt, R. C., Jr. 2006, ApJS, 164, 81
Moustakas, J., Kennicutt, R. C., Jr., Tremonti, C. A., et al. 2010, ApJS, 190, 233
Ogle, P. M., Jarrett, T., Lanz, L., et al. 2019, ApJ, 884, L11
Osterbrock, D. E. 1974, Astrophysics of Gaseous Nebulae (San Francisco: Freeman)
Pettini, M., & Pagel, B. E. J. 2004, MNRAS, 348, L59
Pickering, T. E., Impey, C. D., van Gorkom, J. H., & Bothun, G. D. 1997, AJ, 114, 1858
Pradhan, A. K., Montenegro, M., Nahar, S. N., & Eissner, W. 2006, MNRAS, 366, L6
Rahman, N., Howell, J. H., Helou, G., Mazzarella, J. M., & Buckalew, B. 2007, ApJ, 663, 908
Reshetnikov, V. P., Moiseev, A. V., & Sotnikova, N. Y. 2010, MNRAS, 406, L90
Saburova, A. S., Chilingarian, I. V., Katkov, I. Y., et al. 2018, MNRAS, 481, 3534
Saburova, A. S., Chilingarian, I. V., Kasparova, A. V., et al. 2019, MNRAS, 489, 4669
Schawinski, K., Thomas, D., Sarzi, M., et al. 2007, MNRAS, 382, 1415
Schlegel, D. J., Finkbeiner, D. P., & Davis, M. 1998, ApJ, 500, 525
Sousbie, T. 2011, MNRAS, 414, 350
Sprayberry, D., Impey, C. D., Bothun, G. D., & Irwin, M. J. 1995, AJ, 109, 558
Subramanian, S., Ramya, S., Das, M., et al. 2016, MNRAS, 455, 3148
Taylor, E. N., Hopkins, A. M., Baldry, I. K., et al. 2011, MNRAS, 418, 1587
Thilker, D. A., Bianchi, L., Boissier, S., et al. 2005, ApJ, 619, L79
Thilker, D. A., Bianchi, L., Meurer, G., et al. 2007, ApJS, 173, 538
van Dokkum, P. G., Romanowsky, A. J., Abraham, R., et al. 2015, ApJ, 804, L26
Zhang, J., Abraham, R., van Dokkum, P., Merritt, A., & Janssens, S. 2018, ApJ, 855, 78
Zhu, G. B., Comparat, J., Kneib, J.-P., et al. 2015, ApJ, 815, 48
Zhu, Q., Xu, D., Gaspari, M., et al. 2018, MNRAS, 480, L18

A&A 637, A21 (2020)

Appendix A: Estimation of errors

There are mainly two sources of errors in the data provided in this work (see Table 2): the emission line-fitting error and the slit-positioning error. We calculated these errors separately as detailed below. They are combined and propagated to obtain the final errors in each of our quantities of interest.

A.1. Emission line-fitting error

The emission line fitting of the spectra (both Hα and [O II] data) was carried out using an initial formal fitting followed by a MCMC method to obtain the final fitting results. The formal fitting of the spectrum was done using the *scipy.optimize.leastsq* Python package (see Fig. 2 for fits of continuum + Gaussian emission lines, from which line positions, intensities, line width are derived). From this fit, a model spectra is obtained from the sum of the different component (continuum and lines): $F_{\rm model}(\lambda)$.

The noise standard deviation $\sigma_{\rm noise}$ was estimated by subtracting $F_{\rm model}$ from the observed spectrum ($F_{\rm obs}$) to obtain the residual spectrum. In order to remove any wavelength dependence, this spectrum was fitted with a polynomial of order 3 that was subtracted to it. We then measured the statistics of this flattened residual spectrum to obtain $\sigma_{\rm noise}$.

We then performed an MCMC fitting procedure using an iterative chain of $N = 10\,000$ iterations. In the beginning of each iteration, a synthetic spectrum $F_{\rm syn}$ was created using the $F_{\rm model}$ with the addition of a random noise with standard deviation $\sigma_{\rm noise}$. At each iteration, we performed again a formal fitting of $F_{\rm syn}$, providing in each case a mock determination of the amplitudes, peak wavelengths, widths, and continuum levels of all the emission line components in the fit. Then histograms of these determinations for each parameters (we focussed on the emission line peak wavelength and flux) were created, inspected, and fitted with a normal distribution. The mean value and standard deviation of each histogram distribution gives our best-fit value and fitting error of a parameter, respectively (see Fig. A.1 for an example).

A.2. Slit-positioning error

An additional source of error in our measurements comes from the uncertainty in the precise positioning of the slit on the sky during each observation. As discussed in Sect. 2, we had extracted spectra from three different slit positions for the Hα data and a single slit position for the [O II] data. In order to obtain a precise slit position for each observations and the associated uncertainties, we simulated the expected luminosity along the slit on the basis of an image of the galaxy acquired during the 2016 observation, just before the spectroscopic observations (see Fig. A.2). The 2D spectrum at each slit position was collapsed along its spectral axis to obtain the full luminosity distribution passing through the slit ($L_{\rm slit}$(pixel)). A mock slit luminosity distribution $L_{\rm mock}$(pixel,x, y) is computed from the image for any slit position (x, y), using the same slit width and angle as used in the observations. We started from the position of the slit expected at the telescope during our observations and explored shifts in (x, y) around this position to find the best pixel position for the slit as follows:

$$\chi^2(x,y) = \sum_{\rm slit\,pixels} \frac{\Big\{L_{\rm slit}({\rm pixel}) - [C \times L_{\rm mock}({\rm pixel}, x, y)]\Big\}^2}{\sigma^2_{\rm pixel}}, \qquad \text{(A.1)}$$

where $\sigma^2_{\rm pixel}$ is the total sky level noise and pixel scale Poisson noise measured from $L_{\rm slit}$(pixel). The coefficient C is the matching coefficient, computed from the $L_{\rm slit}$ and $L_{\rm mock}$ by the following relation:

$$C = \left| \frac{\sum_{\rm slit\,pixels} [L_{\rm slit}({\rm pixel}) \times L_{\rm mock}({\rm pixel}, x, y)]}{\sum_{\rm slit\,pixels} L^2_{\rm mock}({\rm pixel}, x, y)} \right|. \qquad \text{(A.2)}$$

Upon minimizing Eq. (A.1), we obtained a pixel position (x, y) for each of the slit positions with a minimum value of $\chi^2_{\rm min}$. The upper and lower confidence levels in the pixel positions were obtained by incrementing the $\chi^2_{\rm min}$ value with a $\Delta\chi^2$ value of 6.63 to get a 99% confidence level (see Table 1 of Avni 1976).

For slit positions 1, 2, and 3 of the 2016 observations, the slit-positioning uncertainties were found to be three pixels, one pixel, and one pixel, respectively. For the slit position of the 2019 observation, since we do not have an image on the same night to perfrom the same calculation, we used the maximum uncertainty of three pixels from the 2016 observations to account for this uncertainty. Considering the observational set-up is the same, we think this will cover the positioning error of the telescope and spectrograph.

De-projecting the above-mentioned pixel uncertainties on the sky provides a maximum error of ∼0.3″, and typically of order 0.1″. This uncertainty in the sky coordinates of our regions were propagated while measuring the radius, azimuth angle ($\cos\theta$) and $V_{\rm rot}$ on the galaxy plane (radius and $\cos\theta$ were computed from the sky coordinates using *astropy.coordinates.SkyCoord* Python package).

A.3. Combining the error

Since $V_{\rm rot}$ on the galaxy plane depends on both the observed wavelength $\lambda_{\rm obs}$ and the de-projection angle $\cos\theta$, it is affected by both the wavelength fitting error and the error in $\cos\theta$ due to the slit-positioning uncertainty. We made a quadratic sum of both of theses error contributions to obtain our final error in $V_{\rm rot}$ shown in this work. In most cases, the error is dominated by the positioning error. Obviously, the wavelength and flux uncertainties are only affected by the fitting error, whereas the radius values are only affected by the slit-positioning error (see Table 2).

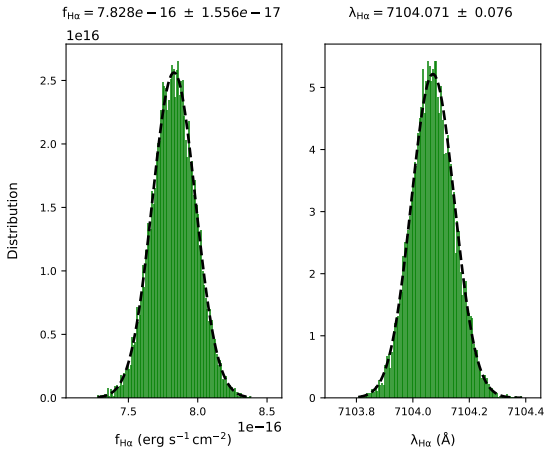

Fig. A.1. Example of the MCMC fitting results for the Hα line in the region *a* (see Table 2). *Left and right panels*: flux distribution ($f_{H\alpha}$) and peak wavelength positions ($\lambda_{H\alpha}$) from the MCMC iterations, respectively. The mean value of this quantities along with their 1σ error bars are labelled on top of each panel.

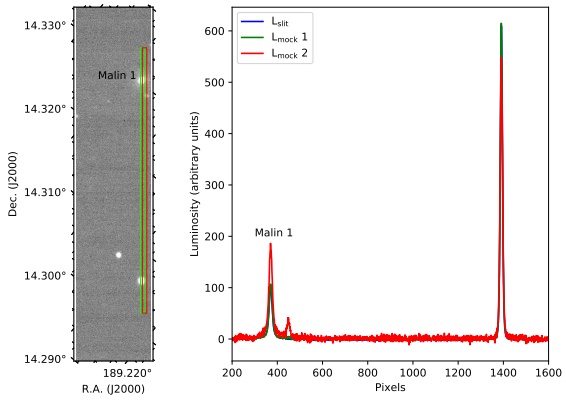

Fig. A.2. *Left*: two mock slits for the slit 1 of our 2016 observations (see Fig. 1), placed on the image of the galaxy acquired during the night of the observation. The two mock slits (green and red) are shifted apart by 1″, with the green slit marking the best slit position obtained in our simulation. *Right*: luminosity profile along the two mock slits are shown in the left panel (from top to bottom). The blue curve is the luminosity distribution passing through the slit obtained from the 2D spectrum (L_{slit}(pixel)) of the slit 1 observation (integrated over wavelength to be consistent with the image).

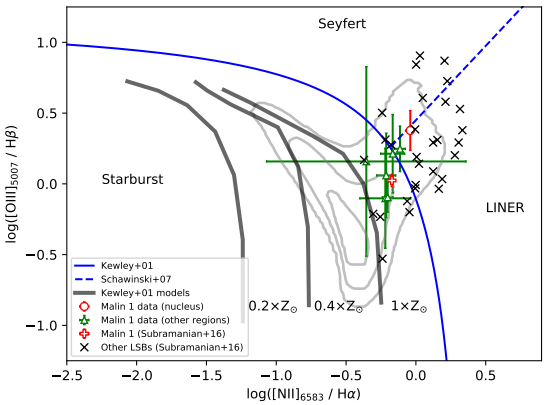

Fig. B.1. Line diagnostic BPT diagram with log([N II]$_{6583}$/Hα) vs. log([O III]$_{5007}$/Hβ). The red circle and the green triangles indicate the data points of Malin 1 for the nucleus and other detected regions in this work, respectively. The red plus and black crosses are the LSB sample from Subramanian et al. (2016), including Malin 1. The blue solid and dashed lines are defined by Kewley et al. (2001) and Schawinski et al. (2007), respectively, for the separation of AGN from star-forming regions. The gray contours show the distribution of a random sample of nuclear spectra of SDSS galaxies in the redshift range 0.01−1 and stellar mass 10^9−10^{11} (Boselli et al. 2018). The black solid thick lines show the expected behaviour of star-forming regions as derived from the photo-ionisation models of Kewley et al. (2001) for three different metallicities (0.2, 0.4, 1 $Z_\odot$).

Appendix B: Malin 1 nuclear activity and metallicity indication

Barth (2007) classified Malin 1 as a LINER nucleus galaxy with an [N II]$_{6583}$/Hα flux ratio of 0.85. This is close to our measured flux ratio of [N II]$_{6583}$/Hα = 0.91 ± 0.06 in the central region of Malin 1. Subramanian et al. (2016) gives a similar classification for Malin 1, placing it in the category of a LINER and composite nuclei with weak ionisation contributions from both AGN and starbursts on the basis of several diagnostics. Our measured central [N II]$_{6583}$/Hα and [O III]$_{5007}$/Hβ flux ratios would place Malin 1 on the borderline of LINER-Seyfert classification in a BPT diagram (Baldwin et al. 1981; Kewley et al. 2006) as shown in Fig. B.1. Other LSBs from Subramanian et al. (2016) are located in a similar place as Malin 1 in this diagram. The flux ratios from the other detected regions (six regions in addition to the nucleus) lie in the starburst region but close to the starburst-AGN demarcation line.

We also show in Fig. B.1 photo-ionisation models of Kewley et al. (2001), showing that the inner regions of Malin 1 may have a large metallicity. Using the calibration of Pettini & Pagel (2004), the corresponding [N II]$_{6583}$/Hα ratio indeed points to metallicities about 0.15 dex above solar (or almost solar if we use the improved calibration of Marino et al. 2013). Such metallicities are close to the values expected from the stellar-mass metallicity relationship derived by Bian et al. (2017) for the SDSS galaxies using the same metallicity indicator (and adopting log($M_*/M_\odot$) = 10.87 for Malin 1 after integrating the profile presented in Sect. 5). On the other hand, the high metallicity is at odds with the large amount of gas, but low attenuation (discussed in Sect. 3.2), and absence of detection in CO (Braine et al. 2000).

A.2. A Virgo Environmental Survey Tracing Ionised Gas Emission (VESTIGE) — X. Formation of a red ultra-diffuse galaxy and an almost dark galaxy during a ram-pressure stripping event

A&A 650, A99 (2021)
https://doi.org/10.1051/0004-6361/202040185

Astronomy & Astrophysics

A Virgo Environmental Survey Tracing Ionised Gas Emission (VESTIGE)

X. Formation of a red ultra-diffuse galaxy and an almost dark galaxy during a ram-pressure stripping event⋆,⋆⋆

Junais[1], S. Boissier[1], A. Boselli[1], M. Boquien[2], A. Longobardi[1], Y. Roehlly[1], P. Amram[1], M. Fossati[3], J.-C. Cuillandre[4], S. Gwyn[5], L. Ferrarese[5], P. Côté[5], J. Roediger[5], S. Lim[5,6], E. W. Peng[7,8], G. Hensler[9], G. Trinchieri[10], J. Koda[11], and N. Prantzos[12]

[1] Aix Marseille Univ, CNRS, CNES, LAM, Marseille, France
e-mail: junais.madathodika@lam.fr; samuel.boissier@lam.fr; lessandro.boselli@lam.fr
[2] Centro de Astronomá (CITEVA), Universidad de Antofagasta, Avenida Angamos 601, Antofagasta, Chile
[3] Dipartimento di Fisica G. Occhialini, Università degli Studi di Milano-Bicocca, Piazza della Scienza 3, 20126 Milano, Italy
[4] AIM, CEA, CNRS, Université Paris-Saclay, Université Paris Diderot, 91191 Gif-sur-Yvette, France
[5] NRC Herzberg Astronomy and Astrophysics, 5071 West Saanich Road, Victoria, BC V9E 2E7, Canada
[6] University of Tampa, 401 West Kennedy Boulevard, Tampa, FL 33606, USA
[7] Department of Astronomy, Peking University, Beijing 100871, PR China
[8] Kavli Institute of Astronomy and Astrophysics, Peking University, Beijing 100871, PR China
[9] Department of Astrophysics, University of Vienna, Türkenschanzstrasse 17, 1180 Vienna, Austria
[10] INAF – Osservatorio Astronomico di Brera, via Brera 28, 20159 Milano, Italy
[11] Department of Physics and Astronomy, Stony Brook University, Stony Brook, NY 11794-3800, USA
[12] Institut d'Astrophysique de Paris, UMR7095 CNRS, Sorbonne Université, 98bis Bd. Arago, 75104 Paris, France

Received 21 December 2020 / Accepted 16 March 2021

ABSTRACT

Context. The evolution of galaxies depends on their interaction with the surrounding environment. Ultra-diffuse galaxies (UDGs) have been found in large numbers in clusters. We detected a few star-forming blobs in the VESTIGE survey, located at ∼5 kpc from a UDG, namely NGVS 3543, in association with an HI gas cloud AGC 226178, suggesting a recent interaction between this low-surface-brightness system and the surrounding cluster environment.
Aims. We use a complete set of multi-frequency data including deep optical, UV, and narrow-band Hα imaging and HI data to understand the formation process that gave birth to this peculiar system.
Methods. For this purpose, we measured (i) the multi-wavelength radial surface brightness profiles of NGVS 3543 and compared them to the predictions of spectro-photometric models of galaxy evolution in rich clusters; and (ii) the aperture photometry of the blue regions in the vicinity of NGVS 3543 in order to determine their age and stellar mass.
Results. Comparisons of the observations with evolutionary models indicate that NGVS 3543 has undergone a ram-pressure stripping that peaked ∼100 Myr ago, transforming a blue gas-rich UDG into a red gas-poor UDG. Star formation has taken place in the ram pressure stripped gas, the mass of which is $\sim 10^8\ M_\odot$, forming star complexes with a typical age of ∼20 Myr and a stellar mass of $\sim 10^4\ M_\odot$.
Conclusions. These results suggest that we are observing for the first time the ongoing transformation of a gas-rich UDG into a red and quiescent UDG under the effect of a ram-pressure stripping event. The same process could explain the lack of star-forming UDGs in rich environments observed in several nearby clusters.

Key words. galaxies: clusters: general – galaxies: clusters: individual: Virgo – galaxies: evolution – galaxies: interactions – galaxies: star formation

1. Introduction

The Virgo cluster is one of the richest clusters of galaxies in the nearby Universe, making it a prime candidate for deep, blind surveys at all wavelengths. Owing to the depth of surveys like the Next Generation Virgo cluster Survey (NGVS; Ferrarese et al. 2012), Virgo Environmental Survey Tracing Ionised Gas Emission (VESTIGE; Boselli et al. 2018b), and GALEX Ultraviolet Virgo Cluster Survey (GUViCS; Boselli et al. 2011), we can now study very low-surface-brightness objects in great detail at unprecedented depths. Found in large numbers in clusters, ultra-diffuse galaxies (UDGs) are a class of galaxy that has attracted a lot of attention in recent years (van Dokkum et al. 2015; Koda et al. 2015; Mihos et al. 2015; van der Burg et al. 2016; Venhola et al. 2017). Although UDGs are a subset of low-surface-brightness galaxies that have been studied for decades (Sandage & Binggeli 1984;

⋆ Reduced images are only available at the CDS via anonymous ftp to cdsarc.u-strasbg.fr (130.79.128.5) or via http://cdsarc.u-strasbg.fr/viz-bin/cat/J/A+A/650/A99
⋆⋆ Based on observations obtained with MegaPrime/MegaCam, a joint project of CFHT and CEA/DAPNIA, at the Canada-French-Hawaii Telescope (CFHT) which is operated by the National Research Council (NRC) of Canada, the Institut National des Sciences de l'Univers of the Centre National de la Recherche Scientifique (CNRS) of France and the University of Hawaii.

A&A 650, A99 (2021)

Caldwell & Bothun 1987; Impey et al. 1988; Conselice et al. 2003; Yagi et al. 2016; Conselice 2018), a vast number of them were found recently with deep surveys. UDGs are often defined as galaxies with an effective radius (R_e) > 1.5 kpc and central disk surface brightness ($\mu_{0,g}$) > 24 mag arcsec^{-2} (van Dokkum et al. 2015; Koda et al. 2015). Lim et al. (2020) recently defined UDGs on a more physical basis as outliers from galaxy scaling relations in the Virgo cluster. In an ongoing analysis of a large sample of low-surface-brightness galaxies (LSBs), UDGs as defined by van Dokkum et al. (2015), Koda et al. (2015), and UDGs as defined by Lim et al. (2020) in the Virgo cluster (Junais et al., in prep.), we noticed blue knots and diffuse emission within a few kiloparsecs of one of our targets, the UDG NGVSJ12:46:41.73+10:23:10.4, which hereafter we refer to as NGVS 3543 (based on the position of this galaxy in the NGVS catalog), as well as Hα emission in the narrow-band image taken during the VESTIGE survey (Fig. 1).

Most of this emission is concentrated in blue knots close to the position of AGC 226178, an HI cloud detected during ALFALFA, an HI blind survey also covering the Virgo cluster (Giovanelli et al. 2005; Haynes et al. 2011). This HI cloud, without any evident optical counterpart[1], was identified as an "almost dark galaxy" by Cannon et al. (2015), who made deeper targeted observations of this source with the VLA. "Dark galaxies" (galaxies with gas but no stars) were looked upon as a possible solution to the large number of small galaxies predicted by the ΛCDM cosmology (Verde et al. 2002). Stars were eventually found in most candidates at low redshift, and the interest turned to "almost dark" or "near dark" objects (gas-rich objects without any clear definition; Cannon et al. 2015; Janowiecki et al. 2015). The origin of AGC 226178 and other almost dark galaxies has been discussed without obtaining definitive answers (Cannon et al. 2015; Janowiecki et al. 2015; Leisman et al. 2017; Brunker et al. 2019). Among the propositions for their origin are suggestions that dark galaxies are: disks of high angular momentum (spin) that are stable against star formation (Jimenez & Heavens 2020; Leisman et al. 2017); galaxies with low star formation efficiency (Janowiecki et al. 2015); galaxies that are gas stripped by or falling onto a companion galaxy (Sorgho et al. 2020); or tidal debris, as in the cases of VIRGO-HI (Duc & Bournaud 2008; Boselli et al. 2018a) and SECCO 1 (Beccari et al. 2017) for example. Cannon et al. (2015) classify their sample of almost dark candidates as either tidal debris or dwarf galaxies (as for AGC 226178). In our new NGVS imaging, the optical counterpart to the elongated UV emission is resolved into very bright blue knots, several of them with detection of Hα emission. More knots and diffuse emission are seen to the south of the galaxy, with a morphology similar to so-called fireball galaxies found in clusters (Yoshida et al. 2008). Star-forming regions formed within the tails of ram-pressure-stripped galaxies were first discovered by Gavazzi et al. (2001) in A1367. These peculiar objects are now quite commonly observed in nearby clusters provided that deep observations sensitive to the ionized gas emission are available (Sun et al. 2007; Cortese et al. 2007; Yoshida et al. 2008; Yagi et al. 2010; Fossati et al. 2016; Poggianti et al. 2019; Gullieuszik et al. 2020). They have also been observed in gas-rich low-surface-brightness systems within the Virgo cluster (VCC1217, Hester et al. 2010; Fumagalli et al. 2011; Jáchym et al. 2013; Kenney et al. 2014; IC 3476, Boselli et al. 2021), but so far have not been found to be associated with dwarf quiescent galaxies.

To our knowledge, it is the first time that fireball-style knots have been seen in connection with a UDG, making NGVS 3543 an important object with which to distinguish some processes that have been suggested for the formation of UDGs. Indeed, many propositions have been made in recent years concerning the formation of UDGs, including the potential role of halo angular momentum, feedback, tidal interactions, ram-pressure stripping (RPS), and collisions (e.g., Amorisco & Loeb 2016; Burkert 2017; Martin et al. 2019; Di Cintio et al. 2019; Tremmel et al. 2020; Silk 2019).

In this paper, we therefore analyze the full system including the UDG galaxy NGVS 3543 and the associated blue knots in its vicinity. In Sect. 2, we discuss details of the multi-wavelength data we use, as well as measurements performed on the images. In Sect. 3 we present the results obtained during this study, and in Sect. 4 we provide a detailed discussion on the implications of these results along with a comparison of existing data and models. We conclude in Sect. 5.

Consistently with other VESTIGE and NGVS studies, we assume the Virgo cluster to be at a distance of 16.5 Mpc (Gavazzi et al. 1999; Mei et al. 2007; Blakeslee et al. 2009), with a projected angular scale of 80 pc arcsec^{-1}.

2. Data and measurements

2.1. Data

Our work is based on the analysis of images obtained by multi-wavelength surveys of the Virgo Cluster: the NGVS in the optical (Ferrarese et al. 2012), GUViCS (Boselli et al. 2011) in the UV, and VESTIGE (Boselli et al. 2018b) for Hα narrow-band and r-band imaging. These surveys provide comprehensive imaging of the Virgo cluster in optical (u, g, r, i, z, Hα) and UV (far-ultraviolet (FUV) and near-ultraviolet (NUV)) bands.

VESTIGE is a blind Hα narrow-band[2] imaging survey of the Virgo cluster carried out with MegaCam at the Canada-France-Hawaii Telescope (CFHT) and was designed to cover the whole Virgo cluster up to its virial radius (104 deg^2). The depth and extremely high image quality of the survey makes it perfectly suitable for studying the effects of the environment on the star formation process in perturbed galaxies down to scales of ∼100 pc. The line sensitivity limit of the survey is f(Hα) ∼ 4×10^{-17} erg s^{-1} cm^{-2} (5σ detection limit) for point sources and Σ(Hα) ∼$2{\times}10^{-18}$ erg s^{-1} cm^{-2} arcsec^{-2} (1σ detection limit at 3″ resolution) for extended sources. The contribution of the stellar continuum emission in the narrow-band Hα filter is determined and removed using a combination of the r- and g-band images, as described in Boselli et al. (2019). The narrow-band Hα filter is optimal to detect the line emission of galaxies at the redshift of the Virgo cluster with a typical recessional velocity of $-500 \leq cz \leq 3000$ km s^{-1}. In the context of UDGs, VESTIGE provides information on recent star formation, but can also confirm the redshift of sources in cases of detection, whereas spectroscopy is challenging for these diffuse objects.

2.2. Radial profiles of NGVS 3543

We gathered all available images of NGVS 3543 in the optical and in the UV bands (u, g, r, i, z, Hα, FUV and NUV).

[1] Cannon et al. (2015) noticed a possible UV counterpart in the GALEX images.

[2] The VESTIGE narrow-band Hα filter includes the Hα line and the two nearby [NII] emission lines at λ6548 and 6583 Å. Hereafter we refer to the Hα+[NII] contribution simply as Hα unless otherwise stated.

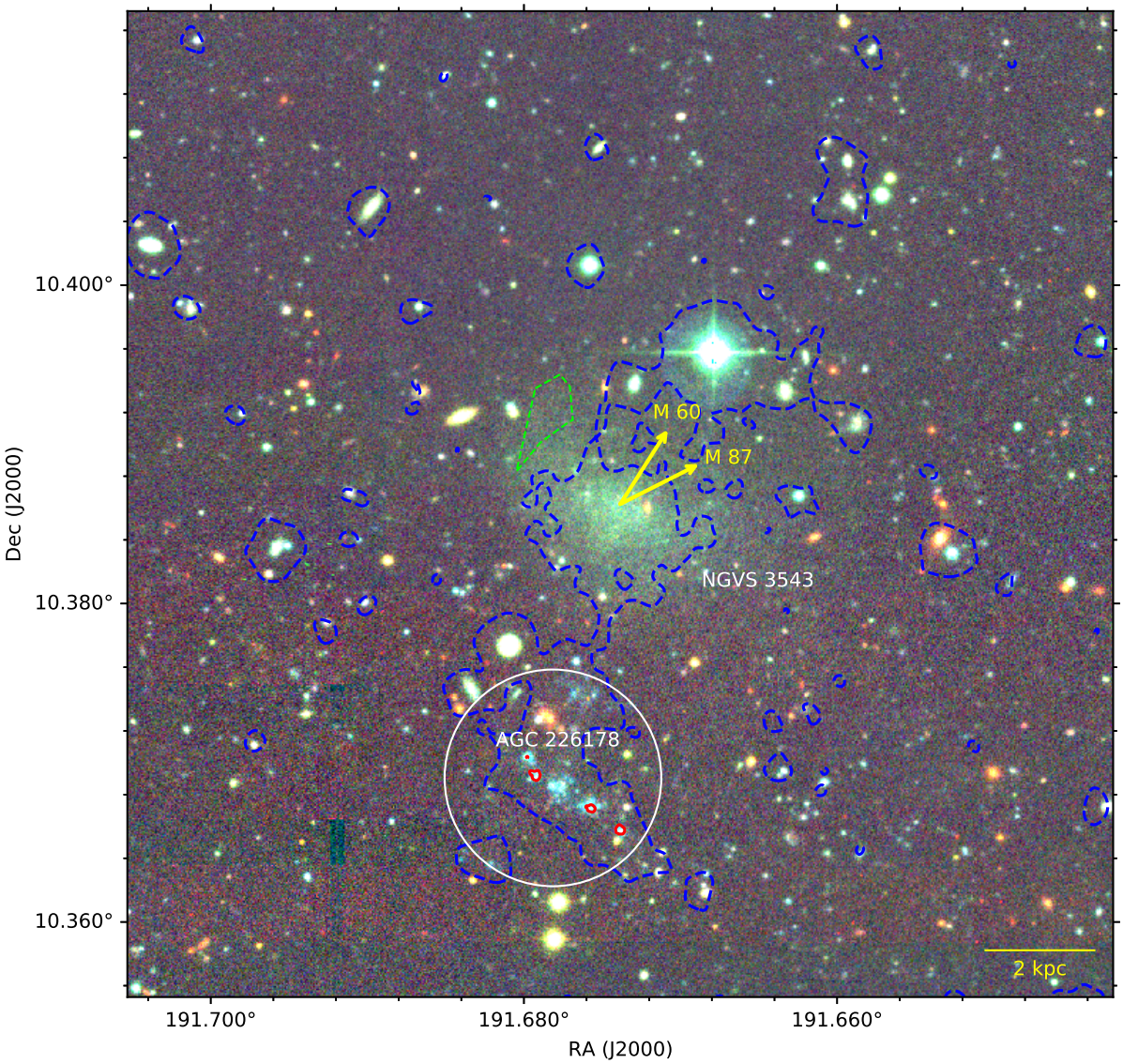

Fig. 1. NGVS *u*, *g*, *i*-colour composite image of the UDG galaxy NGVS 3543. The yellow arrows indicate the direction towards the Virgo cluster elliptical galaxies M 87 and M 60 at a distance of 1.26 Mpc and 0.39 Mpc, respectively. Blue dashed contours indicate the GALEX NUV detection at a surface brightness level of 27 mag arcsec^{-2} and red contours indicate the Hα detection in VESTIGE at the level of 1.6×10^{-17} erg s^{-1} cm^{-2} arcsec^{-2} (3σ). The white circle marks the position of the VLA HI detection of the source AGC 226178 from Cannon et al. (2015) with a beam size of 49″. The green dashed region along the northeast of NGVS 3543 shows the possible tidal feature discussed in Sect. 4.3.

We used the `Montage` tool (Jacob et al. 2010) to co-add all the exposures of the galaxy field in each band, projecting the new images on the pixel scale of the original NGVS and VESTIGE images (with pixels of 0.187″). The NGVS provides a mask for artifacts, foreground stars, stellar halos, background galaxies, and globular clusters in the field of our galaxy which was produced using multiple Sextractor runs (Bertin & Arnouts 1996) followed by a THELI *automask* procedure (Erben et al. 2005, 2009). The detailed procedure followed for the NGVS mask creation is presented in Ferrarese et al. (2020). We manually edited the NGVS mask to remove residual artefacts and faint stars. Our images were then interpolated over the masked regions using the IRAF *fixpix* procedure. For the NGVS and VESTIGE images, a convolution of the above data with a Gaussian kernel was also done to match their initial resolution to that of GALEX (which we assumed to be $FWHM = 5''$; see Table 1). These images were then used to measure the radial surface brightness profiles of NGVS 3543 shown in Fig. 2 using the *Ellipse* task in `Photutils` python package (Bradley et al. 2019), adopting the geometrical parameters for the galaxy taken from the NGVS catalog (see Table 2). We also adopt the Galactic reddening from the same catalog, $E(B-V) = 0.02489$ (Schlegel et al. 1998), and correct for Galactic extinction adopting the Cardelli et al. (1989) extinction curve. We assumed that there was no internal extinction, as it is generally found in low-surface-brightness quiescent galaxies (Hinz et al. 2007; Rahman et al. 2007). Error-bars in the surface brightness profile were computed by combining a pixel-scale and large-scale deviation in the sky, following the

A&A 650, A99 (2021)

Table 1. Properties of the imaging data used in this work.

Survey	Filter	*FWHM*	Exposure time (s)
NGVS	u	0.88″	6402
NGVS	g	0.80″	3170
VESTIGE	r	0.65″	480
NGVS	i	0.54″	2055
NGVS	z	0.75″	3850
VESTIGE	Hα	0.64″	6600
GUViCS	NUV	∼5″	3346
GUViCS	FUV	∼5″	1632

procedures given in Gil de Paz & Madore (2005). Profiles were measured up to three times the effective radius provided by the NGVS catalog (see Table 2).

The surface brightness profiles shown in Fig. 2 are very close to exponential in the u, g, r, i, z and NUV bands. We only obtained an upper limit in the Hα narrow band, and a central detection in FUV, suggesting that star formation has been low throughout the last 100 Myr. We measured the central surface brightness and effective radius of this galaxy from our profiles in the g-band with an exponential fit in order to obtain $\mu_{0,g} = 25.29\,\mathrm{mag\,arcsec^{-2}}$ and $R_{e,g} = 26\farcs05$ (2.08 kpc). These values are close to the NGVS ones given in Table 2 (although the profiles were measured in slightly different ways, with a Galfit Sérsic fit in the case of NGVS and an exponential fit in our case). This confirms that NGVS 3543 falls under the classical definition of the UDG regime (van Dokkum et al. 2015; Koda et al. 2015). NGVS 3543 is not included in the definition by Lim et al. (2020), where UDGs are defined as 2.5σ outliers in scaling relationships (see Fig. 1 of Lim et al. 2020). However, we verified that NGVS 3543 lies very close (at 2.2σ) to the separation curve in these relations.

2.3. Selection of blue regions

To understand the nature of the young stellar systems associated to NGVS 3543 and AGC 226178 seen in Fig. 1, we need first to identify them and then to characterize their spectro-photometric properties. For this purpose, we followed two different selection criteria. The first one is based on the NGVS u-band image, which has the advantage of having an excellent angular resolution (0.88″, corresponding to 70 pc); the second one is based on the GALEX NUV image, which despite its poorer angular resolution (5″, corresponding to 400 pc) is more sensitive to the youngest stellar population and is thus perfectly suited to identifying newly formed objects (e.g., Boselli et al. 2018a, NGC 4254).

2.3.1. u-band selection

We first proceeded with the identification of peaks in the NGVS u-band image. We used the `Photutils` *find_peaks* package to identify all the peaks in u-band image above 5σ of the sky. The identified peaks were used as an initial set of regions, for which we performed aperture photometry within circular regions of 3″ diameter. The size of the aperture was optimally chosen at the same time to include the entire flux of each individual region and to resolve them from nearby companions. The photometry was performed with the `Photutils` *aperture_photometry*

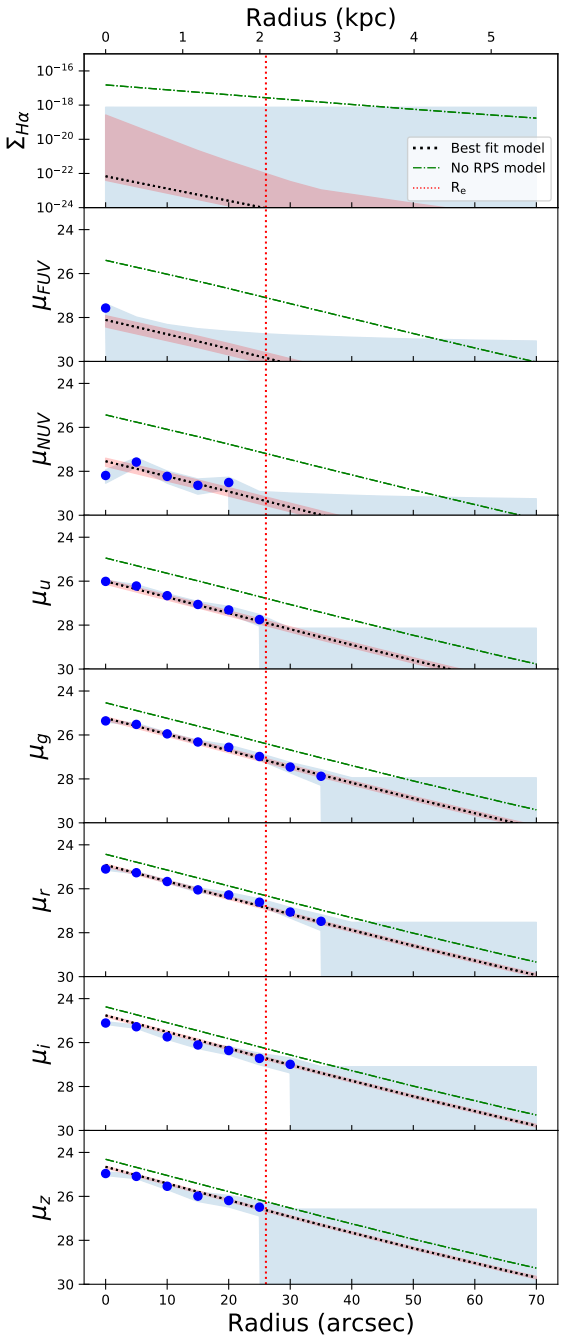

Fig. 2. Radial surface-brightness profiles of NGVS 3543 measured in eight bands, shown as blue filled dots. The surface brightness units are in $\mathrm{mag\,arcsec^{-2}}$ for all the bands except for Hα which is in $\mathrm{erg\,s^{-1}\,cm^{-2}\,arcsec^{-2}}$. The blue shaded area marks the 1σ error (for data points) and upper-limits (3σ). The black dotted line indicates the best-fit model described in Sect. 3.1 for a ram-pressure stripped galaxy ($V = 42^{+8}_{-4}\,\mathrm{km\,s^{-1}}$, $\lambda = 0.14^{+0.02}_{-0.01}$ and $t_{\rm rps} = 13.4 \pm 0.1$ Gyr). The green dot-dashed line shows the same model for an unperturbed system. The red shaded area shows the range of models allowed for the same spin and velocity, but allowing variation in the RPS efficiency and FWHM parameters as discussed in Sect. 3.1. The vertical red dotted line gives our measured g-band effective radius of the galaxy.

Table 2. Properties of the galaxy NGVS 3543 taken from the NGVS catalog.

Property	Value
RA (J2000)	$12^h46^m41.73^s$
Dec (J2000)	$+10°23'10.4''$
Distance (Mpc)	16.5
D_{M87} (Mpc)	1.26
D_{M60} (Mpc)	0.39
Inclination angle	$30.1° \pm 0.4°$
Position angle (PA)	$61.7° \pm 1.1°$
g (mag)	17.495 ± 0.006
$\mu_{0,g}$ (mag arcsec^{-2})	25.05
$R_{e,g}$ (kpc)	1.79 ± 0.06

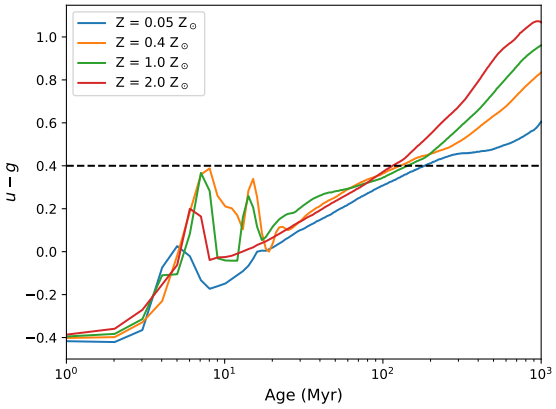

Fig. 3. $u - g$ color evolution of a single-burst population derived using Starburst99 models (Leitherer et al. 1999) for different metallicities. The black dashed line marks the $u - g$ color limit (corresponding to an approximate age of less than 100 Myr) we adopted for the selection of young regions discussed in Sect. 2.3.1.

package in u, g, r, i, z, and Hα bands, and corrected for Milky Way foreground Galactic extinction (as described in Sect. 2.2).

To identify newly formed regions among the peak-selected ones, we compared their $u - g$ color to different models for a single burst population of varying ages and metallicities created with Starburst99 (Leitherer et al. 1999). For this purpose we used the same models adopted in Boselli et al. (2009) created using Starburst99 models, with a Kroupa (2001) initial mass function (IMF) between 0.1 and 100 $M_\odot$, and four different metallicities (0.05, 0.4, 1, 2 $Z_\odot$) based on Geneva stellar evolution tracks. Figure 3 shows that the $u - g$ colors of single bursts are similar ($u - g \sim 0.4$ mag) when close to 100 Myr, regardless of the metallicity, and bluer colors always correspond to younger regions. We therefore adopt the limit of $u - g < 0.4$ mag in order to be sure to include regions dominated by a young stellar population (age <100 Myr)[3].

Following this color cut, we also removed regions corresponding to known background NED sources. Unfortunately, this exercise cannot be done using the catalogue of NGVS photometric redshifts from Raichoor et al. (2014), simply because

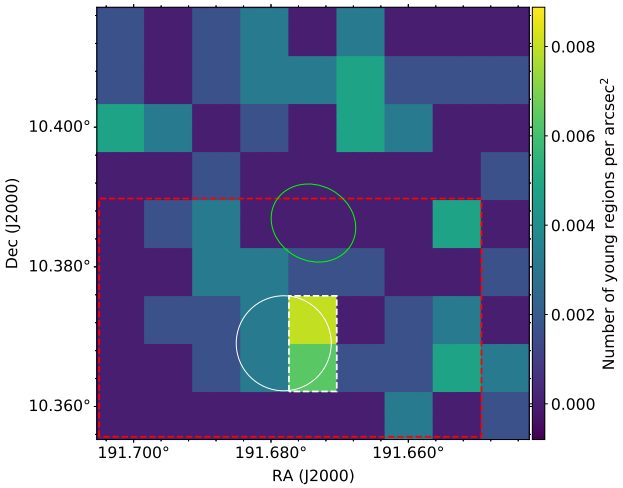

Fig. 4. Number density of the u-selected blue ($u - g < 0.4$ mag) regions around the galaxy NGVS 3543 (marked as the green ellipse). The white circle marks the position of the VLA HI detection of AGC 226178 from Cannon et al. (2015), with a beam size of 49″. The white dashed box indicates the region above 3σ level of the mean background number density. The red dashed box (190″ × 120″) shows the area where the properties of the blue regions are analyzed in this work.

these photo-z were derived using templates not optimized to detect individual HII regions such as those discovered in this work[4]. The number density of our tentative young u-band-selected regions around the galaxy, measured within a grid of 25″ × 25″ boxes, is shown in Fig. 4. The box size of 25″ was chosen to sample the AGC 226178 HI beam size of 49″ from Cannon et al. (2015). We find a clear over-density of young regions south of the galaxy, which coincides with the HI detection of AGC 226178. This confirms the visual impression that the blue knots are associated to AGC 226178. In the following, we focus on this side of the galaxy, keeping only regions in the red dashed box in Fig. 4, where a total of 38 regions are selected (shown as yellow circular regions in Fig. 5).

We estimated the possible contamination of background sources in these u-band-selected regions using the object density map shown in Fig. 4. We obtain that 29 out of our 38 u-band-selected regions fall outside the 3σ level of the mean background density (white-dashed zone in Fig. 4), indicating that we cannot reject the assumption that they are background contaminants. However, for the 9 remaining regions forming an over density coinciding with the AGC 226178 HI detection, we ran a Monte Carlo simulation of a million chains, estimating that the probability of such an over density being due to contaminants is less than 0.0131%.

2.3.2. Ultraviolet selection

Inspection of the NUV image (blue dashed contours in Fig. 5) revealed a diffuse emission in the same area or in the vicinity of the blue knot regions. For the sake of completeness, we also made a manual selection based on the UV images (because of the GALEX resolution, we have to work at a lower resolution). Initially, we created contours on the NUV image of the galaxy

[3] By doing such a color selection, we are aware that we introduce a bias to young regions without taking into to account older regions that could have formed as a result of tidal interactions.

[4] For instance, three sources in this field, cataloged by Raichoor et al. (2014) at $z > 1.75$, 1.67, and 0.44, respectively, have been detected in VESTIGE Hα, and thus are bona fide Virgo cluster objects.

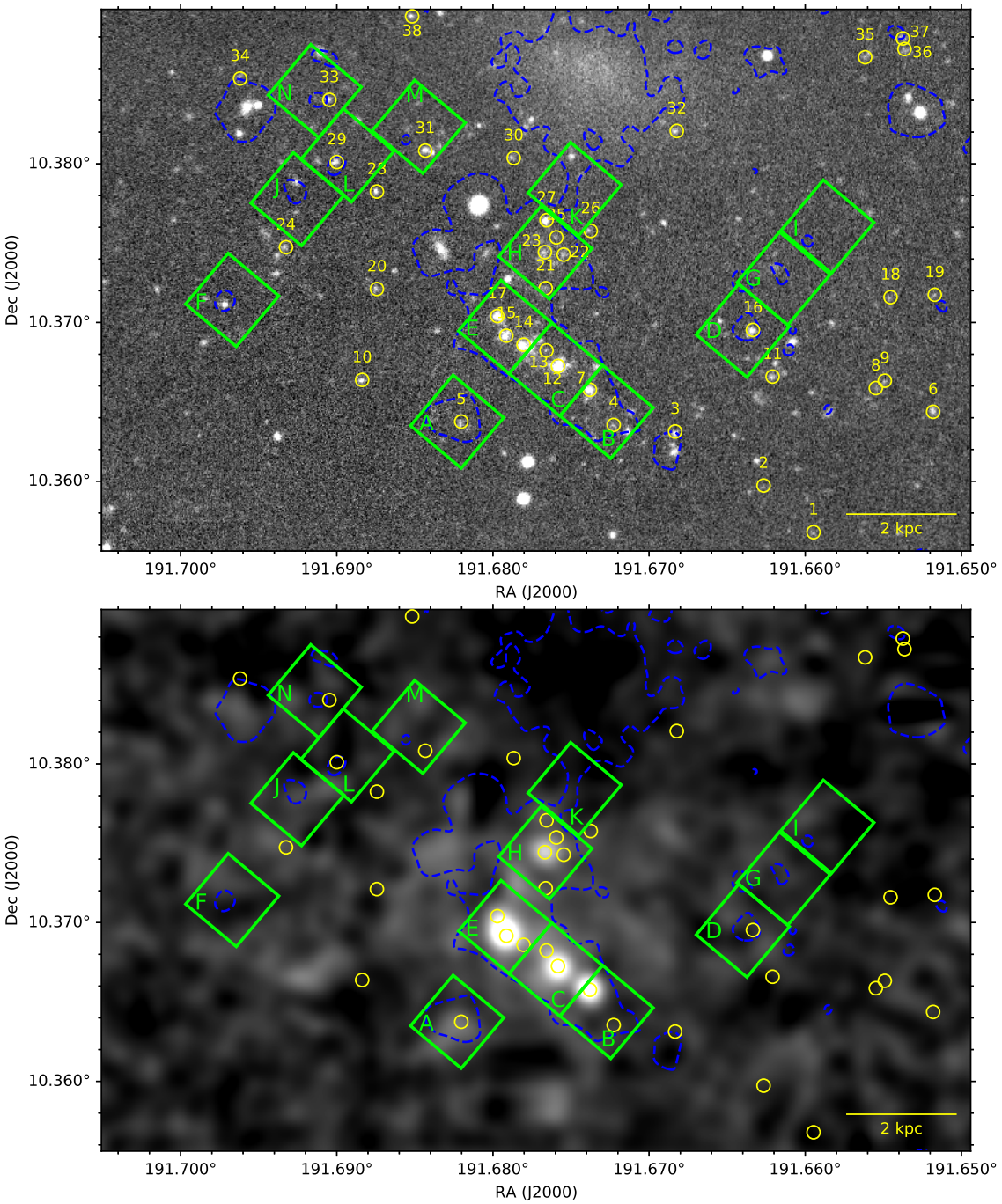

Fig. 5. *Top:* u-band grayscale image along the area selected for our analysis. *Bottom:* VESTIGE continuum-subtracted Hα image smoothed at the resolution of GALEX. The yellow circles and the green boxes, marked with their names, are respectively our u-band-selected and UV-selected regions, as labeled in Table 3. The region names are attributed based on increasing declination. The blue dashed lines are the same NUV contours from GALEX as shown in Fig. 1.

at an arbitrarily low surface brightness level of 27 mag arcsec^{-2} after smoothing the data to 3″ resolution (2 GALEX pixels). These contours (shown in Fig. 5) were used to visually identify UV-emitting regions associated to the galaxy, shown in Fig. 5 as green boxes of size 15″ × 15″, after excluding any background source identified in NED. A total of 14 regions were finally selected. Many of them (9 out of 14 regions) also coincide with some of the regions selected in the u-band (at higher resolution). Following Boselli et al. (2018a), we estimated the possible contamination of background UV sources using the number counts given in Xu et al. (2005). At the limiting magnitude of our detections ($NUV \leq 22.7$ mag, for a GALEX Medium Imaging

Survey; Morrissey et al. 2005), the expected number of background galaxies is ∼1700 sources per deg^2, or equivalently ∼3 for the selected region. We therefore find a clear excess of UV emission likely related to the galaxy.

The photometric measurements for these UV-selected young regions were performed similarly to the *u*-band-selected regions with the `Photutils` *aperture_photometry* package in all available bands, after convolving the optical band images with a Gaussian kernel to match the GALEX resolution, and correcting for Milky Way foreground Galactic extinction as discussed in Sect. 2.2.

3. Analysis

3.1. Galaxy evolution models with ram-pressure stripping applied to NGVS 3543

In previous studies, Boselli et al. (2006, 2008a,b, 2014) reproduced the properties of anaemic and dwarf galaxies located in the Virgo Cluster by adding RPS to chemical and spectrophotometric evolution models initially made for unperturbed galaxies. These models were first developed for the Milky Way and for nearby spirals (Boissier & Prantzos 1999, 2000; Muñoz-Mateos et al. 2011). Their output are radial profiles of stellar density, mass density, metallicity, and spectra. The models are constructed making some assumptions on the final total mass distribution within the disk (in the absence of interactions that remove gas) and the surrounding halo, the gas accretion history, the Kroupa (2001) IMF, and the star formation law. They were calibrated in such a way that the only two free parameters (for the unperturbed case) are the spin (λ, specific angular momentum) and the rotational velocity (V), which is tightly connected to the total mass of the galaxies ($M \propto V^3$). The same models have been adapted to reproduce the evolution of LSB galaxies (Boissier et al. 2003) by assuming large spin parameters, as commonly done in the literature (Jimenez et al. 1998; Amorisco & Loeb 2016).

However, a full grid including both LSB (i.e., large and very large spins) and RPS has not been computed so far. For the study of the sample that will be presented in Junais et al. (in preparation), we prepared a very large grid with the same models, but covering a very large range of spin parameters (from 0.01 to 0.6 in steps of 0.01), in order to include the spin corresponding to the very extended disk of Malin 1 (Boissier et al. 2016), and of velocity (from low-mass dwarf galaxies with $V = 20\,\mathrm{km\,s^{-1}}$ to very massive galaxies with $V = 600\,\mathrm{km\,s^{-1}}$, with steps of 2 and $10\,\mathrm{km\,s^{-1}}$, respectively, below and above $150\,\mathrm{km\,s^{-1}}$ to better sample the low-mass range in which galaxies are more numerous). The ram-pressure stripping event was modeled as described in Boselli et al. (2006). In practice, we remove gas at a rate of $\epsilon\Sigma_{\rm gas}/\Sigma_{\rm potential}$, which is proportional to the galaxy gas column density at any given time but is modulated by the potential of the galaxy, measured by the total (baryonic) local density. ϵ is linked to the RPS efficiency and follows a Gaussian with a maximum value ϵ_0 at the peak time ($t_{\rm rps}$), assuming that the current age of the galaxy is 13.5 Gyr. This time variation was chosen to mimic that obtained by Vollmer et al. (2001) for a galaxy crossing the Virgo cluster potential on an elliptical orbit. To reduce the number of free parameters (λ, V, $t_{\rm rps}$) we keep the same peak efficiency (ϵ_0) of 1.2 $M_\odot$ kpc^{-2} yr^{-1}, and the average full width at half maximum (FWHM) of the Gaussian variation from Vollmer et al. (2001) of ≃150 Myr, as in Boselli et al. (2006). We included various $t_{\rm rps}$ values from 8 (distant past) to 13.6 Gyr (for which the peak of RPS will occur 0.1 Gyr in the future), with steps of 0.1 Gyr (considering the timescale of the various processes involved, including ram pressure, the models are not sensitive to much shorter times).

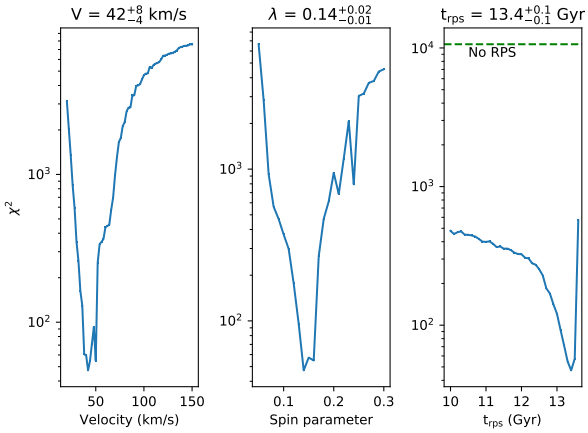

Fig. 6. χ^2 distribution for the determination of the best model parameters (V, λ and $t_{\rm rps}$) for NGVS 3543, as discussed in Sect. 3.1. The best-fit parameters are given in the upper part of each panel. The given confidence limits (3σ) in each parameter are obtained following Avni (1976). The green horizontal dashed line in the right panel marks the χ^2 value corresponding to a model without RPS, keeping the same values of V and λ as in the best-fit model.

The fact that we keep a constant peak efficiency and a unique FWHM is clearly an over-simplification of the problem. Indeed these parameters should depend on the precise orbit within the cluster. However, we choose to do it as it allows us to explore a large grid of models for the other parameters, within reasonable computational time. This grid will also be used for a study of about 150 low-surface-brightness galaxies in the Virgo Cluster (Junais et al., in prep.) for which we cannot fine-tune the orbit parameters. However, below, we discuss the uncertainties that this assumption brings to the properties derived in the present paper.

Figure 6 shows the χ^2 distribution around our best solution. We note that we computed values of χ^2, adopting a minimum error of 0.05 mag to take into account systematic uncertainties (e.g., IMF, stellar tracks, stellar libraries). We rejected any solution violating the 3σ upper limits of our photometry. However, we kept a tolerance of 0.1 mag again to take into account systematic uncertainties in the stellar population models. We found that this helped us to avoid rejecting a good model that only marginally violates one upper limit. Modifying this tolerance within a range of a few tenths of dex changes the best-fit parameters within their error bars.

The best model was obtained for a ram-pressure stripping event peaking 100 Myr ago ($t_{\rm rps} = 13.4$ Gyr) in a low-mass galaxy ($V = 42\,\mathrm{km\,s^{-1}}$) with a large spin ($\lambda = 0.14$). This solution is much better than any model without RPS, as shown in Fig. 6. Values of spin around $\lambda = 0.14$ were already found to reproduce LSB galaxies in Boissier et al. (2003), but on average for more massive and brighter galaxies than our UDG (with V in the range 40–360 $\mathrm{km\,s^{-1}}$ instead of $42\,\mathrm{km\,s^{-1}}$; and absolute magnitudes M_B typically in the range −14 to −22 mag, while the UDG in this paper has an absolute g-band magnitude of −13.6 mag). The low velocity of $42\,\mathrm{km\,s^{-1}}$ obtained from our best model reasonably matches the properties of dwarf galaxies in Virgo (Boselli et al. 2008a,b), but with a more typical spin

of $\lambda = 0.05$. This means that only the combination of a dwarf galaxy velocity and a large spin allows the model to reproduce the properties of NGVS 3543. Cosmological simulations indicate that the spin parameter distribution is expected to be lognormal, with a peak at 0.05, and $\sigma = 0.5$ (Mo et al. 1998), but cold gas accretion could lead to larger angular momentum (Stewart 2017). The value of $\lambda = 0.14$ is beyond the peak of the distribution, but is not totally unexpected based on these considerations.

While our best model was obtained by keeping only three free parameters, we now investigate how our results are affected by the peak efficiency (ϵ_0) and the FWHM of the Gaussian used for modelling the RPS event. For this, we decided to keep a constant spin and velocity, because these two parameters, affecting mostly the long-wavelength range, are weakly affected by a recent RPS event (in Boselli et al. 2006, they were chosen on the basis of the H-band profile alone, and the rotation curve). We then computed models with ϵ_0 in the range of 0.2–1.6 $M_\odot$ kpc^{-2} yr^{-1} that was considered in Boselli et al. (2006), and $t_{\rm rps}$ in the range of 13.0–13.6 Gyr (because our best fit clearly indicates a recent RPS event). We kept any of these models with χ^2 lower than the limit considered above, and not violating upper limits. In another test, we kept the efficiency fixed to 1.2 $M_\odot$ kpc^{-2} yr^{-1} as in the original model, but allowed the FWHM of the Gaussian shape of the RPS event to vary within the range of 100–200 Myr (in steps of 10 Myr) as presented by Vollmer et al. (2001), and carried out the same procedure. We thus obtained several models consistent with the data, for various ϵ_0 and FWHM. For these models the best $t_{\rm rps}$ is found to be 13.3 or 13.4 Gyr. The obtained profiles are within the red-shaded region shown in Fig. 2. They are very similar to the best model derived above, except for Hα in which we obtain a larger dispersion among models due to small values of ϵ_0 allowing the galaxy to keep more gas, and $t_{\rm rps} = 13.3$ leaving more time for some gas to return from old stars after the RPS event. The gas removal still allows the models to be within the observed Hα upper limit. These models allow us to estimate the uncertainty we introduce in the quantities we derive by fixing the RPS model parameters.

The profile of the best model is shown as the black dotted line in Fig. 2. The multi-wavelength profiles (including upper limits) of the UDG galaxy are very well fitted by these RPS models, except for FUV, in which the best-fit model underpredicts the observed FUV central detection by ~0.5 mag. Such a difference can be attributed, for example, to our assumption on the IMF (Muñoz-Mateos et al. 2011), or the adopted stellar spectra library (more uncertain in the UV than the optical). Moreover, our previous tests show that the UV surface brightness is also sensitive to the precise value of FWHM and ϵ_0 in the RPS models, as can be seen in Fig. 2. We also show the profile for a model with the same velocity and spin, but without any ram pressure (i.e., what would have happened to the galaxy in the absence of RPS). We can clearly see that the Hα upper limits and UV data are of paramount importance to show that ram pressure was recently present. Indeed, on short timescales, only these bands are very sensitive to the gas removal and quenching of star formation. Figure 7 illustrates these phenomena at two different radii ($R = 0.8$ and 4.0 kpc), showing the evolution of the gas and star formation rate surface density with time for the best model and the same model without RPS. While the peak of RPS occurred 100 Myr ago, the gas removal and the quenching of the star formation began a few hundred million years before, when the galaxy was first entering into the cluster. Due to the shallow gravitational potential well of this UDG, the gas stripping process was very efficient well before the galaxy reached the core of the cluster (200 Myr ago). While the efficiency of ram pressure

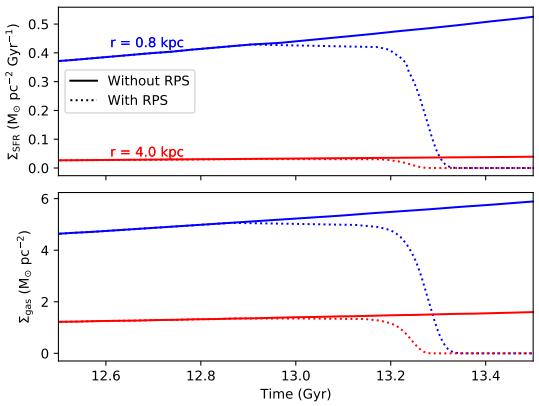

Fig. 7. Evolution of the surface densities of SFR and gas for the disk of NGVS 3543 obtained in our models. The dotted and solid lines show the models with and without RPS, respectively. The blue and red curves show the evolution at 0.8 kpc and 4 kpc from the galaxy center.

evolves as a Gaussian, the gas-loss rate is not symmetric around the peak because most of the gas has already been removed at that time. This is similar to what was found with much more sophisticated models of RPS by Roediger & Hensler (2005).

Finally, several global properties of these models are given in Table 4. For the RPS models, the table provides the average value and the range obtained for the models satisfying our criteria among all those tested with various ϵ_0 and FWHM for the RPS event (removing a couple of outlying metallicity values, see below). For the unperturbed model, we indicate the dispersion obtained when considering the uncertainties on the spin and velocity obtained during the fitting process. The stellar mass, central surface brightness, and effective radius are more affected by the uncertainties on the spin and velocity than by the RPS choices. The uncertainties on the gas left and the SFR in the RPS models are on the contrary dominated by the RPS choices. When plotting these values for the RPS models, we combine the errors due to RPS assumptions and the one related to the fitting of the spin and velocity. Finally, the table does not include the systematic effects that have to be kept in mind, such as the fact that stellar masses are dependent on the IMF, and metallicities are dependent on the yields adopted in the models, implying an uncertainty of about a factor of two in both the cases.

The comparison of the RPS models with the unperturbed one also tells us how much the galaxy is affected by the ongoing RPS event (indeed, the galaxy before the RPS event was almost in the same state as the nonRPS model considering the timescales involved). While the unperturbed galaxy was dominated by the gas (a standard result for models with low mass and large spin in the context of these models; Boissier et al. 2001), because of the weak potential of the galaxy, most of the gas has been removed in the RPS model. Star formation has been almost totally quenched with respect to the nonRPS model, consistent with the faintness of the galaxy at UV and blue optical wavelengths. The gas-phase metallicity is larger in the RPS model. This is to be expected because the metals expelled now by a previous generation of stars reaching the end of their life are diluted in a much smaller amount of remaining gas, as indeed generally observed in gas-poor cluster galaxies (Boselli et al. 2008a; Hughes et al. 2013). The difference is around a factor two, and the gas-phase metallicity of the unperturbed galaxy was around one-tenth solar. However, we note that the gas-phase metallicity

Table 3. Photometry for the *u*-band selected (top panel) and UV selected regions (bottom panel) as denoted in Fig. 5.

ID	Distance (kpc)	*u* (mag)	*g* (mag)	*r* (mag)	*i* (mag)	*z* (mag)	Hα Flux (10^{-16} erg s^{-1} cm^{-2})	*NUV* (mag)	*FUV* (mag)
(1)	(2)	(3)	(4)	(5)	(6)	(7)	(8)	(9)	(10)
1	9.4	24.97 ± 0.21	24.96 ± 0.22	>24.45	24.31 ± 0.34	>23.95	<0.14	–	–
2	8.3	25.26 ± 0.29	25.3 ± 0.32	>24.45	>24.47	>23.95	<0.14	–	–
3	6.8	24.1 ± 0.1	23.84 ± 0.08	23.85 ± 0.22	23.47 ± 0.15	23.42 ± 0.23	<0.14	–	–
4	6.6	24.52 ± 0.14	24.34 ± 0.12	24.06 ± 0.26	23.78 ± 0.2	>23.95	<0.14	–	–
5	6.9	24.26 ± 0.11	24.26 ± 0.12	>24.45	>24.47	>23.95	0.24 ± 0.02	–	–
6	8.9	24.04 ± 0.08	23.82 ± 0.08	23.92 ± 0.23	23.22 ± 0.12	23.22 ± 0.18	<0.14	–	–
7	5.9	23.01 ± 0.05	22.94 ± 0.05	22.44 ± 0.06	22.46 ± 0.06	22.38 ± 0.08	1.54 ± 0.03	–	–
8	7.8	25.08 ± 0.24	25.08 ± 0.25	>24.45	24.3 ± 0.34	>23.95	<0.14	–	–
9	7.8	24.88 ± 0.2	24.93 ± 0.22	>24.45	24.03 ± 0.25	>23.95	<0.14	–	–
10	7.0	24.1 ± 0.1	24.02 ± 0.1	23.48 ± 0.15	23.41 ± 0.14	>23.95	<0.14	–	–
11	6.6	24.12 ± 0.1	23.99 ± 0.09	23.56 ± 0.16	23.04 ± 0.1	23.03 ± 0.16	<0.14	–	–
12	5.5	22.48 ± 0.05	22.4 ± 0.05	22.42 ± 0.06	22.68 ± 0.07	23.12 ± 0.18	1.17 ± 0.02	–	–
13	5.2	24.58 ± 0.15	24.54 ± 0.15	>24.45	>24.47	>23.95	0.27 ± 0.02	–	–
14	5.2	22.63 ± 0.05	22.57 ± 0.05	22.74 ± 0.08	22.9 ± 0.08	23.27 ± 0.2	0.2 ± 0.02	–	–
15	5.1	22.9 ± 0.05	22.95 ± 0.05	22.9 ± 0.08	23.06 ± 0.1	23.84 ± 0.36	1.59 ± 0.03	–	–
16	5.7	23.51 ± 0.05	23.27 ± 0.05	23.02 ± 0.1	22.49 ± 0.06	22.32 ± 0.08	<0.14	–	–
17	4.9	22.85 ± 0.05	22.55 ± 0.05	22.32 ± 0.05	22.4 ± 0.06	22.64 ± 0.11	0.55 ± 0.02	–	–
18	6.9	24.92 ± 0.2	24.85 ± 0.2	>24.45	24.18 ± 0.3	>23.95	<0.14	–	–
19	7.5	24.98 ± 0.21	25.06 ± 0.25	>24.45	>24.47	>23.95	<0.14	–	–
20	5.6	24.47 ± 0.13	24.24 ± 0.12	23.88 ± 0.22	23.52 ± 0.16	23.69 ± 0.3	<0.14	–	–
21	4.1	24.32 ± 0.12	24.08 ± 0.1	23.87 ± 0.22	23.06 ± 0.1	22.86 ± 0.14	<0.14	–	–
22	3.5	24.09 ± 0.09	23.96 ± 0.08	23.77 ± 0.2	23.57 ± 0.16	23.44 ± 0.24	<0.14	–	–
23	3.5	23.74 ± 0.06	23.71 ± 0.07	23.53 ± 0.16	23.74 ± 0.19	23.84 ± 0.36	0.64 ± 0.02	–	–
24	6.4	24.4 ± 0.12	24.28 ± 0.12	23.7 ± 0.18	23.26 ± 0.12	>23.95	<0.14	–	–
25	3.2	24.76 ± 0.17	24.87 ± 0.21	>24.45	24.16 ± 0.29	>23.95	0.2 ± 0.02	–	–
26	3.0	24.53 ± 0.14	24.37 ± 0.13	24.1 ± 0.28	24.08 ± 0.26	23.62 ± 0.29	<0.14	–	–
27	2.9	23.14 ± 0.05	23.14 ± 0.05	22.96 ± 0.1	22.55 ± 0.06	22.6 ± 0.11	<0.14	–	–
28	4.5	24.24 ± 0.11	24.17 ± 0.11	24.27 ± 0.33	23.98 ± 0.24	>23.95	<0.14	–	–
29	4.9	23.9 ± 0.08	23.7 ± 0.07	23.34 ± 0.13	22.74 ± 0.08	22.73 ± 0.12	<0.14	–	–
30	2.2	24.52 ± 0.14	24.32 ± 0.12	24.06 ± 0.26	23.52 ± 0.16	23.46 ± 0.24	<0.14	–	–
31	3.4	23.52 ± 0.06	23.41 ± 0.05	23.08 ± 0.11	23.32 ± 0.12	23.14 ± 0.18	<0.14	–	–
32	2.0	24.08 ± 0.09	23.9 ± 0.08	23.46 ± 0.15	23.38 ± 0.14	23.0 ± 0.15	<0.14	–	–
33	4.8	24.1 ± 0.1	24.21 ± 0.11	23.92 ± 0.23	23.58 ± 0.16	23.64 ± 0.29	<0.14	–	–
34	6.3	24.72 ± 0.16	25.03 ± 0.24	24.15 ± 0.29	24.12 ± 0.28	>23.95	<0.14	–	–
35	5.0	24.46 ± 0.13	24.31 ± 0.12	>24.45	24.16 ± 0.29	23.87 ± 0.37	<0.14	–	–
36	5.7	24.42 ± 0.12	24.34 ± 0.12	23.37 ± 0.14	22.95 ± 0.09	22.55 ± 0.1	<0.14	–	–
37	5.7	24.38 ± 0.12	24.2 ± 0.11	24.22 ± 0.32	23.64 ± 0.17	23.22 ± 0.19	<0.14	–	–
38	3.3	24.16 ± 0.1	23.96 ± 0.08	23.28 ± 0.12	22.78 ± 0.08	22.56 ± 0.11	<0.14	–	–
A	6.9	>22.29	>22.21	>21.64	>21.26	>20.8	<1.79	22.56 ± 0.12	22.48 ± 0.11
B	6.3	21.82 ± 0.24	21.2 ± 0.15	20.7 ± 0.16	20.0 ± 0.12	20.26 ± 0.24	2.82 ± 0.27	21.81 ± 0.06	21.81 ± 0.06
C	5.6	20.94 ± 0.11	20.74 ± 0.1	20.86 ± 0.18	20.48 ± 0.18	>20.8	5.45 ± 0.26	20.89 ± 0.05	20.87 ± 0.05
D	5.6	>22.29	22.0 ± 0.32	>21.64	21.16 ± 0.36	>20.8	<1.79	23.26 ± 0.22	>23.82
E	5.0	20.94 ± 0.11	20.68 ± 0.08	20.69 ± 0.15	20.22 ± 0.14	20.61 ± 0.33	5.63 ± 0.26	20.79 ± 0.05	20.83 ± 0.05
F	7.8	>22.29	>22.21	>21.64	>21.26	>20.8	<1.79	23.7 ± 0.36	>23.82
G	5.2	>22.29	>22.21	>21.64	20.59 ± 0.2	20.42 ± 0.26	<1.79	23.52 ± 0.29	>23.82
H	3.5	21.42 ± 0.16	21.2 ± 0.14	20.63 ± 0.15	19.78 ± 0.1	19.62 ± 0.12	3.16 ± 0.27	21.48 ± 0.05	21.64 ± 0.05
I	5.2	>22.29	>22.21	>21.64	20.97 ± 0.3	20.66 ± 0.34	<1.79	>23.82	>23.82
J	5.8	>22.29	>22.21	>21.64	20.86 ± 0.26	>20.8	<1.79	>23.82	>23.82
K	2.3	22.06 ± 0.32	21.4 ± 0.18	20.78 ± 0.16	20.12 ± 0.13	20.2 ± 0.22	<1.79	22.92 ± 0.16	23.26 ± 0.22
L	4.7	>22.29	>22.21	>21.64	21.17 ± 0.37	>20.8	<1.79	>23.82	>23.82
M	3.3	>22.29	>22.21	>21.64	>21.26	>20.8	<1.79	>23.82	>23.82
N	5.0	>22.29	>22.21	>21.64	>21.26	>20.8	<1.79	23.66 ± 0.34	>23.82

Notes. (1) Name of the region. (2) Projected distance of the region from the center of NGVS 3543. (3)–(7) *u*, *g*, *r*, *i* and *z*-band magnitudes. (8) VESTIGE Hα flux. (9)–(10) GALEX *NUV* and *FUV* magnitudes. The upper limits (3σ) in the broad-band magnitudes and in the Hα fluxes are denoted with > and < symbols, respectively.

Table 4. Properties of the best RPS models, and the model with the same spin velocity but without the RPS.

Property	RPS models	Model without RPS
$R_{e,g}$ (kpc)	1.98 ± 0.03	2.23 ± 0.52
$\mu_{0,g}$ (mag arcsec^{-2})	25.25 ± 0.08	24.61 ± 0.59
log $M_\star$ ($M_\odot$)	7.10 ± 0.02	7.31 ± 0.27
log M_{gas} ($M_\odot$)	5.35 ± 0.42	8.60 ± 0.17
log SFR ($M_\odot$ yr^{-1})	−5.80 ± 0.43	−1.86 ± 0.25
Z_{gas} ($Z_\odot$)	0.38 ± 0.05	0.16 ± 0.05

for RPS models, with very small gas fractions, becomes unreliable as it becomes dominated by the yield of the stars dying at that time, which in some cases leads to artificially high values. The corresponding small amount of gas makes this metallicity impossible to observationally measure in any case.

Finally, we note that in the framework of our models, the effective radius has not changed much and the central surface brightness is dimmer than the nonRPS model by ∼0.7 magnitude. With these values, the unperturbed galaxy would still be a UDG, but a star-forming one with bluer colors. This could correspond to the blue UDGs for which evidence of existence, especially in the field, has been found by Prole et al. (2019).

A caveat of the models used for this study is that they do not take into account other effects that may modify the effective radius and the central (or effective) surface brightness, such as tidal interaction or adiabatic expansion. However, the properties of the UDGs found in the RomulusC Galaxy Cluster simulation by Tremmel et al. (2020) are mostly determined by RPS (with passive evolution after a quenching event), while tidal interactions play a modest role. Another caveat is that the models do not take into account some effects that have been proposed as the origin of UDG galaxies, and that can be included in hydro-dynamical modelling, such as for instance very efficient early feedback (Martin et al. 2019; Di Cintio et al. 2019). These effects could explain why the galaxy needs a large angular momentum before the RPS interaction (the galaxy is extended early on, in a way that is not taken into account explicitly in our case, but that we mimic by adopting a large spin). The RPS event is then crucial in quenching star formation and turning the previously blue UDG into a red UDG like the ones typically found in clusters.

3.2. Stellar mass and age of the blue knots

In order to better understand and characterize the nature of the regions selected around NGVS 3543, we estimated the stellar mass and age of each region based on the photometric measurements given in Table 3. To this aim we used the single burst Starburst99 models discussed in Sect. 2.3.1. For each of the four metallicities, we performed a χ^2 minimization to find the age and stellar mass providing the best fit to our measurements. We considered an arbitrary stellar mass range of 10–10^7 $M_\odot$, with a spacing of 0.04 in log. For each value of the stellar mass, metallicity, and age, we first checked if the model was violating any of our upper limits shown in Table 3. If this was the case, it was rejected. The Hα measurements play a major role in constraining the age of the regions, with an upper limit indicating an age of greater than 10 Myr in massive regions.

The best χ^2 are shown as a function of age and metallicity for an example region in Fig. 8. The uncertainties on the age are

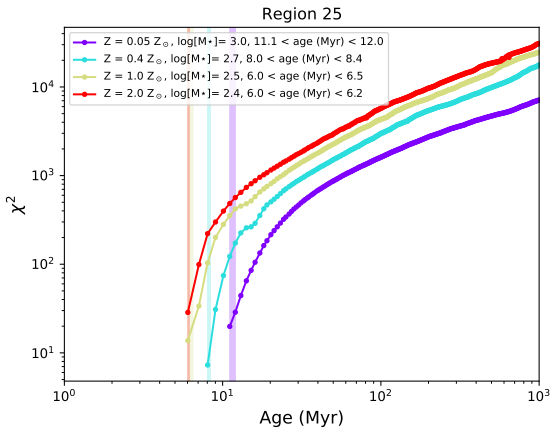

Fig. 8. Example of the χ^2 distribution for determination of the stellar mass, the age and the metallicity of region 25. The confidence limits around the best-fit ages (3σ), indicated by the vertical bands, are obtained from the given χ^2 distribution following Avni (1976). We note that all the models with an age of less than 6 Myr for this region are rejected due to upper limit violations, resulting in the unusual single-sided χ^2 distribution above (the other side could be represented by a vertical line if we assign artificially infinite χ^2 to rejected models). Similar χ^2 distributions for all the other regions are provided in Appendix A.

computed from the χ^2 distribution following Avni (1976), with a 3σ confidence level. We adopt the metallicity providing the least χ^2. Ideally, we would expect the metallicity of the regions to be similar to the metallicity in the gas of the galaxy before the stripping event, that is, at 0.16 $Z_\odot$, which could be tested with our results. However, in most cases, the lack of data in the observed SEDs prevents us from discriminating between different metallicities (see Fig. 8 and Appendix A for all the regions). As a result, we cannot constrain the metallicity. We note that the age and stellar mass usually change by less than a few million years and a few tenths of dex, respectively, over various metallicities. However, with the lowest metallicity ($Z = 0.05\,Z_\odot$), it is sometimes possible to obtain older ages (a few 100 Myr) and (up to ten times) larger stellar masses than for the other metallicities, but we only obtain a metallicity of 0.05 $Z_\odot$ for a few of our regions.

The results of the above procedure for all the regions are given in Table 5. For a few regions, we could only obtain an upper limit or lower limit on age, because our models only cover an evolution within a time range of 1 Myr to 1 Gyr (Δt = 1 Myr) or the χ^2 curve does not favor a better constraint. We note that some of the regions have extremely small χ^2 values. This is due to the fact that these regions have upper limits in most of the bands, which were not used in the χ^2 computation. For instance, regions F, J, L, and N have only one measurement that is not an upper limit. In such cases, it is possible to fine-tune each of the three parameters (age, stellar mass, and metallicity) to go exactly through this point, but the resulting model is not really constrained. However, even then, we can often put a limit on the age of the burst as upper limits would be violated outside the considered range. For region M, we only have upper limits on photometry because the NUV detection observed in this region is too small for the aperture size we used for the photometry (see Fig. 5). Therefore we were not able to perform our χ^2 minimization procedure on this region.

Many sources of uncertainty may affect these results, such as for example the minimization procedure (χ^2 vs. maximum likelihood) and the way upper limits are dealt with, the details

Table 5. Age, stellar mass, metallicity, and reduced χ^2 values determined for our selected regions as discussed in Sect. 3.2.

ID	$M_\star$ ($10^3\,M_\odot$)	Age (Myr)	Metallicity ($Z_\odot$)	$\chi^2_{\rm red}$
1	0.8	13 ± 4	1.00	0.0531
2	0.7	14 ± 6	2.00	0.0054
3	2.8	14 ± 1	1.00	0.4512
4	1.4	13 ± 2	0.40	0.0321
5	0.5	6 ± 1	1.00	0.3271
6	2.8	13 ± 1	1.00	2.1775
7	1.6	7 ± 1	0.40	64.3600
8	1.1	19 ± 6	0.40	0.0818
9	1.3	14 ± 1	0.40	0.2949
10	2.8	13 ± 1	0.40	0.8093
11	2.5	12 ± 1	0.40	1.7665
12	2.3	6 ± 1	1.00	16.5120
13	0.9	10 ± 1	0.05	0.5585
14	10.0	19 ± 1	0.05	2.3020
15	1.1	6 ± 1	0.40	20.2600
16	4.4	12 ± 1	0.40	2.6175
17	2.1	7 ± 1	1.00	29.1400
18	1.1	14 ± 2	0.40	0.0632
19	0.8	18 ± 6	0.05	0.0026
20	1.0	8 ± 1	1.00	0.3750
21	1.9	11 ± 1	0.40	5.7125
22	2.5	13 ± 1	1.00	0.1191
23	0.6	6 ± 1	0.40	4.2900
24	2.3	13 ± 1	0.40	2.4630
25	0.5	8 ± 1	0.40	2.4293
26	1.7	13 ± 2	1.00	0.1094
27	5.2	13 ± 1	1.00	9.2550
28	3.3	21 ± 4	2.00	0.0214
29	3.0	12 ± 1	0.40	4.9275
30	1.7	13 ± 1	0.40	0.2722
31	10.0	36 ± 2	2.00	2.2778
32	2.5	13 ± 1	0.40	0.3292
33	1.9	10 ± 1	2.00	1.3217
34	1.1	13 ± 1	0.40	1.4917
35	3.6	31 ± 7	2.00	0.0322
36	2.1	13 ± 1	0.40	32.9000
37	2.1	13 ± 1	0.40	0.3735
38	2.5	12 ± 1	0.40	16.4300
A	36.3	62 ± 8	0.05	0.0003
B	6.3	7 ± 1	1.00	33.1286
C	11.0	6 ± 1	1.00	3.7817
D	158.0	333 ± 70	0.40	1.2710
E	14.5	7 ± 1	1.00	8.3714
F	39.8	199 ± 98	0.40	1.40×10^{-6}
G	525.0	412 ± 88	2.00	0.0679
H	7.6	7 ± 1	1.00	65.9857
I	63.1	36 ± 19	2.00	0.0035
J	275.0	506 ± 351	0.05	2.61×10^{-6}
K	479.0	872 ± 21	0.05	16.1000
L	398.0	>371	0.05	1.29×10^{-6}
M	–	–	–	–
N	145.0	>363	0.05	1.52×10^{-6}

of the stellar population models, and our assumption of the absence of dust, or a star formation event (single population vs. extended). While in the remainder of the paper, we use the results presented above, we performed two further tests, which are described below.

(i) We compared the color evolution found by Boselli et al. (2018a) for bursts with extended star formation histories while we adopted single bursts. The color evolution of Boselli et al. (2018a) is always within the range of colors found in our single-burst models for different metallicities. These could not be distinguished on the basis of our data. Thus, extended bursts or a single population lead to similar results that cannot be distinguished with the data in hand.

(ii) We determined the age and stellar mass of each region with the SED-fitting code CIGALE[5] (Burgarella et al. 2005; Noll et al. 2009; Boquien et al. 2019), which uses a Bayesian approach and implements different assumptions concerning the sources of uncertainties discussed above. While results for individual regions may vary (with, on average, older ages in CIGALE, with large error bars), with both approaches we find several regions with young ages (<20 Myr), especially for the regions that are detected in Hα. This again shows that Hα measurements allowed by the VESTIGE survey are crucial for studying the very young star forming regions studied in this work. A longer discussion of the results obtained with CIGALE and the properties obtained with Starburst99 is given in Appendix B.

Our tests suggest that although individual values may differ, the existence of young regions with recent star formation is a robust result from our analysis.

4. Discussion

4.1. Ages and stellar masses of the young regions

The analysis performed in Sect. 3 shows that the majority of the star complexes associated with the HI gas cloud AGC 226178 located at a projected distance of ∼5 kpc from NGVS 3543 have ages of a few tens of millions of years. These regions might therefore have formed within the gas removed from the NGVS 3543 after a RPS event that started ∼200 Myr ago. Figure 9 shows the estimated ages and stellar masses of all our selected regions. When the regions have an Hα detection, the u-selected and UV-selected regions have similar ages. In the absence of Hα detection, the ages of the UV-selected regions tend to be larger than those of the u-selected regions, while UV emission is usually related to a younger population than u-band emission. However, the larger apertures of the UV regions make them more likely to be affected by any older underlying stellar population, and we reiterate the fact that we also expect some of them to be background sources. For regions younger than 100 Myr (blue regions), the mean age of u-band- and UV-selected regions are 14 ± 1 Myr and 21 ± 4 Myr, respectively (the uncertainty given in mean age is the formal error, rather than the dispersion of the age distribution). For a few of the fainter regions with low stellar mass and larger error bars, we are close to the u-band detection limit on age, as can be seen in Fig. 9. We obtain a total stellar mass of $9.1 \times 10^4\,M_\odot$ and $1.4 \times 10^5\,M_\odot$ for all the u-band and UV-selected blue regions, respectively. The mean stellar masses of these blue regions are respectively $2.4 \times 10^3\,M_\odot$ and $2.3 \times 10^4\,M_\odot$, which is within the mass range of 10^3–$10^5\,M_\odot$ found in giant molecular clouds and HII regions of irregular galaxies (Kennicutt et al. 1989; Fumagalli et al. 2011). Such relatively low masses support the use of single generation populations to study them. Indeed, smooth extended star formation

[5] https://cigale.lam.fr

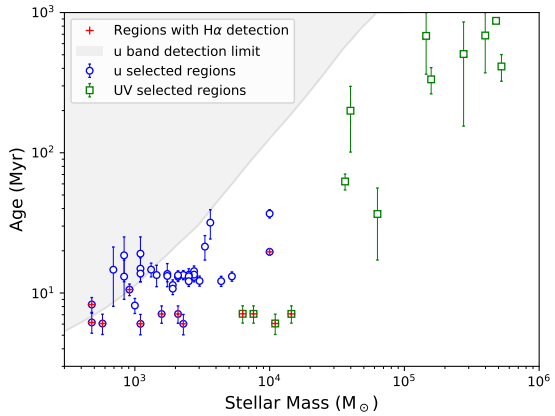

Fig. 9. Age and stellar mass determined for all our selected regions. The blue circles and green squares represent u-band- and UV-selected regions, respectively. The gray shaded area is our u-band detection limit (lower mass or older clusters in the this area would not be detected based on the luminosity predicted by the Starburst99 models). The red crosses identify the Hα detected regions.

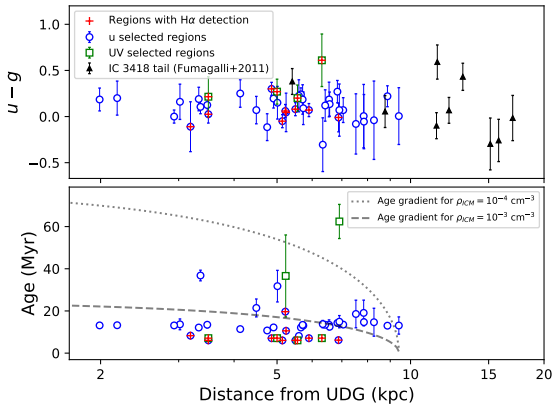

Fig. 10. $u - g$ color and age of our blue regions as a function of their distance from the center of the UDG. Black triangles represent the knots and filaments from Fumagalli et al. (2011). The black dotted and dashed lines indicate the age gradients we measured for a 9.4 kpc stream following Eq. (2) of Kenney et al. (2014), for two different ICM densities with $\rho_{\rm ICM} = 10^{-4}$ and 10^{-3} cm^{-3}, respectively, as discussed in Sect. 4.2. The blue open circles and green open squares mark our u-band and UV-selected regions, respectively. The red crosses identify the Hα detected regions.

histories apply to systems including many molecular clouds and HII regions, while a single burst may better correspond to single clouds. Nevertheless, $M_\star \approx 10^4\,M_\odot$ is close to the limit where the stochastic sampling of the IMF starts to play a role, resulting in over-estimation of ages using population synthesis models (Boselli et al. 2018a). However, our overall results would not be impacted if our ages were over-estimated because we already find many young regions. It is clear from Fig. 9 that the UV-selected regions tend to have a higher stellar mass than the u-band-selected regions. This can be attributed to their larger apertures which clearly capture a larger amount of the light emitted by star formation.

Turning to similar studies in the Virgo cluster, Fumagalli et al. (2011) constrained the ages along the blue tail of a dwarf irregular galaxy VCC 1217/IC 3418. Using optical and UV photometric bands, these latter authors performed SED fitting of the central galaxy and of the blue knots and filaments along its tail, assuming an extended star formation history. For the central galaxy, IC 3418, they found a star formation quenching time of ~400 Myr due to RPS, but a large range of ages in the tail regions, from 80 to 1400 Myr. However, some of the star-forming regions were later spectroscopically confirmed as background objects by Kenney et al. (2014). For the confirmed tail regions, Kenney et al. (2014) obtained ages ranging from 80 to 390 Myr, consistent with the quenching time from their models. In the tail of NGC 4254, which is likely the result of tidal interactions, Boselli et al. (2018a) estimate an age of ≤100 Myr for typical star forming regions, whereas for the tail of a recently ram-pressure stripped (~50 Myr ago) dwarf galaxy IC 3476, Boselli et al. (2021) give a typical age of ≤20 Myr for a few star forming complexes observed in the tail at ~8 kpc from the stellar disk.

Similar to these examples, the ages of the regions we obtained in our analysis are young and point to recent formation (except for a few regions with very large ages and stellar masses that are likely contaminated by background objects). The ages of these young regions are consistent with the quenching of the disk occurring a few 100 Myr ago.

4.2. Gradients along the tail

Figure 10 shows the $u - g$ color and age of the blue regions as a function of their projected distance from the center of the UDG. The top panel of Fig. 10 shows a comparison of the measured $u - g$ color of our regions with that of the knots of IC 3418 from Fumagalli et al. (2011). While our $u-g$ colors are consistent with theirs, we do not find any indication of a clear gradient, contrary to Fumagalli et al. (2011) who observed a small color gradient in the tail of IC 3418, with the outermost part of the tail being relatively blue in comparison to the rest and at a larger radial separation than ours. With a large dispersion in the color and proximity to NGVS 3543, it is hard to draw strong conclusions as to the presence of a color gradient among our regions.

The bottom panel of Fig. 10 shows the age of the blue regions as a function of their distance from the center of the UDG. Kenney et al. (2014) provided a relation for the age gradient from the head to the tail of a linear stream of fireballs (see their Eq. (2)). We assumed a stream of length 9.4 kpc (the farthest region we observe), $\Sigma_{\rm gas} = 1\,M_\odot\,{\rm pc}^{-2}$ in the outskirts of the UDG before undergoing RPS (obtained from the models discussed in Sect. 3.1), and a relative velocity of $v = 1084\,{\rm km\,s}^{-1}$ for the HI gas cloud of AGC 226178 with respect to the Virgo cluster center (Boselli et al. 2014; Cannon et al. 2015). We adopted two different values for the intra-cluster medium (ICM) density, with $\rho_{\rm ICM} = 10^{-4}$ and 10^{-3} cm^{-3}, corresponding to the ICM density at the distance of NGVS 3543 from the cluster center (Simionescu et al. 2017) and a typical ICM density of the Virgo cluster from Vollmer et al. (2001), respectively. Using these values in Eq. (2) of Kenney et al. (2014), we obtain a gradient of a few tens of millions of years from the head to the tail of our stream. The ages that we measure are consistent in order of magnitude with the expected age gradient for a stream of this length. However, considering the uncertainties and the scatter of our data, it is difficult to determine an age gradient from the observations. Moreover it is not surprising to see a lack of age gradient because these regions are very young. Clear gradients are usually seen in galaxies that interacted slightly longer ago (Fumagalli et al. 2011). Also, while our data are consistent with

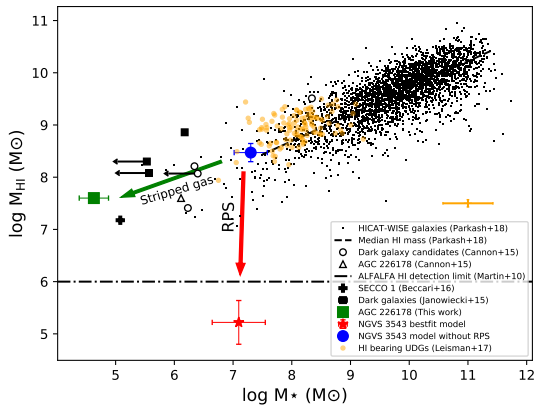

Fig. 11. Stellar mass vs. HI mass of the HI-selected sample of spirals, UDGs and "dark" galaxies. The blue circle and the red star respectively mark the position of NGVS 3543 before and after the RPS event, as given in Table 4. The total gas masses from the models were converted into HI by multiplying by a factor 0.74 to take into account Helium and metals. Part of the stripped gas from the UDG can form AGC 226178, shown as the green square. The small black squares show the dark galaxies from Janowiecki et al. (2015), the black open circles and triangle are those from Cannon et al. (2015). The black cross is SECCO 1 (AGC 226067) from Beccari et al. (2017). The black points and the black dashed line are the HI-selected spirals and their median HI mass, respectively, from Parkash et al. (2018). The small yellow circles and error bars are the HI bearing UDGs and the mean dispersion from Leisman et al. (2017), respectively. The black dot-dashed line marks the HI mass detection limit of the ALFALFA survey (Martin et al. 2010).

some predictions, the uncertainties on the adopted parameters (gas density, ICM density, relative velocity) can lead to a wide range of possible gradients, as can be seen in Fig. 10 for two densities. Moreover, the Kenney et al. (2014) formula may correspond to an ideal situation, but the formation of star clusters is not necessarily a continuous function of the distance from the stripping event, as found in the simulations of Steyrleithner et al. (2020) in which star formation sets in not immediately after the stripping event but in the stream behind.

4.3. A global scenario for the formation of almost dark galaxies and red UDGs

4.3.1. An UDG undergoing a RPS event

The analysis of the ram-pressure models of NGVS 3543 and the identification of some very young star forming regions near it lead us to an interesting question about the formation and evolution of such systems.

Figure 11 shows a comparison of the stellar mass vs. HI mass of our UDG and AGC 226178 with that of an HI-selected sample of regular spirals, UDGs and dark galaxies from the literature. Leisman et al. (2017) provide a sample of HI-bearing UDGs from the ALFALFA survey. We estimated the stellar mass of these UDGs from their g-band absolute magnitudes and $g - r$ color (see Table 1 of Leisman et al. 2017), following the stellar mass-to-light-ratio–color relation for LSB galaxies given in Du et al. (2020). The distribution of UDGs falls along the low-stellar-mass tail of the $M_\star - M_{\rm HI}$ relation for regular galaxies from Parkash et al. (2018). These gas-rich, low-stellar-mass UDGs can be considered as the population of field blue UDGs discussed by Prole et al. (2019). The stellar mass and HI mass of our model for NGVS 3543 before the RPS event ($\sim 10^7\ M_\odot$ and $\sim 10^8\ M_\odot$, respectively) suggest that its progenitor was similar to the population of blue UDGs. The RPS event quickly transformed this galaxy into a gas-poor ($M_{\rm HI} \sim 10^5\ M_\odot$), red UDG and totally quenched its star formation activity. Although our estimates are uncertain (as indicated by the error bars, not including additional sources of systematic error such as IMF choice), Fig. 11 illustrates this scenario in the global context of stellar and gaseous masses of galaxies covering a very large dynamical range.

The HI detection limit of the ALFALFA survey is of the order of $\sim 10^6\ M_\odot$ (Martin et al. 2010). The nondetection in HI for NGVS 3543 (Cannon et al. 2015) is therefore in complete agreement with our RPS scenario. Moreover, the HI mass of AGC 226178 from Cannon et al. (2015) ($M_{\rm HI} = 4 \times 10^7\ M_\odot$) corresponds to ∼10% of the mass of the gas expected to be stripped from NGVS 3543 as indicated by the models. Considering that in similar RPS events a large fraction of the stripped gas can also change phase, becoming ionized gas before hot gas (Boselli et al. 2016, 2021), our analysis is consistent with the gas detected as AGC 226178 having been recently stripped from NGVS 3543 during the RPS event.

4.3.2. Formation of an almost-dark object

We made an estimate of the total stellar mass corresponding to the HI-source AGC 226178 using the combined stellar masses of our u-band or UV-selected regions within the HI contour of AGC 226178 (as shown in Fig. 1). This gives an average stellar mass of $\sim 5 \times 10^4\ M_\odot$ for AGC 226178. This stellar mass and HI mass is consistent with a sample of some other almost dark galaxy candidates from the literature (Cannon et al. 2015; Janowiecki et al. 2015; Beccari et al. 2017). However, we see in Fig. 11 that the stellar mass of AGC 226178 from Cannon et al. (2015) is about 20 times larger than the value we obtained. Cannon et al. (2015) and Janowiecki et al. (2015) used standard mass-to-light-ratio–color relations to estimate their stellar masses. This naturally provides a more massive stellar mass than ours, which is not computed with a standard mass-to-light ratio, but is adapted to the young stellar population. More generally, one has to be cautious when considering the stellar masses derived for dark galaxies, whose distance and nature are not always certain. For example, in the case of AGC 229385, Janowiecki et al. (2015) give a stellar mass of $2 \times 10^6\ M_\odot$ while Brunker et al. (2019) provide $4 \times 10^5\ M_\odot$ for the same object. This difference is due to the different distances they adopted, respectively 25 Mpc and 5 Mpc. In our case, the Hα detection in VESTIGE provides a strong indication of cluster membership and distance of AGC 226178.

While this suggests that knots of young stars may also be associated to other almost-dark galaxies if they formed in a similar way, this is not necessarily the case as star formation is not always present in RPS tails (Boselli et al. 2016), and once formed, the star complexes do not suffer RPS anymore and may decouple from the gas (Cramer et al. 2019).

4.3.3. The possibility of tidal interactions

Beccari et al. (2017) studied another interesting object in the Virgo cluster, SECCO 1, with similar stellar and HI properties to those encountered in AGC 226178. SECCO 1 is characterized by similar compact regions dominated by a young stellar population, but does not have any evident nearby companion. Bellazzini et al. (2018) suggests a possible origin for SECCO 1 as a stripped gas cloud from an interacting triplet of dwarf

galaxies ∼250 kpc away. In this scenario, the stripped gas cloud that formed SECCO 1 could have survived in the ICM for ∼1 Gyr before becoming an isolated object with ongoing star formation.

In our case, we do not find the presence of any massive interacting companion that could explain its properties (e.g., tidal interactions). We investigated the possibility of tidal interactions in NGVS 3543 by looking for low-surface-brightness features extending beyond its effective radius. For the green dashed region shown in Fig. 1 along the NE of NGVS 3543, we observed a faint network of high-frequency structures with a statistically significant detection (signal-to-noise ratio, S/N = 8) characterized by a g-band surface brightness of μ_g = 27.6 mag arcsec^{-2} (the significance of such an estimate has been cross-checked with the photometric procedure described in Fossati et al. 2018; Longobardi et al. 2020). Nevertheless, the retrieved irregular structure could also be related to the fact that the UDG progenitor was a low-mass-star-forming system – which are generally characterized by an irregular morphology – and that a few 100 Myr was not sufficient for the stars to be redistributed into a smooth spheroidal distribution. We thereby consider tidal interaction negligible and conclude that RPS is the dominant process taking place in the galaxy.

4.3.4. Summary

Our analysis strongly suggests that NGVS 3543 is in the process of transformation from a blue UDG into a red UDG by a RPS event. Because red UDGs are very frequent in nearby rich clusters (Koda et al. 2015; Muñoz et al. 2015; Mihos et al. 2015; Román & Trujillo 2017; Janssens et al. 2017), this suggests that RPS could be one of the major processes in the formation of gas-poor red UDGs. As in the case of AGC 226178, our observations also suggest that RPS could be the mechanism responsible for the formation of the almost dark objects discussed in the literature (Duc & Bournaud 2008; Cannon et al. 2015; Janowiecki et al. 2015; Leisman et al. 2017; Brunker et al. 2019). Some gas-poor, faint, still undetected parent galaxies could exist in the vicinity of these almost dark objects (in the form of quenched UDGs similar to NGVS 3543, which was not detectable before data at the depth of those provided by NGVS became available).

5. Conclusions

We present a multi-wavelength study of the Virgo cluster ultra-diffuse galaxy NGVS 3543 and its surroundings using optical, UV, and Hα narrow-band imaging data from the NGVS, GUViCS, and VESTIGE surveys, respectively. We identified an over-density of blue compact regions located at ∼5 kpc south of the stellar disk of the galaxy, the majority of which were detected in Hα and UV. These regions are embedded in a large ($\sim 10^7\ M_\odot$) cloud of HI gas previously detected by ALFALFA and the VLA. Our comparative analysis of the spectro-photometric properties of the UDG galaxy and of its associated extra-planar star-forming regions, combined with tuned multi-zone models of galaxy evolution, led us to the following conclusions:

- The UDG galaxy NGVS 3543 has undergone a RPS event over the last few hundred million years, transforming it from a gas-rich, blue UDG to a gas-poor, red UDG. The predominance of red UDGs in clusters could be related to similar events at earlier times.
- A fraction of the gas lost from the perturbed gas-rich UDG during the RPS event has undergone a star formation episode, forming compact young star clusters in the tail of stripped gas.
  These newly formed regions have a mean age and stellar mass of the order of 20 Myr and $10^4\ M_\odot$, respectively, consistent with being byproducts of the recent RPS event.
- These young star complexes are located well inside an HI gas cloud of $\sim 10^7\ M_\odot$, previously identified as an almost dark galaxy by Cannon et al. (2015).

While many mechanisms have been proposed in the literature for the formation of these peculiar families of objects populating nearby clusters (UDGs and almost dark clouds), our results indicate that RPS, already known to be a major process shaping galaxy evolution in young clusters, has recently had a major driving effect in the formation of the NGVS 3543 system. This galaxy may be representative of other objects with similar characteristics, in which the same process has occurred, albeit in a more distant past.

Narrow-band Hα imaging data gathered during the VESTIGE survey have been of paramount importance in the study of the star formation history of this peculiar system. We are therefore planning to extend this study of the origin of UDGs and LSB galaxies to the whole Virgo cluster once the survey is completed.

Acknowledgements. We are grateful to the whole CFHT team who assisted us in the preparation and in the execution of the observations and in the calibration and data reduction: Todd Burdullis, Daniel Devost, Bill Mahoney, Nadine Manset, Andreea Petric, Simon Prunet, Kanoa Withington. We acknowledge financial support from "Programme National de Cosmologie and Galaxies" (PNCG) funded by CNRS/INSU-IN2P3-INP, CEA and CNES, France, and from "Projet International de Coopération Scientifique" (PICS) with Canada funded by the CNRS, France. Co-author Matteo Fossati has received funding from the European Research Council (ERC) under the European Union's Horizon 2020 research and innovation programme (grant agreement No 757535).

References

Amorisco, N. C., & Loeb, A. 2016, MNRAS, 459, L51
Avni, Y. 1976, ApJ, 210, 642
Beccari, G., Bellazzini, M., Magrini, L., et al. 2017, MNRAS, 465, 2189
Bellazzini, M., Armillotta, L., Perina, S., et al. 2018, MNRAS, 476, 4565
Bertin, E., & Arnouts, S. 1996, A&AS, 117, 393
Blakeslee, J. P., Jordán, A., Mei, S., et al. 2009, ApJ, 694, 556
Boissier, S., & Prantzos, N. 1999, MNRAS, 307, 857
Boissier, S., & Prantzos, N. 2000, MNRAS, 312, 398
Boissier, S., Boselli, A., Prantzos, N., & Gavazzi, G. 2001, MNRAS, 321, 733
Boissier, S., Monnier Ragaigne, D., Prantzos, N., et al. 2003, MNRAS, 343, 653
Boissier, S., Boselli, A., Ferrarese, L., et al. 2016, A&A, 593, A126
Boquien, M., Burgarella, D., Roehlly, Y., et al. 2019, A&A, 622, A103
Boselli, A., Boissier, S., Cortese, L., et al. 2006, ApJ, 651, 811
Boselli, A., Boissier, S., Cortese, L., & Gavazzi, G. 2008a, ApJ, 674, 742
Boselli, A., Boissier, S., Cortese, L., & Gavazzi, G. 2008b, A&A, 489, 1015
Boselli, A., Boissier, S., Cortese, L., et al. 2009, ApJ, 706, 1527
Boselli, A., Boissier, S., Heinis, S., et al. 2011, A&A, 528, A107
Boselli, A., Voyer, E., Boissier, S., et al. 2014, A&A, 570, A69
Boselli, A., Cuillandre, J. C., Fossati, M., et al. 2016, A&A, 587, A68
Boselli, A., Fossati, M., Ferrarese, L., et al. 2018a, A&A, 614, A56
Boselli, A., Fossati, M., Cuillandre, J. C., et al. 2018b, A&A, 615, A114
Boselli, A., Fossati, M., Longobardi, A., et al. 2019, A&A, 623, A52
Boselli, A., Lupi, A., Epinat, B., et al. 2021, A&A, 646, A139
Bradley, L., Sipocz, B., Robitaille, T., et al. 2019, https://doi.org/10.5281/zenodo.3478575
Brunker, S. W., McQuinn, K. B. W., Salzer, J. J., et al. 2019, AJ, 157, 76
Bruzual, G., & Charlot, S. 2003, MNRAS, 344, 1000
Burgarella, D., Buat, V., & Iglesias-Páramo, J. 2005, MNRAS, 360, 1413
Burkert, A. 2017, ApJ, 838, 93
Caldwell, N., & Bothun, G. D. 1987, AJ, 94, 1126
Calzetti, D., Armus, L., Bohlin, R. C., et al. 2000, ApJ, 533, 682
Cannon, J. M., Martinkus, C. P., Leisman, L., et al. 2015, AJ, 149, 72
Cardelli, J. A., Clayton, G. C., & Mathis, J. S. 1989, ApJ, 345, 245
Chabrier, G. 2003, PASP, 115, 763
Conselice, C. J. 2018, Res. Notes Am. Astron. Soc., 2, 43

Conselice, C. J., Gallagher, J. S. I., & Wyse, R. F. G. 2003, AJ, 125, 66
Cortese, L., Marcillac, D., Richard, J., et al. 2007, MNRAS, 376, 157
Cramer, W. J., Kenney, J. D. P., Sun, M., et al. 2019, ApJ, 870, 63
Di Cintio, A., Brook, C. B., Macciò, A. V., Dutton, A. A., & Cardona-Barrero, S. 2019, MNRAS, 486, 2535
Du, W., Cheng, C., Zheng, Z., & Wu, H. 2020, AJ, 159, 138
Duc, P.-A., & Bournaud, F. 2008, ApJ, 673, 787
Erben, T., Schirmer, M., Dietrich, J. P., et al. 2005, Astron. Nachr., 326, 432
Erben, T., Hildebrandt, H., Lerchster, M., et al. 2009, A&A, 493, 1197
Ferrarese, L., Côté, P., Cuillandre, J.-C., et al. 2012, ApJS, 200, 4
Ferrarese, L., Côté, P., MacArthur, L. A., et al. 2020, ApJ, 890, 128
Fossati, M., Fumagalli, M., Boselli, A., et al. 2016, MNRAS, 455, 2028
Fossati, M., Mendel, J. T., Boselli, A., et al. 2018, A&A, 614, A57
Fumagalli, M., Gavazzi, G., Scaramella, R., & Franzetti, P. 2011, A&A, 528, A46
Gavazzi, G., Boselli, A., Scodeggio, M., Pierini, D., & Belsole, E. 1999, MNRAS, 304, 595
Gavazzi, G., Boselli, A., Mayer, L., et al. 2001, ApJ, 563, L23
Gil de Paz, A., & Madore, B. F. 2005, ApJS, 156, 345
Giovanelli, R., Haynes, M. P., Kent, B. R., et al. 2005, AJ, 130, 2598
Gullieuszik, M., Poggianti, B. M., McGee, S. L., et al. 2020, ApJ, 899, 13
Haynes, M. P., Giovanelli, R., Martin, A. M., et al. 2011, AJ, 142, 170
Hester, J. A., Seibert, M., Neill, J. D., et al. 2010, ApJ, 716, L14
Hinz, J. L., Rieke, M. J., Rieke, G. H., et al. 2007, ApJ, 663, 895
Hughes, T. M., Cortese, L., Boselli, A., Gavazzi, G., & Davies, J. I. 2013, A&A, 550, A115
Impey, C., Bothun, G., & Malin, D. 1988, ApJ, 330, 634
Jáchym, P., Kenney, J. D. P., Ržuička, A., et al. 2013, A&A, 556, A99
Jacob, J. C., Katz, D. S., Berriman, G. B., et al. 2010, ArXiv e-prints [arXiv:1005.4454]
Janowiecki, S., Leisman, L., Józsa, G., et al. 2015, ApJ, 801, 96
Janssens, S., Abraham, R., Brodie, J., et al. 2017, ApJ, 839, L17
Jimenez, R., & Heavens, A. F. 2020, MNRAS, 498, L93
Jimenez, R., Padoan, P., Matteucci, F., & Heavens, A. F. 1998, MNRAS, 299, 123
Kenney, J. D. P., Geha, M., Jáchym, P., et al. 2014, ApJ, 780, 119
Kennicutt, R. C. Jr., Edgar, B. K., & Hodge, P. W. 1989, ApJ, 337, 761
Koda, J., Yagi, M., Yamanoi, H., & Komiyama, Y. 2015, ApJ, 807, L2
Kroupa, P. 2001, MNRAS, 322, 231
Leisman, L., Haynes, M. P., Janowiecki, S., et al. 2017, ApJ, 842, 133
Leitherer, C., Schaerer, D., Goldader, J. D., et al. 1999, ApJS, 123, 3
Lim, S., Côté, P., Peng, E. W., et al. 2020, ApJ, 899, 69
Longobardi, A., Boselli, A., Fossati, M., et al. 2020, A&A, 644, A161
Martin, A. M., Papastergis, E., Giovanelli, R., et al. 2010, ApJ, 723, 1359
Martin, G., Kaviraj, S., Laigle, C., et al. 2019, MNRAS, 485, 796
Mei, S., Blakeslee, J. P., Côté, P., et al. 2007, ApJ, 655, 144
Mihos, J. C., Durrell, P. R., Ferrarese, L., et al. 2015, ApJ, 809, L21
Mo, H. J., Mao, S., & White, S. D. M. 1998, MNRAS, 295, 319
Morrissey, P., Schiminovich, D., Barlow, T. A., et al. 2005, ApJ, 619, L7
Muñoz, R. P., Eigenthaler, P., Puzia, T. H., et al. 2015, ApJ, 813, L15
Muñoz-Mateos, J. C., Boissier, S., Gil de Paz, A., et al. 2011, ApJ, 731, 10
Noll, S., Burgarella, D., Giovannoli, E., et al. 2009, A&A, 507, 1793
Parkash, V., Brown, M. J. I., Jarrett, T. H., & Bonne, N. J. 2018, ApJ, 864, 40
Poggianti, B. M., Gullieuszik, M., Tonnesen, S., et al. 2019, MNRAS, 482, 4466
Prole, D. J., van der Burg, R. F. J., Hilker, M., & Davies, J. I. 2019, MNRAS, 488, 2143
Rahman, N., Howell, J. H., Helou, G., Mazzarella, J. M., & Buckalew, B. 2007, ApJ, 663, 908
Raichoor, A., Mei, S., Erben, T., et al. 2014, ApJ, 797, 102
Roediger, E., & Hensler, G. 2005, A&A, 433, 875
Román, J., & Trujillo, I. 2017, MNRAS, 468, 703
Sandage, A., & Binggeli, B. 1984, AJ, 89, 919
Schlegel, D. J., Finkbeiner, D. P., & Davis, M. 1998, ApJ, 500, 525
Silk, J. 2019, MNRAS, 488, L24
Simionescu, A., Werner, N., Mantz, A., Allen, S. W., & Urban, O. 2017, MNRAS, 469, 1476
Sorgho, A., Chemin, L., Kam, Z. S., Foster, T., & Carignan, C. 2020, MNRAS, 493, 2618
Stewart, K. R. 2017, in Gas Accretion and Angular Momentum, eds. A. Fox, & R. Davé, 430, 249
Steyrleithner, P., Hensler, G., & Boselli, A. 2020, MNRAS, 494, 1114
Sun, M., Donahue, M., & Voit, G. M. 2007, ApJ, 671, 190
Tremmel, M., Wright, A. C., Brooks, A. M., et al. 2020, MNRAS, 497, 2786
van der Burg, R. F. J., Muzzin, A., & Hoekstra, H. 2016, A&A, 590, A20
van Dokkum, P. G., Romanowsky, A. J., Abraham, R., et al. 2015, ApJ, 804, L26
Venhola, A., Peletier, R., Laurikainen, E., et al. 2017, A&A, 608, A142
Verde, L., Oh, S. P., & Jimenez, R. 2002, MNRAS, 336, 541
Vollmer, B., Cayatte, V., Balkowski, C., & Duschl, W. J. 2001, ApJ, 561, 708
Xu, C. K., Donas, J., Arnouts, S., et al. 2005, ApJ, 619, L11
Yagi, M., Yoshida, M., Komiyama, Y., et al. 2010, AJ, 140, 1814
Yagi, M., Koda, J., Komiyama, Y., & Yamanoi, H. 2016, ApJS, 225, 11
Yoshida, M., Yagi, M., Komiyama, Y., et al. 2008, ApJ, 688, 918

A&A 650, A99 (2021)

Appendix A: χ^2 distributions for the determination of stellar mass and age of the regions

Figures A.1 and A.2 give the χ^2 fitting results used for the determination of stellar mass and age of all the *u*-band- and UV-selected regions discussed in this work. See Sect. 3.2 and Fig. 8 for a detailed description of the models and one example figure.

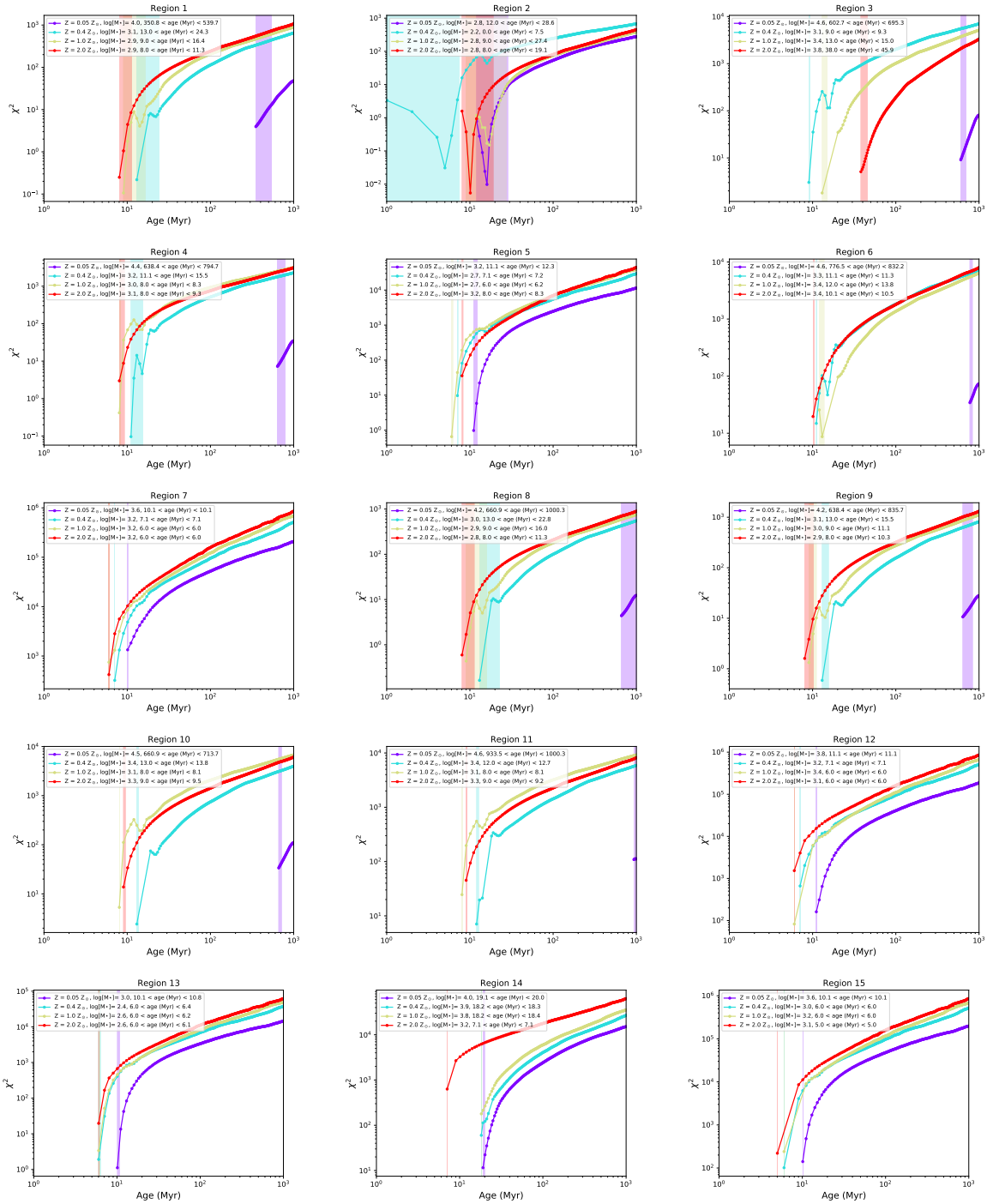

Fig. A.1. χ^2 as a function of age for the *u*-band-selected regions. See Fig. 8 for an example and details in Sect. 3.2.

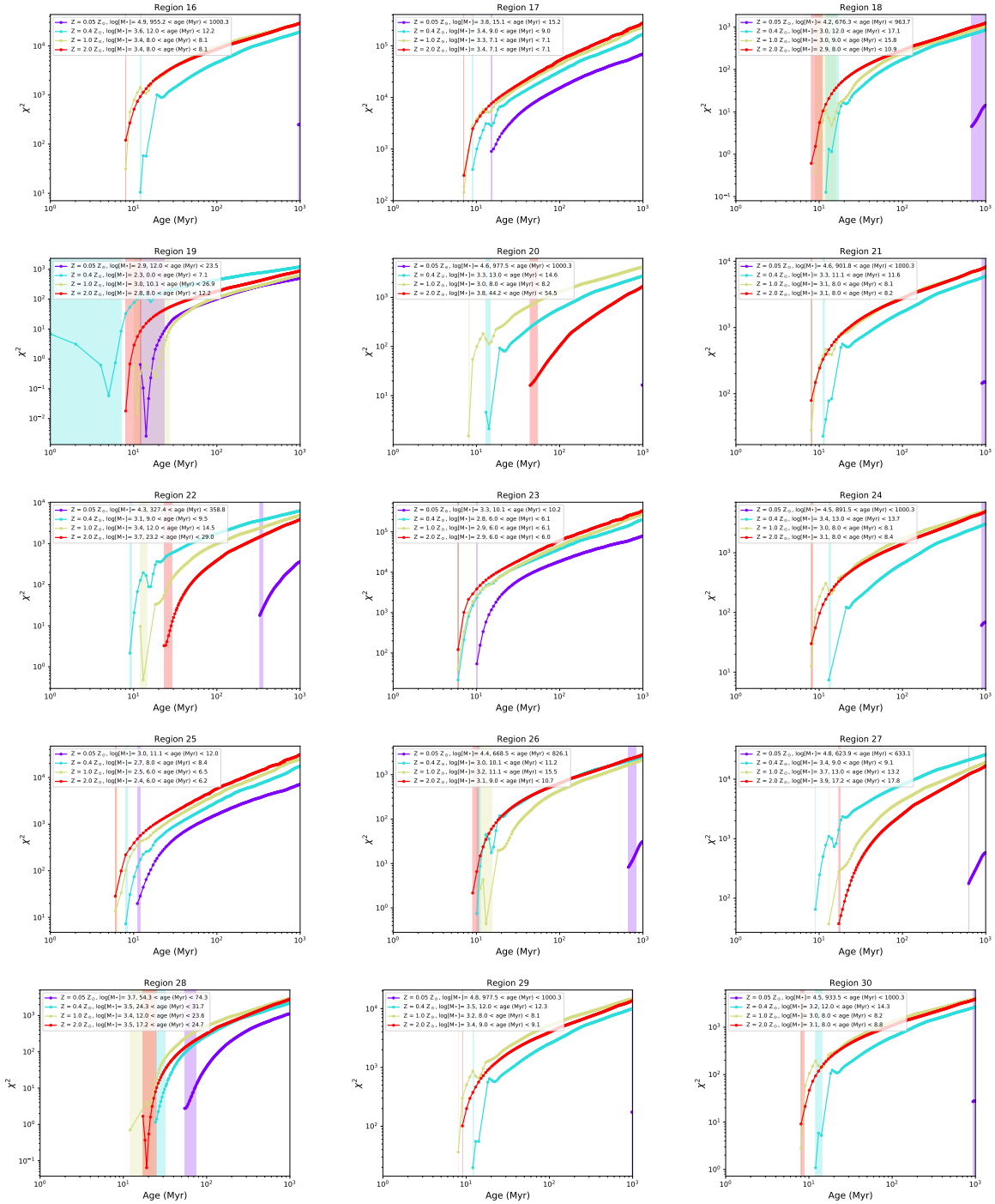

Fig. A.1. continued.

A&A 650, A99 (2021)

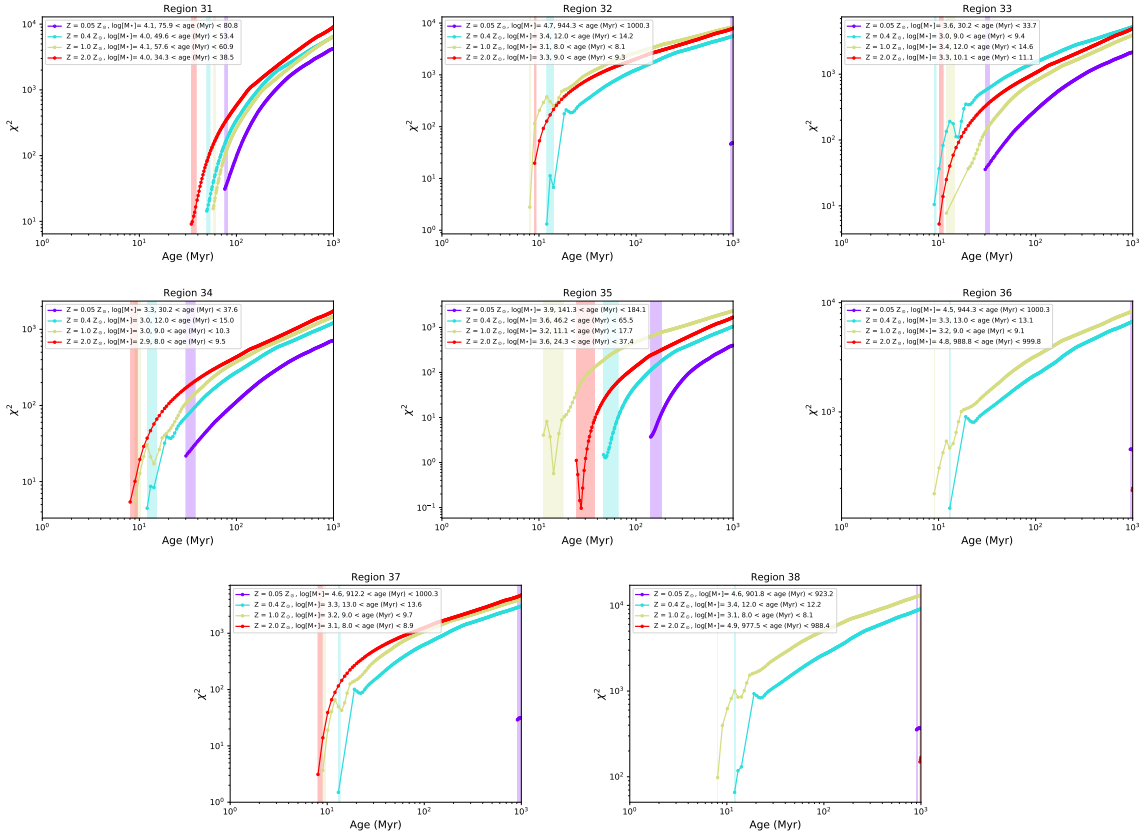

Fig. A.1. continued.

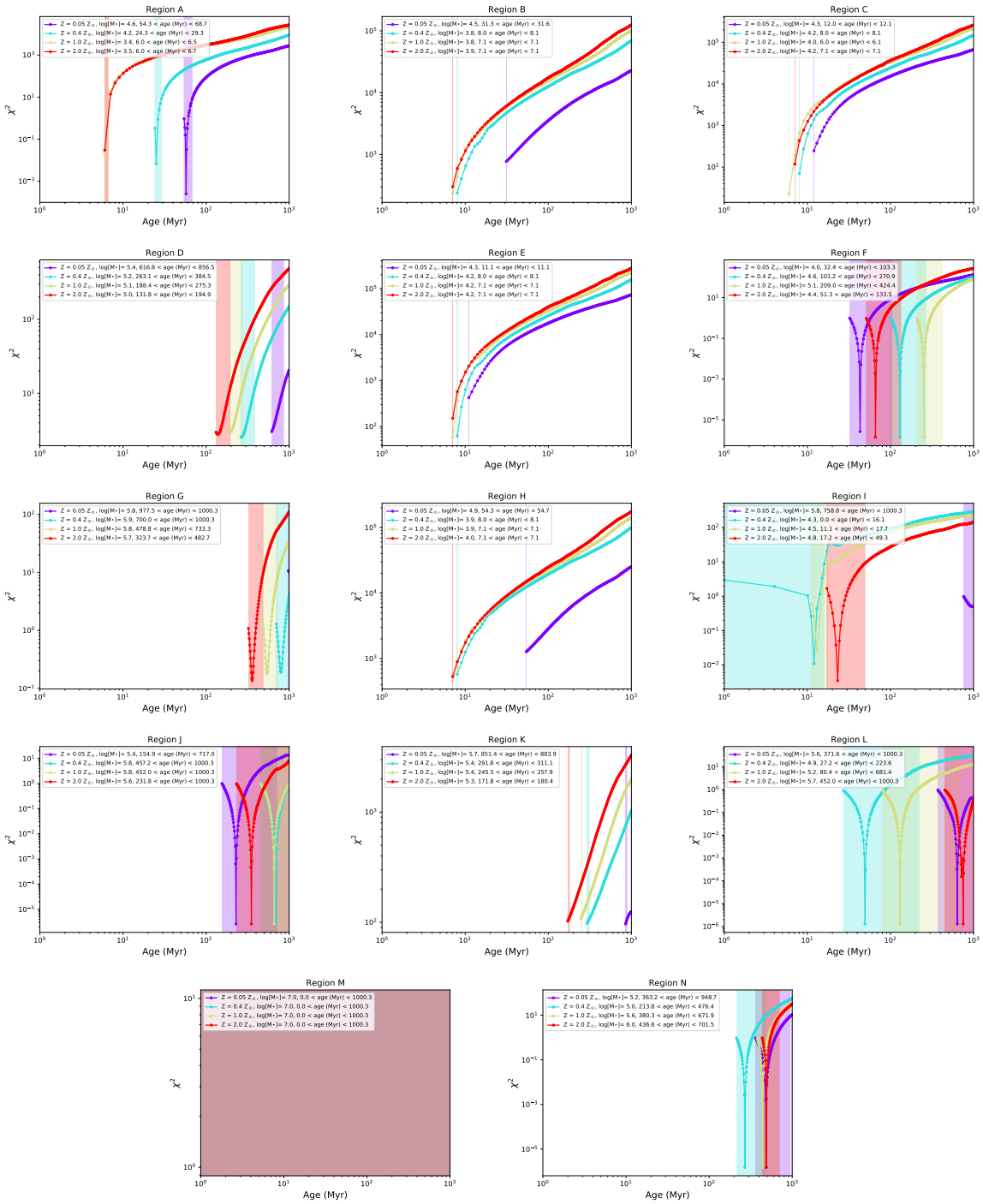

Fig. A.2. χ^2 as a function of age for the UV-selected regions. See Fig. 8 for an example and details in Sect. 3.2.

Appendix B: CIGALE determination of ages and stellar masses of *u*-band- and UV-selected regions

Numerous assumptions in the stellar population models and fitting methodology could affect our results. To investigate this, we carried out a completely independent estimation of the properties of the regions using the SED modelling code CIGALE (Burgarella et al. 2005; Noll et al. 2009; Boquien et al. 2019). We fitted each region given in Table 3 with single burst population models from CIGALE, using the input parameters given in Table B.1 and following the same approach we adopted with Starburst99 models (Leitherer et al. 1999). The differences with respect to the fit made with Starburst99 include the use of the Chabrier (2003) instead of Kroupa (2001) IMF, and different population synthesis models. Instead of relying on just the best-fit model, CIGALE estimates the physical properties from the probability distribution function. It also naturally takes into account upper limits in the computation of the goodness of fit. Finally, we performed two sets of fits, one with dust, and another without (as for Starburst 99).

The stellar masses and ages obtained with CIGALE are shown in Fig. B.1, and can be directly compared to those derived using Starburst99 (see Fig. 9). CIGALE gives older ages and larger scatters than Starburst99 for many of the *u*-band- and UV-selected regions. This effect can be due to the different spectrum of very young stellar populations between Starburst99 and Bruzual & Charlot (2003). Leitherer et al. (1999) stress that stellar evolutionary models are very uncertain when red super giant are important contributors, and the codes predictions may vary. It is especially the case in the age range 5–20 Myr for single star populations, and the reason for the presence of peaks in Fig. 3, with a relatively red $u - g$ color around that age (these peaks are less large when Bruzual & Charlot (2003) populations are considered). On the other hand, for regions with Hα detection, CIGALE gives young ages, as we obtained with Starburst99. The Hα measurements prove to be a very strong constraint in the modelling of very young star forming regions.

Comparison between the two panels from Fig. B.1 shows that the inclusion of dust leads to even younger ages. Although our modelling using Starburst99 models did not account for dust, we obtained young ages (<20 Myr) for the majority of the regions. The inclusion of dust in these models would only produce even younger ages, like it is the case with CIGALE.

In conclusion, regardless of the code used for the stellar population, the fitting procedure, or the inclusion or not of dust, we always find that a significant number of regions are indeed young (<20 Myr), with similar stellar masses. We are therefore confident that our results are robust.

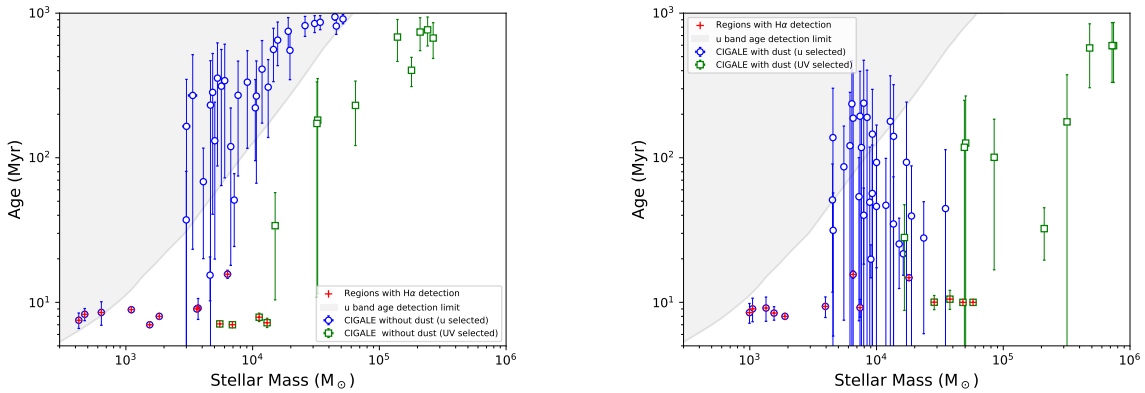

Fig. B.1. Age and stellar mass determined using CIGALE for all the regions in Table 3. These panels can be directly compared to Fig. 9 obtained with Starburst99. *Left and right panels*: results obtained with CIGALE without and with dust, respectively. The blue circles and green squares represent *u*-band- and UV-selected regions, respectively. The gray shaded area is our *u*-band detection limit in stellar mass and age. The red crosses identify the Hα detected regions.

Table B.1. Input parameters for CIGALE.

Paremeter	Model without dust	Model with dust
Pop. synth. mod.	Bruzual & Charlot (2003)	Bruzual & Charlot (2003)
Dust model	No dust	Calzetti et al. (2000)
IMF	Chabrier (2003)	Chabrier (2003)
Metallicity	0.004, 0.008, 0.02, 0.05	0.004, 0.008, 0.02, 0.05
Age	1–1000 Myr, step 1	1–1000 Myr, step 1
$E(B-V)$	0	0–0.7 mag, step 0.01
UV bump amplitude	0	0

Notes. Line 1: Population synthesis model. Line 2: Dust model. Line 3: IMF. Line 4: Stellar metallicity. Line 5: Age interval and sampling. Line 6: Attenuation. Line 7: Amplitude of the UV bump (Noll et al. 2009).